UNIVERSITÀ DEGLI STUDI DI BERGAMO

DOTTORATO DI RICERCA
IN
TECNOLOGIE PER L'ENERGIA E L'AMBIENTE
XXVIII ciclo
anno 2016

WETTABILITY EFFECTS ON INTERFACE DYNAMICS AND PHASE-CHANGE

Doctoral thesis:
Ileana Malavasi

Supervisor:
Prof. Marco Marengo

Università degli studi di Bergamo
ISBN 978-88-97413-16-5
Open access copy available at: http://hdl.handle.net/10446/52325

Abstract

The present thesis is a result of three year research study aimed at understanding the wettability effects on interface dynamics and phase-change. The project was performed in between University of Bergamo, University of Mons, CNR-ISTEC Institute of Science and Technology for Ceramics (Faenza, Italy), Politecnico di Milano and Italian Space Agency (ASI).

The scope was to add a piece of the puzzle in understanding the basic physics knowledge on the wettability influence on: 1) pool boiling heat transfer; 2) liquid-surface interaction.

Energy saving and research for the development of alternative energy sources are the major concerns of the twenty-first century. The solution is twofold:

- dependence on traditional energy sources should be eliminated and it serves to found renewable energy sources;

- serves to determine innovative methods to increase the efficiency of the current energy systems in order to save conventional energy resources, increasing their sustainability.

Researches shown that the miniaturization in the production of electro-mechanical systems is a key factor in the development of energy-efficient systems.

The requests, for example, of electronic devices, such as smartphones, tablet and laptop, more and more small and thin, but with increasingly high performance, lead to a denser associated electronics packaging, in which the

heat generated per unit area is increased. Heat that must be removed and that is dissipated through the use of innovative heat exchange devices, such as microfluidic devices. The increase of the performance of these devices involves focusing on the heat exchange phenomena that occur inside these systems, and in particular on the boiling process, that is the evaporation at the solid-liquid interface when the surface temperature is higher than the temperature of the fluid in saturation condition. Research also show that the heat exchange performance of a surface is in function of its roughness and wettability. For this reason, pool boiling experiments were carried out with degassed water on stainless steel substrates with different surface topography and wettability. Boiling curves have been measured together with visual high-speed observations of the boiling process. The onset temperature of nucleate boiling has been measured and the influence of surface roughness and wettability has been quantified for different surfaces, with the aim to better understand the effect of superhydrophobicity on pool boiling. The original finding is that the boiling curve shape is rather different between hydrophilic and superhydrophobic case, keeping the same surface roughness: superhydrophobic surfaces show a peculiar behaviour similar to an early “quasi-Leidenfrost” regime for low superheat, i.e. once boiling is initiated, the boiling process immediately enters the film boiling regime. Also, for the roughness range analysed, the wettability has a predominant effect with respect to the roughness, when the contact angle exceeds the typical value for superhydrophobic surfaces (receding contact angle $\theta_{rec} > 135°$).

The theme of the energy saving also concerns the impact of drops on dry solid surfaces, since the process is involved in many industrial processes, i.e. spray cooling, ink-jet printing, spray painting, fuel injection, raindrop erosion. The investigation and the comprehension of the dynamics of a single drop impact is the first step to understand and control the liquid-solid interaction of more complex phenomena, such as the formation of fouling in the marine environment, the formation of ice on aircraft wings, the pressure drops in the ducts and the oxidation in the pipe-line. For this reason, a considerable part of the work has been then devoted to study experimentally, using a high-speed camera, the normal impact of water and hexadecane liquid drops onto dry, rigid surfaces with different wettabilities. The results highlighted that it is not possible to easily correlate contact angles (receding, advancing and hysteresis) and drop impact outputs on different surfaces. In order to explain the observed phenomena, physical and chemical characteristics of both the liquid drops and the surfaces have to be taken into account. Surface morphology is crucial in defining the critical velocity over which impalement occurs. Also surface chemistry is relevant, as dipolar interactions between

surface functional groups and molecules in the liquid phase can favour impalement. As far as the liquid properties are concerned, with increasing viscosity and lower fluid surface tension the Cassie-to-Wenzel transition, i.e. impalement of the liquid meniscus into the texture, shifts to smaller Weber. These results emphasize how an accurate design of the surface properties must be pursued in the future research towards dynamically amphiphobic surfaces.

Moreover, the construction of an experimental apparatus for the evaluation of the heat exchange coefficients of an oscillating interface is reported. This part of the work is included in the appendix as such apparatus has been designed and built, however no experiments were performed.

Keywords: wettability, superhydrophobic surfaces, amphiphobicity, phase-change, pool boiling, interface dynamics, drop impact

Alla mia famiglia

Contents

List of Figures

List of Tables

Chapter 1

1 Introduction

1.1 Motivation

Both wetting and dewetting of liquids play an important role in many natural and technological processes. Wettability is a fundamental property of a solid surface, which play an important role in our daily life, industry and agriculture. Functional surfaces with the desired wettability have aroused much interest because of their great advantages in applications.

In the last decade, notwithstanding the open issue of their durability, superhydrophobic surfaces (SHS) have attracted an increasing interest in both the academic and industrial sectors, due to their remarkable self-cleaning and anti-sticking properties involving a wide range of potential applications: biomedical, microfluidic, corrosion resistance, drag reduction, anti-icing, contamination and oxidation protection, etc.

Since the last twenty years, minichannel heat sinks receive much attention from scientific and industrial community due to their very promising and effective cooling potential. Minichannels have comparatively larger heat transfer surface area and higher surface-area-to-volume ratio as compared to their conventional counterparts, therefore, the use of minichannels in heat exchangers makes them compact, lightweight and thermally more efficient. Latent heat associated with phase change of the fluids can be exploited to maintain the required temperature of the micro-electronics devices, as during the phase change process, the temperature of the fluid is dictated by saturation temperature and pressure. Also the use of the fluid boiling allows the design of compact heat exchange devices using the less fluid inventory, for the same heat transfer performance, in comparison to the cases when single phase liquid is used as a coolant.

Two-phase cooling is attractive over single-phase liquid cooling from two main considerations: high heat transfer coefficient during pool/flow boiling and higher heat fluxes for a given mass flow rate of the coolant. One advantage of pool/flow boiling systems is the ability of the fluid to carry larger amounts of thermal energy through the latent heat of vaporization. With water, the latent heat is significantly higher (2257 kJ/kg) than its specific heat of 4.2 kJ/kg°C at 100°C. This feature is especially important for refrigerant systems. Although the latent heat of many potential refrigerants is around 150–300 kJ/kg at temperatures around 30–50°C, the biggest advantage is that a suitable refrigerant can be chosen to provide desirable evaporation temperatures [1]. Miniaturization in the field of electronics leads to dense packaging and integration of more components on an electronic circuit. Integration of components in an electronic circuit has been driven by Moore's law according to which the number of transistors incorporated on a chip roughly doubles every 24 months. Apparent consequences of Moore's law are the reduced size and increased performance of a microprocessor, and at the same time a decrease in production cost of transistors. If production cost of transistors decreases surprisingly, miniaturization of electronics, motivated by new application areas and modern fabrication techniques, allows obtaining faster chip speeds but at the same time the chip power densities increases dramatically. Consequently, recent developments in the field of microelectronics results in dissipation of much higher heat fluxes than ever before, which exceed the fan cooling limits. Heat fluxes generated in microelectronics reaches about 100 W/cm^2 today, and this number keeps rising in near future. The surface temperature of high heat dissipating microchips has to be maintained below 80 to 85°C in order to ensure the effective and reliable operation of the electronic circuitry. Practically, the ineffective cooling of high heat flux devices is a major constraint in dense packaging of microelectronics and has to be resolved in order to nurture the miniaturization process. Smaller and light-weight design of space crafts also needs miniaturization of different electronics and avionics components including integration of single components in a small space/volume and the resulting dense packaging of components poses serious thermal management problems. Therefore, novel technologies for thermal management need to be developed in order to promote the miniaturization process, as the use of passive two-phase heat transfer devices and microfluidic devices. Although the impetus for mini two-phase heat transfer devices work comes from miniaturization of microelectronics, their application is not limited to microelectronics industry. Mini heat exchangers may be used in automotive industry to reduce the refrigerant charge significantly as compared to conventional sized heat exchangers for the same effectiveness and heat transfer performance. Great design flexibility may be achieved and space constraints can be overcome due to compactness of the heat exchanger. The overall weight and cost of the heat exchange system may be reduced due to the less material required for manufacturing and less requirements of fluid inventory. The compact and efficient evaporators and condensers will increase the performance of the refrigeration and air-conditioning system at the same time reducing the charge of refrigerant. There are also many others possible application areas, e.g. fuel cells, chemical processing industry, microfluidic devices, separation and modification of cells in bio applications etc. Several experiments in the literature show the higher and effective heat transfer in case of compact mini heat exchangers as compared to their macro counter parts. Higher and effective heat transfer offered by compact heat exchangers can help to promote sustainability and at the same time effective use of natural resources may be achieved.

Whatever configuration of compact heat exchangers is used, the heat energy removed at the chip is transported away and rejected from the system by condensation at a remote location [2] [3]. Therefore, it is necessary to gain a fundamental understanding of phase change heat transfer in miniature/micro devices. Despite the attractive and motivating advantages of these devices, the understanding of the fundamental hydrodynamic and thermal transport mechanisms is far from satisfactory. Therefore, more studies are essential focusing on the understanding of governing phenomena. In addition, it is also necessary to understand how it is possible to increase the heat exchange coefficients and how it is possible to influence such factors. Moreover, the deep knowledge of the physical phenomena involved allows also to build and develop numerical models that can be used to analyze and evaluate similar physical scenarios. The tools currently available can usually not produce simple and reliable answers. The reason for this is that both the models and the input data rely on simplifications and approximations. As so often in engineering, it is essential to have a good understanding of the underlying assumptions and mechanisms, and to investigate where the greatest uncertainties are likely to be found. Cross-checking the results as far as possible, a much more difficult task in multi-phase than in single-phase flow, is also essential.

Moreover, the surface wettability influences the phenomenon concerning the behavior and outcome of droplets impact. The impact of drops onto dry solid surfaces is a phenomenon involved in many industrial applications, i.e. spray cooling, ink-jet printing, spray painting, fuel injection, raindrop erosion, etc. Drop impact analysis can be also linked to fields concerning applications non directly connected to the engineering disciplines, i.e. aerosol droplets containing the pathogen and disease spread (influenza, ebola, tuberculosis, varicella pox), air conditioning mists (sometimes used to maintain the freshness of meat and vegetables in supermarkets, and fine mists for cooling people in hotter climates is sometimes used in restaurants), external and internal skin and mucous membranes of the body (face, hand/foot, throat, nose, eye), sunspray, sunscreen and mosquito repellent products, pesticide crop spray (superspreading of defoliants or protectants on foliage), cosmetics and fake tan application, upholstery and industrial surface cleaning formulas, drug inhalers (salbutamol and cortico-steroidal and other metered dose inhalers for asthma, rhinitis). Understand the basic physics and design surfaces with a wettability able to facilitate the application of interest can once again impact on lower energy consumption.

1.2 Thesis outline

The present Ph.D. work thesis deals with investigating the wettability effects on interface dynamics and phase-change. After the present chapter of introduction, a suitable literature analysis and experiments are proposed in order to understand the basic physics on this important issue which it has to deal with energy savings and energy efficiency. The second chapter takes up the basic knowledge, useful in understanding the Ph.D. work thesis here presented. The aim of chapter three is to identify how good the role of the wettability in the basic pool boiling phenomena is understood, and experimental analysis is done in order to fill the gap in understanding how the surface wettability influences the heat exchange in the pool boiling phenomenon. By doing this, one expects to contribute for the investigation of pool boiling heat transfer enhancement to proceed in a more systematic manner. In chapter four, the normal impact of both water and hexadecane drops on solid dry surfaces with different wettability was experimentally followed by a high-speed camera. Throughout the impact on such surfaces, the drop mobility is related to a sort of “dynamic superamphiphobicity”, defined as the critical wetting value under which an impacting drop with a given impact velocity does not wet the surface, i.e. a complete drop rebound is observed. In this case the impact velocity, the interfacial tension, the viscosity of the liquid, the chemical and physical properties of the surface determine the drop outcome as well as the spreading and the retraction dynamic. In chapter five the overall results are presented and discussed, and conclusions and future perspective are drawn. In appendix, the construction of an experimental apparatus for the evaluation of the heat exchange coefficients of an oscillating interface is reported. This part of the work is included in the appendix as such apparatus has been designed and built only, no experiments were performed that allowed to estimate the coefficients of interest.

Chapter 2

2 Basic knowledge

2.1 Interfacial phenomena

An interface is a surface forming a common boundary among two different phases of matter, such as an insoluble solid and a liquid, two immiscible liquids, a liquid and an insoluble gas or a liquid and vacuum. The importance of the interface depends on the type of system: the bigger the quotient area/volume, the more effect the surface phenomena have. Therefore interfaces are very important in systems with big area to volume ratios, such as colloids. A liquid interface is defined as the interface between a liquid and a solid or as the interface between two fluids, either two liquids or a liquid and a gas/vapor. Interfaces can be flat or curved. For example oil droplets in a salad dressing are spherical but the interface between water and air in a glass of water is mostly flat. Interfacial effects on the dynamic behavior of flow systems can be profound, even when the proportion of matter in interfacial regions is extremely small. Furthermore, motion may originate in an interface in systems that are not in thermal or compositional equilibrium. Summary of the different liquid interfaces types, their occurrence and their applications are shown in Table 2.1.

Interface type	Occurrence	Importance/applications
Liquid-Solid	Any situation where a solid surface is in contact with a liquid	Coatings/corrosion Lubrication Wetting Biomaterials (fouling) ….
Liquid-Liquid	Contact between two immiscible (or partially miscible) liquids	Emulsions (food, chemistry, cosmetics, pharma, mining, ….) Environment (oil spills,…) Biomembranes ….
Liquid-Gas (Vapor)	Liquid in direct contact with a gas or in equilibrium with its vapor	Foams (food, chemistry, cosmetics, pharma, mining, ….) Free liquid surfaces ….

Table 2.1: Summary of the different liquid interfaces types, their occurrence and their importance.

2.2 Surface tension in liquid-gas interfaces

Surface tension is a contractive tendency of the surface of a liquid that allows it to resist an external force. At liquid-air interfaces, surface tension results from the greater attraction of liquid molecules to each other (due to cohesion) than to air (due to adhesion) (Figure 2.1). For the molecules within the liquid phase, the intermolecular forces from all directions are balanced. Although the forces acting on the molecules at the liquid-vapor interface are balanced along the tangential direction, the attractive force from the molecules in the liquid phase, F_i, tends to pull the molecules at the liquid-vapor interface toward the liquid phase because the attractive force from the vapor phase, F_o, is much weaker. The net inward force $F_i - F_o$ causes movement of the liquid molecules until the maximum number of molecules is in the interior. The net effect is an inward force at its surface that causes liquid to behave as if its surface were covered with a stretched elastic membrane. This creates some internal pressure and forces liquid surfaces to contract to the minimal area. In addition to the surface tension at a liquid-vapor (lv) interface, surface tensions can also exist at interfaces between solid-liquid interface (sl) and solid-vapor interface (sv). Surface tension has the dimension of force per unit length, or of energy per unit area. The two are equivalent - but when referring to energy per unit of area, people use the term surface energy - which is a more general term in the sense that it applies also to solids and not just liquids.

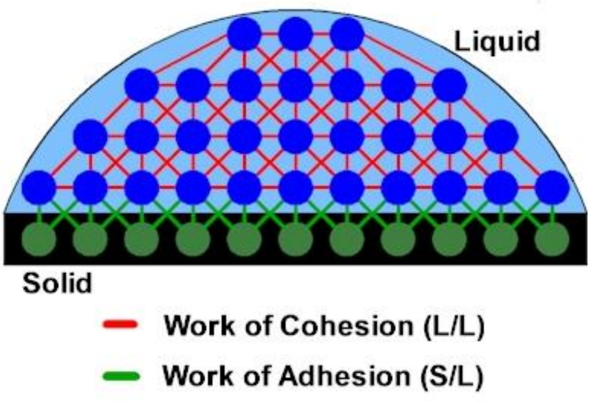

Figure 2.1: Diagram of the forces on liquid molecules and on liquid/surface interface [4]. Because of the relatively high attraction of water molecules for each other, water has a high surface tension (72.8mN/m at 20°C) compared to that of most other liquids.

Surface tension effects on the shape of interfaces. Surface tension is responsible for the shape of liquid droplets. Although easily deformed, droplets tend to be pulled into a spherical shape by the cohesive forces. In the absence of other forces, including gravity, drops of virtually all liquids would be perfectly spherical. The spherical shape minimizes the necessary "wall tension" of the surface layer according to Laplace's law. Another way to view surface tension is in terms of energy. A molecule in contact with a neighbor is in a lower state of energy than if it were alone (not in contact with a neighbor). The interior molecules have as many neighbors as they can possibly have, but the boundary molecules are missing neighbors (compared to interior molecules) and therefore have a higher energy. For the liquid to minimize its energy state, the number of higher energy boundary molecules must be minimized. The minimized quantity of boundary molecules results in a minimized surface area. As a result of surface area minimization, a surface will assume the smoothest shape it can (mathematical proof that "smooth" shapes minimize surface area relies on use of the Euler–Lagrange equation). Since any curvature in the surface shape results in greater area, a higher energy will also result.

The force due to surface tension is generally negligible in comparison with the pressure and gravitational forces but the force due to surface tension assumes predominance for narrow liquid columns such as those in capillary tubes, in bubble mechanics and liquid-jet studies for flow through porous substances (Figure 2.2, Figure 2.3).

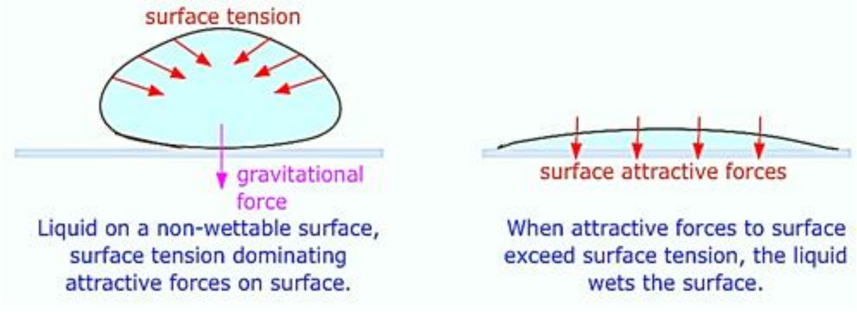

Figure 2.2: Surface tension and wettability.

Capillary action (sometimes capillarity, capillary motion, or wicking) is the ability of a liquid to flow in narrow spaces without the assistance of, and in opposition to, external forces like gravity. The effect can be seen in the drawing up of liquids between the hairs of a paint-brush, in a thin tube, in porous materials such as paper, in some non-porous materials such as liquefied carbon fiber, or in a cell. It occurs because of intermolecular forces between the liquid and surrounding solid surfaces. If the diameter of the tube is sufficiently small, then the combination of surface tension (which is caused by cohesion within the liquid) and adhesive forces between the liquid and container act to lift the liquid. In short, the capillary action is due to the pressure of cohesion and adhesion which cause the liquid to work against gravity. Capillary implies the rise or depression of the level of a liquid in a capillary tube when it is held vertically or inclined in the liquid (Figure 2.3). The phenomenon is explained with reference to the angle of contact between the liquid and the capillary material and the balance of force on the column of the liquid in them. If the liquid wets a surface and spreads out, the angle of contact between them is small, but if a liquid does not do so, the angle is large. The extent to which a liquid may wet solid surface depends upon properties of adhesion and cohesion. If the adhesion is greater than the cohesion, the wetting tendency is greater and the angle of contact is smaller. Whether a liquid would rise or drop in a capillary tube depends upon the angle of contact between the liquid and the capillary material. Acute angle of contact corresponds with capillary rise and obtuse angle of contact with capillary depression.

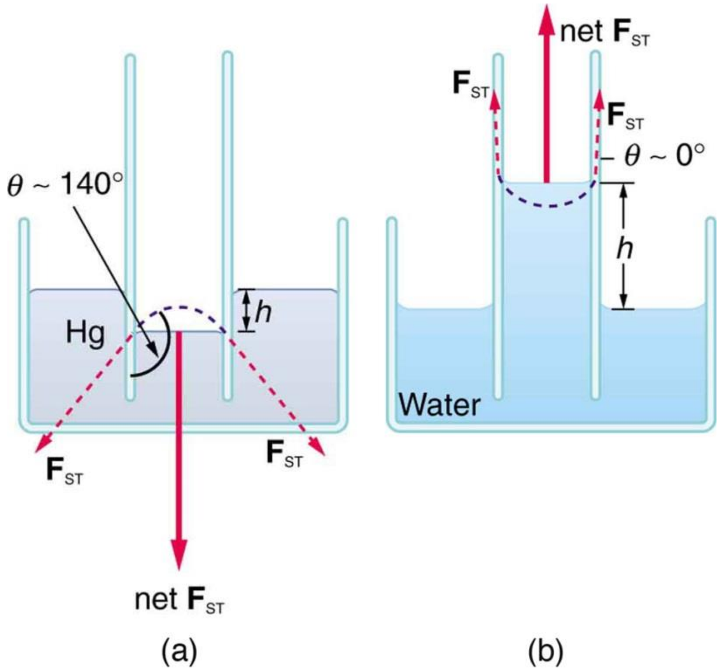

Figure 2.3: Capillary phenomenon in an open tube [5]. (a) Mercury is suppressed in a glass tube because its contact angle is greater than 90º. Surface tension exerts a downward force as it flattens the mercury, suppressing it in the tube. The dashed line shows the shape the mercury surface would have without the flattening effect of surface tension. (b) Water is raised in a glass tube because its contact angle is nearly 0º. Surface tension therefore exerts an upward force when it flattens the surface to reduce its area.

The interaction of the liquid with the capillary surface will cause the meniscus rise (or fall) at this interface. If the tube diameter is very small, these surface interactions become large enough to raise (or lower) the entire volume of liquid in the tube.

The height of liquid in the capillary can be determined by a balance between the hydrostatic pressure and the pressure drop across the meniscus computed using the Young-Laplace equation. The Young–Laplace equation states that this pressure difference is proportional to the interfacial tension, γ, and inversely proportional to the effective radius, r, of the interface. The pressure difference also depends on the wetting angle, θ, of the liquid on the surface of the capillary.

$$p_c = \rho g h = \frac{2\gamma \cos\theta}{r} \quad (1)$$

The equation for capillary pressure is only valid under capillary equilibrium, which means that there cannot be any flowing phases.
Capillary rise phenomena can be observed when the liquid wets the tube wall. If the liquid cannot wet the tube wall, the capillary rise h is negative, which indicates that there is a capillary depression, as shown in Figure 2.3. The pressure drop generated by capillary effects becomes large as the capillary diameter decreases; capillary forces are significant in microfluidic channels.
Surface tension, equilibrium contact angles, and capillary pressure determine the behavior of liquids in small-diameter tubes, slots, and porous media. If the channel surface is hydrophilic (e.g. θ<90°), capillary forces will pull liquid into the channel. If the channel surface is hydrophobic (e.g. θ > 90°), capillary forces will resist the flow of liquid inside the channel, and additional pressure will be required to fill (Figure 2.4).

Figure 2.4: Capillary forces in microchannels for hydrophilic and hydrophobic case.

Since surface tension depends on temperature, a permanent non uniformity of temperature or concentration (for a multicomponent system) at a liquid-vapor interface causes a surface tension gradient. Consequently, the liquid in the lower surface tension region near the interface will be pulled toward the region with higher surface tension. The interfacial area with small surface tension expands at the expense of the area with greater surface tension, which in turn establishes a steady flow pattern in the liquid; this flow caused by the surface tension gradient along the liquid-vapor (gas) interface is referred to as the Marangoni effect.

2.3 Contact angle and wettability

When a liquid is in contact with a solid surface, its behavior depends on the relative magnitudes of the surface tension forces and the attractive forces between the molecules of the liquid and of those comprising the surface. The contact line is the locus of points where the three phases intersect. The contact angle, θ, is the angle through the liquid between the tangent to the liquid-vapor interface and the tangent to the solid surface (Figure 2.5). The contact angle is defined for the equilibrium condition. In 1805, Young published the basic equation for the contact angle on a smooth and homogeneous solid:

$$\gamma_{ls} \cos\theta = \gamma_{sg} - \gamma_{sl} \tag{2}$$

where γ_{lg}, γ_{sg} e γ_{sl} are the interfacial tensions between the liquid and the vapor, the solid and the vapor and the solid and the liquid, respectively. However, Young’s equation expresses a theoretical and ideal condition since real surfaces are never absolutely smooth. On a real surface, where chemical and morphological heterogeneities exist, multiple metastable configurations (i.e., multiple contact angles) can be observed. As such, to better characterize a surface, it is necessary to provide both the advancing and receding contact angles (θ_A and θ_R respectively), measured by expanding and contracting sessile water drops on a horizontal surface: this method is called “sessile drop method” (Figure 2.6).

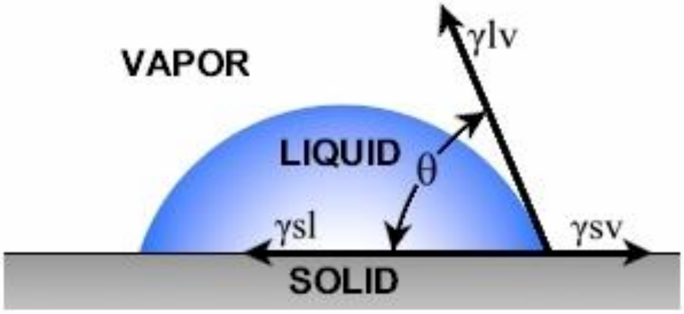

Figure 2.5: Drop of liquid on a planar surface.

Besides the equilibrium or static angle, the quasi-static dynamic advancing and receding contact angles are more convenient to characterize the motion of the contact line mainly when the velocity of the contact line significantly departs from zero. Advancing contact angle is the maximum stable angle and receding contact angle is the minimum stable angle. θ_A and θ_R provide the range of contact angles at equilibrium, but also provide an indication of the drop mobility, which is related to their difference, the contact angle hysteresis, $\Delta\theta = \theta_A - \theta_R$. The difference between the advancing and the receding contact angle is related to the energy dissipated (irreversibility) at the contact line (e.g. [6]).

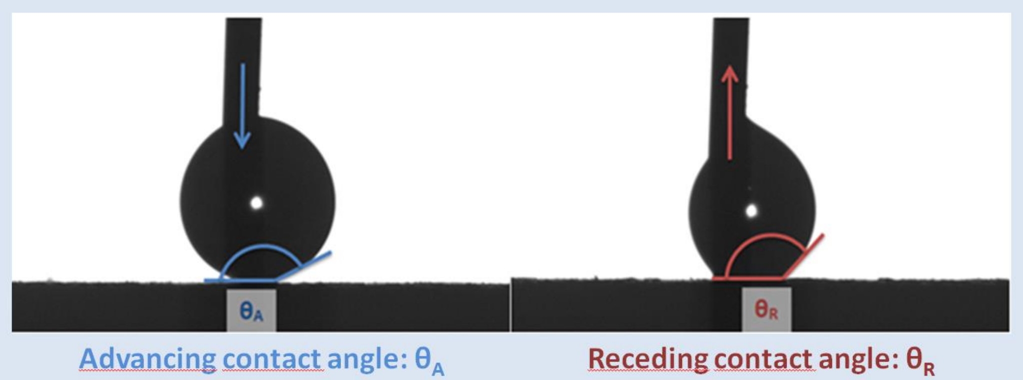

Figure 2.6: Illustration of advancing and receding contact angles.

If the liquid molecules are strongly attracted to the solid molecules then the liquid drop will completely spread out on the solid surface, corresponding to a contact angle of 0°. This is often the case for water on bare metallic or ceramic surfaces [7], although the presence of an oxide layer, or contaminants, on the solid surface can significantly increase the contact angle. Generally, if the water contact angle is smaller than 90°, the solid surface is considered hydrophilic and if the water contact angle is larger than 90° (Figure 2.7a), the solid surface is considered hydrophobic. Highly hydrophobic surfaces made of low surface energy (e.g. fluorinated) materials may have water contact angles as high as ~120° [7]. Some materials with also highly rough surfaces may have a water contact angle even greater than 150°, due to the presence of air pockets under the liquid drop. These are called superhydrophobic surfaces (SHS) (Figure 2.7b). In literature, superhydrophobic surfaces are traditionally defined as surfaces on which advancing contact angles exceed 150° and the hysteresis is less than 10° [8-14]. However, such criteria are somewhat arbitrary and should be not taken strictly. As an example, Rioboo et al. [15] recently defined a new methodology based on controlled drop slide on a horizontal surface. The authors found that only when the receding contact angle is above 135° the surface can be defined as superhydrophobic and the drop slides. The proposed limit is also close to the value 138.6°, which was identified using a theoretical model by Li and Amirfazli [16], as the minimum receding contact angle on a pillar like surface. As such, the two conditions for superhydrophobicity are: i) $\theta_R > 135°$, since the authors find it developed on a more rational basis than the conventionally θ_A reported value of 150°; and ii) $\Delta\theta < 10°$, as traditionally indicated in literature.

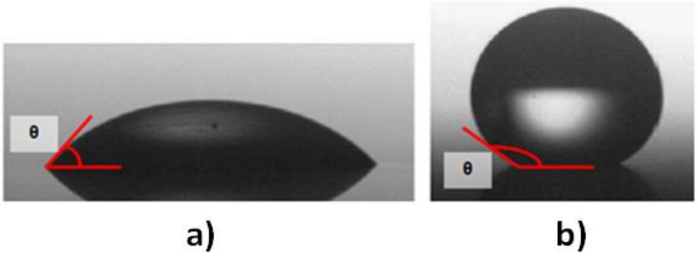

Figure 2.7: Water drop on a hydrophilic surface (a) and on a superhydrophobic surface (b). Drops have the same volume, equal to 11.5µl (corresponding to a spherical drop with diameter 2.8 mm). Highlighted the contact angles.

A schematic representation of the correlation between contact angle and wettability is shown in Figure 2.8.

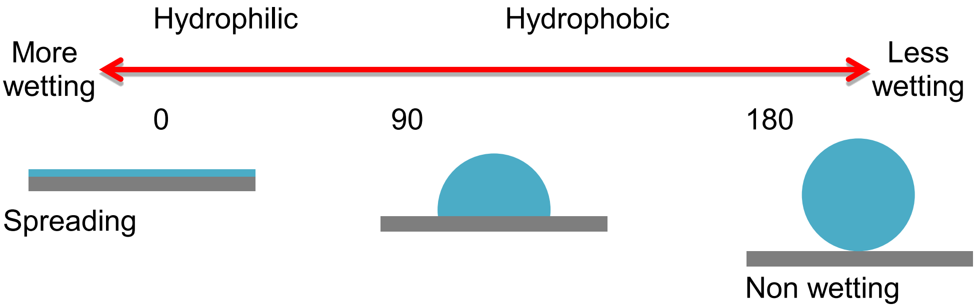

Figure 2.8: Correlation between contact angle and wettability.

Contact angles are extremely sensitive to contamination; values reproducible to better than a few degrees are generally only obtained under laboratory conditions with purified liquids and very clean solid surfaces.

Wettability can be explained by the relative strength of the cohesive (liquid/liquid) and adhesive (solid/liquid) forces (Table 2.2). Strong adhesion with weak cohesion produces very low contact angles with nearly complete wetting. As the solid/liquid interactions let more weak and the liquid/liquid interactions get stronger, wetting diminishes and contact angle increases. Wettability can be attributed to a strong intermolecular attractive force near the interface between the solid and liquid; there is a significant decrease in the surface free energy per unit area in a wetting liquid.

Contact angle	**Wetting**	**S/L**	**L/L**
0°	Complete	Strong	Weak
60°	High	Strong	Weak
90°	Moderate	Weak	Weak
120°	Low	Weak	Strong
180°	None	Weak	Strong

Table 2.2: Correlation between wettability and solid/liquid and liquid/liquid interactions strengthen.

Wetting regimes are classified also into three distinct states: the Cassie-Baxter state, the Wenzel state and the intermediate state [17,18]. When the liquid is in contact with the entire exposed surface of the solid, i.e. the drop penetrates into the corrugation of the surface; the Wenzel model describes the wetting regime (Figure 2.9). According to Cassie−Baxter model exists a state in which the liquid does not penetrate into the hollows of the surface, i.e. the liquid does not wet the entire surface but remains suspended on top of the surface asperities (Figure 2.9). Consequently, it has an interface consisting of both solid and vapor. This is the case of the superhydrophobic surfaces. Lastly, the transition state represents that the droplet partially penetrates between the pillars [17,18]. The discussion thus far has treated the three phases – solid, liquid, and vapor – as though their boundaries were sharply-delineated lines or surfaces. This idealization, which serves as a useful analytical device at the macroscopic level, does not hold at the microscopic level. At that level, the interfaces between phases appear as regions over which properties vary continuously, rather than as lines or surfaces with discontinuous property changes. Intermolecular forces of both repulsion and attraction influence how material in the various phases is distributed throughout these interfacial regions. Adsorption – which is one of the consequences of this intermolecular action – occurs when a liquid or solid phase adjacent to a second phase (solid, liquid, or gas) retains molecules, atoms, or ions of the second phase at the shared interface. Adsorption affects the wetting process because it alters the interfacial tension of the solid-liquid interface.

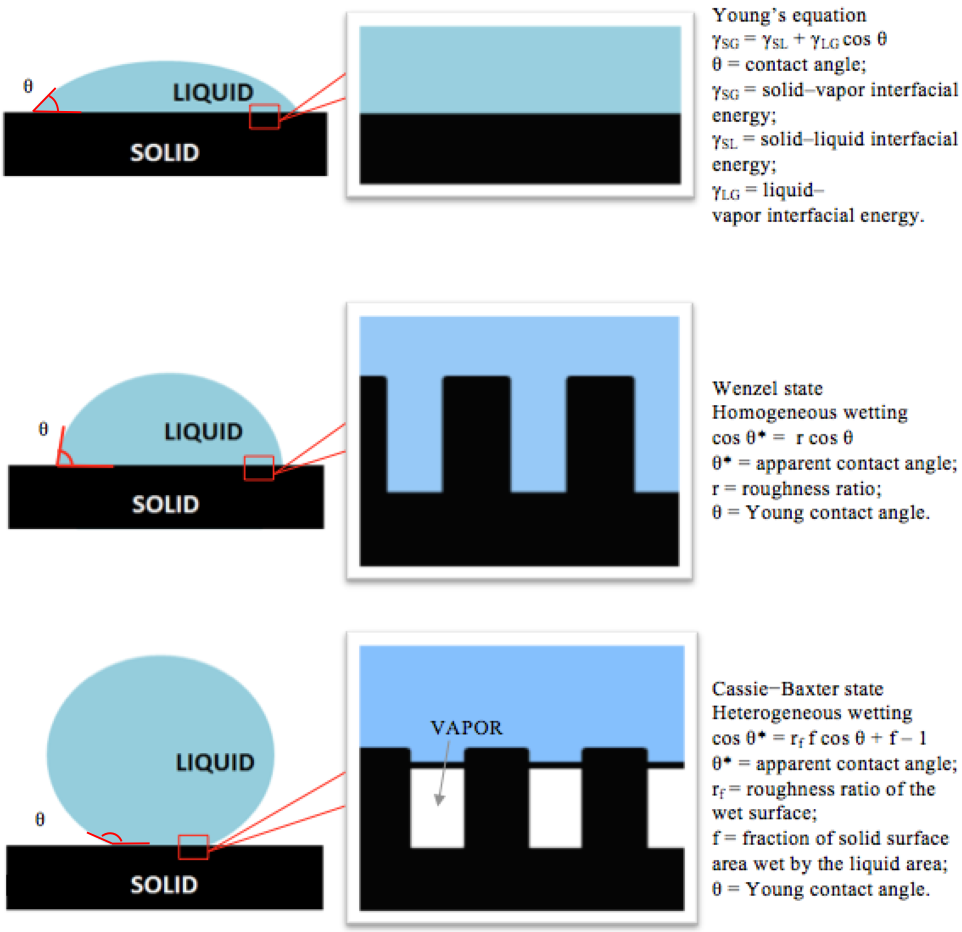

Young's equation
$\gamma_{SG} = \gamma_{SL} + \gamma_{LG} \cos\theta$
θ = contact angle;
γ_{SG} = solid–vapor interfacial energy;
γ_{SL} = solid–liquid interfacial energy;
γ_{LG} = liquid–vapor interfacial energy.

Wenzel state
Homogeneous wetting
$\cos\theta^{*} = r\cos\theta$
θ^{*} = apparent contact angle;
r = roughness ratio;
θ = Young contact angle.

Cassie–Baxter state
Heterogeneous wetting
$\cos\theta^{*} = r_f f \cos\theta + f - 1$
θ^{*} = apparent contact angle;
r_f = roughness ratio of the wet surface;
f = fraction of solid surface area wet by the liquid area;
θ = Young contact angle.

Figure 2.9: Representation of the different states.

Hydrophilic materials allow water to wet its surface forming a film or coating. Hydrophilic materials are usually charged or have polar side groups to their structure that attract water. A hydrophilic material's ability to absorb and transport water gives it numerous applications in cleaners, housings, cables, tubes and hoses, waterproofing, catheters, surgical garments, etc. A hydrophilic coating on a tube or hose eliminates the need for other lubricants, which is useful to prevent cross-contamination. Hydrophilic coatings on plugs and O-rings increase their ability to stop leaks; this is the basis for water-stop and sealants. Hydrophobic materials repeal water. There are many cases of hydrophobic surfaces in nature, including some plant leaves, butterfly wings, duck feathers and some insects' exoskeletons.

There are many synthetic hydrophobic materials available including waxes, alkanes, oils, Teflon, and Gortex. There are numerous applications for using these materials such as protection of stone, wood, and concrete from the effects of rain, waterproofing fabrics and the removal of water from glass surfaces, such as a windshield, to increase transparency.

Hydrophobic materials are also used for cleaning up oil spills, removal of oil from water and for chemical separation processes to remove nonpolar from polar compounds. Another use for hydrophobic and hydrophilic materials is the storage and distribution of water and methanol in miniature direct methanol fuel cells (DMFCs). For the distribution of methanol, a material is chosen that wets methanol but is hydrophobic to water. This type of material is a preferential wicking material. This allows neat methanol to be stored and distributed in a DMFC without water diffusion into the methanol storage layers. The water storage layer at the anode of the fuel cell is a hydrophilic material. It is not preferential to either water or methanol and provides a layer in which they can mix.

2.4 Superhydrophilic surfaces

Superhydophilicity involves strong interactions with water. Superhydrophilic surfaces are commonly identified via their complete wetting by water, i.e. water assumes a contact angle CA of ≈0°. Generally surfaces are considered superhydrophilic if θ_A is less than 10° within 1 s of the initial wetting [19]. Anyway, such surfaces are prone to contamination by oily liquids due to their superhydrophilic nature, which appears to be generally unavoidable. While a plethora of articles have been written on the phenomenon of superhydrophobicity, relatively little is available on this topic.

Superhydrophilicity is prevalent throughout nature including a broad range of plant species [20,21]. Examples can be found in the aquatic plants or macrophytes, which grow in or near water sources. Their superhydrophilic surfaces can be divided into three categories: permanently wet, water absorbing and super water spreading; each possessing distinctly different structures and characteristics [22]. Permanently wet plants possess larger thin leaves with large specific surface areas. Water absorbing plant surfaces usually possess pores or hairs. Super water spreading are typical of several insect capturing carnivorous plants (Nepenthes rafflesiana traps insects using wet and slippery pitcher rim) and of plants with shorter drying periods by increasing the size of the water-air interface (the leaf structures of Calathea zebrine which possess relatively uniform conical structures), with a composite leaf structure that includes hair papilla, glands and channel-like structures [22].

Structures similar to those present in plants (Figure 2.10) are utilized in many industrial micro-nanoporous membrane-based separations, including microfiltration (pore size: 0.1-10 µm), ultrafiltration (pore size: ~10 nm), nanofiltration (pore size: ~1 nm), gas separation (pore size: 0.2-0.5 nm) [22]. Nanofiltration is generally applied for sterilization of pharmaceutical products and medical facilities, while ultrafiltration and nanofiltration are more often employed to purify and condense (bio)macromolecules, such as polymers and proteins. Operations such as hydrogen recovery, collection of refinery gases, and olefin/paraffin separations are common examples of gas separations [22].

Superhydrophilic surfaces have their own advantages such as ultrafast drying, antifogging and antireflective proprieties: by allowing water vapor to completely spread and form a uniform ultrathin film of water, reducing the amount of area scattering light to maintain transparency of the surface [23] [24]. Use of superhydrophilicity to combat fogging has potential applications for window, mirrors, lenses, glasses, etc. as well as for easy-clean household goods and road signs, anticondendsation air condition air, and anti-fouling paints [21]. Running water on superhydrophilic surfaces can easily wash out dirt and contamination, which impart to the surface self-cleaning ability. Due to the strong adhesion between water and the surface, water will tend to penetrate under bound dirt, debris, and liquid contaminants essentially acting as a wedge between contaminants and substrate. The water forms a crack layer and marks the surface slippery, which greatly diminishes adhesion between the contaminants and substrate, allowing for their removal. This means that superhydrophilicity works better than superhydrophobicity when contaminants are hydrophobic [21].

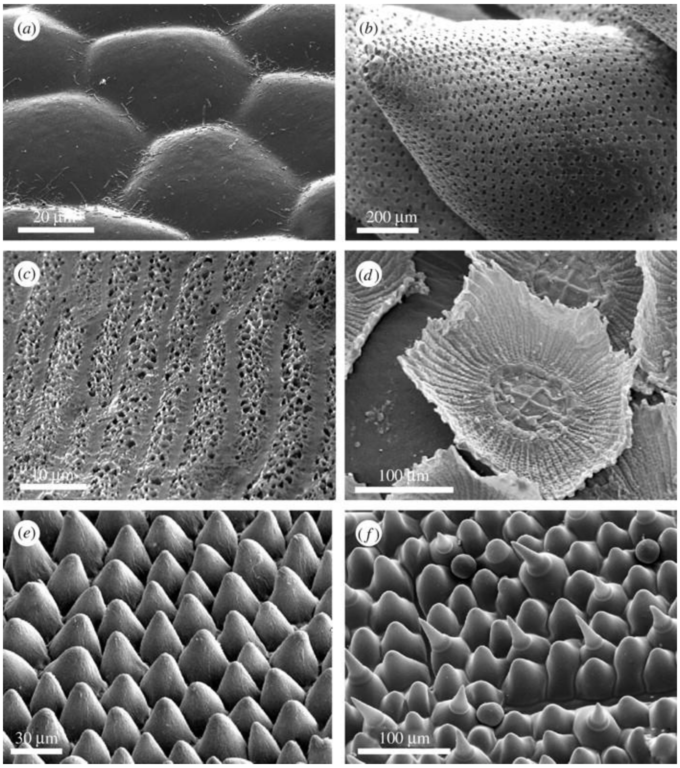

Figure 2.10: SEM micrographs of plant surfaces. (a) The flat and unstructured surface of the water plant (Anubias barteri) is shown. (b) The surface of a water-adsorbing moss (Sphagnum squarrosum) is shown. In this, the pores are formed by dead and collapsed cells. (c) The water-adsorbing porous cell structure of the epidermis of moss Rhacocarpus purpurescens is shown. (d) The epiphytic growing Spanish moss (Tillandsia usneoides) with its characteristic multicellular water-absorbing hairs is shown. (e) The uniform conical cells on a leaf of Calathea zebrina and (f) the composition of different cell types of the superhydrophilic leaves of Ruellia devosiana are shown [20].

Other applications in the drag delivery [25], heat transfer [26,27], biomolecular immobilization [28] have also been reported. For example: boiling heat transfer can be significantly affected by surface wettability, as reported in the previous chapter. The continuous water film formed on a hydrophilic or superhydrophilic surface can delay the formation of a vapor film in boiling and thus improve CHF [27]. Superhydrophilic surfaces can find application also in the biomedical sector [27], such as osseointegration of dental implants [29], reducing platelet adhesion in vascular stents [30].

Thermodynamically the wettability of a surface is related to its surface free energy, with high surface free energy corresponding to hydrophilicity. In general, modification of surface free energy can be attained through roughening the surface or lowering through chemical modification the surface free energy of a rough surface. A universal strategy to create a superhydrophilic surface is to control the surface microstructure and the surface chemical composition. Rough structure and high surface energy material are the two factors leading to extreme wetting. The two most common approaches for fabricating superhydrophilic surfaces are photo-induced and texture-induced superhydrophilic surfaces.

Photo-induced superhydrophilic surfaces are generated by coating substrates with photochemically active (photo-sensitive) materials, such as titanium dioxide (TiO_2), that became superhydrophilic when exposed to radiation [22,31]. It is produced a high energy surface, which interacts strongly with water, and apparently an interfacial energy that is substantially lower than the original surface. Moreover, many organic compounds can be oxidatively degraded on the surface of TiO_2 subsequent to its UV light radiation, which has led to its use in antibacterial, anti-fouling and deodorant coatings. In addition to TiO_2, there are a number of other photosensitive semiconductor materials for which the band gap energies correspond to the UV light region [22].

Texture-induced superhydrophilic surfaces result from the texturing of substrates that intrinsically provide for partial wetting by water, i.e. to create rough structures with hydrophilic component [22]. As suggested by Wenzel, wetting of surfaces that have a CA less than 90° can be enhanced through surface roughness [32]. The results is a superhydrophilic surface due to the combination of the hydrophilicity and the roughness (micro/nano hierarchical structures are no a requirement) structure of the surface. There are numerous structures and approaches for imparting roughness that result in superhydrophilic surfaces [33]. Both lithographically texturing and introduction of microporosity can render surfaces superhydrophilic. Examples are sol-gel [28,34] and electrochemical methods [28,35], electrospinning [28,36], plasma technique [28,37], chemical and hydrothermal methods [28,38], phase separation [28,39], vapor deposition [28,40,41], templating method [28,42], layer-by-layer (LbL) assembly [28,43]. The sol-gel method [28,34] is a low temperature technique and the process is simple, inexpensive, and easy to control. By adjusting the composition of the precursor solution along with the hydrolysis and polycondensation process, the resulted films can exhibit different morphologies and surface chemical components. Electrochemical method [28,35] involves electrochemical deposition, anodization, galvanic cell reaction, and electrochemical polymerization. Rought structures can be easily fabricated by electrochemical method. Electrospinning [28,36] is applicable to generate nonwoven web of micro nanofibers. In the process, high electric voltage is applied to the liquid solution and a collector to let the solution extrude from a nozzle forming a jet. Plasma technology [28,37] takes advantage of highly reactive plasma species to modify the functionality of various substrates. Plasma consists of a collection of free moving electrons and ions (atoms that have lost electrons). Energy is needed to strip electrons from atoms to make plasma. This energy is usually provided by an electric source, which can be direct current (DC), radio frequency (RF), low frequency (LF) or microwave frequency (MW). With insufficient sustaining power, plasma recombines into neutral gas. Plasma can be accelerated and steered by electric and magnetic fields, which allows it to be controlled and applied. Chemical and hydrothermal methods [28,38] provide the preparation of superhydrophilic surfaces by synthesis of organic or inorganic materials. Depending on the synthesis condition, the as-formed material can gain natural microroughness, leading to a magnified wettability. Rough surfaces can also be formed by the phase separation of a multi-component mixture [28,39]. If a stable mixture becomes unstable due to some change, such as cooling, it will begin to separate into two phases, one of which may be a solid or become solid at some point in the process. In a phase-separation progress, it is of common occurrence that solid/liquid phases separate and liquid/liquid phases separate. Due to the interactions of these phase-separation processes, the solute will form rough microstructures after crystallization. The rough microstructures usually possess nanometer scale roughness. Vapor deposition is a popular technique to create a variety of thin films. It can be further separated into physical vapor deposition (PVD) [40] and chemical vapor deposition (CVD) [41], depending on whether chemical reaction are involved. CVD involves the dissociation and/or chemical reactions of gaseous reactants in an activated (heat, light, plasma) environment, followed by the formation of a stable solid product. The deposition involves homogeneous gas phase reactions, which occur in the gas phase, and/or heterogeneous chemical reactions which occur on/near the vicinity of a heated surface leading to the formation of powders or films, respectively. PVD has a wide scope including evaporative deposition, electron beam phase vapor deposition and sputtering deposition. The process comprises evaporation at high temperature and condensation on cool substrate. The templating process includes preparing a featured template master, then molding the replica and finally removing the template. The original prototypes of the template can be filter paper [44], insect wings [45], reptile skins [46] and plant leaves [47]. From a chemical and morphological point of view, the template can even be molecules [48] and polymers [49]. Layer-by-Layer (LbL) deposition is a thin films fabrication technique. The films are formed by depositing alternating layers of oppositely charged materials with wash steps in between [50]. The bilayers and wash steps can be performed in many different ways including dip coating, spin-coating, spray-coating and flow based techniques. Layer-by-layer deposition is based on the electrostatic charge interactions between different layers such as polyanion and polycation. Microscale roughness can also be easily obtained by sandblasting [51], while dip-coating [52] from nanoparticle suspension can be used to provide nanoscale surface features. For example, silica nanoparticle films have shown extreme wetting behavior, which is postulated to be the result of the inherent nanoporosity of silica nanoparticle films [53]. Fabrication of these films via Layer-by-Layer method has been heavily studied, creating functional coatings of non-spherical nanoparticles [54], hierarchical silica structures [55] and composite silica/polystyrene structures [55]. Although the LbL method affords a great degree of control over proprieties of the nanoparticle films, such as thickness and morphology, the simpler direct dip-coating method has been shown to produce silica nanoparticle films with extreme surface wettability as well [53]. All these methods, if suitably dedicated, as shown in the next chapter, can be also used to create superhydrophobic surfaces.

Moreover, there are materials whose surfaces can be switched between hydrophilic and hydrophobic states when exposed to certain stimuli such as changes in temperature [56], pH [57], electric potential [58], solvent environment [59], and mechanical stress [21]. When combined with proper surfaces texturing, these states can become superhydrophilic/phobic [21].

Furthemore, increasing the surface roughness of a hydrophilic surface, also increases the hysteresis between advancing and receding contact angles [60]. It is possible to increase the hydrophobic grade of the surface simply with an acid treatment: inserting an aluminum surface in a solution of water and hydrochloridric acid 1:2 at room temperature for enough time, the acid erodes the aluminum surface and a surface on which the water drop spreads immediately and completely, almost as was adsorbed, is obtained.

Challenges still exist in designing artificial superhydrophilic surfaces. The major issue is the degradation of the surface wettability to standard hydrophilicity over time. This degradation is often attributed to organic surface contamination. To increase the practicality of these surfaces, it is desirable for these surfaces to exhibit superhydrophilic stability over long periods of time and through multiple wetting-dewetting cycles [53]. Moreover, also cost and availability of photosensitive materials are serious barriers in designing photo-induced superhydrophilic surfaces. These issues are avoided with texture-induced superhydrophilic surfaces, but the light transmittance of structured films is usually greatly reduced due to diffuse scattering limiting their applications. Another challenge is their mechanical stability. The investigation of this issue may provide some and more interesting future findings and applications for superhydrophilic surfaces. For details and recent reviews about superhydrophilic surfaces refer to [27,28].

2.5 Superhydrophobic surfaces

There are many examples of highly hydrophobic and self-cleaning surfaces in nature, like butterfly wings, lotus leaves, and water strider legs (Figure 2.11). On these surfaces, water does not stick and rolls away easily, without really wetting the material. SHS are defined as characterized by high values of water contact angle and low values of the contact angle hysteresis, which is the difference between advancing and receding angle of a moving drop (see Figure 2.5). The latter must be low (about 10°) in order to let the drop move easily and allow the self-cleaning effect [61,62].

Many studies confirmed that it is the particular combination of micrometer-scale and nanometer-scale roughness, together with low surface energy, that leads to superhydrophobic surfaces (SHS) [63]. Electron microscopy of the surface of the lotus leaves shows protruding nubs about 20-40 μm apart, each being covered with a smaller scale of epicuticular wax crystalloids [64]. It is noteworthy that the lotus leaf achieves the self-cleaning effect with a particular two-scale roughness coated with paraffinic wax crystals containing predominantly $-CH_2-$ groups. That means that the key issue is the control of surface morphology on micron and nanometer scales.

It is believed that in order to be superhydrophobic, a rough surface should be able to maintain a composite interface with air pockets or bubbles trapped in the valleys between the asperities [9,65-68] as opposed to a homogeneous solid-liquid interface. As a matter of fact, it is possible to prepare SHS even from hydrophilic materials, such as PMMA, carefully setting superficial roughness [69,70].

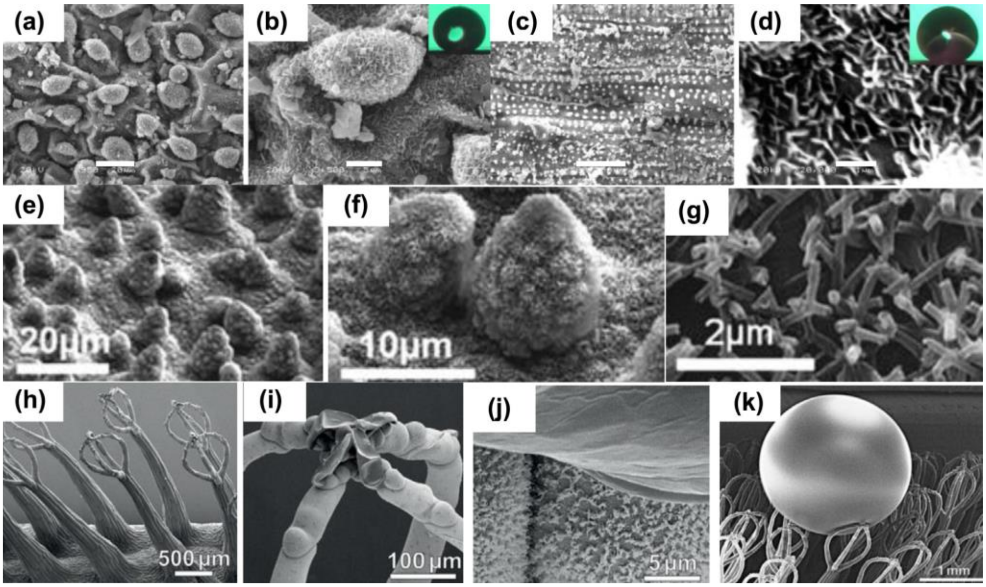

Figure 2.11: SEM micrographs [18] of some hierarchical structure of some plant leaves. (a and b) Taro leaf (Colocasia), (c and d) rice leaf (Oryza sativa L.); (e) Nelumbo Nucifera. The micrographs (f and g) show the microstructure of Nelumbo Nucifera leaves formed by papillose epidermal cells covered with epicuticular wax tubules on the surface which create the nanostructures. Morphology of Salvinia molesta: (h) the eggbeater-shaped structure of the leaf surface of Salvinia molesta, (i) terminal cells collapsed forming a cap, (j) the wax crystal covering the whole surface except the terminal cells (k) low temperature SEM of a frozen leaf with applied droplet of a water glycerol solution. In the inset of (b and d) the water contact angle is shown. The scale bar is 20 µm in (a), 5 µm in (b), 50 µm in (c) 1 µm in (d), respectively.

To fabricate self-cleaning materials, conventionally, two main routes can be followed: roughening a low energy surface material, or depositing a low energy coating/grafting on a rough surface. De facto, often, the surface is first micro-/nano structured and then functionalized with a hydrophobic coating/grafting.

A schematic list of the process for creating micro/nanoroughness and SHS is shown in Table 2.3.

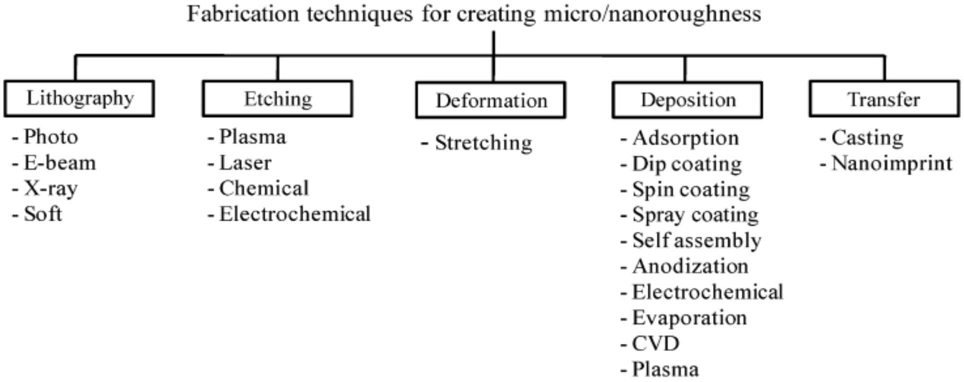

Table 2.3: Processes for creating micro/nanoroughness and SHS [71].

Roughening a material with lithography by means of photons [72], electron beams, X-rays and softer techniques is useful because usually it allows modifying just the upper part of the material, while maintaining the bulk properties unchanged. It is a precise and pointed way to obtain a microscale roughness. Other techniques can be used to obtain a random roughness on the material surface. On conductive surfaces, electro erosion [73] is a suitable way for removing material by a series of current discharges between two electrodes separated by a dielectric layer. There is no direct contact between the tool and workpieces, but the procedure is slow, quite expensive, and it can be used just with conductive materials (like metals). Micromachining [74] is the precise milling of various materials, allowing the building of microstructures by etching and subsequent (or almost contemporaneous) deposition of different structural layers on the top of the substrate. It is quick and cheap, with high precision (±0.5μm), but it is not suitable for large-area modification.

As an alternative, the use of etching technique (plasma, laser, chemical or electrochemical etching) is also one of common ways to provide micro-/nano-rough surfaces. Chemical etching [75] is a quick and unselective way to impart nanoroughness on a material, in a very homogeneous way. It can also be tuned in order to perform selective removal of one component of a particular alloy, or unselective erosion of target material. It produces diffuse roughness, and is quick, cheap but unorganized and difficult to tune precisely. A one step way to prepare SHS on metal substrates consists in the selective etching of the material with femtosecond pulsed laser and subsequent re-deposition of target materials on it, with a precise geometrical pattern [76]. Nanostructured metallic SHS with hysteresis between 2-6° are obtained, after a certain amount of time, due to the recombination of atmospheric molecules on the surfaces after laser stimulation. It is a very precise and promising technique, but also slow and quite expensive [77].

On the other hand, a functionalization, i.e. hydrophobization, process is needed in order to impart superhydrophobicity to the target material.

A plenty of procedures have been reported in the literature, from the simple dip coating [78] of a material in a liquid which can contain molten or dissolved polymers, or various mixture of macromolecules and inorganic materials (such as carbon nanotubes [79] or silica nanoparticles [80]), to more complex procedures such as physical or chemical vapor deposition [81] (i.e. deposition from the gas state). All these procedures allow the precise tuning and selection of the chemical species to be deposited, together with the possibility to perform chemical reactions in one step. These methods, combined with the variety of polymers existing, allow the creation of almost infinite combinations of coatings. As an example, while depositing, the polymer (molten or dissolved in a solvent) can be added with different nano materials such as carbon nanotubes, silica or other nanopowders, glass fibers, in order to reinforce the structure, while maintaining surfaces characteristics [76]. For instance, in [82] silica nanoparticles were added to an epoxy resin; the composite material was used to cover a wind turbine blade, to give a superhydrophobic coating, with self-cleaning ability and UV resistance.

Cold plasma deposition of diamond like carbon (DLC), obtained through the ionization of a low pressure carbon gas, and suitably combined with silicon and oxygen precursors, leads to a very robust and tough coating, with most of DLC properties, but with a high water contact angle. This is a very attractive technique, though difficult to replicate, due to the particular combination of tetrahedral structure that must be present in the coating in order to keep it “diamond like”, but it is slow, expensive and more suitable for flat surfaces. It can however be used for small areas [83,84].

Also numerous wet-chemistry approaches capable to turn surfaces into SHS are reported in literature. They are much easier to perform and can be applied even to rough substrates on large scale [85,86]. The involved reactions are homogenous, thus leading to chemically and physically uniform coatings of different materials. The thickness is typically on nanometer scale, the reactions methods are cheap, and different chemical routes and grafting molecules can be used, in order to produce the targeted surface.

A novel approach to enable stable non-wetting properties involves replacing the delicate air pockets by an ad-hoc lubricant that preferentially wets the substrate, the so called Slippery Liquid-Infused Porous Surfaces (SLIPS). The microporous structure of the substrate is also of paramount importance as it contributes to securing the lubricant by capillary forces. This in turn confers stability to the resulting liquid infused porous surface. To construct the so-called SLIPS onto the metal surface, e.g. low alloy steel, three criteria should be met [87]. First, a rough hydrophobic solid surface with micro/nano-scale structure is required, since it can exert high capillary effect to anchor the lubricant as a stable liquid coating. Second, the lubricant should be immiscible with the outer medium, e.g. water phase. Third, the affinity between lubricant and rough substrate is required higher than that between the medium and the substrate. Inspired by the leaves of the pitcher plant, this novel class of liquid impregnated surfaces exhibits remarkable properties such as liquid repellency, smoothness or self-healing (by capillary motion upon damage) [88,89]. In addition recent studies have shown that such surfaces can demonstrate promising anti-biofouling as well as anti-icing properties [90,91].

Self-healing materials have recently attracted a lot of attention. However, such materials, especially those combining both self-cleaning and self-healing effects, are still more known conceptually, since it is still a real challenge to combine both the micro-/nano-rough surface with effective superhydrophobic properties and the ability of the coating actively to heal itself in case of (typically abrasive) mechanical damage [92]. So far, such coatings are believed to be based on polymer materials incorporating micro-containers with a healing agent that would be released “on demand” in the case of a mechanical damage to the surface and would actively participate in its recovery. However, this research is still mainly underway, and such highly anticipated smart coatings are still to be actively searched, prepared and tested before they can be delivered and available for applications.

In conclusion, the analysis of the literature on the recent progress in the field suggests that the development of superhydrophobic surfaces with robust self-cleaning properties (i.e. enhanced service time) is one of current priorities [93].

2.6 Oleophobic, omniphobic and amphiphobic surfaces

Superoleophobic surfaces are surfaces on which liquid oil adhesion is low. The construction of superoleophobicity is more difficult rather than of superhydrophobicity because the surface tension of oil or other organic liquids is lower than that of water and, in order to construct a superoleophobic surface, the surface energy of the solid surface should be lower than that the oil one. However, superoleophobic surfaces have drawn a great deal of attention for both fundamental research and practical applications in a variety of fields. For the design, the fabrication and the application of superoleophobic materials refer to [94].

Superomniphobic surfaces, typically defined as having a contact angle (CA) for liquids greater than 150°, are of interest for their unique characteristics such as liquid repellency, self-cleaning, fluid drag reduction and/or chemical protection [21,95,96]. For some superomniphobic self-cleaning applications such as electronic touch screens or pads, window glasses, textile clothing, and penetration of oils in hearing aids, a good mechanical durability of the surface and in some applications anti-smudge characteristics are required. Transparency, which is critical in various applications including self-cleaning windows and electronic touch screens, depends on coating thickness, particle size and surface morphology [97]. The superomniphobic surfaces should possess both superhydrophobic (repellency against water) [64] and superoleophobic (repellency against non-polar organic liquids, for example, hexadecane) [98,99] properties. In order for a surface to repel various organic liquids, its surface energy should be lower than the liquid's (typically 20–35 mN/m). The optimal design of such surfaces involves a combination of appropriate material or coating selection, in order to minimize the surface energy of the solid, and optimal choice of surface texture, including recognition of the important role of re-entrant curvature [100-105] (such as micronail forests, microhoodoo arrays, woven textiles, fiber mats) of the designed surface topography. There are a number of reports in the literature that systematically discuss the impact of surface texture on wettability [9,98,106-112]. By optimizing the interaction between the textured surfaces and contacting liquids, surfaces with a wide range of wettability starting from superwetting (contact angle ≈0°) to superhydrophobic surfaces can be produced. Low surface tension liquids such as methanol (γ_{lv}=22.7 mN/m) and octane (γ_{lv}=21.6 mN/m) wet most materials, and for such liquids, the impact of the surface texture on wettability is critical. For a selected type of textured surface, the separate roles of feature size and relative spacing as well as the independent contribution of surface chemistry can be highlighted most effectively by using a suitably constructed framework for presenting measured values of the apparent contact angle with various contacting liquids [113].

Generally omniphobic surfaces are produced using binder and nanoparticle systems [114]. Commonly used resin binders include: fluorinated acrylic copolymer [114-119], modified polyhedral oligomeric silsesquioxane (fluoroPOSS) [105], PTFE amorphous fluoropolymer [120,121], fluorinated monoalkylphosphates [98], n-perfluoroeicosane [99], tridecafluoro-1,1,2,2-tetrahydrooctyltrichlorosilane [122], fluorinated 3,4-ethylenedioxypyrrole (EDOP) polymer [122,123] semifluorinated silane ((tridecafluoro-1,1,2,2-tetrahydrooctyl)-1-trichlorosilane) [124], Viton ETP-600S (copolymer of ethylene, tetrafluoroethylene and perfluoromethylvinyl ether, and a cure site monomer) [125] and fluorosurfactant ((tridecafluoro-1,1,2,2-tetrahydrooctyl) trichlorosilane) [126]. In some cases, complex processing routes are used, that involve coaxial-electrospinning [120], CVD [124] for fabrication, or photolithography for preparing the substrate geometry [99,121,122].

Also superomniphobic magnetic microtextures with remote wetting control have been described recently [127]. Grigoryev et al. proposed a remote control of wetting behavior enabling the transition from a superomniphobic to an omniphilic wetting state in an external magnetic field via the alternation of reentrant curvature of a microstructured surface. This specially designed reconfigurable microtexture made of ferromagnetic metal micronails repels water, water−surfactant solutions, and practically all organic liquids (except for fluorinated solvents), including such superspreading amphiphiles as tributyl phosphate and alcohols. The nonwetting-to-wetting transition is obtained by magnetically induced bending of the micronails.

As previously mentioned, re-entrant surface curvatures, in conjunction with chemical composition and roughened texture, can be used to design surfaces that display extreme resistance to wetting from a number of liquids with low surface tension, including alkanes such as decane and octane [104]. Recent studies have shown that the wax on the surface of the lotus leaf is weakly hydrophilic ($\theta \approx 74°$) [128]. From the preceding discussions, it would be expected then that water should fully wet the lotus leaf surface and thus lead to apparent contact angles $\theta << 90°$, as predicted by the Wenzel relation [32]. Herminghaus [129] first pointed out that the various surface constituents of the leaves of a number of superhydrophobic plants, such as the common smoketree (Cotinus coggygria) or wild cabbage (Brassica oleracea), are hydrophilic. The surprising superhydrophobicity of such plant leaves is expected to be a consequence of reentrant surface texture [100,104,130] that is, the surface topography cannot be described by a simple univalued function z=h(x,y), and a vector projected normal to the x–y plane intersects the texture more than once. If θ<ψ, where ψ is the local texture angle, i.e. the angle measured through the solid between the different faces of the pillar, as in Figure 2.12a, the net traction on the liquid–vapor interface is downward, thereby facilitating the imbibition of the liquid into the solid structure, leading to a fully wetted interface. On the other hand, if θ>ψ, as shown in Figure 2.12b, the net traction is directed upward, thereby supporting the formation of a composite interface [130]. In other words, either of these surfaces can support the formation of a composite interface provided that θ>ψ [67,103,104] and any liquid for which θ<ψ will immediately yield a fully wetted interface. The presence of reentrant texture (or ψ<90°) in the surface illustrated in Figure 2.12b allows for the formation of a composite interface and thus extremely high apparent contact angles even if θ<90°.

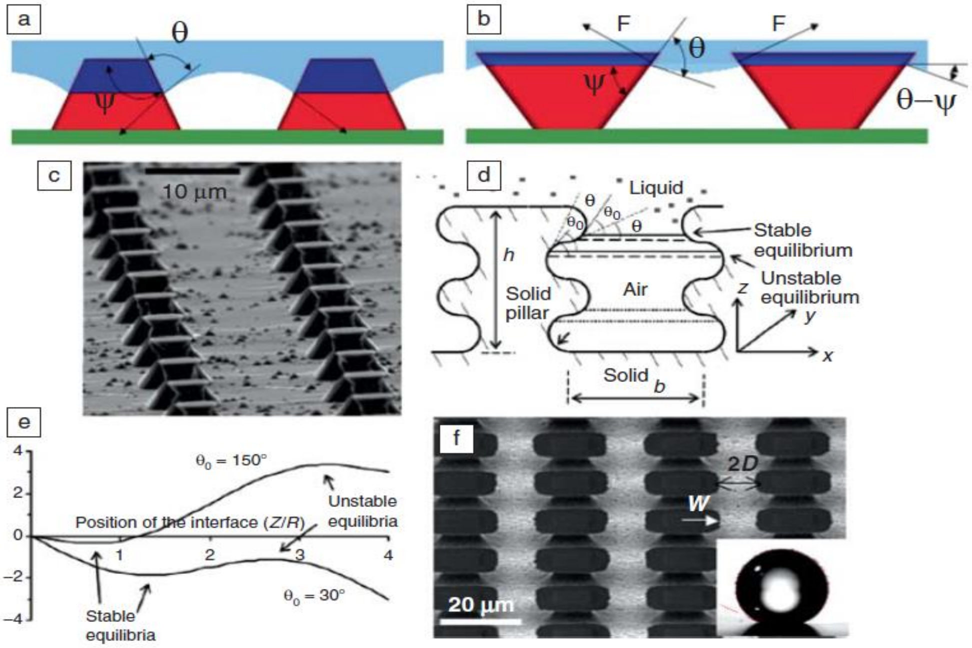

Figure 2.12: (a), (b) Schematic diagrams illustrating the expected liquid–vapor interface on two idealized surfaces with different values of the equilibrium contact angle (θ). The liquid is light blue. Air is white. The dark blue surface is

wetted, whereas the red surface is nonwetted. (c) Silicon micropost arrays developed by Cao et al. (d) Schematic of a surface exhibiting reentrant curvature proposed by Nosonovsky. The height of the pillars is h; b is inter-pillar spacing. (e) Computed overall free energy as a function of the penetration depth (z) for two cases, one in which the surface is considered to be extremely hydrophobic (θ = 150°) and one in which the surface is considered to be hydrophilic (θ = 30°). A local minimum in free energy leads to an energetically stable droplet configuration (composite or fully wetted), whereas a local maximum is unstable. (f) Scanning electron micrograph of the micro-hoodoo surface. The inset shows a droplet of octane with θ = 155° on the micro-hoodoo surface [131].

In further studies of reentrant texture, Nosonovsky [103] analyzed the stability of composite interfaces on surfaces having different roughness profiles. He argued that the creation of a stable composite interface on any rough surface requires two criteria to be satisfied. One is that there must exist a local texture angle (ψ) equal to the equilibrium contact angle θ. The second condition states that, in the vicinity of the local region where $\theta = \psi$, the differential quantities related to changes in the solid–liquid contact area (dA_{sl}) and the local contact angle ($d\theta$) with the advancing or receding of the liquid have opposite signs such that $dA_{sl}d\theta < 0$. Based on these criteria, Nosonovsky proposed a liquid-repellent structure of rectangular pillars, covered with semicircular ridges and grooves. Because of the presence of reentrant curvature at several locations on this structure (where $0° < \psi < 90°$), such a surface provides the possibility of obtaining a composite interface with any liquid for which $\theta > 0°$ [104]. The correct choice of surface texture can lead to the formation of “metastable” (energetically trapped) composite interfaces [131] and extremely high apparent contact angles, even though the solid surface by itself might be hydrophilic. Given these considerations, it might similarly be possible to develop superoleophobic surfaces, even though the candidate substrates are limited to solid materials with $\theta < 90°$ for various low-surface-energy alkanes. Amphiphobic or lyophobic surfaces are instead surfaces able to repel liquids with a different polarity and physical properties (i.e. surface tension) [132], with both terms being usually related to the liquids molecules and not to the surfaces. Such particular non-wetting surfaces can provide additional performances with respect to the hydrophobic ones in many sectors. Similarly, superamphiphobic surfaces exhibit even larger values of static contact angles and contact angle hysteresis CAH lower than 5°. Different approaches can be used to achieve these surface properties. For recent trends in the development, fabrication, and characterization of superamphiphobic surfaces, the papers of Cavalli and Mugele [132], Chua and Seeger [133] give useful insights.

2.7 Wear resistance and surface durability

Neinhuis and Barthlott [134] suggested that hierarchical surfaces are less vulnerable to mechanical damage caused by nanostructures and therefore maintain their functionality even after being damaged.

Artificial superhydrophobic surface however would typically suffer from weak wear resistance (i.e. their superhydrophobicity does not persist for a long time and/or in particular environmental conditions [70])) with the result in loss of superhydrophobic properties and of the ability to repel water. The robustness of the superhydrophobic surfaces is generally unattainable at the micro/nano scales [135]. Any loss of the micro/nano scale topographical structures will lead to loss of superhydrophobicity and self-cleaning. Moreover, the surface chemistry is also possible to be degraded during the use of the surface, which will also result in loss of superhydrophobicity and self-cleaning. Therefore, the mechanical properties and the chemical stability of the superhydrophobic surface should be studied to identify materials that can be used in real applications. As such, the success of a superhydrophobic surface depends not only on its wetting performances, but also on its ability to last over time and resist to erosion and abrasion [135,136]. Nonetheless, only few papers so far have addressed the durability issues, each of them using a different method to assess surface durability [93,137,138], so that a systematic approach to the issue of durability is still lacking in the literature.

Li et al. [139] reported an approach for preparing superhydrophobic surfaces by spray coating of polymerized organosilane/attapulgite (POS/APT) nanocomposites, showing the coatings were stable after being kept at a water pressure of 6000 Pa for 5 minutes, against UV irradiation (200–400 nm for 30 min) and high (200°C for 1 h) and low (-30°C for 1 h) temperature, resistant to weak basic solution (0.1m NaOH for 1 h) and organic solvents. Cheek et al. [140] investigated the loss of superhydrophobicity only under continuous submersion in water, which is characterized by the degradation of the trapped air layer, for various superhydrophobic polymer nanocomposite coatings. The loss of superhydrophobic performance under continuous submersion, which is characterized by the degradation of the trapped air layer, is defined as saturation. The organoclay/MCPU/PMC nanocomposite resisted not more than 3 h before saturation was reached. The ZnO/PMC coating resisted more than 12 h before full saturation was reached. Finally, the organoclay/PUR/PMC formulation yielded a period, before full saturation, greater than 48 h. Jin et al. [126] obtained superhydrophobic and superoleophobic surfaces from surfactant-modified silica aerogels and evaluated the wear resistance of the produced surfaces by means of a mechanical sandpaper abrasion test. Cho et al. [141] fabricated superhydrophobic surfaces with nano-scale structures by alkali surface modification method and self-assembled monolayer coating of fluorinated molecules. Hierarchical structuring of the surface was achieved by combining sandblasting techniques for microtexturing and forming an aluminum hydroxide layer for nanostructuring. Abrasive test was utilized to evaluate the mechanical durability of the fabricated surfaces and the result shows that the superhydrophobicity of aluminum hydroxide structure becomes more robust by forming hierarchical roughened structures. Zhou et al. [142] investigated mechanical properties of superhydrophobic fluoropolysiloxane/TiO_2 nanocomposite coatings using pendulum hardness rocker measurements and nanoindentation measurements. Wang et al. [143] prepared superhydrophobic PTFE/PVDF composite surfaces and tested their mechanical stability with a homemade scratch tester. Guo et al. [144] fabricated superhydrophobic surfaces with hierarchical flowerlike structure and tested their stability in acidic and basic conditions. Feng et al. [145] prepared superhydrophobic alumina surfaces and studied the effect of the time and of various corrosive solutions on the wettability of the prepared SHS. Zhu et al. [146] evaluated the mechanical durability of the obtained superhydrophobic fabric by finger touching and abrasion with sandpaper. Zhang et al. [147] checked the easy-to-clean property and the durability of a superhydrophobic γ-alumina coated stainless steel in a paper machine. The superhydrophobic stainless steel was field-tested near size roll in a real paper machine producing release base paper for labeling, as compared with an uncoated reference stainless steel. In paper making process the primary slurry consists of wood fibers and fillers mixed in water. The function of paper machine is to remove water by different steps to obtain dry and homogeneous paper. From the field test, the easy-to-clean property of the superhydrophobic surface was quite clear, as compared with the uncoated reference stainless steel. The surface survived rather well after 16 days in the field test, but lost superhydrophobicity due to wear. Steele et al. [148] investigated substrate adhesion for superhydrophobic coatings fabricated from polyurethane modified with waterborne perfluoroalkyl methacrylic copolymer and a montmorillonite clay nanofiller. The authors characterized the adhesion strength with a 90° tape testing method. High contact angles and low contact angle hysteresis could be preserved under 1750 N/m adhesion strength tape testing and significant resistance could be observed as high as 3850 N/m. Zhu et al. [149] prepared a superhydrophobic metal/polymer composite surface and the mechanical durability of the surface was evaluated by scratch and friction tests. The scratch test was conducted on a homemade scratch tester: 1500 mesh sandpaper served as an abrasion surface, with the surface to be tested facing this abrasion material. The friction test was studied using a ball-on-plate tribometer under reciprocating motion. Schutzius et al. [150] synthesized elastomeric superhydrophobic nanostructured composite coatings by solution-based processing of nitrile rubber and two separate particle fillers, nanoscale carbon black and submicron-scale poly (tetrafluoroethylene). The coatings were applied on various flexible substrates, which are subsequently stretched uniaxially. The authors shown that mechanical failure of the superhydrophobicity of the composite coating on silicone rubber occurs at strains at around 30% and that permanent deformation of the coating on the polyester fabric substrate began to occur beyond 70% of strain. Amirfazli [151] investigated how superhydrophobic surfaces change due to wear. The author used an abrasive wear device to evaluate material durability based on change in surface properties, such as roughness. He found that advancing and receding contact angles are not equally susceptible to wear; receding contact angle is more sensitive to wear than advancing contact angle, with a consequent increase of contact angle hysteresis and reduction of drop mobility. Boinovich et al. [152] analyzed the durability of superhydrophobic surfaces evaluating the contact angle time evolution after soaking the sample in water for a long time. Larmour et al. [153] reported a method for preparing a new type of superhydrophobic composite material by compression of superhydrophobic metal particles. Since the entire material and not only the surface is functionalized, removing outer layers by abrasion did not result in loss of superhydrophobicity, since it led to exposure of a fresh portion of the underlying superhydrophobic material. Jung and Bhushan [136] investigated the durability of their surfaces conducting waterfall/jet tests and monitoring the surface degradation by AFM and a ball-on-flat tribometer. Bayer et al. [154] reported fabrication of superhydrophobic hybrid anaerobic adhesive films, which was capable to resist exposure to acidic (pH 2) and basic (pH 10) aqueous solutions: no change in superhydrophobicity was measured within 3 days of observation of liquid blobs placed on the adhesive coatings for both liquids. Moreover these films preserved their superhydrophobicity even if by removal of few microns of the coating by sanding: gentle surface polishing was performed by using a 3M 1000 grit aluminum oxide sand paper mounted on a rotating disk applying ~ 0.06 kg/cm^2 downward force. Yanagisawa et al. [138] evaluated the abrasion resistance of transparent superhydrophobic coating, fabricated by combining crater-like silica films with boehmite powder. Cui et al. [155] prepared superhydrophobic surface with multi-scale structures on paint films and tested its durability to the high speed scouring test and in neutral and basic aqueous solutions and in some common organic solvents. Cui et al. [156] also studied the stability of four superhydrophobic surfaces by high-speed current scouring method. Zimmermann et al. [157] studied the long term environmental durability of a superhydrophobic silicone nanofilament coating with natural and artificial weathering test. Zimmermann et al. [158] tested the chemical stability of a superhydrophobic silicone nanofilament coating dipping the surface in various liquid media over a period of 6 months. Wang et al. [159] fabricated a superhydrophobic copper fatty acid carboxylate surface and they reported that the surface had stability in observance to organic solvent treatment and exposure to air. Wang et al. [137] studied the stability of the superhydrophobic polybenzoxazine surface for all the pH environments. Guo et al. [160] tested the durability of superhydrophobic surfaces after a long time immersion in acid and alkali environment.

The durability of superhydrophobic surfaces in operational conditions is a severe issue that currently represents a bottle-neck for the technology transfer from laboratory to industrial applications. Although some efforts have been done in the direction of assessing surface durability, to the best of our knowledge no systematic procedure was developed so far. With few exceptions (e.g. Li et al. [139] and Bayer et al. [154]), the majority of articles reported only partial tests, e.g. only mechanical stability or only chemical stability, but not both. In addition, methods to test mechanical stability can vary significantly, so that performances of different coatings can be hardly compared.

As already mentioned, the same problem exists for the artificial superhydrophilic surfaces, often attributed to organic surface contamination, and also for oleophobic and omniphobic surfaces. Anyway, as in the present work the experimental part is focused mainly on superhydrophobic surfaces, the discussion refers mostly to this type of surfaces.

Bibliography Chapter 2

[1] S. Kandlikar, S. Garimella, D. Li, S. Colin, M. King. Heat transfer and fluid flow in minichannels and microchannels (2005) Chapter 1.

[2] E. Begg, D. Khrustalev, A. Faghri. Complete condensation of forced convection two-phase flow in a miniature tube. ASME Journal of Heat Transfer 121 (1999) 904-915.

[3] Y. Zhang, A. Faghri, M.B. Shafii. Capillary blocking in forced convective condensation in horizontal miniature channels. Journal of Heat Transfer 123 (2001) 501-511.

[4] http://www.ramehart.com/glossary.htm.

[5] http://cnx.org/contents/031da8d3-b525-429c-80cf-6c8ed997733a@8.9:83/College_Physics.

[6] X.B. Zhou, J.T.M. Hosson. Influence of surface roughness on the wetting angle. Journal of Materials Research 10 (1995) 1984-1992.

[7] W.A. Zisman, F. Fowkes. Contact Angle, wettability and adhesion. American Chemical Society (1964) 1-51.

[8] N. Patankar. On the modeling of hydrophobic contact angles on rough surfaces. Langmuir 19 (2003) 1249-1253.

[9] B. He, N.A. Patankar, J. Lee. Multiple equilibrium droplet shapes and design criterion for rough hydrophobic surfaces. Langmuir 19 (2003) 4999-5003.

[10] M. Miwa, A. Nacajima, A. Fujishima, K. Hashimoto, T. Watanabe. Effects of the surface roughness on sliding Angles of water droplets on superhydrophobic surfaces. Langmuir 16 (2000) 5754-5760.

[11] S. Wang, L. Jiang. Definition of superhydrophobic states. Advanced Materials 19 (2007) 3423-3424.

[12] X.M. Li, D. Reinhoudt, C.C. Mercedes. What do we need for a superhydrophobic surface? A review on the recent progress in the preparation of superhydrophobic surfaces. Chemical Society Reviews 36 (2007) 1350-1368.

[13] D. Öner, T.J. McCarthy. Ultrahydrophobic surfaces. Effects of topography length scales on wettability. Langmuir 16 (2000) 7777-7782.

[14] J. Bico, C. Tordeux, D. Quéré. Rough wetting. Europhysics Letters 55(2) (2001) 214-220.

[15] R. Rioboo, B. Delattre, D. Duvivier, A. Vaillant, L. De Coninck. Superhydrophobicity and liquid repellency of solutions on polypropylene. Advances in Colloid and Interface Science 175 (2012) 1-10.

[16] W. Li, A. Amirfazli. A thermodynamic approach for determining the contact angle hysteresis for superhydrophobic surfaces. Journal of Colloid and Interface Science 292 (2005) 195-201.

[17] G.Y. Li, X.P. Li, H. Wang, Z.Q. Yang, J.Y. Yao, G.F. Ding. Fabrication and characterization of superhydrophobic surface by electroplating regular rough micro-structures of metal nickel. Microelectronic Engineering 95 (2012) 130-134.

[18] E. Celia, T. Darmanin, E.T. De Givenchy, S. Amigoni, F. Guittard. Recent advances in designing superhydrophobic surfaces. Journal of Colloid and Interface Science 402 (2013) 1-18.

[19] A.F. Robert, M. Zou. Fabrication of stable superhydrophilic surfaces on titanium substrates. Journal of Adhesion Science and Technology 28(8-9) (2014) 823-832.

[20] K. Koch, W. Barthlott. Superhydrophobic and superhydrophilic plant surfaces: an inspiration for biomimetic materials. Philosophical Transactions of the Royal Society A 367(1893) (2009) 1487-1509.

[21] B. Bhushan. Biomimetics: lessons from nature–an overview. Philosophical Transactions of the Royal Society A 367(1893) (2009) 1445-1486.

[22] J. Zhanga, S.J. Severtson. Fabrication and use of artificial superhydrophilic surfaces. Journal of Adhesion Science and Technology 28(8-9) (2014) 751-768.

[23] L. Zhang, Y. Li, J. Sun, J. Shen. Mechanically stable antireflection and antifogging coatings fabricated by the Layer-by-Layer deposition process and postcalcination. Langmuir 24(19) (2008) 10851-10857.

[24] V. Zorba, X. Chen, S.S. Mao. Superhydrophilic TiO2 surface without photocatalytic activation. Applied Physics Letters 96 (2010) 093702.

[25] T. Nakatani, K. Okamoto, I. Omura, S. Yamashita. Imparting superhydrophilicity to Diamond-Like Carbon by plasma surface treatment technique. New Diamond and Frontier Carbon Technology 17(6) (2007) 289-300.

[26] Y. Takata, S. Hidaka, M. Masuda, T. Ito. Pool boiling on a superhydrophilic surface. International Journal of Energy Research 27(2) (2003) 111-119.

[27] J. Drelich, E. Chibowski, D.D. Mengb, K. Terpilowskic. Hydrophilic and superhydrophilic surfaces and materials. Soft Matter 7 (2011) 9804-9828.

[28] L. Zhang, N. Zhao, J. Xu. Fabrication and application of superhydrophilic surfaces: a review. Journal of Adhesion Science and Technology 28(8-9) (2014) 769-790.

[29] F. Iwasa, N. Hori, T. Ueno, H. Minamikawa, M. Yamada, T. Ogawa. Enhancement of osteoblast adhesion to UV-photofunctionalized titanium via an electrostatic mechanism. Biomaterials 31 (2010) 2717-2727.

[30] Y. Chun, D.S. Levi, K.P. Mohanchandra, G.P. Carman. Superhydrophilic surface treatment for thin film NiTi vascular applications. Materials Science and Engineering 29(8) (2009) 2436-2441.

[31] R. Wang, K. Hashimoto, A. Fujishim, M. Chikuni, E. Kojima, A. Kitamura, M. Shimohigoshi, T. Watanabe. Light-induced amphiphilic surfaces. Nature 388 (1997) 431-432.

[32] R.N. Wenzel. Resistance of solid surfaces to wetting by water. Industrial & Engineering Chemistry Research 28(8) (1936) 988-994.

[33] D. Quéré. Wetting and roughness. Annual Review of Materials Research 38 (2008) 71-99.

[34] A. Fujishimaa, X. Zhangb, D.A. Tryk. TiO2 photocatalysis and related surface phenomena. Surface Science Reports 63 (2008) 515-582.

[35] J. Ye, Q. Yin, Y. Zhou. Superhydrophilicity of anodic aluminum oxide films: from “honeycomb” to “bird's nest”. Thin Solid Films 517(21) (2009) 6012-6015.

[36] S.Y. Gu, Z.M. Wang, J.B. Li, J. Ren. Switchable wettability of thermo-responsive biocompatible nanofibrous films created by electrospinning. Macromolecular Materials and Engineering 295(1) (2010) 32-36.

[37] J. Fang, A. Kelarakis, L. Estevez, Y. Wang, R. Rodriguez, E.P. Giannelis. Superhydrophilic and solvent resistant coatings on polypropylene fabrics by a simple deposition process. Journal of Materials Chemistry 20(9) (2010) 1651-1653.

[38] X. Liu, J. He. One-step hydrothermal creation of hierarchical microstructures toward superhydrophilic and superhydrophobic surfaces. Langmuir 25(19) (2009) 11822-11826.

[39] W. Song, D.D. Veiga, C.A. Custódio, J.F. Mano. Bioinspired degradable substrates with extreme wettability properties. Advanced Materials 21(18) (2009) 1830-1834.

[40] M. Mirshekari, R. Azimirad, A. Z. Moshfegh. Superhydrophilic stability enhancement of RF co-sputtered Ti x Si 1− x O 2 thin films in dark. Applied Surface Science 256(8) (2010) 2500-2506.

[41] A. Borras, A. Barranco, A.R. González-Elipe. Reversible superhydrophobic to superhydrophilic conversion of Ag@TiO2 composite nanofiber surfaces. Langmuir 24(15) (2008) 8021-8026.

[42] T. Saison, C. Peroz, V. Chauveau, S. Berthier, E. Sondergard, H. Arribart. Replication of butterfly wing and natural lotus leaf structures by nanoimprint on silica sol–gel films. Bioinspiration & Biomimetics 3 (2008) 046004.

[43] F.Ç. Cebeci, Z. Wu, L. Zhai, R.E. Cohen, M.F. Rubner. Nanoporosity-driven superhydrophilicity: a means to create multifunctional antifogging coatings. Langmuir 22(6) (2006) 2856-2862.

[44] W. Hou, Q. Wang. Stable polytetrafluoroethylene superhydrophobic surface with lotus-leaf structure. Journal of Colloid and Interface Science 333(1) (2009) 400-403.

[45] O. Sato, S. Kubo, Z.Z. Gu. Structural color films with lotus effects, superhydrophilicity, and tunable stop-bands. Accounts of Chemical Research 42(1) (2009) 1-10.

[46] W.K. Cho, I.S. Choi. Fabrication of hairy polymeric films inspired by geckos: wetting and high adhesion properties. Advanced Functional Materials 18(7) (2008) 1089-1096.

[47] Z. Yuan, H. Chen, J. Tang, H. Gong, Y. Liu, Z. Wang, P. Shi, J. Zhang, X. Chen. A novel preparation of polystyrene film with a superhydrophobic surface using a template method. Journal of Applied Physics 40 (2007) 3485-3489.

[48] F. Shi, Z. Liu, G. L. Wu, M. Zhang, H. Chen, Z. Q. Wang, X. Zhang, I. Willner. Surface imprinting in Layer-by-Layer nanostructured films. Advanced Functional Materials 17(11) (2007) 1821-1827.

[49] E. Bormashenko, T. Stein, G. Whyman, Y. Bormashenko, R. Pogreb. Wetting properties of the multiscaled nanostructured oolymer and metallic superhydrophobic surfaces. Langmuir 22(24) (2006) 9982-9985.

[50] G. Decher, J.B. Schlenoff. Multilayer Thin Films. John Wiley & Sons (2006) 543-555.

[51] B. Aksakal, C. Hanyaloglu. Bioceramic dip-coating on Ti-6Al-4V and 316L SS implant materials. Journal of Materials Science: Materials in Medicine 19(5) (2008) 2097-104.

[52] M. Guglielmi, S. Zenezini. The thickness of sol-gel silica coatings obtained by dipping. Journal of Non-Crystalline Solids 121(1–3) (1990) 303-309.

[53] R.A. Fleminga, M. Zou. Fabrication of stable superhydrophilic surfaces on titanium substrates. Journal of Adhesion Science and Technology 28(8-9) (2014) 823-832.

[54] X. Li, X. Du, J. He. Self-cleaning antireflective coatings assembled from peculiar mesoporous silica nanoparticles. Langmuir 26(16) (2010) 13528-13534.

[55] H. Du, X. Li, J. He. Facile fabrication of hierarchically structured silica coatings from hierarchically mesoporous silica nanoparticles and their

excellent superhydrophilicity and superhydrophobicity. Applied Materials & Interfaces 2(8) (2010) 2365-2372.

[56] T. Sun, G. Wang, L. Feng, B. Liu, Y. Ma, L. Jiang, D. Zhu. Reversible switching between superhydrophilicity and superhydrophobicity. Angewandte Chemie International Edition 43(3) (2004) 357-360.

[57] F. Xia, L. Feng, S. Wang, T. Sun, W. Song, W. Jiang, L. Jiang. Dual-responsive surfaces that switch between superhydrophilicity and superhydrophobicity. Advanced Materials 18 (2006) 432-436.

[58] L. Xu, W. Chen, A. Mulchandani, Y. Yan. Reversible conversion of conducting polymer films from superhydrophobic to superhydrophilic. Angewandte Chemie International Edition 44 (2005) 6009-6012.

[59] P. Uhlmann, L. Ionov, N. Houbenov, M. Nitschke, K. Grundke, M. Motornov, S. Minko, M. Stamm. Surface functionalization by smart coatings: Stimuli-responsive binary polymer brushes. Progress in Organic Coating 55(2) (2006) 168-174.

[60] R.H. Dettre, R.E. Johnson. Contact angle hysteresis: contact angle measurements on rough surfaces. Advances in Chemistry Series 43 (1964) 136-144.

[61] A. Marmur, E. Bittoun. When Wenzel and Cassie are right: reconciling local and global considerations. Langmuir 25(3) (2009) 1277-1281.

[62] B. Bhushan, Y. C. Jung. Natural and biomimetic artificial surfaces for superhydrophobicity, self-cleaning, low adhesion, and drag reduction. Progress in Materials Science 56 (2011) 1-108.

[63] N. Michael, B. Bhushan. Hierarchical roughness makes superhydrophobic states stable. Microelectronic Engineering 84(3) (2002) 382-386.

[64] W. Barthlott, C. Neinhuis. Purity of the sacred lotus, or escape from contamination in biological surfaces. Planta 202(1) (1997) 1-8.

[65] A.B.D. Cassie, S. Baxter. Wettability of porous surface. Transactions of the Faraday Society 40 (1944) 546-551.

[66] R.E. Johnson, R. H. Dettre. Contact angle, wettability and adhesion. Advances in chemistry series. American Chemical Society 43 (1946).

[67] A. Marmur. Wetting on hydrophobic rough surfaces: to be heterogeneous or not to be? Langmuir 19 (2003) 8343-8348.

[68] A. Lafuma, D. Quere. Superhydrophobic states. Nature Materials 2 (2003) 457-460.

[69] X.S. Cui, W. Li. On the possibility of superhydrophobic behavior for hydrophilic materials. Journal of Colloid and Interface Science 347 (2010) 156-162.

[70] Y. Ma, X. Cao, X. Feng, Y. Ma, H. Zou. Fabrication of super-hydrophobic film from PMA with intrinsic water contact angle below 90°. Polymer 48(26) (2007) 7455-7460.

[71] B. Bushan, Y.C. Jung. Natural and biomimetic artificial surfaces for superhydrophobicity, Self-cleaning, low adhesion and drag reduction. Progress in Materials Science 56 (2011) 1-108.

[72] V. Grigaliūnasa, S. Tamulevičius, R. Tomašiūnas, V. Kopustinskas, A. Guobien, D. Jucius. Laser pulse assisted nanoimprint lithography. Thin Solid FIlms 13 (2004) 453-454.

[73] S. Kumar, R. Singh, T.P. Singh, B.L. Sethi. Surface modification by electrical discharge machining: a review. Journal of Materials Processing Technology 209(8) (2009) 3675-3687.

[74] Q. He, Z.X. Luo, X. Y. Chen. Comparison of residual stress measurement in thin films using surface micromachining method. Thin Solid Films 516(16) (2008) 5318-5323.

[75] A.J.B. Milne, A. Amirfazli. Drop shedding by shear flow for hydrophilic to superhydrophobic surfaces. Langmuir 25(24) (2009) 14155-14164.

[76] R. Jagdheesh, B. Pathiraj, E. Karatay, G.R.B.E. Romer, A.J. Huisin‘t Veld. Laser-induced nanoscale superhydrophobic structures on metal surfaces. Langmuir 27(13) (2011) 8464-8469.

[77] A.M. Kietzig, S. G. Hatzikiriakos, P. Englezos. Patterned superhydrophobic metallic surfaces. Langmuir 25(8) (2009) 4821-4827.

[78] K. Jittavanich, C.B. Clemons, K.L. Kreider, M. Aljarrah, E. Evans, G.W. Young. Modelling, simulation and fabrication of coated structures using the dip coating technique. Chemical Engineering Science 65(23) (2010) 6169-6180.

[79] J. Liu, A. Rasheed, M. L. Minus, S. Kumar. Processing and properties of carbon nanotube / poly (methyl methacrylate) composite films. Polymer 112 (2008) 142-156.

[80] P. Pareo, G. De Gregorio. Ultra lightweight PMMA-based composite plates with robust super-hydrophobic surfaces. Journal of Colloid and Interface Science 363(2) (2011) 668-675.

[81] Y. Wu, H. Sugimura, Y. Inoue, O. Takai. Preparation of hard and ultra water-repellent silicon oxide films by microwave plasma-enhanced CVD at low substrate temperatures. Thin Solid Films 435 (2003) 161-164.

[82] R. Karmouch, G.G. Ross. Superhydrophobic wind turbine blade surfaces obtained by a simple deposition of silica nanoparticles embedded in epoxy. Applied Surface Science 257 (2010) 665-669.

[83] M. Grischke, A. Hieke, F. Morgenweck, H. Dimigen. Variation of the wettability of DLC-coatings by network modification using silicon and oxygen. Diamond and Related Materials 7 (1998) 454-458.

[84] Y. Rahmawan, M. Moon, K. Kim, K. Lee, K. Suh. Wrinkled, dual scale structures of damond like carbon (DLC) for superhydrophobicity. Langmuir 26(1) (2010) 484-491.

[85] G.K. Kannarpady, R. Sharma, B. Liu, S. Trigwell, C. Ryerson, A. S. Biris. Silane decorated metallic nanorods for hydrophobic applications. Applied Surface Science 256(6) (2010) 1679-1682.

[86] S.A. Kulinich, S. Farhadi, K. Nose, X. W. Du. Superhydrophobic surfaces: are they really ice-repellent? Langmuir 27(1) (2011) 25-29.

[87] T.S. Wong, S.H. Kang, S.K.Y. Tang, J.S. Elizabeth, B.D. Hatton, A. Grinthal, J. Aizenberg. Bioinspired self-repairing slippery surfaces with pressure-stable omniphobicity. Nature 477 (2011) 443-447.

[88] J.D. Smith, R. Dhiman, S. Anand, E. Reza-Garduno, R.E. Cohen, G.H. McKinley, K.K. Varanasi. Droplet mobility on lubricant-impregnated surfaces. Soft Matter 9 (2013) 1772-1780.

[89] S. Cicely, M. Noah, W. Tak-Sing, K. Philseok, A. Joanna. Fabrics coated with lubricated nanostructures display robust omniphobicity. Nanotechnology 25 (2014) 014019.

[90] J. Li, T. Kleintschek, A. Rieder, Y. Cheng, T. Baumbach, U. Obst, T. Schwartz, P.A. Levkin. Hydrophobic Liquid-Infused Porous Polymer Surfaces for Antibacterial Applications. Applied Materials & Interfaces 5(14) (2013) 6704-6711.

[91] L. Zhu, J. Xue, Y. Wang, Q. Chen, J. Ding, Q. Wang. Ice-phobic Coatings Based on Silicon-Oil-Infused Polydimethylsiloxane. Applied Materials & Interfaces 5 (2013) 4053-4062.

[92] S.R. White, M.M. Caruso, J.S. Moore. Autonomic healing of polymers. MRS Bulletin 33(8) (2008) 766-769.

[93] T. Verho, C. Bower, P. Andrew, S. Franssila, O. Ikkala, R.H.A. Ras. Mechanically durable superhydrophobic surfaces. Advanced Materials 23(5) (2011) 673-679.

[94] K. Liu, Y. Tian, L. Jiang. Bio-inspired superoleophobic and smart materials: design, fabrication, and application. Progress in Materials Science 58 (2013) 503-564.

[95] Y. Bar-Cohen. Biomimetics: nature based innovation. CRC Press (2011).

[96] B. Bhushan. Biomimetics: bioinspired hierarchical-structured surfaces for green science and technology. Springer-Verlag: Heidelberg (2012).

[97] D. Ebert, B. Bhushan. Transparent, superhydrophobic, and wear-resistant coatings on glass and polymer substrates using SiO2, ZnO, and ITO nanoparticles. Langmuir 28 (2012) 11391-11399.

[98] K. Tsujii, T. Yamamoto, T. Onda, S. Shibuichi. Super oil-repellent surfaces. Angewandte Chemie International Edition 36 (1997) 1011-1012.

[99] Y.C. Jung, B. Bhushan. Wetting behavior of water and oil droplets in three-phase interfaces for hydrophobicity/philicity and oleophobicity/philicity. Langmuir 25 (2009) 14165-14173.

[100] A. Ahuja, J.A. Taylor, V. Lifton, A.A. Sidorenko, T.R. Salamon, E.J. Lobaton, P. Kolodner, T.N. Krupenkin. Nanonails: a simple geometrical approach to electrically tunable superlyophobic surfaces. Langmuir 24(1) (2008) 9-14.

[101] L.Cao, T.P. Price, T., M. Weiss, D. Gao. Super water- and oil-repellent surfaces on intrinsically hydrophilic and oleophilic porous silicon films. Langmuir 24 (2008) 1640-1643.

[102] A. Marmur. From hygrophilic to superhygrophobic: theoretical conditions for making high-contact-angle surfaces from low-contact-angle materials. Langmuir 24 (2008) 7573-7579.

[103] M. Nosonovsky. Multiscale roughness and stability of superhydrophobic biomimetic interfaces. Langmuir 23(6) (2007) 3157-3161.

[104] A. Tuteja, W. Choi, M. Ma, J.M. Mabry, S.A. Mazzella, G.C. Rutledge, G.H. McKinley, R.E. Cohen. Designing superoleophobic surfaces. Science 318 (2007) 1618-1622.

[105] A. Tuteja, W. Choi, J.M. Mabry, G.H. McKinley, R.E. Cohen. Robust omniphobic surfaces. Proceedings of the National Academy of Sciences 105 (2008) 18200-18205.

[106] S.A. Brewer, C.R. Willis. Structure and oil repellency: textiles with liquid repellency to hexane. Applied Surface Science 254 (2008) 6450-6454.

[107] M. Ma, Y. Mao, M. Gupta, K.K. Gleason, G.C. Rutledge. Superhydrophobic fabrics produced by electro-spinning and chemical vapor deposition. Macromolecules 38 (2005) 9742-9748.

[108] G. McHale, N.J. Shirtcliffe, S. Aqil, C.C. Perry, M.I. Newton. Topography driven spreading. Physical Review Letters 93 (2004) 036102.

[109] D. Quere. Rough ideas on wetting. Physica 313 (2002) 32-46.

[110] A. Marmur. Solid-surface characterization by wetting. Annual Review of Materials Research 39 (2009) 473-489.

[111] H. Ohshima. Sedimentation potential in a concentrated suspension of spherical colloidal particles. Journal of Colloid and Interface Science 208 (1998) 295-301.

[112] M. Nosonovsky, B. Bhushan. Patterned non-adhesive surfaces: Superhydrophobicity and wetting regime transitions. Langmuir 24 (2008) 1525-1533.

[113] S.S. Chhatre, W. Choi, A. Tuteja, K.C. Park. Scale dependence of mniphobic mesh surfaces. Langmuir 26(6) (2010) 4027-4035.

[114] P. Muthiah, B. Bhushan, K. Yun, H. Kondo. Dual-layered-coated mechanically-durable superomniphobic surfaces with anti-smudge properties. Journal of Colloid and Interface Science 409 (2013) 227-236.

[115] C.T. Hsieh, J.M. Chen, R.R. Kuo, T.S. Lin, C.F. Wu. Influence of surface roughness on water- and oil-Repellent surfaces coated with nanoparticles. Applied Surface Science 240 (2005) 318-326.

[116] A. Steele, I. Bayer, E. Loth. Inherently superoleophobic nanocomposite coatings by spray atomization. Nano Letters 9 (2009) 501-505.

[117] C.T. Hsieh, F.L. Wu, W.Y. Chen. Super water- and oil-repellencies from silica-based nanocoatings. Surface and Coatings Technology 203 (2009) 3377-3384.

[118] A. Das, T.M. Schutzius, I.S. Bayer, C.M. Megaridis. Superoleophobic and conductive carbon nanofiber/fluoropolymer composite films. Carbon 50 (2012) 1346-1354.

[119] C.T. Hsieh, D.Y. Tzou, C.C. Chen, C.Y. Lai, Y.Y. Liu. Deposition and super liquid repellency of fluorinated ZnO nanoparticles on carbon fabrics. Surface and Coatings Technology 206 (2012) 4639-4644.

[120] D.W. Han, A.J. Steckl. Superhydrophobic and oleophobic fibers by coaxial electrospinning. Langmuir 25 (2009) 9454-9462.

[121] M. Im, H. Im, J.H. Lee, J.B. Yoon, Y.K. Choi. A robust superhydrophobic and superoleophobic surface with inverse-trapezoidal microstructures on a large transparent flexible substrate. Soft Matter 6 (2010) 1401-1404.

[122] H. Zhao, K.Y. Law, V. Sambhy. Fabrication, surface properties, and origin of superoleophobicity for a model textured surface. Langmuir 27 (2011) 5927-5935.

[123] H. Bellanger, T. Darmanin, F. Guittard. Superoleophobic surfaces. Langmuir 28 (2012) 186-192.

[124] X. Deng, L. Mammen, H.J. Butt, D. Vollmer. Candle soot as a template for a transparent robust superamphiphobic coating. Science 335 (2012) 67-70.

[125] C.W. Extrand. Designing for optimum liquid repellency. Langmuir 22(4) (2006) 1711-1714.

[126] H. Jin, X. Tian, O. Ikkala, R.H.A. Ras. Preservation of superhydrophobic and superoleophobic properties upon wear damage. ACS Applied Materials & Interfaces 5 (2013) 485-488.

[127] A. Grigoryev, I. Tokarev, K. G. Kornev, I. Luzinov, S. Minko. Superomniphobic magnetic microtextures with remote wetting control. Journal of the American Chemical Society 134 (2012) 12916-12919.

[128] Y.T. Cheng, D.E. Rodak. Is the lotus leaf superhydrophobic? Applied Physics Letters 86(14) (2005) 144101.

[129] S. Herminghaus. Roughness-induced non-wetting. Europhysics letters 52(2) (2000) 165-170.

[130] L. Cao, H.H. Hu, D. Gao. Design and fabrication of micro-textures for inducing a superhydrophobic behavior on hydrophilic materials. Langmuir 23(8) (2007) 4310-4314.

[131] A. Tuteja, W. Choi, G.H. McKinley, R.E. Cohen, M.F. Rubner. Design parameters for superhydrophobicity and superoleophobicity. MRS Bulletin 33 (2008) 752-758.

[132] A. Cavalli, F. Mugele. Superamphiphobic Surfaces. In Droplet Wetting and Evaporation; Brutin, D.; Academic Press (2015) 57-69.

[133] Z. Chua, S. Seeger. Superamphiphobic surfaces. Chemical Society Reviews 43 (2014) 2784-2798.

[134] C. Neinhuis, W. Barthlott, A. Botany. Characterization and distribution of water repellent, self-cleaning plant surfaces. Annals of Botany 79 (1997) 667-677.

[135] J.P. Youngblood, N.R. Sottos. Bioinspired Materials for Self-cleaning and self-healing. MRS Bulletin 33 (2008) 732-741.

[136] Y.C. Jung, B. Bhushan. Mechanically durable carbon nanotube-composite hierarchical structures with superhydrophobicity, self-cleaning, and low-drag. ACS Nano 3 (2009) 4155-4163.

[137] C.F. Wang, Y.T. Wang, P.H. Tung, S.W. Kuo, C.H. Lin, Y.C. Sheen, F.C. Chang. Stable Superhydrophobic Polybenzoxazine Surfaces over a Wide pH Range. Langmuir 22 (2006) 8289-8292.

[138] T. Yanagisawa, A. Nakajima, M. Sakai, Y. Kameshima, K. Okada. Preparation and abrasion resistance of transparent super-hydrophobic coating by combining crater-like silica films with acicular boehmite powder. Materials Science and Engineer 161 (2009) 36-39.

[139] B. Li, J. Zhang, L. Wu, A. Wang. Durable Superhydrophobic Surfaces Prepared by Spray Coating of Polymerized Organosilane/Attapulgite Nanocomposites. ChemPlusChem 78 (2013) 1503-1509.

[140] J. Cheek, A. Steele, I.S. Bayer, E. Loth. Underwater saturation resistance and electrolytic functionality for superhydrophobic nanocomposites. Colloid & Polymer Science 291 (2013) 2013-2016.

[141] H. Cho, D. Kim, C. Lee, W. Hwang. A simple fabrication method for mechanically robust superhydrophobic surface by hierarchical aluminum hydroxide structures. Current Applied Physics 13 (2013) 762-767.

[142] S. Zhou, X. Ding, L. Wu. Fabrication of ambient-curable superhydrophobic fluoropolysiloxane/TiO2 nanocomposite coatings with good mechanical properties and durability. Progress in Organic Coatings 76 (2013) 563-570.

[143] F.J. Wang, S. Lei, J.F. Ou, M.S. Xue, W. Li. Superhydrophobic surfaces with excellent mechanical durability and easy repairability. Applied Surface Science 276 (2013) 397-400.

[144] F. Guo, X. Su, G. Hou, P. Li. Bioinspired fabrication of stable and robust superhydrophobic steel surface with hierarchical flowerlike structure. Colloids Surface A 401 (2012) 61-67.

[145] L. Feng, Y. Liu, H. Zhang, Y. Wang, X. Qiang. Superhydrophobic alumina surface with high adhesive force and long-term stability. Colloids and Surfaces A 410 (2012) 66-71.

[146] X. Zhu, Z. Zhang, J. Yang, X. Xu, X. Mena, X. Zhou. Facile fabrication of a superhydrophobic fabric with mechanical stability and easy-reparability. Journal of Colloid and Interface Science 380 (2012) 182-186.

[147] X. Zhang, X. Liu, J. Laakso, E. Levänen, T. Mäntylä. Easy-to-clean property and durability of superhydrophobic flaky-alumina coating on stainless steel in field test at a paper machine. Applied Surface Science 258 (2012) 3102-3108.

[148] A. Steele, I. Bayer, E. Loth. Adhesion strength and superhydrophobicity of polyurethane/organoclay nanocomposite coatings. Journal of Applied Polymer Science 125 (2012) 445-452.

[149] X. Zhu, Z. Zhang, X. Men, J. Yang, K. Wang, X. Xu, X. Zhou, Q. Xue. Robust superhydrophobic surfaces with mechanical durability and easy repairability. Journal of Materials Chemistry 21 (2011) 15793-15797.

[150] T.M. Schutzius, M.K. Tiwari, I.S. Bayer, C.M. Megaridis. High strain sustaining, nitrile rubber based, large-area, superhydrophobic, nanostructured composite coatings. Composites A 42 (2011) 979-985 .

[151] A. Amirfazli. Superomniphobic surfaces for military applications: nano- and micro-fabrication methods. Defence R&D Canada – Atlantic, Contract Report DRDC Atlantic (2011).

[152] L. Boinovich, A.M. Emelyanenko, A.S. Pashinin. Analysis of long-term durability of superhydrophobic properties under continuous contact with water. Applied Materials & Interfaces 2 (2010) 1754-1758.

[153] I.A. Larmour, G.C. Saunders, S.E.J. Bell. Compressed metal powders that remain superhydrophobic after abrasion. ACS Applied Materials & Interfaces 2 (2010) 2703-2706.

[154] Bayer, A. Brown, A. Steele, E. Loth. Transforming anaerobic adhesives into highly durable and abrasion resistant superhydrophobic organoclay nanocomposite films: a new hybrid spray adhesive for tough superhydrophobicity. Applied Physics Express 2 (2009) 125003-125006.

[155] Z. Cui, L. Yin, Q. Wang, J. Ding, Q. Chen. A facile dip-coating process for preparing highly durable superhydrophobic surface with multi-scale structures on paint films. Journal of Colloid and Interface Science 337 (2009) 531-537.

[156] Z. Cui, Q. Wang, Y. Xiao, C. Su, Q. Chen. The stability of superhydrophobic surfaces tested by high speed current scouring. Applied Surface Science 254 (2008) 2911-2916.

[157] J. Zimmermann, F.A. Reifler, U. Schrade, G.R.J. Artu, S. Seeger. Long term environmental durability of a superhydrophobic silicone nanofilament coating. Colloids and Surfaces A 302 (2007) 234-240.

[158] J. Zimmermann, G.R.J. Artus, S. Seeger. Long term studies on the chemical stability of a superhydrophobic silicone nanofilament coating. Applied Surface Science 253 (2007) 5972-5979.

[159] S. Wang, L. Feng, L. Jiang. One-step solution-immersion process for the fabrication of stable bionic superhydrophobic surfaces. Advanced Materials 18 (2006) 767-770.

[160] Z. Guo, F. Zhou, J. Hao, W. Liu. Stable Biomimetic super-hydrophobic engineering materials. Journal of the American Chemical Society 127 (2005) 15670-15671.

Chapter 3

3 Wettability effect on pool boiling

3.1 Introduction

Nucleate boiling is characterized by the liquid–vapor phase change associated with the bubble formation. Compared to single-phase, this process involves heat transfer coefficients (HTC) typically one order of magnitude higher than single-phase forced convection and two orders of magnitude higher than single-phase natural convection [1], thus enabling to exchange more energy with a relatively lower temperature difference at the wall. The high heat transfer rates delivered by boiling at low superheat surface temperature are needed in many industrial applications at diverse spatial scales, such as electronics cooling, boilers, nuclear and chemical reactors, refrigeration systems, thermal generation of electricity, metallurgy or food processing (e.g. [2]). In particular, the potential to attain high heat transfer coefficients have been widely explored for cooling purposes (e.g. [3,4]). Configurations based on pool boiling are particularly attractive, given their hardware simplicity, without pumping or clogging issues, as the fluid heated on a hot surface is simply transported by buoyancy [5-6].

Following the boiling curve (or Nukiyama curve [7]), several regimes can be identified, namely free convection, nucleate boiling, transition boiling, and film boiling [7] (See Figure 3.1).

Within the nucleate boiling regime one may in turn distinguish 2 regions. The region of partial nucleate boiling, below line A-B in Figure 3.1, in which isolated bubbles form at nucleation sites and detach from the surface. This separation induces considerable fluid mixing near the surface, substantially increasing the heat transfer coefficient and the heat flux. In this regime, most of the heat exchange occurs through the direct transfer from the surface to liquid in motion at the surface and not through the vapour bubbles rising from the surface. The second region is defined bellow B-C in Figure 3.1 and is called fully developed nucleate boiling. Here, as the wall superheat ∆T, i.e. the difference between the surface temperature and the saturation temperature, rises beyond ΔT_B, i.e. the wall superheat in point B, more nucleation sites become active and increased bubble formation causes bubble interference and coalescence.

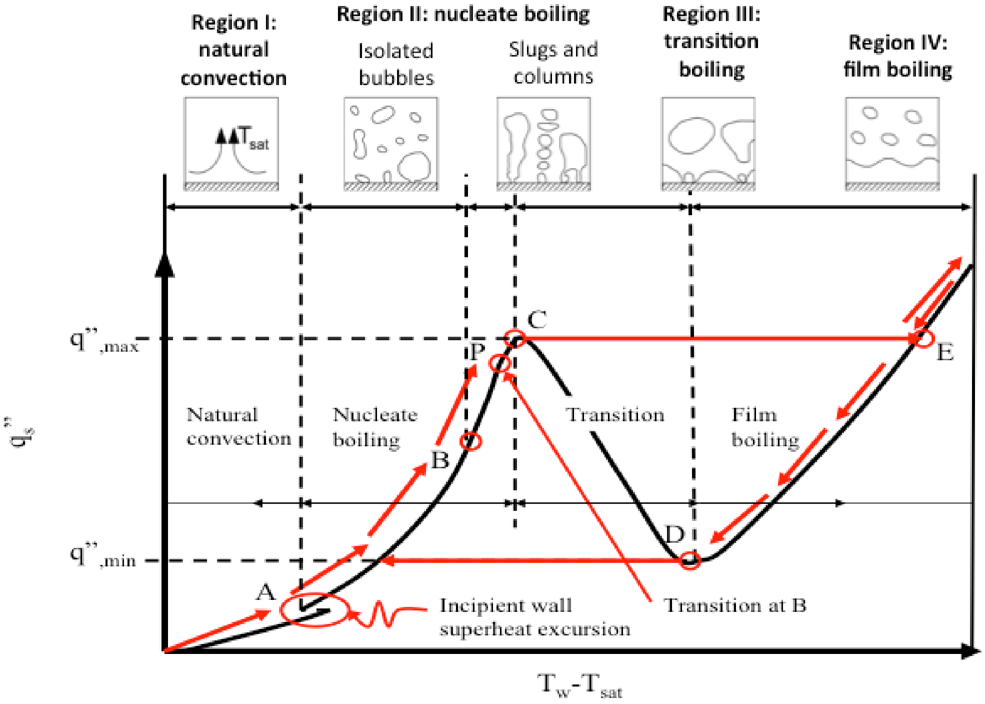

Figure 3.1: Boiling curve for saturated water at 1 atm. Adapted from Dhir [8].

The vapour escapes as jets or columns, which subsequently merge into slugs of vapour. This condition leads to interference between densely populated bubbles which inhibit the motion of liquid near the surface. The nucleate boiling region is upper limited by the Critical Heat Flux (CHF), which is the highest heat flux that a surface can exchange with a boiling fluid before the individual bubbles merge into a vapor layer that insulates the surface from the liquid. Under these conditions, the HTC is drastically reduced, which induces a significant and often destructive surface temperature increase ([9-11]) called dry-out. Hence, for most of the aforementioned applications, it is desirable to work within the nucleate boiling region, where the HTC typically increases with the heat flux, as the solid surface interacts with an increased number of liquid and vapor pockets, maximizing the opportunity to transfer heat and mass across the liquid wedges of the multiple wetting lines. Therefore, one must assure that the working conditions are safely far away from the CHF.

Subsequently to this line of thought, it is understandable that, at the light of the literature reviewed, efforts have mostly been put in delaying the CHF and/or increasing the HTC. This is quite a complex task since such parameters depend on the thermophysical properties of the boiling liquid and of the surface material (thermal conductivity and thermal absorption), interactions between the solid surface, liquid and vapor (wettability, adhesion, adsorption) and surface microgeometry (dimensions and shape of cracks and pores) (e.g. [12]). Also, some of these characteristics are difficult to assess quantitatively and are in turn dependent on other factors such as the presence of surface contamination and oxide films, the method of surface treatment, the manufacturing processes, among others [13].

Amongst this intricate list, two parameters of primary importance can be highlighted: surface topography [14-19] and wettability [9,13,20-32]. These parameters are strongly related and they incorporate the dynamics interaction between the working liquid and the heated solid. Also, they are at least as important as the solid thermal conductivity [20]. So, many authors have focused on modifying the wettability acting on its topography, by means of surface roughening, etching of cavities [33-34], or even microporous coatings [35-36], both with regular arrangements and/or with stochastic organization. Additionally, with the development of micro-and-nano-fabrication techniques, the researchers were able to cover various scales and shapes. Hence, from the pioneering research of Corty and Foust [22] and the early “micro-patterns” with hundreds of microns in size created by Anderson and Mudawar [17], the surface treatment methods swiftly evolved to increasing the surface area with micro pin-fins [37], applying wicking structures to promote the liquid supply by capillary pumping [38,39] and depositing nano-particles or coating with nanomaterials [40-42]. Others chose to change wettability by chemical modification of the surface (e.g. [43-49]). Finally, the wettability can be changed by acting on the working fluid instead of altering the surface, which may be achieved using surfactants (e.g. [27]) or nanofluids (e.g. [50]), although the latter, consisting basically in the suspension of nanoparticles in the fluid, may act as a surface topography modification strategy, as further explained.

Looking at the extensive list of studies that have been performed to enhance pool boiling heat transfer, one can observe that researchers have been mostly determined on strategies to achieve their goal as fast as possible, which is important as it has stimulated the advance of many of the current surface treatment techniques, but the understanding of the physics governing the underlying phenomena was somehow left to a secondary plan. As a result, many authors altered both surface topography and wettability in a way that is difficult to control and differentiate, so that the results are fairly scattered and it is quite unclear of how the wettability is being changed, which its role is and how it can be controlled to efficiently act on particular pool boiling mechanisms. The need for acting independently on wettability and on topography in order to better isolate the effect of wettability on pool boiling has only recently been shown by Bourdon et al. [51-52].

The results can further be misleading when comparing the works of different authors since they are not all acting on the same mechanisms or even are in the same region of the boiling curve. Hence, to date one can identify that research, addressing surface wettability modification, is mainly acting on two distinct regimes: i) at low heat fluxes, in partial nucleate boiling, for which the HTC can be enhanced by promoting nucleation [53] and ii) at high heat fluxes, in the fully developed regime of nucleate boiling, in which the main objective, besides having high HTC, is to delay the occurrence of the CHF. This is important to take into account, as the heat transfer and bubble dynamics characteristics are quite dissimilar in each of these regimes, so they are more likely to demand for quite diverse wetting conditions.

In line with the aforementioned issues, the first part of this chapter concerns a review of the wettability role on the pool boiling heat transfer, giving particular emphasis on its role on the physics of the observed phenomena. A short but necessary review of the relation between wettability and surface topography is presented; afterwards, the fundamentals of nucleation and inception are briefly explained to remind the vital role of wettability in the elemental pool boiling mechanisms. The methods to alter the wettability are then described divided in i) modification of the liquid properties , ii) modification of surface chemistry and iii) modification of surface topography; their diverse effects on nucleation, bubble dynamics and heat transfer mechanisms are discussed. Finally, the theoretical approaches to describe the boiling curve and to predict the heat fluxes and heat transfer coefficients are addressed targeting to understand how the effects of wettabilitty are currently described. The aim here is to identify how good the role of the wettability in the basic pool boiling phenomena is understood and recognize hot topics for further research. The following experimental analysis is done due by the literature analysis conducted, and considering the remaining gaps in understanding how the surface wettability influences the heat exchange in the pool boiling phenomenon. By doing this, one expects to contribute for the investigation of pool boiling heat transfer enhancement to proceed in a more systematic manner.

3.2 Wettability and surface topography

When a liquid vaporizes onto a heated solid surface, the triple contact lines establishing the boundaries between the three phases (liquid, solid and gas) can move, expand or shrink during phase change heat transfer being the motion controlled by the balance between the interfacial tensions, i.e. governed by wettability. In practical terms, the wettability quantifies the extent at which the surface keeps wetted by the liquid. It can be characterized by different quantities, but the contact angle of a sessile droplet onto a flat rigid surface is the most commonly used. From a thermodynamic point of view, determining the equilibrium conditions of a liquid droplet deposited onto a surface is a problem of minimization of the system Gibbs energy G. At constant temperature, pressure and chemical composition, the equilibrium (dG=0) can be expressed by the well-known and already mentioned in the previous chapter Young's equation [54]. Several efforts have been made, particularly by experimentalists, to establish functional relations between the contact angle and more specific geometrical parameters associated with the topography of the surface. In an early study, Hitchcock et al. [55] investigated sixteen substrates and liquid combinations and reported a general linear increase of the contact angle with the dimensionless roughness R_a/λ_R defined as the ratio of the average amplitude, R_a, to the average wavelength of the grooves, λ_R. Exceptions to this generalization were observed for good wetting drops on roughened silica and nickel substrates, which were interpreted by the authors to be associated with the energy required by the advancing liquid front to overcome energy barriers associated with surface features. In the contrary, Hong et al. [56] observed a monotonic decrease of the static contact angles of water, refrigerants, and alcohols on metal surfaces of decreasing roughness and/or degree of oxidation for mean roughness below 0.5µm. More recently, Kandlikar and Steinke [57-58] reported, for water droplets deposited onto copper and stainless steel targets, that the contact angle first decreases as the surface roughness is increased, but starts increasing with increasing surface roughness above 0.3μm.

Numerous experimental studies on the effects of substrate roughness on wettability, such as those reported above, make use of natural surfaces and take into account the mean amplitude of asperities only to characterize the topography, sometimes also their wavelength. But it is known that other topographical characteristics rather than R_a and λ_R (e.g. the shape of the rough peaks) change the energy barriers that the liquid must overcome to reach the minimum energy contact angle, as referred by Hong et al. [56], so the derived empirical correlations and/or trends may be of limited validity. In this context, many researchers attempted to use regular surfaces with well-defined geometrical interfacial conditions and focused on the modification of surface wettability by acting on its topography, very often establishing geometrical relations between the features of the surface topography, disposed in regular patterns and the apparent contact angle (e.g. [59-65]). Despite this extensive research, the classification of the wetting regimes, the applicability of the Wenzel and Cassie and Baxter theories and the transition between states are still hot topics in discussion, as recently revisited by Marmur [66].

In contrast, the effects of the liquid and/or the surface temperature have not been addressed so often. Though static contact angles are not much sensitive to the surface temperature, except for large temporal scales, for which they decrease due to evaporation at the interface (e.g. Crafton and Black [67]), variations of the dynamic contact angles are noteworthy. However, some contradictions are reported for instance when analysing the results reported by Bernardin et al. [68-70], Kandlikar and Steinke [57-58] and by Petke and Ray [71], as dissimilar trends are reported for advanced and receding angles. Here, mostly dynamic angles are worth to analyse as the motion of the contact line is much affected during evaporation. Also, it is not clear weather this effect is due to interfacial forces and due to the surface properties or is mostly governed by evaporation since, for instance, the largest variations in the contact angles, as reported by Kandlikar and Steinke [57-58], do not seem to occur at the rougher surfaces and no clear trend is taken between the evolution of the contact angles and the nature of the surface.

The description of the wettability, as discussed above, is typically related to a liquid (e.g. a droplet) in contact with the solid surface and surrounded by vapour. In pool boiling, nevertheless, the wettability is related to the bubble formation, so vapour is surrounded by liquid. In this context, surface roughness is important as it provides micro-cavities that besides may alter the

wettability, are also likely to act as nucleation sites. Looking at the surface topography mainly as a promoter of nucleation sites, the role of the wettability can be interpreted as follows: low wetting liquids, like water, are more likely not to fill completely the micro-cavities, due to the balance of the interfacial tensions within the cavity while; on the other hand, liquids wetting well the surfaces (e.g. refrigerants) are more likely to completely penetrate into the rough cavities. Measured contact angles reported in the literature, for water, commonly range from about 90º to 140º. This means that wettability may decrease the work required for vapour bubble creation on smooth surfaces by 2–3 times. Nevertheless, the probability for vapour bubble generation would be still quite small, and the required overheating would be quite high. According to Skripov [72], even at θ = 129º for water at atmospheric pressure, the required overheating decreases only by 32K compared to the ultimate overheating of 202K at bulk boiling. On the other hand, Kolev [73], using literature data on the boiling of water on different surfaces and surface finishes, concluded that the contact angle was perhaps the single most important factor in determining the nucleation site density and the heat flux and is responsible for the large spread in the experimental data on boiling heat transfer. Balss et al. [74] showed that on smooth uniform surfaces, low wettability decreased the onset temperature for nucleate boiling in fast transient events. Hibiki and Ishii [28] correlated active nucleation site density with static contact angle, obtaining very good agreement with their model for a wide variety of liquids and test conditions. So, one may state that the triggering of boiling on a superhydrophilic surface requires larger overheating and the formed bubbles tend to slide, while superhydrophobicity favors the nucleation and the high contact angles tend to stabilize bubble adhesion.
This becomes clearer after introducing the basic mechanisms of nucleation, in the following paragraphs.

3.3 Fundamentals on the boiling onset: the role of wettability

3.3.1 Nucleation, inception and bubble dynamics

Nucleation normally occurs at nucleation sites on surfaces contacting the liquid or vapour. Also suspended particles or minute bubbles provide nucleation sites. This is called heterogeneous nucleation. Nucleation without preferential nucleation sites is called homogeneous nucleation. Homogeneous nucleation requires very particular conditions of completely pure and carefully degassed substance and it occurs spontaneously and randomly, but it requires superheating or supercooling of the medium (e.g. Stephan [75]). Homogeneous nucleation, compared to the heterogeneous nucleation, occurs with much more difficulty in the interior of a uniform substance. So, homogeneous nucleation is not the mechanism observed in most of the literature works or in practice. Therefore, despite nucleation can be either homogenous or heterogeneous, only heterogeneous nucleation will be revised here.

The heterogeneous mechanism considers that vapour/gas is trapped in the microscopic cavities and crevices existing on the surfaces, which act as nuclei for bubbles. Naturally, the number density, size range and geometric shapes of these crevices depend on the surface material, finishing, and level of oxidation or contamination. Corty and Foust [22] were the first to postulate a vapour-trapping mechanism in nucleate boiling based on their observations, which was later confirmed by Clark et al. [76]. Once the nucleus is formed, it will only subsist if its internal temperature equals the saturation temperature for the pressure of the vapour phase, determined from the Young-Laplace equation. Assuming ideal gas behavior for the vapour and that the specific volume of the liquid compared to the one of the vapour is negligible, the Clausius-Clapeyron equation can be applied, so the temperature needed to activate a vapour nucleus is given by:

$$T_g - T_{sat} = \frac{2\sigma_{lg}}{R_c h_{fg} \rho_g} \qquad (1)$$

being Tg and Tsat respectively the vapour temperature and the liquid saturation temperature, Rc the characteristic length of the cavity, hfg the latent heat of vaporization and ρg the vapour density. This means that smaller cavities can be activated with increasing nucleus vapour temperature.

Bankoff [23] was the first to provide a criterion for entrapment of gas in a wedge by an advancing liquid front. In wedge-shaped grooves for which the contact angle is higher than the wedge angle, vapor will not be completely displaced by the advancing liquid front and trapping occurs. If the contact angle is lower than the wedge angle the vapor will be completely displaced by liquid and the cavity deactivated. According to this criterion, a conical cavity can trap vapour/gas as long as the contact angle θ between the surface of the inflowing liquid and the wall of the liquid front is twice larger the aperture angle of the conical section β (see Figure 3.2), i.e.:

$$\theta > 2\beta \qquad (2).$$

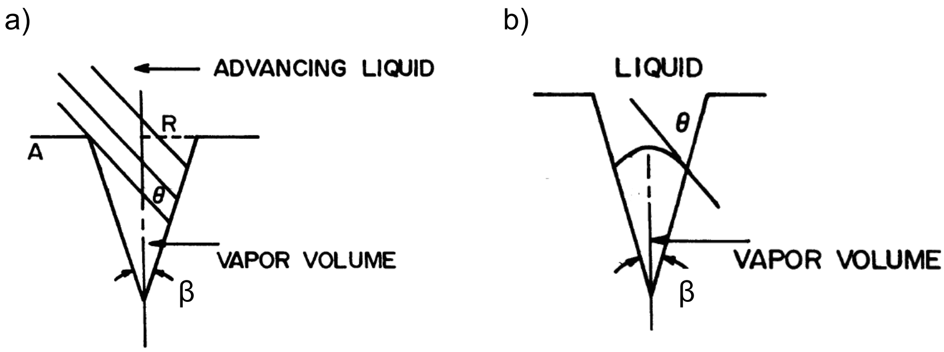

Figure 3.2: a) Vapor trapping process. b) Formation of radius of curvature.

On the other hand, Wang and Dhir [29] developed a vapour/gas entrapment criterion by minimizing the Helmholtz free energy of a system involving a liquid-gas interface in a cavity. According to this criterion, a cavity will trap vapour/gas if:

$$\theta > \Psi_{min} \qquad (3)$$

where Ψ_{min} is the minimum cavity-side angle of a spherical, conical, or sinusoidal cavity. Although Bankoff's criterion (eq. (2)) provides a necessary condition for vapour/gas entrapment in a wedge, eq. (3) provides a sufficient condition [8].

Regarding inception, several approaches have been proposed for determining the incipient wall superheat for boiling from pre-existing nuclei. Hsu [49] suggests that an embryo will become a bubble if the temperature of the liquid at the tip of the embryo is at least equal to the saturation temperature corresponding to vapour pressure in the bubble. So, this criterion requires that the embryo should be surrounded everywhere by superheated liquid. In a different approach, boiling incipience is proposed to correspond to a critical point of instability of the vapour-liquid interface. The interface is considered to be stable or quasi-stable if the curvature of the interface increases with vapour volume (e.g. Mizukami [77], Forest [78]). Wang and Dhir [29,30] studied the instability of the vapour-liquid interface in a spherical cavity and showed that nucleation occurs when non dimensional curvature of the interface attains a maximum value, following the relation:

$$T_W - T_{sat} = \frac{2\sigma_{lg} T_{sat}}{\rho_g h_{fg} R_c} K_{max} \qquad (4)$$

where $K_{max}=1$ for $\theta_e \leq 90°$, $K_{max}= \sin\theta$ for $\theta > 90°$, and R_c is the radius of a nucleating cavity.

The implicit assumption required to obtain this equation is that the interface temperature is the same as the surface temperature.

Up to now, this section shows the vital importance of the wettability on the onset of boiling. Here, surface topography has a major role to increase the number of nucleation sites. These sites must, nonetheless, satisfy particular geometric and energetic minimal conditions to become active. The wettability acts directly as the balance of the interfacial forces at the nucleation sites. So, higher wettability (larger contact angles) endorses the onset of heterogeneous boiling and consequently increases the nucleation sites density. This remains true even for smoother surfaces. For instance, Balss et al. [74] showed a significant decrease on the onset temperature for nucleate boiling in fast transient events for smooth and uniform surfaces.

Naturally that, subsequently to the onset of boiling, the wettability will also affect bubble dynamics, which for a single bubble can be followed by monitoring three main quantities: bubble growth, bubble departure diameter and bubble departure frequency. Such quantities are important as they provide key information related to the cooling of the surface, through the energy required to the bubble formation and growth and further re-heating, which is related to the time available between succeeding bubbles.

From the fundamental point of view, heat transfer initially dominates the bubble growth. Fritz and Ende [79] suggested that the thermal conduction is responsible for the heat transport to the bubble surface. However, the bubble growth is not only controlled by heat flow to the bubble surface, but it is also depends on the forces acting on the bubbles, so that momentum equation must also be taken into account (in the so-called mechanistic approach) [80]. Such approach was followed by Forster and Zuber [81] and Plesset and Zwick [82]. However, compared to [79] the relations deduced in [83] and [84] are only different in the factor of $\sqrt{4/\pi}(4/\pi)^{1/2}$. Bier et al. [85] argues that the absence of considerable differences between these expressions is caused by the dominance of the energy equation during bubble growth. In fact, both energy and momentum equations are important, although not all the relevant acting forces are taken into account in most of the models and correlations, which is the main reason for these similarities and actually is the largest source of inaccuracy of many of the models reported in the literature [86].

It is obvious that bubble growth requires an energy supply. However, while some authors such as Mikic et al. [87] stand for the fact that bubble grows from the evaporation of the interface all around itself, others such as Snyder and Edwards [88] argue for the existence of a liquid micro-layer at the bubble base between the vapour-liquid interface and the heater surface. High heat wall and bulk temperatures tend to promote the formation of this micro-layer. According to the theory of Mikic et al. [87] the bubble growth radius is a function of the waiting time t_w, of the Jacob number $J_a = (r_l C_{pl})(T_W - T_{sat})/(r_g h_{fg})$, of the bulk liquid temperature T_∞ and of the thermal diffusivity α:

$$R_b(t) = \left(\frac{12}{\pi}\right)^{1/2} \left\{1 - \frac{T_W - T_\infty}{T_W - T_{sat}} \left[\left(1 + \frac{t_w}{t}\right)^{1/2} - \left(\frac{t_w}{t}\right)^{1/2}\right]\right\} J_a(\alpha t) \quad (5)$$

This means that if T_∞ equals T_{sat} and t_w is zero, then the bubble radius would be zero. If there is no waiting time in between succeeding bubbles for the superheated thermal liquid layer to recover, no heat could be conducted from the liquid into the bubble and therefore any bubble could grow [80].

On the other hand, Moore and Messler [89] confirmed the existence of the micro-layer with oscillation in the temperature measurements at nucleation sites. Cooper and Lloyd [90] also reported the presence of the micro-layer under an isolated bubble for experiments under low pressure. The experimental results of Kenning and Yan [91] and of Takagi and Yamamoto [91] are consistent with the micro-layer model, and therefore with the cooling of the wall during bubble growth. Anyway, Plesset and Prosperetti [92] disagree about the importance of the micro-layer and claim that its contribution to the heat transfer during boiling is only of the order of 20%. More recently, Sodtke et al. [93] studied single bubble growth in a low gravity environment from a 10μm thin, electrically heated, stainless steel foil covered with thin black tape and a top cover of a thermochromic liquid crystals (TLC) layer. Their results provide quite good validation of the micro-layer theory by showing that the heat transfer near the micro region of a length in the order of 1μm was 100 times stronger than in the circumjacent liquid.

Lately, Stephan et al. [94] showed that during bubble growth and detachment period the heat removed by evaporation was larger than that supplied to the overall system from the outside. Hence, the temperature in the liquid thermal boundary layer and of the substrate would drop, especially near the moving apparent 3-phase contact line at the bubble base. During waiting time and bubble rise, the opposite trend occurs in terms of the heat exchanges: the temperature in the substrate and the liquid thermal boundary layer rises again. In line with this, the numerical nucleate boiling models should consider these temperature fluctuations. Considering this last model, the role of the wettability is evidenced during the motion of the apparent contact line at the bubble base.

When dealing with bubble departure, the most used parameter is the bubble departure diameter. Despite being regularly evaluated and discussed in both experimental and theoretical approaches, the bubble departure diameter is actually quite difficult to measure accurately (e.g. McHale and Garimella [95]). Hence, most of the existing information is based on empirical correlations. A well-known correlation to predict the bubble departure diameter D_b was proposed by Fritz [96] and provides a characteristic length. It mainly considers the balance between buoyancy ($\sim g(\boldsymbol{\rho}_l - \boldsymbol{\rho}_g)$) and surface tension forces ($\sim \boldsymbol{\sigma}_{lg} D_b^2$). The wettability effect is also introduced in a very simple manner, so that the bubble departure diameter is increasing with the equilibrium contact angle θ (given in °) and with the surface tension, and it decreases with gravity and density difference, which defines buoyancy potential:

$$D_b = 0.0208\theta\left(\frac{\sigma_{lg}}{g(\rho_l - \rho_g)}\right) \tag{6}$$

Despite the equilibrium contact angle is introduced in a very simple manner, this correlation predicts the correct length scale, but many deviations are reported in the literature, especially at high pressure. Many more expressions, which were obtained empirically or analytically can be found in the literature (e.g. Cole [97], Kutateladze and Gogonin [98], Jenson and Memmel [99]). They are often contradictory since, in some sources the bubble departure diameter is increasing with wall superheat while in others it is insensitive or it even decreases with increasing wall superheat. McHale and Garimella [95] and more recently Moita et al. [100] compared experimental data of several authors, including their own, with various correlations predicting the bubble departure diameter and they both concluded that none of the correlations agrees with the experimental data in a reasonable way. The authors argue that one of the reasons for this is that in most of these studies, altering the surface topography in a stochastic manner, which is difficult to model, creates nucleation sites. Additionally, this procedure leads to complex interaction mechanisms between the bubbles and between the nucleation sites, which besides being still far to be completely understood, are not considered in these correlations. This is indeed a relevant issue that will be revised in detail in the following sub-section. Additionally to the arguments of McHale and Garimella [95], one may also refer that almost none of relations discussed above clearly addresses the effect of the wettability. Nevertheless, the importance of the wettability quantified by the contact angle, as earlier suggested by Fritz [96] has been later confirmed several times (e.g. [13,101-102]). In more recent studies, Phan et al. [45] and Nam et al. [103] showed that the use of superhydrophilic surface with artificial nucleation sites causes a significant decrease of bubble departure diameter with decreasing contact angle. In order to balance the evaporation rate with smaller bubbles their generation has to become more numerous. Hence, wettability does not only affect the bubble departure diameter but it has a significant impact on the departure frequency (e.g. Hazi and Markus [104]).

The inaccuracy of the existing correlations to predict the bubble departure diameter and frequency was recent very revisited, in a detailed analysis reported by Matkovic and Koncar [86]). These authors present a qualitative estimation of the bubble departure diameter prediction modelling through the calculated uncertainty values over a wide range of test conditions. Although they highlight some limitations of prior models, namely in accurately considering all the forces involved in bubble formation and departure, Matkovic and Koncar [86] do not actually propose a new model, but instead they validate previously existing models. [86] confirms the role of the wettablity in bubble formation, quantified by the contact angle and even argue that better accuracy is obtained in bubble diameter prediction for boiling over more hydrophobic surfaces. [86] further recognize the lack of understanding of the driving mechanisms, particularly under extreme wetting conditions.

In outline, a number of studies have reported that surface wettability is an important factor affecting the boiling heat transfer [45,105]. However, there is still a lack of understanding of the role of the wettability at the fundamental phenomena of the boiling process, which disables any accurate description of this effect. From the revision of the nucleation fundamentals, one may observe that the wettability affects the pool boiling right at the inception. Hence, at low heat fluxes, higher contact angles (hydrophobic/superhydrophobic conditions) and lower hysteresis promote the activation of the nucleation sites and the regular departure of larger bubbles, which consequently influences the pool boiling heat transfer [106]. This is usually associated to an improvement of the heat transfer coefficient. As the heat flux increases and one enters in the regime of slugs and columns, large bubbles will actually be less beneficial, so higher wettability actually lead to a fast formation of large vapor blankets thus decreasing the heat transfer coefficient and promoting the establishment of the Critical Heat Flux condition.

In this context, Betz et al. [107] suggest that dissimilar wettability conditions are required for the different heat transfer regimes, namely weather one is focused on the low or higher heat fluxes. So they propose the use of biphilic surfaces, which juxtapose hydrophilic and hydrophobic regions and show experimentally an overall better performance of these surfaces in pool boiling, when compared to those with spatially uniform wettability, both in terms of critical heat flux and heat transfer coefficient. They even state that heat transfer coefficients measured on the so called superbiphilic surfaces are up to three times higher than on state-of-the-art nanostructured surfaces with uniform wettability.

It is worth mentioning that it is experimentally very difficult to vary the contact angle while keeping all other parameters constant. This issue, associated to the fact, already advanced in the introduction of the present chapter, that it is not always referred in which boiling regime one is working, easily leads to contradictory results. For instance, Truong et al. [108] showed the mechanisms of the CHF intensification and heat transfer coefficient deterioration, for lower heat fluxes, both attributed to the decrease of the contact angle. On the other hand, Jo et al. [6] focused on nucleate pool boiling under different wetting conditions, in the absence of microscale roughness, which was coupled with wetting phenomena. They reported the occurrence of heterogeneous boiling both on hydrophilic (54°) and hydrophobic (123°) surfaces, even without microstructures. Once again, these authors state that hydrophobic surfaces allow better heat transfer performance in the low heat flux regimes.

Additionally, several authors change the wettability by altering the surface topography, so it is natural to infer that they are also acting on the active nucleation sites [6,8,49] and consequently on the interaction mechanisms. However, only recently, by analysis of the bubble dynamics (e.g. [266]) it was confirmed that changes in wettability based on topography modification, could lead to totally different boiling performance under heterogeneous wetting conditions, which was related to the number and shape of the dots (for instance the hydrophobic structures imposed by [107]) or other structures as well as the pitch distance between them, which inevitably act on the nucleation sites. By playing in a random way with the nucleation sites density one is also altering the interaction mechanisms. This leads easily to misinterpretations of the results. For instance, the unaccounted effect of the surface topography on the active nucleation sites and consequently on the interaction mechanisms can partially explain the discrepant reports of Truong et al. [108] and of Jo et al. [6] (although they did not work exactly in the same region of the boiling curve). This may also contribute to understand the fact, referred in [6], that both hydrophilic and hydrophobic surfaces with nanoscale roughness are adequate to produce heterogeneous boiling, which is an apparent contradiction to the classic predictions of the trapped vapor theory.

3.3.2 Interaction mechanisms

Research on the interaction mechanisms among nucleation sites is still quite sparse. Pioneering work was performed by Chekanov [109] and by Judd et al. [110-112]. These authors altered the surface topography by producing two artificial nucleation sites differently spaced and identified diverse regions of interaction among nucleation sites, which they categorized as a function of the dimensionless cavity spacing S/D_{dm}, where S is the distance between two cavity centres (thus the distance among nucleation sites) and D_{dm} is the mean bubble departure diameter. There is no agreement between the conclusions reported within the different studies, probably due to some differences in the experimental conditions, but also to the lack of consistency in the identification of the various mechanisms which may occur. A universal interpretation of the results was later tried by Zhang and Shoji [113], who proposed an alternative set of interaction regions, also as a function of S/D_{dm}, based on the dominance of different effects. More recently, few authors such as Nimkar et al. [114] and Yu et at. [115] focused on the effect of the spacing between arrays of cavities with different shapes. Both authors reported the degradation of the heat transfer coefficient at high imposed heat fluxes, which was attributed to bubble interaction mechanisms, but again, different optimum values of the spacing between the cavities are recommended. Moita et al. [100] and Teodori et al. [5] revisited this issue considering regular patterning of multiple cavities, with fixed shape, size and depth, altering solely the distance S. Based on the analysis of bubble dynamics (characterized using Particle Image Velocimetry and high-speed imaging) combined with heat transfer measurements, [5] [100] highlighted the major importance of the bubble interaction mechanisms in the HTC of pool boiling of water over micro-textured surfaces. The authors could empirically relate the heat transfer coefficient with the dimensionless parameter S/L_c, being $L_c=(\boldsymbol{\sigma}_{lg}/g(\rho_l-\boldsymbol{\rho}_v)^{1/2}$ the characteristic bubble size, following for instance Fritz [96]. Nevertheless the authors also report that this role is significantly less important for well wetting fluids such as dielectric liquids, although they have not quantified the effect of the wettability (e.g. via the contact angles).

Based on the key issues raised up to now, the following sections will revise the various strategies to alter the surface or the liquid properties in order to enhance pool boiling heat transfer. The analysis will always focus on how these strategies alter the wettability of the system and which are its consequent effects. To avoid misinterpretations, one will try to divide the studies performed at lower heat fluxes and at higher heat fluxes.

3.4 Strategies to alter wettability

3.4.1 Modification of the liquid properties (surfactant addition and nanofluids)

Liquid properties and particularly surface tension, which is directly related to the wettability, will affect the pool boiling heat transfer. Viscosity will also directly interfere with the force balance at bubble formation. Effects of surface tension and viscosity have been extensively investigated for a long time. For instance, Kotchaphakdee and Williams [116] investigated nucleate pool boiling heat transfer with dilute aqueous polymer solutions and found significant differences in bubble size and dynamics between polymeric and nonpolymeric liquids. They attributed such phenomena to the effects of changing viscosity, but did not explore the effect of surface tension. A controllable way of changing the liquids surface tension is adding surfactants, as earlier suggested by Wen and Wang [27], who showed that the value of the superheat at the onset of nucleate boiling could be lowered from 14 to 7°C depending on the type and concentration of surfactant in water. However, the addition of a surfactant may also change the viscosity of the working fluid (e.g. Hetsroni et al. [117]). Despite this, the concentrations to be used are usually low enough, so that the addition of surfactant to the working fluid (commonly, water) causes any significant changes in any other physicochemical properties of the liquid, including the saturation temperature. The presence of a surfactant in the solution can be expressed as either individual monomer or micelles, which are an aggregation of a large number of monomers and can have spherical, cylindrical or lamellar type structure, depending on the nature of the surfactant. The transition point from monomers to micelles is referred as critical micelle concentration (CMC). The presence of large number of micelles is reported to increase the fluid viscosity and reduce heat transfer coefficient. Addition of small amount of surfactants has been reported to be enough to produce dramatic enhancement in the boiling heat transfer (e.g. [118,119]). Nevertheless, the extent of enhancement has been found to be dependent on additive concentrations, its type and chemistry, wall heat flux, and the heater geometry, as reviewed by Wasekar and Manglik [118]. During nucleate pool boiling of pure water and water with cationic surfactant, Hetsroni et al. [117] recorded the motion of bubbles and the temperature of the heated surface with a high-speed video camera and an infrared radiometer. They found that the heat transfer coefficient depends both on the surface tension and on the kinematic viscosity; the increase of the heat transfer coefficient at low concentration was attributed to the decreasing of surface tension, while for high concentration, the increase in kinematic viscosity decreased the heat transfer coefficient.

Different types and concentrations of the surfactant may have dissimilar effects on the boiling heat transfer. In their preliminary experiments [120] reported that addition of Sodium Dodecil Sulphate - SDS could significantly decrease the incipient superheat and shorten the waiting period, which can be reasonably explained by taking into account the equilibrium surface tension and contact angle changed due to the surfactant. But in their later experiments [121] showed that such conclusions could not be extended to the addition of Aerosol-22, Triton X-100 and DTMAC on water boiling, so any consistent conclusions could be drawn. Hence, the effect of surfactant addition must be well explored. The apparent inconsistency of the results reviewed in the last paragraph can be cleared out as one understands the role of liquid surface tension and its relation with the wettability of the system. The appropriate choice of the surfactant (chemical composition) applied in the adequate concentration allows decreasing the surface tension, promoting the departure of smaller bubbles at higher frequency (shorter waiting period). This may indeed contribute to decrease the incipient superheat (also because lower surface tension is usually associated to lower latent heat of evaporation), but will mainly result in an enhanced convection and enhanced latent heat parcel (resulting from larger rate of formation and departure of the vapor bubbles), which, in turn, is translated in the increase of the heat transfer coefficient. However, as one increases the concentration, there are two factors playing against boiling enhancement: one is the abovementioned increase of the kinematic viscosity, while the other is the substantial decrease of the contact angle. This naturally depends on the chemical composition of the surfactant. In this case, the decrease of the contact angle will promote a difficult activation of the nucleation sites. This effect easily overcomes the possible advantages of reducing the surface tension, and the pool boiling heat transfer will be significantly reduced. This effect of the wettability explains the worse heat transfer performance obtained by [121] after the addition of surfactants such as the Triton X-100 to the water. Such explanation is also consistent with the findings reported by Wang and Dhir [143], who studied the effects of surface wettability on active nucleation site density during pool boiling of water on a vertical surface. In their experiments, the nucleate site density was reduced more than 20 times when the equilibrium contact angle of water was changed from 90° to 18°.

On the other hand, when dealing with high heat fluxes, the wettability requests are different, given that in that case, one intends to extend the region of columns and slugs, so we want to keep the bubbles small and the boiling frequency moderately low.

Once more this review highlights that different optimum wetting conditions are requested for low and high heat flux regimes (i.e. for different regions of the boiling curve) and stresses the relevant role of the wettability by itself. Additionally, it is clear that using a surfactant is an interesting, but very difficult strategy to use, given that one must reduce the surface tension without a noteworthy decrease of contact angles, which is particularly important to trigger the boiling. This depends on many variables, namely on the chemistry of the surfactant and on the concentration, which are still far to be completely understood and optimized. It is true that smaller contact angle could be more advantageous when working closer to the CHF, but this is very difficult to achieve as the liquid cannot be changed during the boiling process. A successful approach would probably require a “self-adapted” custom made fluid, with variable wetting characteristics.

This idea of a custom made fluid was further worked in the development of nanofluids, which are basically colloid suspensions of common fluids like water or refrigerants added with solid particles of particular materials, with diameters between 1 and 100nm [122]. These particles are relatively close in size to the molecules of the base fluid and thus, if properly prepared, can realize very stable suspensions with little erosion and gravitational deposition over long periods of time. This new concept was initially proposed by [122] early in the 1990s. The basic principle is to improve the relatively low thermal conductivities of most of the fluids (e.g. 0.607W/mK for water and only 0.145W/mK for engine oil) by adding small particles whose thermal conductivities can be up to 21000 times larger, when compared for instance with carbon nanotube coatings. This is quite impressive considering that for instance the thermal conductivity of multi-walled carbon nanotubes - MWCNTs is 3000W/mK. Materials used for nanoparticles include chemically stable metals (e.g. gold, silver, copper), metal oxides (e.g., alumina, zirconia, silica, titania) and carbon in various forms (e.g., diamond, graphite, carbon nanotubes, fullerene). Given that metals have higher thermal conductivity compared to ceramics (or metallic oxides), the thermal conductivities of fluids that contain suspended metallic are expected to be significantly higher (e.g. [123-128]). Although nanoparticles-suspensions were used in heat transfer studies as early as 1984 by Yang and Maa [129], who used nano-sized Al_2O_3 particles as small as 50nm in water and afterwards by Masuda et al. [130], it was only in 1995 that Choi [122] at Argonne National Laboratory of USA coined the concept of “nanofluid” to meet the cooling challenges facing many high-tech industries. Besides these researchers, it is worth to refer the work of Grimm [131], who won a German patent on the enhanced thermal conductivity of nano- and micro-sized particles suspensions in 1993. In the work of Grimm [131], aluminum particles of sizes ranging between 80nm and 1μm were suspended into a fluid, which resulted in 100% increase of the thermal conductivity of the fluid for loadings of 0.5–10 vol.%, as reported in his patent.

Nanofluids have been reported to be particularly efficient in CHF enhancement ([50,132-134]), which is reported to occur at relatively low nanoparticle concentrations, typically less than 1% by volume (e.g. [133-134]). Such enhancement is actually attributed to the deposition of the particles over the surface which alters the wettability of the system (e.g. [50,135]). Actually, the deposition of the nanoparticles over the surface is reported by several authors to be an import reason for the enhancement of the CHF, as it alters the wettability of the system. Usually, this deposition increases the surface wettability (i.e. the contact angles are smaller) [50], thus delaying all the bubble dynamics process previously discussed, and consequently enhancing the CHF. This trend is obviously related to the particle concentration (e.g. [136]), to the pH of the solution, but also to the relative magnitudes of the average surface roughness and the average particle diameter. (e.g. [27,30,50,132]).

There are also set-backs due to this deposition of the nanoparticles: [50] report a decrease of the heat transfer coefficient due to a build-up of nanoparticle layer, which reduces heat transfer from the metal surfaces in pool boiling. Also, the authors observed a reduction of nucleation site density caused by a decrease in the contact angle. These trends are in agreement with those discussed before.

Despite these clear trends, additional work is still required to develop fully functional nanofluids, as many contradictions can be found in the reviewed literature: some studies report no change of heat transfer in the nucleate boiling regime [132,137], some report heat transfer deterioration [138,139] while others heat transfer enhancement [140]. Heat flux (also critical heat flux) data relative to superheat reported by various research groups vary widely. Some of these differences can be explained by differences in characterization of nanofluids, different size and concentration of nanoparticles used and different types of heaters used in various research groups. In addition, only a couple of efforts are made on flow boiling of nanofluids. For instance, most of the researchers used alumina nanofluids, whereas very few efforts have been made with carbon nanotubes (CNTs)-nanofluids; despite some authors have observed that the latter exhibit much higher thermal performance compared to those of ceramic-nanofluids [126,127]. Regardless of these limitations, the review in [126] clearly evidences that the substantial increase in the boiling critical heat flux of nanofluids is undisputed. Nonetheless [126] also supports that it is imperative to conduct more research on flow boiling of nanofluids under the influence of various factors such as pressure, mass flux and sub-cooling besides performing more systematic experimental and theoretical investigations on pool boiling features of nanofluids. The reported data are still too limited and scattered to allow a clear understanding of the underlying mechanisms and trend of boiling heat transfer performance of nanofluids. Also, any comprehensive theory explains the energy transfer processes in nanofluids [134]. Recent work of Gerardi et al. [141] brought some theoretical development to explain CHF enhancement and deterioration when using nanofluids (which is attributed to wettability changes resulting from the deposition of the nanoparticles over the surface), but the approach followed is still slightly empirical. Methodical understanding of the interaction of nanoparticles and flow boundary layers also needs to be achieved by performing careful experimental observations and numerical simulations, to uncover mechanisms underlying convective heat transfer enhancement. Bubble dynamics in boiling nanofluids with consideration of suspended particles, additives used, and nanoparticle distributions, should be investigated experimentally and numerically to identify the exact contribution of suspended nanoparticles to boiling heat transfer and CHF enhancement [134].

Hence, nanofluids are a wide potential strategy for pool boiling enhancement, although they still need intensive research. The possible CHF and HTC enhancement or deterioration is evidently dependent on the way the nanofluids deposit on the surface and in this context they can be seen also as a strategy to alter the surface. Actually, the recent work in the field of nanofluids has led to an increasing interest of the potential to modify surface topography at the nanoscale. The expected advantages of nanoscale modifications include finer control over porosity and surface roughness, thinner coating layers to reduce thermal resistance and thermal stress and ultimately higher durability. This and other strategies to alter the surface wettability are discussed in the following sub-section.

3.4.2 Modification of surface chemistry

Researchers have early recognized surface wettability as a major factor in boiling heat transfer, but they were not able to conduct accurate experiments due to the lack of technology. With new techniques (e.g. MOCVD, PECVD and NNBD) researchers could provide more complete set of experimental data to explore the effects of surface wettability (associated to surface chemistry, without significant change on the topography) on the nucleation mechanisms and thereby on the heat transfer coefficient (e.g. [45]). Most common approach is to coat the surface with hydrophilic or hydrophobic materials (e.g. [27]). Despite changing the surface topography, even if at the nanoscale level, nanoparticle deposition was actually a very popular strategy to enhance the critical heat flux [40-42,139,142]. Different methods, including MEMS technique [37] mechanical surface treatment and nanoparticle coating of various materials such as alumina [143], zirconia [143], and silica [143,144] have been employed to fabricate appropriate surfaces with improved boiling characteristics. Nonetheless, once again these techniques alter the surface topography. For instance, coating of carbon nanotubes has shown to be highly effective in improving both HTC and CHF [15-16,145-147], particularly in the low heat flux region, but this is mainly due to an increased surface cavity density and increase of roughness amplitude. Significant enhancements in both the CHF and the HTC have also been obtained from surfaces coated with Cu nanorod and nanowire arrays [40-42,148-150]. Due to the pin fin effect on the liquid-surface contact line, nanorod structures greatly increase the active heat transfer area, which is again a geometric effect of surface topography and not of wettability. This is confirmed by the fact that their height was found to directly affect the heat transfer [151]. However, the nanowire structures are usually preferred to favor CHF increase, thus delaying the dry-out condition [35,150] which is mainly attributed to wetting effects (superhydrophilicity). Ahn et al. [147] demonstrated that multiwalled carbon nanotube forests, up to 25nm in height, increased both HTC and CHF in the pool boiling of the refrigerant PF-5060 [147]. Ujereh et al. [145] reported that carbon nanotubes coating on silicon and copper substrates is highly effective in reducing the incipience boiling superheat, and enhancing both heat transfer coefficient and CHF for the boiling of FC-72. Chen et al. [148] report 100% increase in heat transfer rate and CHF with copper and silicon nanowires about 200–300nm in diameter and 50nm long. They attributed the heat transfer enhancement to high nucleation site density, superhydrophilicity, and capillary pumping effect. Decher and Hong [152] later demonstrated the ability to construct multilayers using charged polymers. More recently, Lee et al. [53,153-154] have demonstrated the ability to create nanoparticle thin-film coatings of controlled thickness and composition using different types of nanoparticles and deposition conditions. Jo et al. [6] studied nucleate pool boiling under different wetting conditions. They observed that hydrophobic surfaces exhibit better nucleate boiling heat transfers in very low heat flux regimes than do hydrophilic surfaces. Stutz et al. [155] investigated not only the effects of surface nanostructuring on boiling heat transfer and critical heat flux but also the effect of coating duration on boiling characteristics. They performed their boiling experiments on platinum wire immersed in saturated water or pentane and concluded that deposition of nanoparticles onto the heated surface induced a significant increase in the boiling critical heat flux attributable to the increased wettability and decreased heat transfer coefficient when the wire was entirely covered with nanoparticles. Considering that many parameters, including but not limited to wettability and contact angle, number of nucleation sites, roughness, and surface topography, affect the critical heat flux and heat transfer coefficient, more investigations are needed to explain the discrepancies currently reported in the literature. Chen et al. [156] studied the boiling performance of a surface covered with superhydrophilic titanium oxide nanotube array. The surfaces yielded approximately half the values of wall superheats during boiling at a given heat flux compared to the bare Ti surface. It is concluded that the nanotube array introduced a large number of active nucleation sites that promoted bubble generation. Wu et al. [157] reported a coating of hydrophilic titanium oxide nanoparticles on the heating surface that increased the critical heat flux by 50.4% in pool boiling with FC-72. The enhancement is attributed to the hydrophilicity of the nanoporous layer.

Comparatively to hydrophilic surfaces, few studies investigated nucleate boiling mechanism on nonwetting material (e.g. [49,158]), as summarized in Webb and Kim [159]. However, it is worth to refer some interesting studies in which the use of nanoparticle thin-film coatings has been investigated for glass and other non-metallic substrates for use in a variety of applications including anti-fog, anti-reflection, and self-cleaning coatings. For instance, [160] investigated pool boiling characteristics of polymer/SiO_2 nanoparticle multilayers applied to nickel wire using the layer-by-layer (LbL) deposition method. Gaertner [161] carried out further work with artificial nucleation sites, covering the inside surface of the cavities with a nonwetting material. The coated cavity surface boiled at a lower superheat and remained active for a much longer time. However, the heat transfer coefficient was considerably reduced if the coating was deposited on the entire surface because of the bubble coalescence that caused the entire surface to become vapor blanketed. Hummel [47] boiled water on a stainless steel surface which had been sprayed with Teflon, producing 30–60 spots/cm^2 with a spot diameter of

0.25mm or less. The author observed a significant heat transfer enhancement. Gaertner [161] and Hummel [47] argue against the merits of a continuous surface coating because of the tendency of the surface to become vapor blanketed. Nevertheless, Vachon et al. [162] did not observe vapor blanketing when boiling water on stainless steel covered by an 8μm thick layer of Teflon. Phan et al. [45] also investigated the influence of surface wettability on nucleate boiling heat transfer, using nano-coating techniques. They were able to vary the contact angle from 20° to 110° by modifying the topography and chemistry of the nano-scale surface and they obtained the best heat transfer coefficient with the surface that had a water contact angle close to either 0° or 90°. They confirm that lower superheat is required for the initial growth of bubbles on hydrophobic (unwetted) surfaces. At higher heat fluxes, for hydrophobic surfaces, the bubbles spread over the surface and coalesce with bubbles formed at other sites, causing a large area of the surface to become vapor blanketed. Takata et al. [102] produced superhydrophobic and hydrophobic surfaces using coatings over a copper surface. They do not specify the manufacturing of the superhydrophobic surface. They only refer that the coatings were applied over copper surfaces. They also refer that the hydrophobic surfaces are obtained using a polytetrafluoroethylene (PTFE) coating. Additionally they modified both superhydrophobic and hydrophobic surfaces with spotted patterns of TiO_2, which is a hydrophilic material. The coating did not cover the entire surface so they could clearly observe the differences on boiling over the coated and the non-coated regions. The coatings of both superhydrophobic and hydrophobic surfaces however alter the surface roughness, acting as nucleation sites and, therefore, bubble nucleation starts at very low superheating. At lower heat flux, bubbles with uniform size are generated on the SWR or PTFE coated regions. These bubbles depart from the heat transfer surface when the contact line reaches the boundary from the coated to the uncoated regions. Nucleate boiling with PTFE surface was enhanced by seven times compared with the normal copper surface. Best performance was obtained with the spotted PTFE surface coated with the hydrophilic TiO_2 pattern. The spotted patterns of TiO_2 were probably suggested by Takata et al. as a result from previous work [40,48,84] focused on TiO_2 photocatalysis, in which the authors observed a significant decrease of water contact angle when a surface coated with TiO_2 is irradiated by UV light. Due to this property of TiO_2, they made superhydrophilic surfaces. Consistently with the analysis performed until now, Takata et al. [102] conclude that the hydrophobic surfaces promote the boiling to start at lower superheating, while better performance is obtained in the regime of columns and slugs when the superhydrophilic surfaces are used [40,48,84]. Hsu et al. [163] used nano-silica particle coatings to vary the copper surface wettability from superhydrophilic to superhydrophobic, by modifying surface topography and chemistry. Their results confirm once again that critical heat flux (CHF) values are higher in the hydrophilic region. Conversely, CHF values are lower in the hydrophobic region. Copper surfaces with different wettability values were used as heating surfaces to investigate the effects of CHF values on pool boiling heat transfer. The CHF values increase with the decrease in surface CA when the surface is relatively wetted. However, with a CA close to 150° (superhydrophobic), the heat flux has difficulty flowing through into the pool due to the larger growth bubbles, causing a decrease in CHF values. The bubble growth phenomenon occurs on the surface in the nucleate boiling region. The sizes of growth bubbles were smaller on the hydrophilic surface and growth bubbles on the surface increase of de-wetting with increasing bubble size due to the boiling. Stagnant bubble growth on the heating surface decreased the heat flux through the pool, demonstrating that surface wettability influences the growth of bubbles, which in turn affects CHF values. This is also consistent with the recent work of Betz et al. [107], although in both studies the surface topography was somehow changed, so the enhancement of the pool boiling was also caused by the roughness that altered the active nucleation sites density.

Microparticle coating has also been explored: Hwang and Kaviany [164] have demonstrated increases in CHF up to 96% for pool boiling of n-pentane using thin and uniform microparticle coatings on heater surfaces. Kim et al. have reported enhancement for both nucleate boiling heat transfer and CHF in FC-72 using microparticle coatings [42] or wires [165]. An alternative treatment by microcoating consists in the deposition of a microlayer of different materials on the heater surfaces [47,162,166]. However, this may disrupt the boiling process by changing the microcavities density on the heater.

Oxidizing copper is another method widely applied. The surface wettability is modified by controlling the degree of oxidation of the surface. Using this method, Liaw and Dhir [83] found that for a given heat flux, the wall void fraction increases as the surface wettability decreases, whereas the maximum heat flux decreases with an increase in contact angle. However, oxidizing copper may change the surface topography at microscale, which is the characteristic scale of nucleation sites.

As a summary, one may argue that apart from few discrepancies, the majority of the studies reported in the literature are consistent in the fact that superhydrophobic surfaces facilitate the triggering of the boiling at lower superheats, but at higher superheats the bubbles stay attached to the surface and easily merge with others, forming vapor blanket which leads to reaching the CHF condition. On the other hand, a reduced contact angle (hydrophilic surfaces) is interpreted as enhanced wettability, which leads to an increase in CHF [155]. Therefore, the heat removal from these surfaces is significantly more effective, since they tend to prevent formation of vapor layer near the surface.

In all the works reviewed in this subsection so far, there is a dominant effect of changing the wettability by altering the surface chemistry, but many of the techniques involved, still alter simultaneously surface topography. Hence, we still see confusing conclusions such as those reported in [156,157] where, despite recognizing the importance of the wettability, the authors are obliged to refer the simultaneous influence of the surface topography modification, which provides sufficient active nucleation sites at low wall superheats, facilitates the evaporation of liquid film within a very small confined space and increases the effective heat transfer area. At the light of the literature reviewed, only recently, very few authors were able to modify the wettability of the surface without affecting significantly its topography. They have used glass or silicon wafer surfaces with self-assembling monolayer over the substrate to study both transient events [42,167] and stationary conditions [52,168,169]. In this context, Bourdon et al. [51,52] presented quite detailed works. These authors characterized the onset of nucleate boiling and quantified the influence of the wettability. Such quantification was possible as the inherent mean roughness of the glass substrates, even after treatment, was lower than one nanometer. The boiling curve was determined and the heat transfer coefficient calculated. The wettability was changed by weather using hydrophobic (grafted) and hydrophilic (ungrafted) surfaces. The grafted and ungrafted cases present a clear difference in the boiling curve, since in the hydrophobic case, the first bubbles appear at lower superheat and a significant change in the shape of the boiling curve occurs. The opposite trend is observed for the hydrophilic surfaces. This result is quite consistent with the discussion that has been performed so far. Also in agreement with the trends discussed up to now, in the hydrophobic case, large bubbles are formed that stay attached due to the stability promoted by the low hysteresis, which coalesce to form bigger bubbles that afterwards detach due to buoyancy.

3.4.3 Modification of surface topography

One of the pioneering strategies used to enhance pool boiling is the modification of surface topography [6,35,45,170,171]. In 1962 Berenson [12] already observed that increasing surface roughness can affect the heat transfer coefficient by 500–600%, which stems from an increased nucleation sites density. In line with this, Carey [6] investigated the boiling heat transfer by controlling the surface roughness and thickness.

Numerous studies have been also performed involving mainly artificial cavities that have been created and studied from nanometric to micrometric scales, covering a wide range of shapes. Other recent surface treatment methods include increasing the surface area with micro pin-fins [37] or applying wicking structures to promote the liquid supply by capillary pumping [38,39]. Webb et al. [159] summarize a number of surface treatment techniques.

At the microscopic level, Corty and Foust [22] observed that the surfaces roughened with cavities required lower superheat for incipience, which was attributed to the presence of larger unwetted cavities on the surfaces, which would increase the number of active nucleation sites. Vachon et al. [80], Griffith and Wallis [166], Kurihara and Myers [14], Hsu and Schmidt [16] and Marto and Rohsenow [172] later reported similar conclusions.

A common issue that can be identified in all of the aforementioned studies is the so-called “surface roughness“, which is not defined precisely. This leads to misinterpretations of the results and turns any comparison or attempt to correlate the results very tricky, since one may be comparing different quantities. In addition, the surface topography in all of them is stochastic, which, as referred by McHalle and Garimella [95], does not allow establishing any accurate relation between the cavities and nucleation inception and/or bubble formation. Hence, many other authors considered instead an approach of using regular patterns of cavities or grooves. Grooves, pillars and pins favour capillary pumping, while the cavities provide more nucleation sites. Anderson and Mudawar [17] experimentally showed that surfaces with microgrooves and square microstuds are highly effective in enhancing the nucleate boiling heat transfer coefficient in FC-72 and increasing critical heat flux. This enhancement is mainly due to an increase of the liquid-solid contact area. Also promoting capillary pumping, Honda and Wei [173], Wei and Honda [37] and Wei et al. [174] performed a series of experimental studies on pool boiling enhancement using micro-pin-fins (10–50μm in thickness and 60–200μm in height) which were fabricated by dry etching. From the boiling incipience to the critical heat flux, the micro-pin-finned surfaces caused a sharp increase in the heat flux with increasing wall superheat. The behaviour is therefore similar to that of micro-pillars. Other authors working with micro-fins, such as Yeh [175], Guglielmini et al. [176,177], Klein and Westwater [178] and Hirono et al. [179] arrived to similar conclusions. However, they all recommend different optimum distances to achieve maximum HTC. This may be due to the fact that they did not relate the surface topography to the phenomena fundamentals, namely to the way the micropatterns were affecting the interaction mechanisms. An extensive literature review on this subject is reported by Poniewski and Thome [180].

With the advance of the micro-and-nano technologies and with the use of more sophisticated diagnostic techniques, deeper study on the fundamental phenomena was possible. For instance, regarding the role of micro-cavities, it has been recently shown that single cavities of the order of 10μm large on silicon wafers can trigger the boiling [181]. The shape of the cavity is also of primary importance for the nucleation [101,173,182]. Several works have revealed, using highly smooth surfaces, that nanometric features also influence nucleation [42,43,52,95,167,183]. These studies also allowed relating the surface topography with the fundamental phenomena of nucleation and bubble formation.

To sum up, the effect of surface topography on the fundamental phenomena of nucleation must be well established, since, depending on the scale at which the topography is modified, one may be acting mostly on the nucleation phenomena and less on wettability. So, the best approach can be indeed to isolate the effect of wettability, from that of surface topography. Surface wettability maybe altered by topography modification, even at the micro-scale, following the relations previously revised, as suggested by Kim et al. [50]. At such scale however, it is still possible to affect on the nucleation sites density [145,146,148,149,184-186]. Hence, one must determine the conditions to trigger the boiling at on micro to millimetric scale patterns, to understand and devise the basic theoretical models and then nanometric structures can be approached. Micron to millimeter size structures can also give a better two-phase change heat transfer performance than the nanometer size structures due to the geometric effect on the vapor escaping, as explained in detail by Li and Peterson [184,187].

Surfaces with microporous

A special case study of interest, which can be considered as a modification of surface topography, is microporous coatings. This strategy has reported to be particularly effective to enhance the CHF (e.g. [38,39,42,188-198]), although [197] reports that CHF enhancement strongly depends on the coating thickness, volumetric porosity, and pore size. Hence, increasing the nucleation sites density enhances CHF, extending heating surface area, and controlling bubble dynamics, especially when the heat flux demand is over

150W/cm^2. Following this line of thought, [149] suggests that when the heat flux reaches relatively high values, a modulated porous structure is expected to achieve much better heat transfer performance than the uniform thickness porous structures, due to the fact that the modulated structures can separate the adjacent vapor columns for vertical liquid replenishment, suppress the hydrodynamic instability and delay the formation of the vapor blanket covering the heating surface. At the same time, nanoscale porous structure coatings should help to increase the active nucleation site density and to enhance the horizontal liquid replenishing to the dryout hotspots. Doing so, [149] report up to 40% reduction of superheat temperature at CHF over a plain surface in their studies. Consistently, Li et al. [2] argue that modulated porous structures could dramatically increase the CHF and heat transfer coefficients of nucleate boiling heat transfer by delaying the onset of hydrodynamic instability and enhancing the capillary pumping for the liquid vertical and horizontal replenishments. The authors suggest that small pore sizes, below 100μm are desired for the modulated porous structures to enhance the capillary pumping effects.

A good and comprehensive example of experimental results for pool boiling heat transfer at pressures near atmospheric from different structured or porous surfaces has been taken from Memory et al. [199].

3.5 Theoretical approaches describing the role of wettability

A great number of experimental investigations of enhanced pool boiling heat transfer have been reported in the literature, as extensively reviewed, for example in [200,201]. Most of those experiments were performed, at saturation pressures near atmospheric, and the correlations developed on the basis of the experimental results - also several containing a physical model of enhanced heat transfer fitted to the particular geometric configuration of the heating surface - mainly use the data obtained at atmospheric pressure, but claim applicability in a broader sense, see e.g. [202-205]. However, this may be not as straightforward. By increasing the system pressure, the boiling temperature of the liquid will increase and higher temperatures are required to conduct boiling experiments. By reducing the system pressure the opposite will occur. Recently, Kim et al. [50] compared experimental data obtained by several researchers and found a higher bubble growth rate at sub-atmospheric pressure compared to experiments conducted under atmospheric pressure conditions. Chien and Webb [206] and Liter and

Kaviany Kaviany [38] recently developed very detailed but highly complex models.

During the last half of the twentieth century, significant advances were made in developing an understanding of the boiling heat transfer modes. Yet, because of the complexity of the process, the models and correlations developed often contain much simplification and could not explain recent observations. To explore the physics of the nucleate boiling process, further fundamental research is needed, especially on interfacial phenomena, as the introduction of the wettability effect is usually correlated in a purely empirical form.

As revised in the previous sections, the nucleation sites density depends not only on the surface physical properties and the surface finish, but also on the liquid physical properties and the wall superheat [32]. One of the best-known correlations for nucleate pool boiling heat transfer, which tries to include the effect of surface properties (topography and wettability, distinguished by different materials) was early proposed by Rohsenow [207]. Surface properties are included in the parameter C_{sf}, which is a constant whose values are tabulated for various surface-liquid combinations. Apparently, this parameter should take into account the contact angle, the surface microroughness, and their interaction in determining the nucleation site density. However, it was simply determined from empirical fitting to experimental data, so that several inconsistencies were observed. As a result, the heat flux calculated according to Rohsenow [207] :

$$q_s'' = \mu_l h_{fg} \left(\frac{g(\rho_l - \rho_g)}{\sigma_{lg}} \right)^{1/2} \left(\frac{C_{pl} \Delta T}{C_{sf} h_{fg} Pr_l^n} \right)^3 \tag{7}$$

can be quite acceptable when fitting to experimental data, as reported for instance by [208] or can be up to 100% inaccurate (e.g. [209]). Here, C_p stands for the specific heat and $Pr=C_{pl}\mu_l/k_l$ is the Prandtl number. Additional improvements were later introduced, mostly considering a more mechanistic approach (the Mikic–Rohsenow correlation [24]), although their empirical nature was still strongly present.

Wang and Dhir [29,30] found that, as wettability increases, the fraction of the cavities that nucleate decreases. Their correlation for the nucleation site density was in terms of cavity mouth diameter and contact angle, being one of the few, up to that date, explicitly considering the effect of the wettability, quantified by the contact angle, in bubble formation, with evident consequences in terms of the heat flux derivation. Later, Wen and Wang [27] proposed the inclusion of the wettability on a modified Mikic–Rohsenow correlation, to describe the boiling behavior of liquids when a surfactant was added. Afterwards, wettability has been derived from the theory of bubble nucleation [22,23,29] as a means of predicting the critical heat flux, e.g. [9,22,23,26,29,56]. Based on a mechanistic approach, i.e. on the balance of forces acting on the forming bubble, these authors used surface wetting characteristics to develop a criterion for gas entrapment, which acts as a nucleus for bubble initiation. Several investigations suggest that at the base of a bubble, the three phases (solid, liquid and vapor) coexist in the so-called "triple contact line" (TCL). However, the way TCL affects bubble formation and detachment is yet not fully understood, so that not even the classic approaches like that of Fritz [96] are not completely confirmed.

Other researchers [14-18,27-32] have used wettability as an important parameter for describing activated nucleate site density, HTC and CHF, although it is usually associated to surface topography. Hence, the trapped vapor theory, developed to explain heterogeneous nucleation at low superheat, is suggested when microstructures or defects are present on the heating surface [22,23]. The intricate relation between surface topography and wettability, affecting the experimental data is transposed to the theoretical correlations. Although such relation is difficult to isolate and limitations of the theory are primarily due to the fundamental complexity of these close relations between these and other parameters involved in boiling phenomena e.g. ([22,23,28-31]), which may affect each other (e.g. [19,210]), the inaccuracy of the existing correlations is also strongly related to their empirical nature.

Many existing correlations focus on the prediction of the CHF. There are two theories regarding to the CHF enhancement. One is the fairly accepted hydrodynamic instability mechanism developed by Zuber [211] and further modified by Polezhaev and Kovalev [212]. The other is the surface liquid replenishment of dryout hotspots [145,146,148,149,184-186]. It is believed in the first theory that CHF will take place once the hydrodynamic instability limit has been reached. By reducing vapor/liquid counter flow and/or separating adjacent vapor/liquid columns, it can delay the onset of hydrodynamic instability, and in turn inhibit the onset of CHF. So using modulated porous structures to separate the vapor and liquid flow paths would prevent the interaction of the vapor/liquid counter flow and delay/eliminate the onset of hydrodynamic instability. For the theory of a replenishment limit, it is believed that if the hydrodynamic instability has not happened yet, the CHF may still occur once the liquid replenishing of the dryout hotspots has reached its limit. Hence, changing surface energy to achieve superhydrophilic property will

dramatically increase the limit of liquid replenishing of the dryout hotspots. This explains why the nanoscale and microscale porous structures have been employed to address the hydrodynamic instability and liquid replenishing limit. On the other hand, porous structure coatings on a heating surface will increase bubble nucleation site density which could improve the heat transfer coefficient at the early stage of nucleate pool boiling. And at the late stage of pool boiling, the modulated porous structure will improve the CHF by delaying the occurrence of hydrodynamic instability [38,187].
Zuber's correlation [211] predicts CHF values, as given in eq. (8):

$$q''_{CHF} = K\rho_g h_{fg}\left[\frac{g\sigma_{lv}(\rho_l - \rho_g)}{\rho_g^2}\right]^{1/4} \tag{8}$$

where K is a constant that depends on the geometry of the surface. This theory does not successfully predict the CHF values for nanofluid boiling and boiling on porous surfaces. The discrepancies observed can be due to the disused surface characteristics such as wettability in Zuber's theory. Kim et al. [50] showed that surface characteristics of modified surfaces are effective in the value of CHF whereas they are not accounted for in the hydrodynamic instability theory, but could be included in the hot/dry spot theory. Theofanous and Dinh [213] proposed the following correlation for evaluating the CHF value by means of hot/dry spot theory:

$$q''_{CHF} = K^{-1/2}\rho_g h_{fg}\left[\frac{g\sigma_{lg}(\rho_l - \rho_g)}{\rho_g^2}\right]^{1/4} \tag{9}$$

where K is derived from Kim et al. [214] as in Eq. (10):

$$K = \left(1 - \frac{\sin\theta}{2} - \frac{\pi/2 - \theta}{2\cos\theta}\right)^{-1/2} \tag{10}$$

Based on a mechanistic approach, Kandlikar [25] also proposes a relation to predict the CHF, which explicitly includes the effect of the wettability quantified by the contact angle:

$$q''_{CHF} = \rho_g h_{fg}\left(\frac{1+\cos\theta}{16}\right)\left[\frac{2}{\pi} + \frac{\pi}{4}(1+\cos\theta)\cos\phi\right]^{1/2}\left[g\sigma_{lg}(\rho_l - \rho_g)\right]^{1/4}$$

(11)

where ϕ represents the heater slope angle relative to the horizon. The last two correlations show the adverse dependence of CHF on contact angle. This correlation is not valid for complete wetting fluids, so [62] slightly modified it into:

$$q''_{CHF} = \rho_g^{1/2} h_{fg} \left(\frac{1+\cos\theta}{16} \right) \left[\frac{2((1+\xi)}{\pi(1+\cos\theta)} + \frac{\pi}{4}(1+\cos\theta)\cos\phi \right]^{1/2} \left[g\sigma_{lv}\left(\rho_l - \rho_g\right)\right]^{1/4} \tag{12}$$

where $\xi = r_f \cos\theta_r$ is a modified Wenzel angle, being θ_r the receding angle of the liquid over a smooth surface and r_f the roughness ratio in Wenzel's equation [19].

Gerardi et al. [141] also used Kandlikar's correlation to predict the CHF of the pool boiling of nanofluids, with quite good agreement. In addition, Gerardi et al. [215] propose an estimation of the heat transfer, dividing the heat flux in different parcels, namely the parcel of latent heat of evaporation, the parcel of heat convection and the parcel of the so-called quenching heat flux, following the approach earlier suggested by Han and Griffith [216]. Despite the efforts in going through the physics of the phenomena, analyzing bubble formation and detachment, many of the devised parameters must be empirically and/or experimentally evaluated, so that the empirical nature of [215] model is still not eliminated.

To conclude, despite the great efforts to describe theoretically, the boiling phenomena, fundamental research on the basic processes is still required to eliminate the strong empirical nature of most of the correlations and/or models devised. This has already been recognized by Saeidi et al. [217]. As many of these relations are based on an empirical fitting to the existing experimental data, the difficulty in separating the effect of wettability from that of surface topography is, somehow, transposed to the correlations, so that defining the role of wettability on the basics boiling mechanisms is still an unfinished task. It is worth mentioning that the surface topography itself alters the wettability in a non-straightforward manner. However, one must avoid at any cost affecting the nucleation sites, when playing with the surface topography, which has not been accomplished in most of the works to far.

3.6 Experiments

On the basis of the analysed literature and of the above considerations, pool boiling experiments have been performed with degassed water on stainless steel substrates with different surface topographies and wettabilities. Boiling curves and visual observations of the boiling process have been performed. The superheat needed to have the onset of boiling on hydrophilic, hydrophobic and superhydrophobic surfaces (SHS) has been measured, and the influence of surface roughness and wettability has been quantified.

3.6.1 Pool boiling experimental setup

The pool boiling set up is described in [51] in details. The boiling chamber is made in aluminum and an internal heater (80W) heats up the water. Moreover, two external heating tapes are placed on the walls of the chamber and are connected to a PID controller to balance thermal leakage in order to maintain the saturation temperature in the chamber. Two K-thermocouples are placed in the water and connected to a proportional–integral–derivative (PID) controller to check the water temperature. A pressure gauge is connected to the tank to provide the value of the pressure inside the chamber and a bellows is used to modify the internal pressure of the chamber in order to work at saturation conditions. A ceramic cartridge (Acim Jouanin H6.5X32X175) of 175 Watts is placed in a house made in copper to heat the surface and reach boiling on it; this heater is surrounded by Teflon. A heat flux meter with 3 embedded T-thermocouples (Captec, France) is placed between the copper housing of the heater and the tested surface to provide a direct measure of the heat flux to the tested surface. A spring is placed between the bottom of the copper housing and the bottom of the Teflon box to press the heater with a constant strength on the surface. All the thermocouples and the pressure gauge are connected to a computer using a data acquisition system (Agilent A34970A data acquisition/switch unit, USA). Figure 3.3 shows a scheme of the experimental setup. Furthermore, to acquire the boiling process, a high-speed camera HCC-1000 (VDS Vosskuhler) located in front of the chamber was used. The measurement accuracy of the T and K-thermocouples is 0.5K, and the accuracy of the pressure gauge is 0.1% FS, equivalent to 5hPa.

3.6.2 Experimental procedure

The chamber was vacuumed down to 30mbar before adding water in order to remove air and adsorbed gases inside the tank. The chamber was then filled with a small quantity of degassed water, and vacuum was pulled once more in order to extract the residual air replacing it with water vapor. Finally the chamber was filled completely, and the internal heater was switched on in order to bring the water at its saturation temperature. When the water saturation temperature was reached, the internal heater was switched off and the cartridge heater was switched on to bring the copper housing at the saturation temperature of water. Having reached a null wall superheat (difference between the surface temperature T_{wall} and the water temperature at saturation T_{sat}), the cartridge power was increased by a tiny amount (1W) and temperature and flux measures were recorded. The boiling curve was built by slowly increasing step by step (max 5 volt each 5 minutes) the cartridge power, in order to work always in stationary conditions. i.e every power step was kept the necessary time to achieve a stable surface temperature (within 0.5K).

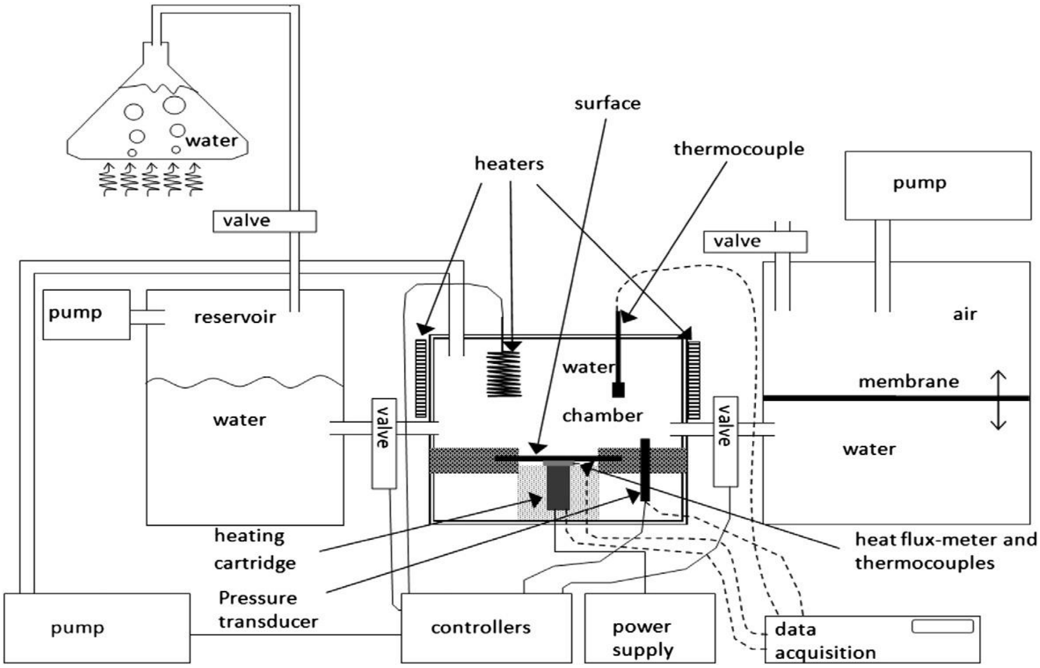

Figure 3.3: Experimental setup [51].

3.6.3 Materials and preparation of the test surfaces

With the goal to measure the influence of the surface topography and wettability on the boiling curve, and specifically the case of superhydrophobic surfaces, treated steel surfaces (stainless steel 304S15, 1mm thickness) were used. It was decided to use stainless steel because it is a material widely used for industrial applications, very replicable and therefore interesting also from the practical point of view. Knowing that the surface durability of the superhydrophobic coatings is still an important issue [218], after different tests with different surface treatments, the superhydrophobic surfaces able to resist the thermal stress during at least two boiling curves have been finally produced using a coating prepared with a commercial product - Glaco Mirror

Coat “Zero” (Soft 99 Co.). As reported in the supplementary information of [52], it is an alcohol-based suspension of silica nanoparticles functionalized by organic hydrophobizing agent.

Boiling experiments were carried out on 6 different types of surfaces:

- stainless steel as by purchase, hereinafter referred to as Raw;
- rough stainless steel, obtained by inserting the normal surface in a solution 6M of distilled water and hydrochloric acid for 15 minutes, then rinsed with distilled water and dried in air, hereinafter referred to as RoAc;
- rough stainless steel, obtained by grinding, with circular motion, a normal surface with sandpaper 500. A blasting process in order to obtain a more homogeneous roughness was not possible, due to the surface deformations. Using surfaces with greater thicknesses did not allow the necessary temperature homogeneity for the boiling tests. This surfaces is hereinafter referred to as RoSand;
- stainless steel as by purchase, coated with a commercial coating agent containing nanoparticles and organic reagent, hereinafter referred to as RawG_SHS;
- rough stainless steel, based on RoAc, coated with a commercial coating agent containing nanoparticles and organic reagent, hereinafter referred to as RoAcG_SHS;
- rough stainless steel, based on RoSand, coated with a commercial coating agent containing nanoparticles and organic reagent, hereinafter referred to as RoSandG_SHS.

The following procedure has been used for cleaning the surfaces: surfaces have been immersed in water at 80°C for 30 minutes, then inserted in acetone at 60°C, and finally in alcohol at 60°C. All the procedure was made in an ultrasonic bath. To coat the surfaces with the Glaco Mirror the following procedure has been used:

- the surfaces were cleaned and dry in standard air under the hood for 24h;
- the surfaces were placed in a vertical position, then sprayed with the Glaco Mirror until a thin liquid film weted the entire surface, and finally left to dry in air under the hood for 24h.

3.6.4 Surface characterization

The roughness of the surfaces was measured using a confocal microscopy and interferometry (Sensofar PLu Neox, Spain). The results are presented in Table 3.1. The mean roughness is quantified by the 3D parameters Sa and

Sq. Sa expresses the average of the absolute values of the profile heights Z(x,y) in the measured area. Sq expresses the root mean squared of Z(x,y) in the measured area. Since the key parameter for the incipient boiling is not only the mean roughness, but either the peak-to-valley depth or a parameter able to properly quantify the size of cavities present on the surface [52], also Sv and Sz parameters are evaluated. Sv expresses the maximum value valley depth on the surface in the measured area. Sz expresses the sum of the maximum value of peak height and the maximum value of valley depth on the surface within the measured area.
The Glaco Mirror layer, added to the stainless steel substrate to modify its wettability, affects also its mean roughness, as shown in Table 3.2.

	Raw [µm]	***RawG_SHS [µm]***	***RoAc [µm]***	***RoAcG_SHS [µm]***	***RoSand [µm]***	***RoSandG_SHS [µm]***
Sa	**1.672**	**2.044**	**8.108**	**9.983**	**2.537**	**2.849**
St Dev Sa	0.016	0.111	0.155	0.342	0.103	0.078
Sq	**2.091**	**2.608**	**12.909**	**77.831**	**3.516**	**4.027**
St Dev Sq	0.021	0.102	0.282	18.895	0.163	0.151
Sv	**10.960**	**14.058**	**140.681**	**202.606**	**85.494**	**94.215**
St Dev Sv	1.422	0.938	2.141	2.848	2.269	2.588
Sz	**22.456**	**28.198**	**215.188**	**253.810**	**105.437**	**126.897**
St Dev Sz	1.362	1.275	2.787	2.968	1.952	2.458

Table 3.1: Roughness parameters for the substrates.

Surfaces RoSand and RoSandG_SHS may be not completely homogeneous, since at the microscope it is possible to detect scratches due to the sandpaper and the procedure to prepare them (see Figure 3.4).

To define the surface wettability, advancing and receding contact angles, θ_A and θ_R, were classically measured by expanding and contracting sessile water drops on the horizontal surface (sessile drop method) [102]. θ_A and θ_R measurements are shown in Table 3.2. Typical drop volume of the analyzed drops was ~5µl. To measure the contact angle, the drop profile in the vicinity of the contact line was extracted and fitted with a circle; the contact angle was computed from the slope of the circle at the surface [64,219]. It is here necessary to specify that the contact angles, and in particular the superhydrophobicity of the surfaces, were maintained during the boiling test, as evidenced by the work of Yu et al. [220]. They noticed that superhydrophobic surfaces maintain their wettability when the surface temperature is greater than of the water temperature.

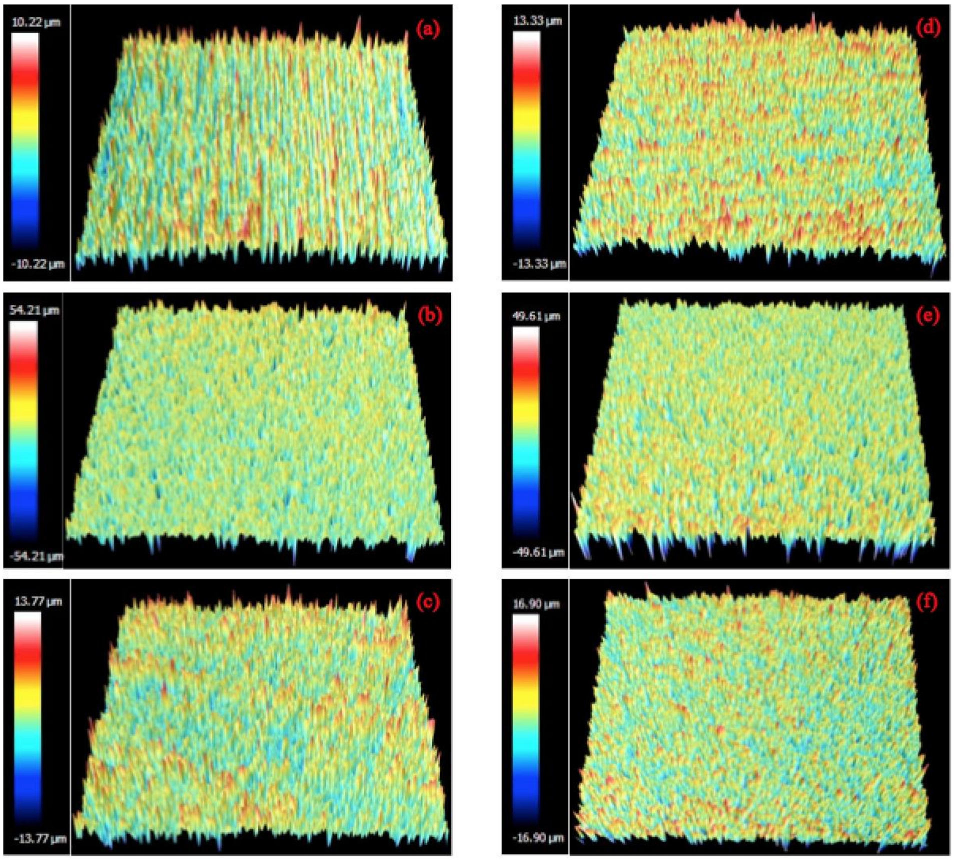

Figure 3.4: Topography of the analyzed surfaces: (a) Row, (b) RoAc, (c) RoSand, (d) RowG_SHS, (e) RoAcG_SHS, (f) RoSandG_SHS.

	Raw	***RawG_SHS***	***RoAc***	***RoAcG_SHS***	***RoSand***	***RoSandG_SHS***
θ_A [°]	91	151	29	149	72	153
θ_R [°]	53	150	<20	149	31	152

Table 3.2: Average θ_A and θ_R for the substrates. The standard deviations are lower than ±3°.

The chemical composition of each surface was analyzed using a SEM−EDX (Bruker Nano GmbH, K-series). The raw data of the normalized percentage composition by weight of each element are shown in Table 3.3.

Element	Raw	RawG_ SHS	RoAc	RoAcG _SHS	RoSand	RoSand G_SHS
iron	67.54	60.05	65.37	60.89	65.16	61.19
chrome	15.21	13.74	16.12	15.35	14.73	14.14
nickel	7.40	6.15	6.88	6.47	7.09	6.65
carbone	7.96	5.66	7.15	6.02	8.97	8.38
manganese	1.89	1.67	2.15	1.84	1.93	1.81
oxygene	0.00	8.34	1.87	6.68	2.12	5.14
silicium	0.00	4.40	0.00	2.75	0.00	2.71
Sum:	100.00	100.00	100.00	100.00	100.00	100.00

Table 3.3: Normalized percentage composition by weight of each element [norm. wt.%] for each surface type (average values).

After every boiling test, measures of roughness, contact angle and chemical composition analysis were again performed. Results do not show any discrepancy with the analysis performed before the boiling tests.

3.6.5 Results and discussion

In Figure 3.5 boiling curves with the standard deviation of data and the onset of nucleate boiling (ONB) are presented for each surface. ONB is here determined by a visualization of the incipient boiling. For the raw stainless steel (Raw) ONB appears at a superheat of 12°C. In the case of rough steel surfaces (RoAc and RoSand) the ONB appears at slightly lower superheat (between 7 and 10°C). At the boiling onset only few small bubbles appear on Raw, RoAc and RoSand surfaces (Figure 3.5) and even when the superheat reaches 30°C a small number of tiny bubbles is present on the surfaces. On the Raw surface, bubbles are rapidly upward elongated and detach from the surface, while on RoAc and RoSand surfaces, the bubbles are more spherical, and detach rapidly from the surface, facilitating the rewetting of the boiling surface. The vapour bubbles on the RoAc surface have a lower diameter with respect to the bubbles on the RoSand surface, which has higher contact angles. Hence, keeping the same surface roughness, bubble departure diameter decreases with the decrease of the contact angle, and a lower superheat is required for bubble nucleation on the rough surfaces with respect to the raw surface.

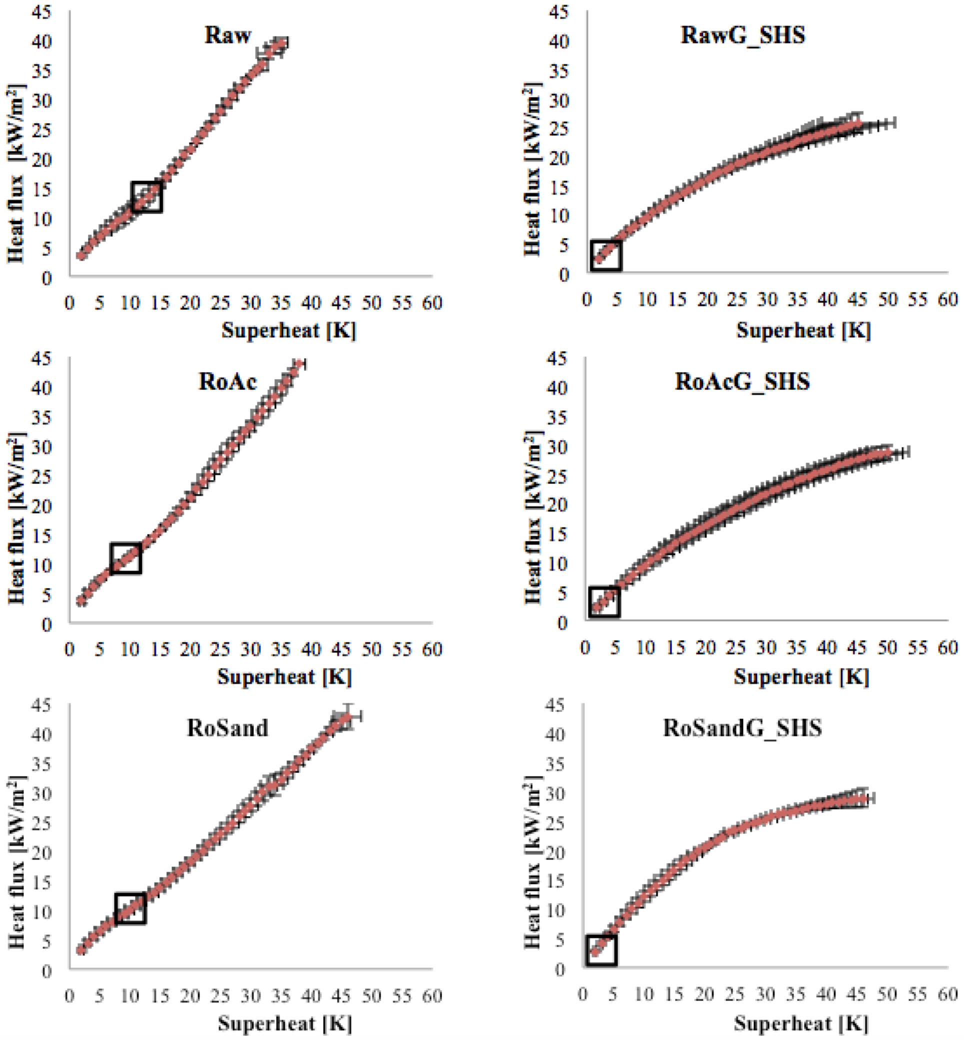

Figure 3.5: Boiling curves with standard deviation of temperature and input heat flux. In the black box the ONB is highlighted.

In the case of superhydrophobic surfaces (RawG_SHS, RoAcG_SHS and RoSandG_SHS), the ONB appears at superheat very close to zero (i.e. at the first step of increasing power), and sometimes first small bubbles are formed even when the surface has a temperature lower than the water saturation temperature (Figure 3.6). Therefore it seems that the initial gas film is sometimes formed not by the vapour, but by the air initially trapped between the roughness peaks of the superhydrophobic surfaces, even if the water was properly degassed. The presence of such air bubble entrapped in the surface cavities can explain also other literature results [52,102]. This outcome confirms also what Carey reported in his book [6] for rough surfaces, even without an explicit reference to experimental results: “If the liquid does not wet the heated surface, vapor and/or air will be trapped in virtually every cavity on the surface. Vaporization is initiated immediately when the surface temperature begins to exceed saturation and the vapor produced at one location will displace liquid adjacent to the surface and spread laterally to form a vapor blanket on the surface”. Thus, once boiling is initiated, the boiling process immediately enters the film boiling regime.

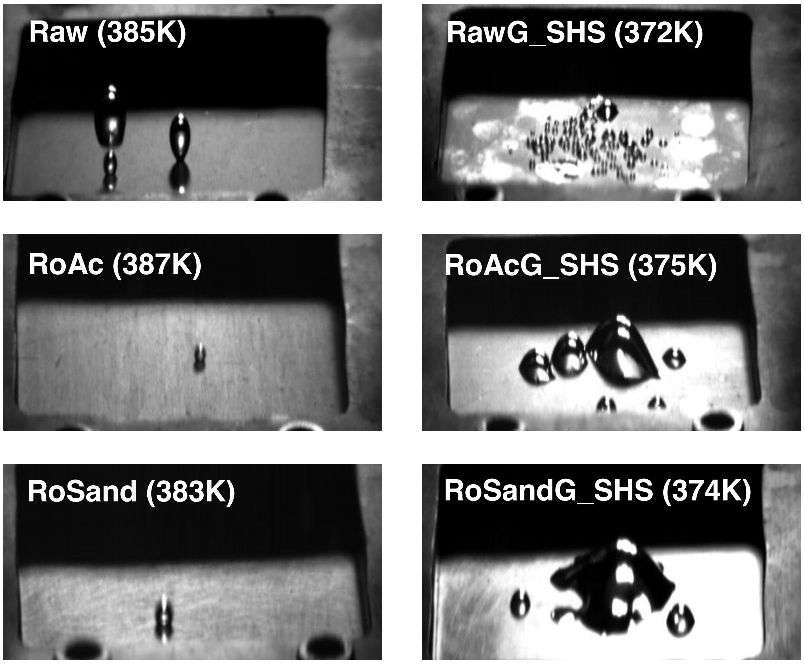

Figure 3.6: Incipient boiling. Between brackets the surface temperature to which the image refers. The error on the temperature is about ±0.5K.

On superhydrophobic surfaces, as soon as the flux increases, in few seconds the bubbles coalesce and form one single bubble, like a steam blanket, which covers most of the heated surface. When a bubble is detached from a superhydrophobic surface another bubble immediately forms, i.e. a thin vapor layer is present in a constant mode after the ONB. Therefore the vapour film formed on the SHS is stable, as also shown for a different experiment and application by Vakarelski et al. [52]. When the superheat is about 20K the departure frequency is reaching a value of approximately 1Hz and intermittent rewetting occurs. Such typical bubble dynamic behavior on SHS is shown in Figure 3.7.

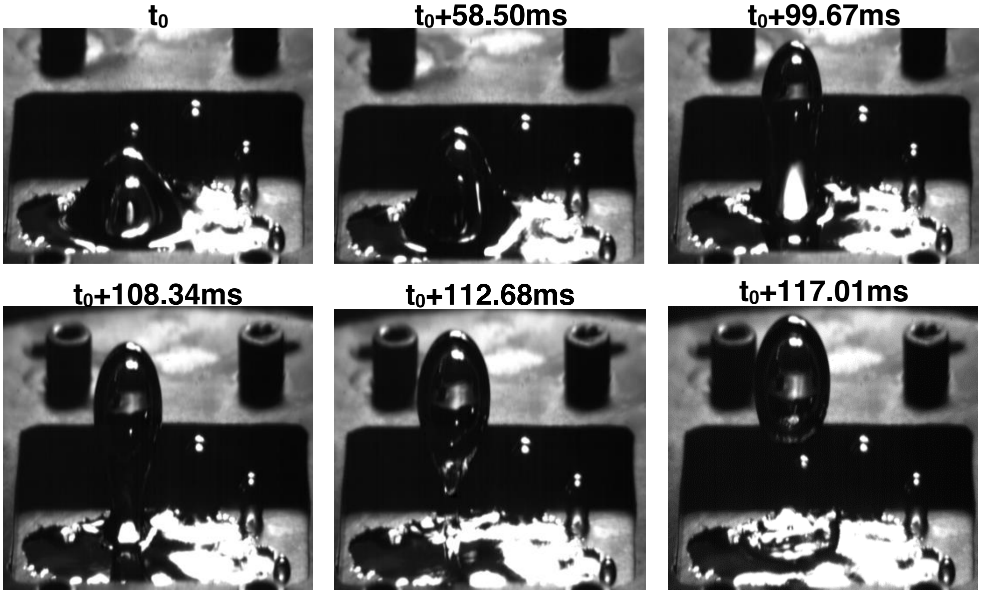

t_0　**t_0+58.50ms**　**t_0+99.67ms**

t_0+108.34ms　**t_0+112.68ms**　**t_0+117.01ms**

Figure 3.7: Bubble dynamics on the surface RoSandG_SHS. The time (with respect to the time of the first image) is reported above the image.

A significant change in the shape of the boiling curve is visible in Figure 3.8. The slope of the boiling curves for Raw, RoAc and RoSand cases suggests a standard boiling behavior (solid symbols), and a higher heat removal with respect to the superhydrophobic surface cases (open symbols). From Figure 3.85a the boiling curves for the SH surfaces RawG_SHS, RoAcG_SHS and RoSandG_SHS are almost constant around a heat flux equal to 25kW/m^2, i.e. a further increase of the heat flux is bringing the surfaces to very high values of temperature. From Figure 3.8a it is also possible to see that the curve referred to surface Raw is practically superimposed to RoAc boiling curve. The surface RoAc has a higher roughness and a higher wettability respect surface Raw, i.e. θ_A of 29° instead of 91° respectively. It follows that, when the surfaces have a low contact angle, the surface roughness is controlling the boiling process. In Figure 3.85b the heat transfer coefficients are shown: it is possible to notice a marked difference of the HTC between superhydrophobic surfaces and their corresponding reference case, confirming the fact that superhydrophobic surfaces do not follow the typical trend of known boiling curves. SHS surfaces show a peculiar behavior reaching a sort of early Leidenfrost regime, i.e. a lower HTC just after the ONB.

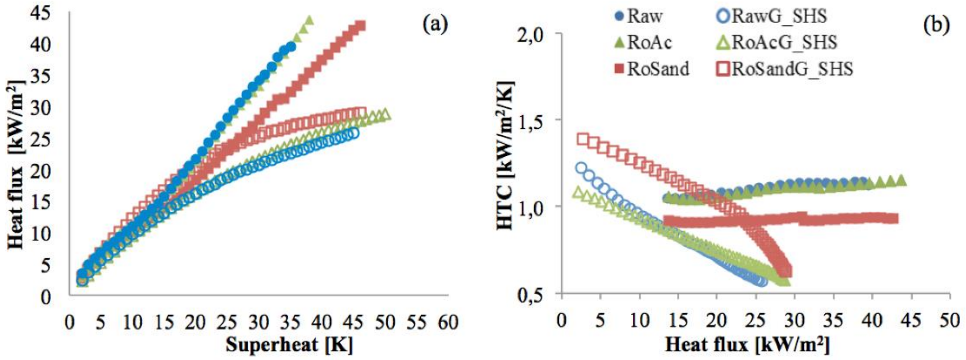

Figure 3.8: Experimental boiling curves (a). HTC vs heat flux (b).

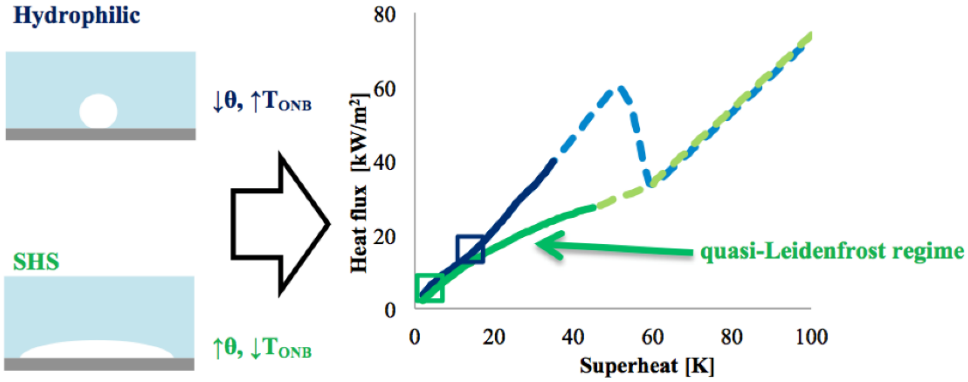

Figure 3.9: Schematic representation of the bubble formation on hydrophilic and superhydrophobic surfaces with the corresponding boiling curve. Continuous lines represent the experimental curves found for hydrophilic (blue

line) and SHS (green line) cases. Dashed lines represent the respective boiling curves hypothesized as a result of the experimental data obtained; the Captec flux sensor did not allow higher temperatures. In the box is highlighted the ONB for the respective cases.

3.7 Conclusions

This chapter reviews the role of wettability on pool boiling heat transfer. Numerous theoretical and experimental studies have focused on the enhancement of pool boiling heat transfer, using strategies that alter the liquid and/ or the surface properties. In this context, nanofluids and surface micro-and-nano coatings have shown great potential in improving the heat transfer coefficients and enhancing the Critical Heat Flux, although much research is still required to optimize these strategies. Such optimization involves a deeper understanding on how these strategies act on the pool boiling phenomena, so that significant fundamental research is of major importance. Additionally, there is still room for more specific studies related to the composition (chemistry) and morphology of the coatings. Similar exercise is required to quantify the effect of the chemical composition and concentration of the particles added in nanofluids.

Careful analysis of the various strategies to enhance pool boiling heat transfer leads to the conclusion that all these strategies mainly act on modifying the boundary conditions at the liquid-solid-vapour interfaces, by altering the wettability and/or surface topography. These two parameters are strongly related, so it is very difficult to distinguish the effect of the surface wettability alone on most of the experimental work reported in the literature. However, it is important to isolate these effects, as much as possible, namely by separating the effect of wettability related to the chemistry form that of surface morphology. Misinterpretation of the results due to unclear boundary conditions will be passed to most of the existing correlations and models, since they have a strong empirical nature. Hence, only a systematic approach, which allows quantifying the effect of the various influencing parameters, may overtake the empirical nature of the models to describe such a complex phenomena as pool boiling heat transfer. In this context, many questions still remain open in the theoretical description of the wettability role on bubble formation and on the heat transfer fundamentals.

Despite this topic requires as aforementioned, significant further research at both experimental and theoretical levels, one may identify the following trends, from the literature reviewed here.

Wettability has a vital role, which starts at the nucleation fundamentals: at low heat fluxes, higher contact angles (hydrophobic/superhydrophobic conditions) and lower hysteresis promote the activation of the nucleation sites and the stable bubble detachment, thus triggering the nucleate boiling to start at lower superheat. The opposite trend is observed for hydrophilic conditions.

This will affect bubble detachment and the interaction mechanisms: the hydrophobic conditions favor the regular departure of larger bubbles, which are more likely to coalesce. This is particularly relevant as the heat flux increases and one enters in the regime of slugs and columns, since large bubbles will actually be less beneficial, leading to a fast formation of large vapor blankets, thus decreasing the heat transfer coefficient and promoting the establishment of the Critical Heat Flux condition. Hence "optimal" wetting properties also depend on the part of the boiling curve that is covered on the working conditions.

Despite it alters surface wettability, changing surface topography mainly works, according to nucleation fundamentals, as a way to increase improve capillary pumping, increase liquid solid surface area and increase the number of nucleation sites. In particular, altering surface topography will mainly act on the nucleation sites density and consequently on interaction mechanisms such as bubble coalescence, which, in turn, should improve the heat transfer coefficients, but may promote the Critical Heat Flux condition to occur at lower degrees of superheat.

On the basis of the reviewed literature and considering the importance in understanding the effect of the surface wettability alone on pool boiling heat transfer mechanisms, pool boiling experiments were carried out with degassed water on stainless steel substrates with different surface topography and wettability. Boiling curves have been measured together with visual high-speed observations of the boiling process. The onset temperature of nucleate boiling (ONB) has been measured and the influence of surface roughness and wettability has been quantified for different surfaces, with the aim to better understand the effect of superhydrophobicity on pool boiling. The original finding is that the boiling curve shape is rather different between hydrophilic and superhydrophobic case, keeping the same surface roughness, as schematically depicted in Figure 3.9. Superhydrophobic surfaces show a peculiar behavior similar to an early "quasi-Leidenfrost" regime for low superheat. The ONB appears after less than 5K of superheat on superhydrophobic surfaces, while, for the hydrophilic cases the ONB appears at more than 7K of superheat, which is a standard value using water on steel with a mean surface roughness above 2μm [221]. Bubble nucleation on SHS builds up a large and stable vapour film with a very long departure time of the order of one minute. Only when the superheat is about 15/20K the departure time starts decreasing and it get down to the more standard value of one second. Regardless of the surface roughness and topology, the boiling curves obtained with the superhydrophobic surfaces (RawG_SHS, RoAcG_SHS and RoSandG_SHS) are very similar. This means that the wettability has a predominant effect with respect to the roughness, when the contact angle exceeds the typical value for superhydrophobic surfaces (receding contact angle $\theta_{rec} > 135°$).

Bibliography Chapter 3

[1] F.P. Incropera, D.P. DeWitt. Fundamentals of Heat and Mass Transfer. 3rd ed., Wiley (1995).

[2] C.H. Li, T. Li, P. Hodgins, C. Hunter, A. Voevodin, G. Peterson. Comparison study of liquid replenishing impacts on critical heat flux and heat transf. coeff. of nuclate multiscale modulated porous structures. International Journal of Heat and Mass Transfer 54 (2011) 3146-3155,

[3] S.G. Singh, A. Agrawal, S.P.J. Duttagupta. An active control strategy for reduction of pressure instabilities during flow boiling in a microchannel. Journal of Micromechanics and Microengineering 21 (2011) 035021.

[4] M.A. Ebadian, C.X. Lin. A Review of High-Heat-Flux Heat Removal Technologies. Journal of Heat Transfer 133 (2011) 110801-11012.

[5] E. Teodori, A.S. Moita, A.L.N. Moreira. Characterization of pool boiling mechanisms over micro-patterned surfaces using PIV. International Journal of Heat and Mass Transfer 66 (2013) 261-270.

[6] V.P. Carey. Liquid vapor phase change phenomena: an introduction to the thermophysics of vaporization and condensation processes in heat transfer equipment. Taylor & Francis (1992).

[7] S. Nukiyama. The maximum and minimum values of the heat Q transmitted from metal to boiling water under atmospheric pressure. International Journal of Heat and Mass Transfer 9 (1966) 1419-1433.

[8] V.K. Dhir. Boiling heat transfer. Annual Review of Fluid Mechanics 30 (1998) 365-401.

[9] H.S. Ahn, C. Lee, H. Kim, H. Jo, S. Kang, J. Kim, J. Shin, M.H. Kim. Pool boiling CHF enhancement by micro/nanoscale modification of zircaloy-4 surface. Nuclear Engineering and Design 240 (2010) 3350-3360.

[10] Y.H. Kim, S.J. Kim, K.Y. Suh, J.L. Rempe, F.B. Cheung, S.B. Kim. Internal vessel cooling feasibility attributed by critical heat flux in inclined rectangular gap. Nuclear Engineering and Technology 154 (2006) 13-40.

[11] J.C.M. Leung, K.A. Gallivan, R.E. Henry, S.G. Bankoff. Critical heat flux predictions during blowdown transients. International Journal of Multiphase Flow 7 (1981) 677-701.

[12] P.J. Berenson. Experiments on pool-boiling heat transfer. International Journal of Heat and Mass Transfer 5 (1962) 985-999.

[13] I.L. Pioro, W. Rohsenow, S.S. Doerffer. Nucleate pool-boiling heat transfer. I: review of parametric effects of boiling surface. International Journal of Heat and Mass Transfer 47 (2004) 5033-5044.

[14] H.M. Kurihara, J.E. Myers. The effects of superheat and surface roughness on boiling coefficients. American Institute of Chemical Engineers Journal 6 (1960) 83-91.

[15] A.D. Messina, E.L. Park Jr. Effect of precise arrays of pits on nucleate boiling. International Journal of Heat and Mass Transfer 24 (1981) 141-145.

[16] S.T. Hsu, F.W. Schmidt. Measured variations in local surface temperatures in pool boiling of water. Journal of Heat Transfer 83 (1961) 254-260.

[17] T.M. Anderson, I. Mudawar. Microelectronic cooling by enhanced pool boiling of a dielectric fluorocarbon liquid. Journal of Heat Transfer 111 (1989) 141-145.

[18] K. Ferjancic, I. Golobic. Surface effects on pool boiling CHF. Experimental Thermal and Fluid Science 25 (2002) 565-571.

[19] R.N. Wenzel. Resistance of solid surfaces to wetting by water. Industrial and Engineering Chemistry 28 (1936) 988-994.

[20] M. Mann, K. Stephan, P. Stephan. Infuence of heat conduction in the wall on nucleate boiling heat transfer. International Journal of Heat and Mass Transfer 43 (2000) 2193-2203.

[21] H.T. Phan, R. Bertossi, N. Caney, P. Marty, S. Colasson. A model to predict the effect of surface wettability on critical heat flux. International Communication of Heat and Mass Transfer 39 (2012) 1500-1504.

[22] C. Corty, A.S. Foust. Surface variables in nucleate boiling. Chemical engineering progress symposium series 51(17) (1955) 1-12.

[23] S.G. Bankoff. Entrapment of gas in the spreading of a liquid over a rough surface. American Institute of Chemical Engineers Journal 4 (1958) 24-26.

[24] B.B. Mikic, W.M. Rohsenow. A new correlation of pool-boiling data including the effect of heating surface characteristics. Journal of Heat Transfer 91 (1969) 245-250.

[25] S.G. Kandlikar. A theoretical model to predict pool boiling FC incorporating effects of contact angle and orientation. Journal of Heat Transfer 123 (2001) 1071-1079.

[26] H.S. Ahn, H.J. Jo, S.H. Kang, M.H. Kim. Effect of liquid spreading due to nano/microstructures on the critical heat flux during pool boiling. Applied Physics Letters 98 (2011) 071908.

[27] D.S. Wen, B.X. Wang. Effects of surface wettability on nucleate pool boiling heat transfer for surfactant solutions. International Journal of Heat and Mass Transfer 45 (2002) 1739-1747.

[28] T. Hibiki, M. Ishii. Active nucleation site density in boiling systems. International Journal of Heat and Mass Transfer 46 (2003) 2587-2601.

[29] C.H. Wang, V.K. Dhir. On the gas entrapment and nucleation site density during pool boiling of saturated water. Journal of Heat Transfer 115 (1993) 670-679.

[30] C.H. Wang, V.K. Dhir. Effect of surface wettability on active nucleation sited density during pool boiling of water on a vertical surface. Journal of Heat Transfer 115(3) (1993) 659-669.

[31] S.R. Yang, R.H. Kim. A mathematical model of the pool boiling nucleation site density in terms of the surface characteristics. International Journal of Heat and Mass Transfer 31(6) (1988) 1127-1135.

[32] R.J. Benjamin, A.R. Balakrishnan. Nucleation Site Density in Pool Boiling of Saturated Pure Liquids: Effect of Surface Microroughness and Surface and Liquid Physical Properties. Experimental Thermal and Fluid Science 15 (1997) 32-42.

[33] S. Kotthoff, D. Gorenflo, E. Danger, A. Luke. Heat transfer and bubble formation in pool boiling: Effect of basic surface modifications for heat transfer enhancement. International Journal of Thermal Sciences 45 (2006) 217-236.

[34] N.A. Patankar. Supernucleating surfaces for nucleate boiling and dropwise condensation heat transfer. Soft Matter 6 (2011) 1613-1620.

[35] A.R. Betz, J. Xu, H. Qiu, D. Attinger. Do surfaces with mixed hydrophilic and hydrophobic areas enhance pool boiling? Applied Physics Letters 97 (2010) 141909.

[36] R. Furberg, B. Palm, S. Li, M. Toprak, M. Muhammed. The use of a nano- and microporous surface layer to enhance boiling in a plate heat exchanger. Journal of Heat Transfer 131 (2009) 1-8.

[37] J.J. Wei, H. Honda. Effects of fin geometry on boiling heat transfer from silicon chips with micro-pin-fins immersed in FC-72. International Journal of Heat and Mass Transfer 46 (2003) 4059-4070.

[38] S.G. Liter, M. Kaviany. Pool boiling CHF enhancement by modulated porous-layer coating: theory and experiment. International Journal of Heat and Mass Transfer 44 (2001) 4287-4311.

[39] C.H. Li, G.P. Peterson. Parametric study of pool boiling on horizontal highly conductive microporous coated surfaces. Journal of Heat Transfer 129 (2007) 1465-1475.

[40] Y. Takata, S. Hidaka, M. Masuda, T. Ito. Pool boiling on a superhydrophilic surface. International Journal of Energy Research 27 (2003) 111-119.

[41] M.E. Davis. Ordered porous materials for emerging applications. Nature 417 (2002) 813-821.

[42] S. Vemuri, K.J. Kim. Pool boiling of saturated FC-72 on nano-porous surface. International Communication of Heat and Mass Transfer 32 (2005) 27-31.

[43] Y. Nam, J. Wu, G. Warrier, Y.S. Ju. Experimental and numerical study of single bubble dynamics on a hydrophobic surface. Journal of Heat Transfer 131 (2009) 1-7.

[44] Y. Nam, Y.S. Ju. Bubble nucleation on hydrophobic islands provides evidence to anomalously high contact angles of nanobubbles. Applied Physics Letters 93 (2008) 103115.

[45] H.T. Phan, N. Caney, P. Marty, S. Colasson, J. Gavillet. Surface wettability control by nanocoating: the effects on pool boiling heat

transfer and nucleation mechanism. International Journal of Heat and Mass Transfer 52 (2009) 5459-5471.

[46] J.J. Henley, R.L. Hummel. A third factor in boiling nucleation. Industrial & Engineering Chemistry Fundamentals 6 (1967) 603-606.

[47] R.L. Hummel. Means for increasing the heat transfer coefficient between a wall and boiling liquid. U.S. Patent 3.207.209 (1965).

[48] Y. Takata, S. Hidaka, T. Uraguchi. Boiling feature on a super water-repellent surface. Heat Transfer Engineering 27 (2006) 25-30.

[49] Y.Y. Hsu. On the Size Range of Active Nucleation Cavities on a Heating Surface. Journal of Heat Transfer 84 (1962) 193-204.

[50] S.J. Kim, I.C. Bang, J. Buongiorno, L.W. Hu. Surface wettability change during pool boiling of nanofluids and its effect on critical heat flux. International Journal of Heat and Mass Transfer 50 (2007) 4105-4116.

[51] B. Bourdon, P. Di Marco, R. Rioboo, M. Marengo, J. De Coninck. Enhancing the onset of pool boiling by wettability modification on nanometrically smooth surfaces. International Communications in Heat and Mass Transfer 45 (2013) 11-15.

[52] B. Bourdon, R. Rioboo, M. Marengo, E. Gosselin, J. De Coninck. Influence of the wettability on the boiling onset. Langmuir 28 (2012) 1618-1624.

[53] D. Lee, D. Omolade, R.E. Cohen, M.F. Rubner. pH-dependent structure and properties of TiO2/SiO2 nanoparticle multilayer thinfilms. Chemistry of Materials 19 (2007) 1427-1433.

[54] T. Young. An essay on the cohesion of fluids. Philosophical Transactions of the Royal society of London 95 (1805) 65-87.

[55] S.J. Hitchcock, N.T. Carrol, M.G. Nicholas. Some effects of substrate roughness on wettability. Journal of Materials Science 16 (1981) 714-732.

[56] K.T. Hong, H. Imadojemu, R.L. Webb. Effects of oxidation and Surface Roughness on Contact Angle. Experimental Thermal and Fluid Science 8 (1994) 279-285.

[57] S.G. Kandlikar, M.E. Steinke. Contact angles of droplets during spread and recoil after impinging on a heated surface. Chemical Engineering Research and Design 79 (2001) 491-498.

[58] S.G. Kandlikar, M.E. Steinke. Contact angles and interface behaviour during rapid evaporation of liquid on a heated surface. International Journal of Heat and Mass Transfer 45 (2002) 3771-3780.

[59] M. Sakai, H. Kono, A. Nakajima, X. Zhang, H. Sakai, M. Abe, A. Fulishima. Sliding of water droplets on the superhydrophobic surface with ZnO nanorods. Langmuir, 25(24) (2009) 14182-14186.

[60] N.A. Patankar. Consolidation of hydrophobic transition criteria by using an approximate energy minimization approach. Langmuir 26(11) (2010) 8941-8945.

[61] B. Bhushan, E.K. Her. Fabrication of superhydrophobic surface with high and low adhesion inspired from rose petal. Langmuir 26(11) (2010) 8207-8217.

[62] K.H. Chu, R. Enrigh, E.N. Wang. Structured surfaces for enhanced pool boiling heat transfer. Applied Physics Letters 100 (2012) 241603.

[63] W.J. Jeong, H. Yeong, S.Y. Hyun, M. Ambrosia. Dynamic behaviour of water droplets on solid surfaces with pillar-type nanostructures. Langmuir 28 (2012) 5360-5371.

[64] C. Antonini, A. Amirfazli, M. Marengo. Drop impact and wettability: from hydrophilic to superhydrophobic surfaces. Physics of Fluids 24 (2012) 102104.

[65] I. Bernagozzi, C. Antonini, F. Villa, M. Marengo. Fabricating superhydrophobic aluminum: An optimized one-step wet synthesis using fluoroalkyl silane. Colloids and Surfaces A 441 (2014) 919-924.

[66] A. Marmur. Measures of wettability of solid surfaces. The European Physical Journal Special Topics 197 (2011) 193-198.

[67] E.F. Crafton, W.Z. Black. Heat transfer and evaporation rates of small liquid droplets on heated horizontal targets. International Journal of Heat and Mass Transfer 47 (2004) 1187-1200.

[68] J.D. Bernardin, I. Mudawar, C.B. Walsh, E.I. Franses. Contact angle temperature dependence for water droplets on practical aluminum surfaces. International Journal of Heat and Mass Transfer 40 (1997) 1017-1033.

[69] J.D. Bernardin, C.J. Stebbins, I. Mudawar, Mapping of impact and heat transfer regimes of water drops impinging on a polished surface. Int. J. Heat Mass Transf., 40(2) (1997) 247-267.

[70] J.D. Bernardin, C.J. Stebbins, I. Mudawar. Effects of surface roughness on water droplet impact history and heat transfer regimes. International Journal of Heat and Mass Transfer 40(1) (1997) 73-78.

[71] F.D. Petke, B.R. Ray. Temperature dependence of contact angles of liquids on polymeric solids. Journal of Colloid Interface Science 31 (1969) 216-227.

[72] V.P. Skripov. The boiling crisis and the thermodynamic stability of a liquid. Foreign Technology Div. Wright-Patterson AFB Ohio, Ed. Defense Technical Information Center, Ohio, USA (1962).

[73] N.I. Kolev. How Accurately Can We Predict Nucleate Boiling? Experimental Thermal and Fluid Science 10 (1995) 370-378.

[74] K.M. Balss, C.T. Avedisian, R.E. Cavicchi, M.J. Tarlov. Nanosecond imaging of microboiling behavior on pulsed-heated Au films modified with hydrophilic and hydrophobic self-assembled monolayers. Langmuir 21 (2005) 10459-10467.

[75] K. Stefan. Heat transfer in condensation and boiling. Springer, Berlin, Germany (1992) 127-128.

[76] H.B. Clark, P.S. Strenge, J.W. Westwater. Active sites for nucleate boiling. Chemical engineering progress symposium series 55(29) (1959) 103-110.

[77] K. Mizukami. Entrapment of vapor in reentrant cavities. Lett. Heat and Mass Transfer 2 (1977) 279-284.

[78] T.W. Forest. The stability of gaseous nuclei at liquid-solid interfaces. Journal of Applied Physics 53 (1982) 6191-6201.

[79] W. Fritz, W. Ende. Uber den Verdampfungsvorgang nach kinematographischen Aufnahmen an Dampfblasen. Physik Zeitschrift 37(11) (1936) 391-401.

[80] C. Hutter. Experimental Pool Boiling Investigation of FC-72 on Silicon with Artificial Cavities, Integrated Temperature Micro-Sensors and Heater. PhD Thesis, The University of Edimburg (2009).

[81] H.K. Forster, N. Zuber. Growth of a vapor bubble in a superheated liquid. Journal of Applied Physics 25(4) (1954) 474-478.

[82] M. S. Plesset, S. A. Zwick. The growth of vapor bubbles in superheated liquids. Journal of Applied Physics 25(4) (1954) 493-500.

[83] S.P. Liaw, V.P. Dhir. Void fraction measurements during saturated pool boiling of water on partially wetted vertical surfaces. Journal of Heat Transfer 29 (2008) 731-738.

[84] Y. Takata, S. Hidaka, J.M. Cao, T. Nakamura, H. Yamamoto, M. Masuda, T. Ito. Effect of surface wettability on boiling and evaporation. Energy 30 (2005) 209-220.

[85] K. Bier, D. Gorenflo, M. Salem, Y. Tanes. Effect of pressure and surface roughness on pool boiling of refrigerants. International Journal of Refrigeration 2 (1979) 211-219.

[86] M. Matkovic, B. Koncar. Bubble departure diameter prediction uncertainty. Science and Technology of Nuclear Installations 12 (2012) 1-7.

[87] B.B. Mikic, W. M. Rohsenow, P. Griffith. On bubble growth rates. International Journal of Heat and Mass Transfer 13 (1970) 657-666.

[88] N.R. Snyder, D. K. Edwards. Summary of conference on bubble dynamics and boiling heat transfer. Tech. Rep. Memo 20-137, Jet Propulsion Laboratory, Pasadena, USA (1956).

[89] F.D. Moore, R. B. Mesler. The measurement of rapid surface temperature fluctuations during nucleate boiling of water. American Institute of Chemical Engineers Journal 7 (1961) 620-624.

[90] M.G. Cooper, A.J.P. Lloyd. Micro-layer in nucleate pool boiling. International Journal of Heat and Mass Transfer 12 (1969) 895-913.

[91] D.B.R. Kenning, Y. Yan. Pool boiling heat transfer on a thin plate: Features revealed by liquid crystal thermography. International Journal of Heat and Mass Transfer 39 (1996) 3117-3137.

[92] M.S. Plesset, A. Prosperetti. Flow of vapor in a liquid enclosure. Journal of Fluid Mechanics 78 (1976) 433-444.

[93] C. Sodtke, J. Kern, N. Schweizer, P. Stephan. High resolution measurements of wall temperature distribution underneath a single vapour bubble under low gravity conditions. International Journal of Heat and Mass Transfer 49(5-6) 1100-1101.

[94] P. Stephan, T. Fuchs. Local heat flow and temperature fluctuations in wall and fluid in nucleate boiling systems. Heat and Mass Transfer 45 (2009) 919-928.

[95] J.P. McHale, S.V. Garimella. Bubble nucleation characteristics in pool boiling of a wetting liquid on smooth and rough surfaces. International Journal of Multiphase Flow 36 (2010) 249-260.

[96] W. Fritz. Berechnung des maximalvolume von dampfblasen. Physikalische Zeitschrift 36 (1935) 379-388.

[97] R. Cole. Bubble frequencies and departure volumes at subatmospheric pressures. American Institute of Chemical Engineers Journal 13 (1967) 779-783.

[98] S.S. Kutateladze, I. I. Gogonin. Growth rate and detachment diameter of a vapour bubble in free convection boiling of a saturated liquid. High Temperature 17 (1979) 667-671.

[99] M.K. Jenson, G. J. Memmel. Evaluation of bubble departure diameter correlations. In: Proc. of the 8th International Heat Transfer Conference 4 (1986) 1907-1912.

[100] A.S. Moita, E. Teodori, A.L.M. Moreira. Enhancement of pool boiling heat transfer by surface micro-structuring. Journal of Physics: Conf. Series 395 (2012) 012175.

[101] P. Papon, J. Leblond, P.H.E. Meijer. The Physics of Phase Transitions. 2nd ed., Springer-Verlag, Berlin (2006) 35-51.

[102] Y. Takata, S. Hidaka, M. Kohno. Effect of surface wettability on pool boiling: enhancement by hydrophobic coating. International Journal of Air-Conditioning and Refrigeration 20(1) (2012) 1150003.

[103] Y. Nam, E. Aktinol, V.K. Dhir, Y.S. Ju. Single bubble dynamics on a superhydrophilic surface with artificial nucleation Sites. International Journal of Heat and Mass Transfer 54(7-8) (2011) 1572-1577.

[104] G. Hazi, A. Markus. On the bubble departure diameter and release frequency based on numerical simulation results. International Journal of Heat and Mass Transfer 52 (2009) 1472-1480.

[105] C.P. Costello, W.J. Frea. A salient non-hydrodynamic effect on pool boiling burnout of small semicylindrical heaters. Chemical Engineers Progress 61(57) (1965) 258-268.

[106] M.G. Cooper. The microlayer and bubble growth in nucleate pool boiling. International Journal of Heat and Mass Transfer 12 (1969) 915-933.

[107] A.R. Betz, J. Jenkins, C.J. Kim, D. Attinger. Boiling heat transfer on superhydrophilic, superhydrophobic, and superbiphilic surfaces. International Journal of Heat and Mass Transfer 57 (2013) 733-741.

[108] B. Truong, L.W. Hu, J. Buongiorno. Surface modifications using nanofluids for nucleate boiling heat transfer. 6th International Conference on Nanochannels, Microchannels, and Minichannels, Darmstadt, Germany, ICNMM2008-62085 (2008) 561-567.

[109] V. Chekanov. Interaction of centers during nucleate boiling. Teplofizika Vysokikh Temperature 15 (1977) 121-128.

[110] R.L. Judd, C.H. Lavdas. The nature of nucleation site interaction. Journal of Heat Transfer 102(3) (1980) 461-464.

[111] R.L. Judd. On nucleation sites interaction. Journal of Heat Transfer 110(2) (1988) 475-478.

[112] R.L. Judd, A. Chopra. Interaction of the nucleation processes occurring at adjacent nucleation sites. Journal of Heat Transfer 115(4) (1993) 955-962.

[113] L. Zhang, M. Shoji. Nucleation sites interaction in pool boiling on the artificial surface. International Journal of Heat and Mass Transfer 46(3) (2003) 513-522.

[114] D.N. Nimkar, S.H. Bhavnani, R.C. Jaeger. Effect of nucleation sites spacing on the pool boiling characteristics of a structured surface. International Journal of Heat and Mass Transfer 49 (2006) 2829-2839.

[115] C.K. Yu, D.C. Lu, T.C. Cheng. Pool boiling heat transfer on artificial micro-cavity surfaces in dielectric fluid FC-72. Journal of Micromechanics and Microengineering 16 (2006) 2092-2099.

[116] P. Kotchaphakdee, M.C. Williams. Enhancement of nucleate pool boiling with polymer additives. International Journal of Heat and Mass Transfer 13 (1970) 835-848.

[117] G. Hetsroni, J.L. Zakin, Z. Lin, A. Mosyak, E.A. Pancallo. The effect of surfactants on bubble growth, wall thermal patterns and heat transfer in pool boiling. International Journal of Heat and Mass Transfer 44 (2001) 485-497.

[118] V.M. Wasekar, R.M. Manglik. A review of enhanced heat transfer in nucleate pool boiling of aqueous surfactant and polymeric solutions. Journal of Enhanced Heat Transfer (6) (1999) 135-150.

[119] V.M. Wasekar, R.M. Manglik. Pool boiling heat transfer in adueous solutions of an anionic surfactant. Journal of Heat Transfer 122(4) (2000) 708-715.

[120] W.T. Wu, C.L. Hu, Y.M. Yang. Surfactant effect on boiling incipience and bubble growth dynamics of surface boiling in water. Infection Control and Hospital Epidemiology Journal 24 (1993) 111-118.

[121] W.T. Wu, Y.M. Yang, J.R. Maa. Nucleate pool boiling enhancement by means of surfactant additives. Experimental Thermal and Fluid Science 18 (1998) 195-209.

[122] S.U.S. Choi, J.A. Eastman. Enhancing thermal conductivity of fluids with nanoparticles. International Mechanical Engineering Congress & Exposition, San Francisco, CA, 231 (1995) 99-105.

[123] S. Lee, S.U.S. Choi, S. Li, J.A. Eastman. Measuring thermal conductivity of fluids containing oxide nanoparticles. Journal of Heat Transfer 121 (1999) 280-289.

[124] S.M.S. Murshed, K.C. Leong, C. Yang. Enhanced thermal conductivity of TiO2–water based nanofluids. International Journal of Thermal Sciences 44 (2005) 367-373.

[125] S.M.S. Murshed, K.C. Leong, C. Yang. Investigations of thermal conductivity and viscosity of nanofluids. International Journal of Thermal Sciences 47 (2008) 560-568.

[126] W. Yu, D.M. France, J.L. Routbort, S.U.S. Choi. Review and comparison of nanofluid thermal conductivity and heat transfer enhancements. Heat Transfer Engineering 29 (2008) 432-460.

[127] S.M.S. Murshed, K.C. Leong, C. Yang. Thermophysical and electrokinetic properties of nanofluids-a critical review. Applied Thermal Engineering 28 (2008) 2109-2125.

[128] S.M.S.Murshed, K.C. Leong, C. Yang. Determination of the effective thermal diffusivity of nanofluids by the double hot-wire technique. Journal of Physics D 39 (2006) 5316-5322.

[129] Y.M. Yang, J.R. Maa. Boiling of suspension of solid particles in water. International Journal of Heat and Mass Transfer 27 (1984) 145-147.

[130] H. Masuda, A. Ebata, K. Teramae, N. Hishinuma. Alteration of thermal conductivity and viscosity of liquid by dispersing ultra-fine particles (dispersion of -Al2O3, SiO2, and TiO2 ultra-fine particles). Netsu Bussei 4 (1993) 227-233.

[131] A. Grimm. Powdered aluminum-containing heat transfer fluids. German patent DE 4131516 A1 (1993).

[132] H. Kim, M. Kim. Experimental study of the characteristics and mechanism of pool boiling CHF enhancement using nanofluids. Heat Mass Transfer 45 (2009) 991-998.

[133] J.M. Wu, J. Zhao. A review of nanofluid heat transfer and critical heat flux enhancement-Research gap to engineering application. Progress in Nuclear Energy 66 (2013) 13-24.

[134] S.U.S. Choi. Nanofluids: from vision to reality through research. Journal of Heat Transfer 131 (2009) 1-9.

[135] H.D. Kim, J. Kim, M.H. Kim. Effect of nanoparticles on CHF enhancement in pool boiling of nano-fluids. International Journal of Heat and Mass Transfer 49 (2006) 5070-5074.

[136] G. Harish, V. Emlin, V. Sajith. Effect of surface particle interactions during pool boiling of nanofluids. International Journal of Thermal Sciences 50 (2011) 2318-2327.

[137] P. Vassallo, R. Kumar, S. D’Amico. Pool boiling heat transfer experiments in silica–water nano-fluids. International Journal of Heat and Mass Transfer 47 (2004) 407-411.

[138] S. Das, N. Putra, W. Roetzel. Pool boiling characteristics of nanofluids. International Journal of Heat and Mass Transfer 46 (2003) 851-862.

[139] I.C. Bang, S.H. Chang. Boiling heat transfer performance and phenomena of Al2O3–water nano-fluids from a plain surface in a pool. International Journal of Heat and Mass Transfer 48 (2005) 2407-2419.

[140] D. Wen, Y. Ding. Experimental investigation into the pool boiling heat transfer of aqueous based c-alumina nanofluids. Journal of Nanoparticle Researc. 7 (2005) 265-274.

[141] C. Gerardi, J. Buongirno, L.W. Hu, T. McKrell. Infrared thermometry study of nanofluid pool boiling phenomena. Nanoscale Research Letters 6 (2011) 232-249.

[142] S. Jun, S. Sinha-Ray, A.L. Yarin. Pool boiling on nano-textured surfaces. International Journal ofHeat and Mass Transfer 62 (2013) 99-111.

[143] S.J. Kim, I.C. Bang, J. Buongiorno, L.W. Hu. Effects of nanoparticle deposition on surface wettability influencing boiling heat transfer in nanofluids. Applied Physics Letters 89 (2006) 153107.

[144] E. Forrest, E. Williamson, J. Buongiorno, L.W. Hu, M. Rubner, R. Cohen. Augmentation of nucleate boiling heat transfer and critical heat

flux using nanoparticle thin-film coatings. International Journal of Heat and Mass Transfer 53 (2010) 56-58.

[145] S. Ujereh, T. Fisher, I. Mudawar. Effects of carbon nanotube arrays on nucleate pool boiling. International Journal of Heat and Mass Transfer 50 (2007) 4023-4038.

[146] S. Launay, A.G. Fedorov, Y. Joshi, A. Cao, P.M. Ajayan. Hybrid micronanostructured thermal interfaces for pool boiling heat transfer enhancement. Microelectronics Journal 37 (2006) 1158-1164.

[147] H.S. Ahn, N. Sinha, M. Zhang, D. Banerjee, S.K. Fang, R.H. Baughman. Pool boiling experiments on Multi Walled Carbon Nanotube (MWCNT) Forests. Journal of Heat Transfer 128 (2006) 1335-1342.

[148] R. Chen, M.C. Lu, V. Srinivasan, Z. Wang, H.H. Cho, A. Majumdar. Nanowires for enhanced boiling heat transfer. Nano Letters 9 (2009) 548-553.

[149] C. Li, Z. Wang, P. Wang, Y. Peles, N. Koratkar, G.P. Peterson. Nanostructured copper interfaces for enhanced boiling. Small 4(8) (2008) 1084-1088.

[150] S. Kim, H.D. Kim, H. Kim, H.S. Ahn, H. Jo, J. Kim, M.H. Kim. Effects of nano-fluid and surfaces with nano structure on the increase of CHF. Experimental Thermal and Fluid Science 34 (2010) 487-495.

[151] Y. Im, Y. Joshi, C. Dietz, S.S. Lee. Enhanced boiling of a dielectric liquid on copper nanowire surfaces. International Journal of Micro-Nano Scale Transport 1 (2010) 79-95.

[152] G. Decher, J.D. Hong. Buildup of ultrathin multilayer films by self-assembly process. Makromolekulare Chemie. Makromolecular Symposia 46 (1991) 321-327.

[153] D. Lee, M.F. Rubner, R.E. Cohen. All-nanoparticle thin-film coatings. Nano Letters 6 (2006) 2305-2312.

[154] D. Lee, Z. Gemici, M.F. Rubner, R.E. Cohen. Multilayers of oppositely charges SiO2 nanoparticles: effect of surface charge on multilayer assembly. Langmuir 23 (2007) 8833-8837.

[155] B. Stutz, C.H.S. Morceli, M.D.F.D. Silva, S. Cioulachtjian, J. Bonjour. Influence of nanoparticle surface coating on pool boiling. Experimental Thermal and Fluid Science 35 (2011) 1239-1249.

[156] Y. Chen, D.C. Mo, H.B. Zhao, N. Ding, S.S. Lu. Pool boiling on the superhydrophilic surface with TiO2 nanotube arrays. Science China Technological Sciences 52 (2009) 1596-1600.

[157] W. Wu, H. Bostanci, L.C. Chow, Y. Hong, M. Su, J.P. Kizito. Nucleate boiling heat transfer enhancement for water and FC-72 on titanium oxide and silicon oxide surfaces. International Journal of Heat and Mass Transfer 53 (2010) 1773-1777.

[158] H. Honda, J.J. Wei, H. Takamastu. Enhanced Boiling of FC-72 on Silicon Chips With Micro-Pin-Fins and Submicron-Scale Roughness. Heat Transfer 124 (2002) 383-390.

[159] R.L. Webb, N.H. Kim. Principles of Enhanced Heat Transfer. 2nd ed., Taylor & Francis, New York (2005) 389-391.

[160] F.Ç. Cebeci, Z. Wu, L. Zhai, R.E. Cohen, M.F. Rubner. Nanoporosity-driven superhydrophilicity: a means to create multifunctional antifogging coatings. Langmuir 22 (2006) 2856-2862.

[161] R.F. Gaertner. Methods and means for increasing the heat transfer coefficient between a wall and boiling liquid. U.S. Patent 3.301.314 (1967).

[162] R.I. Vachon, G.H. Nix, G.E. Tanger. Evaluation of constants for the Rohsenow pool-boiling correlation. Journal of Heat Transfer 90 (1968) 239-247.

[163] C.C. Hsu, P.H. Chen. Surface wettability effects on critical heat flux of boiling heat transfer using nanoparticle coatings. International Journal of Heat and Mass Transfer 55 (2012) 3713-3719.

[164] G.S. Hwang, M. Kaviany. Surface wettability change during pool boiling of nanofluids and its effect on critical heat flux. International Journal of Heat and Mass Transfer 49 (2006) 844-849.

[165] J.H. Kim, K.N. Rainey, S.M. You, J.Y. Pak. Mechanism of nucleate boiling heat transfer enhancement from microporous surfaces in saturated FC-72. Journal of Heat Transfer 124 (2002) 500-506.

[166] P. Griffith, G.B. Wallis. The Role of Surface Conditions in Nucleate Boiling. Chemical engineering progress symposium series 56 (1960) 49-63.

[167] T. Chen, J.F. Klausner, S.V. Garimella, J.N. Chung. Subcooled boiling incipience on a highly smooth microheater. International Journal of Heat and Mass Transfer 49 (2006) 4399-4406.

[168] R. Rioboo, M. Marengo, S. Dall'Olio, M. Voué, J. De Coninck. An innovative method to control the incipient flow boiling through grafted surfaces with chemical patterns. Langmuir 25 (2009) 6005-6009.

[169] C. Choi, J.S. Shin, D.I. Yu, M.W. Kim. Flow boiling behaviors in hydrophilic and hydrophobic microchannels. Experimental Thermal and Fluid Science 35 (2011) 816-824.

[170] A.E. Bergles, W.M. Rohsenow. The determination of forced-convection surfaceboiling heat transfer. Journal of Heat Transfer 86 (1964) 365-370.

[171] Z. Yao, Y.W. Lu, S.G. Kandlikar. Effects of nanowire height on pool boiling performance of water on silicon chips. International Journal of Thermal Sciences 50 (2011) 2084-2090.

[172] P.J. Marto, W.M. Rohsenow. Effects of surface conditions on nucleate pool boiling of sodium. Journal of Heat Transfer 88 (1966) 196-204.

[173] H. Honda, J.J. Wei. Enhanced boiling heat transfer from electronic components by use of surface microstructures. Experimental Thermal and Fluid Science 28(2-3) (2004) 159-169.

[174] J. J. Wei, L. J. Guo, and H. Honda. Experimental study of boiling phenomena and heat transfer performances of FC-72 over micro-pin-finned silicon chips. Heat and Mass Transfer 41(8) (2005) 744-755.

[175] R.H. Yeh. Analysis of thermally optimized fin array in boiling liquids. International Journal of Heat and Mass Transfer 40 (1997) 1035-1044.

[176] G. Guglielmini, M. Misale, C. Schenone. Pool boiling heat transfer from square-shaped spines uniformly and non-uniformly spaced. In: Proc. 2nd Int. Symp. Two Phase Flow Modelling and Experimentation, Pisa, (1999) 145-152.

[177] G. Guglielmini, M. Misale, C. Schenone. Pool boiling from extended surfaces in saturated FC-72: Effect of geometry and orientation. In: Proc. 4th Int. Conf. Multiphase Flow—ICMF, New Orleans (2001).

[178] G.J. Klein, J.W. Westwater. Heat transfer from multiple spines to boiling liquids. American Institute of Chemical Engineers Journal 17 (1971) 1050-1056.

[179] Y. Hirono, R. Shimada, S. Kumagai, K. Kaino, T. Takeyama. Optimization of fin array in boiling heat transfer. Technical Report, Tohoku University, 50(1) (1985) 21-39.

[180] M.E. Poniewski, J.R. Thome. Nucleate Boiling on Micro-Structured Surfaces. Heat Transfer Research, Inc. (HTRI), U.S.A. (2008).

[181] J.Y. Lee, M.H. Kim, M. Kaviany, S.Y. Son. Bubble nucleation in microchannel flow boiling using single artificial cavity. International Journal of Heat and Mass Transfer 54 (2011) 5139-5148.

[182] L. Dong, X. Quan, P. Cheng. An analysis of surface-microstructures effects on heterogeneous nucleation in pool boiling. International Journal of Heat and Mass Transfer 55 (2012) 4376-4384.

[183] T.G. Theofanous, J.P. Tu, A.T. Dinh, T.N. Dinh. The boiling crisis phenomenon Part I: nucleation and nucleate boiling heat transfer. Experimental Thermal and Fluid Science 26 (2002) 775-792.

[184] C.H. Li, G.P. Peterson, Experimental study of enhanced nucleate boiling heat transfer on uniform and modulated porous structures, Front. Heat Mass Transfer 1 (2010) 13654.

[185] W. Yan, W. Lin-lin, L. Ming-yan. Antifouling and enhancing pool boiling by TiO2 coating surface in nanometer scale thickness. American Institute of Chemical Engineers 53(12) (2007) 3062-3076.

[186] T.J. Hendricks, S. Krishnana, C. Choib, C.H. Chang, B. Paul. Enhancement of poolboiling heat transfer using nanostructured surfaces on aluminum and copper. International Journal of Heat and Mass Transfer 53 (2010) 3357-3365.

[187] C.H. Li. Nucleate boiling heat transfer on sintered copper porous structure module cone surfaces. Journal of Thermophysics and Heat Transfer 25 (2011) 186-191.

[188] D.H. Min, G.S. Hwang, Y. Usta, O.N. Cora, M. Koc, M. Kaviany. 2-D and 3-D modulated porous coatings for enhanced pool boiling. International Journal of Heat and Mass Transfer 52 (2009) 2607-2613.

[189] G.S. Hwang, M. Kaviany. Critical heat flux in thin uniform particle coatings.International Journal of Heat and Mass Transfer 49 (2006) 844-849.

[190] J. Xu, X. Ji, W. Zhang, G. Liu. Pool boiling heat transfer of ultra-light copper foam with open cells. International Journal of Multiphase Flow 34 (2008) 1008-1022.

[191] E. Melendez, R. Reyes. The pool boiling heat transfer enhancement from experiments with binary mixtures and porous heating covers. Experimental Thermal and Fluid Science 30 (2006) 185-192.

[192] K.N. Rainey, S.M. You. Pool boiling heat transfer from plain and microporous, square pin-finned surfaces in saturated FC-72. Journal of Heat Transfer 122 (2000) 509-516.

[193] J.P. Connor, S.M. You. A painting technique to enhance pool boiling heat transfer in saturated FC-72. Journal of Heat Transfer 117 (1995) 387-393.

[194] J.Y. Chang, S.M. You. Boiling heat transfer phenomena from microporous and porous surfaces in saturated FC-72. International Journal of Heat and Mass Transfer 40 (1997) 4437-4447.

[195] M. Arik, A. Bar-Cohen, S.M. You. Enhancement of pool boiling critical heat flux in dielectric liquids by microporous coatings. International Journal of Heat and Mass Transfer 50 (2007) 997-1009.

[196] C.H. Li, T. Li, P. Hodgins, G.P. Peterson. Characteristics of pool boiling bubble dynamics in bead packed porous. Journal of Heat Transfer 133(3) (2010) 31004-31014.

[197] C.H. Li, G.P. Peterson. Geometric effects on critical heat flux on horizontal microporous coatings. Journal of Thermophysics and Heat Transfer 24 (2010) 449-455.

[198] J.P. McHale, S.V. Garimella, T.S. Fisher, G.A. Powell. Pool boiling performance comparison of smooth and sintered copper surfaces with and without carbon nanotubes. Nanoscale and Microscale Thermophysical Engineering 15 (2011) 133-150.

[199] S.B. Memory, D.C. Sugiyama, P.J. Marto. Nucleate pool boiling of R114 and R114-oil mixtures from smooth and enhanced surfaces—I. Single tubes. International Journal of Heat and Mass Transfer 38 (1995) 1347-1361.

[200] J.R. Thome. Enhanced Boiling Heat Transfer, Hemisphere, Washington, DC (1990).

[201] R.M. Manglik, A.E. Bergles. Enhanced heat and mass transfer in the new millennium: A review of the 2001 literature. Journal of Enhanced Heat Transfer 11 (2004) 87-118.

[202] P.S. O'Neill, C.F. Gottzman, J.W. Terbot. Novel heat exchanger increases cascade cycle efficiency for natural gas liquefaction. Cryogenic Engineering 17 (1972) 420-437.

[203] W. Nakayama, T. Daikoku, H. Kuwahara, T. Nakajima. Dynamic model of enhanced boiling heat transfer on porous surfaces, part I: Experimental investigation, part II: Analytical modeling. Journal of Heat Transfer 102 (1980) 445-456.

[204] S.I. Haider, R.L. Webb. A transient micro-convection model of nucleate pool boiling. International Journal of Heat and Mass Transfer 40 (1997) 3675-3688.

[205] M.H. Saidi, M. Ohadi, M. Souhar. Enhanced pool boiling of R123 refrigerant on two selected tubes. Applied Thermal Engineering 19 (1999) 885-895.

[206] L.H. Chien, R.L.Webb. A nucleate boiling model for structured enhanced surfaces. International Journal of Heat and Mass Transfer 41 (1998) 2183-2195.

[207] W.M. Rohsenow. A Method for Correlating Heat Transfer Data for Surface Boiling of Fluids. Journal of Heat Transfer 74 (1952) 969-976.

[208] J.M.S. Jabardo, E.F. Silva, S.F. Barros. Evaluation of the Rohsenow correltion throught experimental pool boiling of halocarbon refrigerants on Cylindrical surfaces. Journal of the Brazilian Society of Mechanical Sciences and Engine XXVI(2) (2004) 218-230.

[209] F.P. Incropera, D. DeWwitt, T.L. Bergman, A.S. Lavine. Fundamentals of heat and mass transfer. 6th Ed., John Wiley & Soons, NJ, USA (2007).

[210] A.B.D. Cassie, S. Baxter. Wettability of porous surfaces. Transactions of the Faraday Society 40 (1944) 546-551.

[211] N. Zuber. Hydrodynamic aspect of boiling heat transfer. Ph.D. Thesis, University of California, Los Angeles, CA (1959).

[212] Y.V. Polezhaev, S.A. Kovalev. Modeling heat transfer with boiling on porous structures. Applied Thermal Engineering 37 (1990) 617-620.

[213] T.G. Theofanous, T.N. Dinh. High heat flux boiling and burnout of microphysical phenomena: mounting evidence and opportunities. Multiphase Science and Technology 18(1) (2006) 1-26.

[214] H. Auracher, W. Marquardt. Heat transfer characteristics and mechanisms along entire boiling curves under steady-state and transient conditions. International Journal of Heat and Fluid Flow 25(2) (2004) 223-242.

[215] C. Gerardi, J. Buongiorno, L.W. Hu, T. McKrell. Study of bubble growth in water pool boiling through synchronized, infrared, thermometry and high-speed video. International Journal of Heat and Mass Transfer 53 (2010) 4185-4192.

[216] C.Y. Han, P. Griffith. The mechanism of heat transfer in nucleate boiling. Technical Report No 7673-19, Dep. Mech. Eng., M.I.T. (1962).

[217] D. Saeidi, A.A. Alemrajabi. Experimental investigation of pool boiling heat transfer and critical heat flux of nanostructured surfaces. International Journal of Heat and Mass Transfer 60 (2013) 440-449.

[218] I. Malavasi, I. Bernagozzi, C. Antonini, M. Marengo. Towards a standard protocol for assessing durability of superhydrophobic surfaces. Surface Innovations Journal 3(1) (2014) 49-60.

[219] C. Antonini, F. Villa, I. Bernagozzi, A. Amirfazli, M. Marengo. Drop rebound after impact: the role of the receding contact angle. Langmuir 29 (2013) 16045-16050.

[220] Z.J. Yu, J. Yang, F. Wan, Q. Ge, L.L. Yang, Z.L. Ding, D.Q. Yang, E. Sacherc, T.T. Isimjand. How to repel hot water from a superhydrophobic surface? Journal of Materials Chemistry A 2 (2014) 10639-10646.

[221] B.J. Jones, J.P. McHale, S. Garimella. The influence of surface roughness on nucleate pool boiling heat transfer. Journal of Heat Transfer 131(12) (2009) 121009.

Chapter 4

4 Wettability effect on interface dynamics

4.1 Introduction

The phenomenon concerning the behaviour and outcome of droplets impact can be linked to different applications and fields. The impact of drops onto dry solid surfaces is a phenomenon involved in many industrial applications, i.e. spray cooling, ink-jet printing, spray painting, fuel injection, raindrop erosion, etc.

Drop impact analysis can be also linked to fields concerning applications non directly connected to the engineering disciplines, i.e. aerosol droplets containing the pathogen and disease spread (influenza, ebola, tuberculosis, varicella pox), air conditioning mists (sometimes used to maintain the freshness of meat and vegetables in supermarkets, and fine mists for cooling people in hotter climates this is sometimes used in restaurants), external and internal skin and mucous membranes of the body (face, hand/foot, throat, nose, eye), sunspray, sunscreen and mosquito repellent products, pesticide crop spray (superspreading of defoliants or protectants on foliage), cosmetics and fake tan application, upholstery and industrial surface cleaning formulas, drug inhalers (salbutamol and cortico-steroidal and other metered dose inhalers for asthma, rhinitis). Depending on the kind of application, the outcome of droplet impact has to be different in order to obtain a specific result. For example, in the case of painting application, the purpose is to transfer the droplet from a surface to another, so a stick outcome on the first surface would be negative for the transfer on the second surface. On the other hand, in the case of agriculture application, one has to concern about to obtain a stick outcome and avoid the dispersion of the droplet in the ambient. Some problems arise due to the fact that leaves are hydro-repellent in order to prevent bacterial colonization. By adding some kind of specific polymers (or a mixture of them) to agricultural products, one can partially avoid this situation. Another problem is given by the fact that water can remove the agricultural product on the plants. To avoid this, it is possible to create a water insoluble gel by adding hydroxide group like borate ions and titanium dioxides. The components are a polymer, a binding agent and a solvent that will evaporate after the deposition. Because of the evaporation the concentration of the other two components will increase in the time and will allow the formation of a water insoluble gel. In different cases another outcome is wanted. For example, in the case of car windscreen one would like to have a rebound outcome. In this case one possible solution is to apply a hydro-repellant substance to the substrate [250]. Droplet impact analysis can also be used to study different kind of phenomenon, for example it is possible to model cancer invasion by considering an analogy between droplet and cancer cells diffusion on the tissue [2].

The investigation of the single drop impact [3,4] is still the first step toward the understanding and the control of the liquid–solid interactions in complex phenomena where the capillarity, the viscous forces and the impact momentum play a key role. For this reason, in the last 20 years, various researches and studies were dedicated to this argument, in order to perform a better understanding of all the parameters that can influence the droplet behavior. At first we have to distinguish the main factors linked to this kind of phenomenon, i.e. substrate characteristics (roughness, elasticity, porosity, wettability), liquid characteristics (Newtonian liquid, non Newtonian liquid, presence of impurity), droplets properties (impact velocity, droplet dimension, droplet shape).

In the last decade, notwithstanding the open issue of their durability [5], superhydrophobic surfaces (SHS) have attracted an increasing interest in both the academic and industrial sectors, due to their remarkable self-cleaning and anti-sticking properties [6-8] involving a wide range of potential applications: biomedical [9], microfluidic [10], corrosion resistance [255], drag reduction [12,13], anti-icing [256], contamination and oxidation protection [9,15], et.

When a drop impacts onto a SHS, a complete rebound usually occurs, followed by further rebounds, as if the drops were ‘‘dancing’’ on the surface.

At high speed, more complex phenomena appear, such as splash and break-up of the drop into many satellite drops, which also float on the surface. Transition from bouncing to sticky drops may occur, due to water penetration into the air cavities [16-18]: this event may reduce the water repellency performance of the substrate.

To better understand the existence of a general criterion to predict the drop impact outcome, and the key parameters governing the drop-surface interaction, the normal impact of both water and hexadecane drops on solid dry surfaces with different wettability was observed using a high-speed camera. The present study establishes a relationship between drop impact outcomes and surface wettability, taking into account different parameters for both the liquid drop (impact velocity, surface tension, viscosity) and the solid surface (morphology and roughness, chemistry, wettability).

Throughout the impact on such surfaces, the drop mobility is related to a sort of “dynamic superamphiphobicity”, defined as the critical wetting value under which an impacting drop with a given impact velocity does not wet the surface, i.e. a complete drop rebound is observed. In this case the impact velocity, the interfacial tension, the viscosity of the liquid, the chemical and physical properties of the surface determine the drop outcome as well as the spreading and the retraction dynamic.

4.2 Drop impact dynamics and impact outcomes

The dynamic behavior of an individual droplet impacting onto a solid surface includes several individual phenomena, such as deformation and rebound, and the physical description of those phenomena is usually characterized making use of dimensionless numbers taking into account the relative magnitude of the forces acting upon the surface of the droplet:

- Reynolds number, defined as the ratio of momentum forces to viscous forces;
- Webber number, thought as a measure of the relative importance of the fluid's inertia compared to its surface tension;
- Ohnesorge number, it relates the viscous forces to inertial and surface tension forces.

After the droplet hits the surface a thin liquid lamella starts to propagate along the surface. Depending on roughness of the surface, the liquid properties, drop diameter and impact velocity, the advancing lamella may be disturbed leading to fragmentation of the droplet in some cases, denoted as splash. The result of a drop impact brings to the formation and evolution of two different zones, i.e. lamella and rim. The last one bounds the spreading lamella and is characterized by viscosity and surface tension. The evolution of the drop is strictly linked to the evolution of the rim [19].

There are at least six distinct outcomes of a drop impact, not all of which are achievable for a given drop/target combination. The most common outcomes of droplets impact are [1,20] as follow (Figure 4.1).

- ***Rebound* (full or partial):** the droplet reach the surface and is subjected to deformation, reaching a maximal diameter. During this process the kinetic energy is converted in surface energy. The deformation is followed by contraction in which the droplet return to the previous shape. Rebound and partial rebound outcomes occur only when a receding phase is observed. Whether a receding phase occurs or not depends on the maximum diameter reached by the spreading droplet and the receding contact angle. For very energetic impacts this diameter is large, and the maximum diameter is much larger than would be expected given the static receding contact angle. In this case the drop begins to recede. The difference between the rebound and the partial rebound is found in the dynamic receding contact angle. For low value a partial rebound occurs; for high values a complete rebound occurs.
- ***Splash***: it might occurs for higher We, the kinetic energy is more stronger than viscous forces. One can distinguish *corona splash* (connected to the presence of a surrounding gas, a corona is formed during the spreading phase and eventually breaks up into droplets) and *prompt splash* (connected to roughness, droplets are ejected directly from the region between the surface and the liquid in the spreading phase of the lamella). The difference from corona and prompt splash is given by the fact that in the case of prompt splash is not possible to distinguish a lamella detached from the surface before secondary droplet are observed. The prompt splash is observed only with rough surfaces and is characterized by the generation of droplets directly at the contact line at the beginning of the spreading phase, when the lamella has a high radial velocity. The corona splash occurs when droplets are formed around the rim of a corona, remote from the solid surface. This occurs at a later stage of the impact process and it is also very characteristic of drop impacts on liquid films. Splash output can be analyzed by using the principle of energy conservation before and after impact, considering the energy dissipation due to the process.

$$E_k + E_p + E_s = E_{0k} + E_{0p} + E_{0s} + E_{0d}$$

Where E_k, E_p, E_s and E_d are the kinetic, potential surface and dissipated energy. The dissipated energy is difficult to determine, in fact it is not possible to find velocity distribution inside a droplet.

- **Rolling**: drop rolls reducing the contact area.
- **Deposition, stick**: the droplet during the entire process is only deformed and remains attached to the substrate and forms a film, without any breakup. The momentum is totally lost.
- **Break up/ Receding Break up**: The impact allow the formation of smaller droplets that remain attached to the surface during the receding phase of the impact.

There are several parameters that may influence the behavior of a droplet impact, for this reason it is extremely difficult to establish a single model capable to predict it. Comparing the results for different impingement condition, one can observes that an increase of the surface tension brings to an increase of the size of the droplet generated after the impact [21]. In the case of drop-wall interaction, as it happens in applications as spray cooling, turbines blades and icing, drop impact is influenced by different aspects like the characteristic of the liquid, the impact velocity and the type of substrate.

The dimensionless diameter of the spreading film is called spread factor and represents the contact diameter at time t, made dimensionless by dividing it for the initial drop diameter ($\xi(t) = D(t)/D_0$). The time evolution of the spread factor can be divided into four distinct phases: kinematic phase (initial impact and shock wave, formation of gas bubbles), spreading phase (the velocity decreases), relaxing phase (the process will bring to a certain outcome, depending on the surface characteristics), and wetting/equilibrium phase (final phase). In the first phase of impact and for high impact velocities, the liquid is compressed and a shock wave is formed and detaches after reaching a critical angle [259]. During this phase, the drop exhibits the shape of a cut sphere, derivable from purely geometric considerations of the impact. During this phase no spreading lamella is yet visible and the dimensionless contact diameter increases with approximately $t^{0.5}$. After this first phase, the spreading phase is characterized by the formation of a radially expanding film. Increasing the impact velocity or drop diameter leads to faster spreading, and increasing the surface tension or viscosity leads to slower expansion. The spreading phase is followed by a relaxation phase, which may have different outcomes, depending mainly on the magnitude of the receding contact angle. In a final phase, the lamella decelerates strongly and attains some constant diameter (equilibrium phase) or, for highly wettable surfaces, continues slowly to wet the surface (wetting phase). Furthermore, the maximum diameter achieved by the spreading film increases with the impact velocity [260]. Moreover, the ratio between the spreading velocity and the impact velocity diminishes as the impact velocity increases [261].

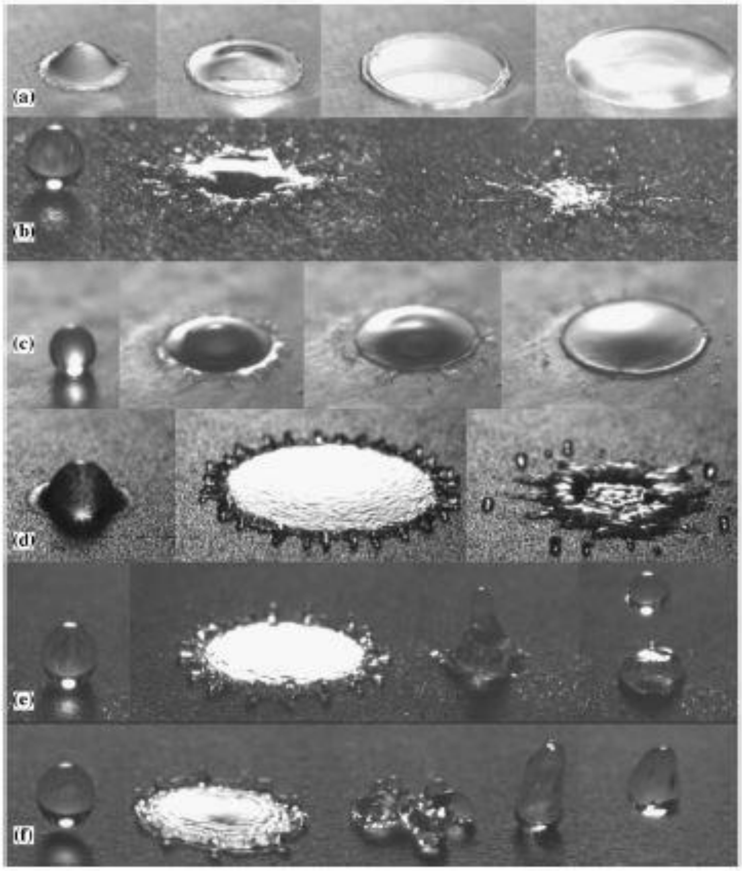

Figure 4.1: Outcomes of drop impact onto various substrates [25]. (a) deposition: isopropanol on rough glass (D_0=1.7 mm, U_0=1.8 m/s); (b) prompt splash: water drop on rough PE (D_0=2.4mm, U_0=3.1 m/s); (c) corona splash: isopropanol on light rough ceramic (D_0=1.7 mm, U_0=2.51 m/s); (d) receding breakup: water on porous stainless steel (D_0=2.4mm, U_0=3.44 m/s); (e) partial rebound: water on porous bronze (D_0=2.44 mm, U_0=2.44 m/s); (f) rebound: water on porous PTFE (D_0=2.44 mm, U_0=1.86 m/s).

Capillary forces are the motor behind the droplet retraction, which are, for the first regime countered by inertial forces. In the second regime the main force slowing the retraction is viscous. The drop retraction rate (the retraction speed divided by the maximum radius) does not depend on the impact velocity for strong enough impacts [26]. The dimensionless number that governs the retraction rate is the Ohnesorge number, $Oh = \eta/(\rho R\gamma,)^{1/2}$ with η the dynamic viscosity, ρ the liquid density, R the impacting drop radius, and γ the surface tension. The Ohnesorge number therefore compares the dissipative (viscous) forces to the non-dissipative (capillary and inertial) forces. The crossover between the two regimes is found to occur at a critical Ohnesorge number on the order of 0.05 [26]. Bartolo et al. [26] established the existence of two different regimes for the retraction rate: a viscous one and an inertial one. In the inertial regime, for high-velocity drop impact, liquid spreads out into a thin film of thickness h and radius R_{max}. The liquid subsequently dewets the surface rapidly, and forms a rim that collects the liquid that is initially stored in the film. The shape of the drop surface is therefore never in a steady state and consists of a liquid film formed during the spreading stage and a receding rim. At the opposite limit of very viscous liquids, the drops adopt pancake shapes upon impact. During the first stages of retraction, the pancake shape rapidly relaxes towards a roughly spherical cap, and remains like this during the retraction since the capillary number is small. In a viscous regime, D_{max}, which is the maximal diameter reached by the droplet after the impact, depends solely on the Reynolds number, whereas in a capillary regime only on the Weber number [4]. For very high value of We the crown splash becomes more evident. If the roughness increase it is more difficult to obtain a perfect rebound. The deposition may occur if θ_R>100° or for lower Weber number.

Bartolo et al. (2006) [265] observed that bouncing occurs only in a range of impact velocities ($V_{NB} < V_I < V_{BS}$), and the contact time does not depend on the impact velocity V_I. They identified three distinct regime as follow.

– $V_I > V_{BS}$: sticky droplets. In this regime, the contact line hardly retracts and the instantaneous contact angle reaches values as small as 40°. This strong pinning is a clear evidence that the microstructure has impaled the liquid surface. Observations with a microscope have systematically confirmed that the pillars are impregnated.

– $V_{NBB} < V_I < V_{BS}$: bouncing droplets. At intermediate velocities, the drop bounces on the surface, and several bouncing events can be observed. Finally, the drop remains on the surface adopting a large contact angle consistent with the Cassie-Baxter prediction. The initial kinetic energy of the drop is not sufficient to overcome the energy barrier hindering the impalement transition.

– $V_I < V_{NBB}$: non-bouncing droplets. A low speed threshold below which droplets do not bounce anymore exists. In this regime, the drop weakly expands after impact. Then, the drop undergoes damped oscillations to reach a quasi-spherical shape, corresponding again to a fakir non-wetting state. Though bouncing is not observed, water does not fill the microstructure.

In the literature [18,27,28], a pressure balance argument is used to explain the local meniscus transition. Any textured hydrophobic surface should resist penetration of liquid meniscus into it due to its unfavorable wettability condition. This liquid penetration resistance can be quantified through so called capillary pressure. This resistive pressure must be overcome by pressure generated by the droplet impact process in order to realize penetration of liquid meniscus into the surface texture. The capillary pressure P_C must be overcome for any meniscus penetration to occur. Because the dynamic pressure, expressed as $P_d = 0.5\rho_l V^2$ alone is not able to account for the local penetration effect, typically the concept of water hammer pressure is invoked to explain the preferential penetration of liquid meniscus near the point of droplet impact. The water hammer pressure comes from sudden deceleration of the liquid upon encountering a solid substrate. It is a manifestation of the liquid compressibility and it can be written as $P_{WH}= k\rho_l CV$, where k is the water hammer pressure coefficient, C is the velocity of sound in water, and V is the droplet impact velocity. Right after impact, the contact line of the droplet is moving faster than sonic speed, thus the impact shock remains pinned to the contact line. Eventually, the contact line slows down and the shock can overtake it. Deng et al. [266] suggested three different wetting states, i.e., the fakir state ($P_C>P_{WH}>P_D$), the Wenzel state ($P_{WH}>P_D>P_C$), and the partially impaled state ($P_{WH}>P_C>P_D$). The manner by which impalement transition occurs is considered to determine the P_C of the textured surfaces. The two possible mechanisms for the transition are the de-pinning mechanism [18,29,30] and sag mechanism [30,31] (Figure 4.2). In the fakir state, the liquid/air interface between pillars is pinned at the pillar tops with a certain contact angle CA that corresponds to the pressure inside the droplet. If the CA exceeds the local advancing CA (θ_A) due to the increased drop pressure, the pinning fails, and the contact line slides downwards to touch the basal surface. This phenomenon is the de-pinning mechanism. For shorter pillars, the sag in the liquid/air interface can touch the basal surface before CA reaches θ_A.

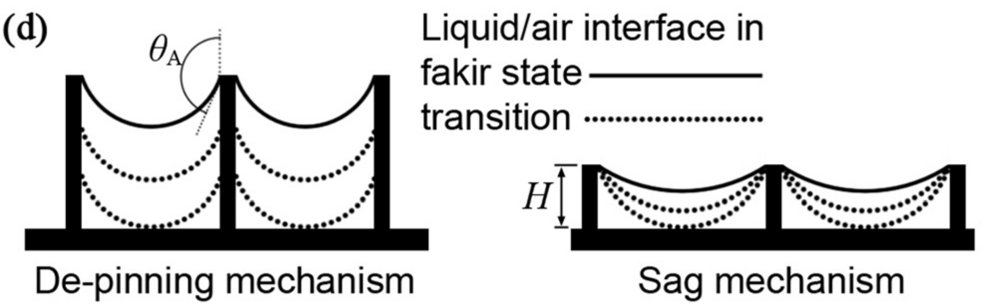

Figure 4.2: Schematic diagram (side view) of the impalement transition mechanisms [267].

Liu et al. (2014) [32] analyzed the pancake bouncing outcome on tapered surfaces and straight square posts surfaces. They demonstrated that pancake shape behavior is due to the rectification of capillary energy stored in the penetrated liquid into upward motion adequate to lift the drop; by designing the surfaces with tapered micro/nanotexture that can behave like harmonic spring the time scale becomes independent of impact velocity, fact that can bring to a rapid drop detachment. The difference between conventional rebound and pancake bouncing can be estimated by the ratio between the two diameters, before the rebound at the maximal spreading and after the rebound. If the ratio $d_{jump}/d_{max} > 0.8$ one obtain a pancake bouncing.

Romdhani et al. (2014) [33] observed the effect of the drop impact on virgin glass and coating film (uncoated and coated woven fabric). The drop was allow to fall from two different distances, 5 and 10cm. The transformation of the potential energy in surface energy is the main reason because of drop deformation occurs. In the first phase the drop partially takes of the surface whereas it is again in a phase of vertical elongation, than its deformation is influenced by the presence of air bubble. This deformation is followed by the variation of contact angle. During the second phase, the initial energy is dissipated or convert in surface energy, until the drop reaches its maximal diameter. The fabric structure influences the spreading rate and timing. Also porosity and permeability can influence the phenomenon, the adimensional diameter variation shows greater spreading ratio probably due to the porosity that enhanced penetration.

The splashing threshold, above which the drop splashes, is described as a combination of the Reynolds and Weber numbers. The critical value of the dimensionless number $K' = WeOh^{-0.4}$ ($Oh = We^{1/2}/Re$), below which deposition occurs and above which splash occurs, was shown to be a function of mean roughness amplitude [21,34]. Also, different materials with similar surface roughness yield different K'_{cr} [250].

Palacios et al. (2010) [35] conduced an experimental study to analyze the splash/deposition threshold, in order to understand the influence of Reynolds Number. Due to the fact that the shape of the drops was not totally spherical, in order to calculate the Reynolds and Weber number it was used an equivalent diameter:

$$D_{eq} = (D_v D_h^2)^{\frac{1}{3}}$$

where v and h are referred to vertical and horizontal direction. Analyzing the different results obtained for different parameters combination, they derived the following formula:

$$We_{crit} = 1.886\ Re^{0.637}\ + 1.068856\ Re^{-1.40}$$

where We_{crit} is the critical Weber at which splashing occurs. The results shows that high viscosity brings to splashing for Re above than 1000, whereas the opposite occurs for smaller Re.

Gipperich et al. (2010) [25] analyzed the splash threshold by varying surface properties like roughness and porosity, using two different kind of liquids: water and isopropanol. They observed the different output that can occur in the case of a structured substrate or an unstructured substrate by varying porous size and distribution. In order to define a splashing threshold, a specific Weber number is introduced:

$$We_s = \frac{\rho D U_S^2}{\sigma}$$

If $We < We_s$ no splash occurs, if $We > We_s$ lamella breaks up into a larger number of fragments. Comparing the two fluids they noticed that the prompt splash threshold for rough surfaces falls into the same range and concluded that viscosity plays a minor role for the two fluid. Talking about porous surface they obtained a different result. In fact, the distilled water splashing threshold is equal or higher for all investigated targets compared to the rough targets, so the splashing threshold in the case of porous surfaces is really different respect to the one in the case of rough surface. If We>200, the characteristics of the substrate and its wettability don't influence the phenomenon.

Roisman et al. (2015) [36] developed a model in order to describe the different regimes of splash thresholds by analyzing substrate characteristics: roughness and porosity. They concluded that it is not possible to find a boundary of the transition region between splash and deposition, in fact the surface morphology is irregular. It is possible to delimit a region, near the splashing boundary, in which the splash probability varying from one to zero and distinguish two different areas: lower splash thresholds below which the probability of prompt splash is negligibly small; upper deposition thresholds, above which the probability of deposition is negligibly small. It is found that the absolute length scales of the substrate roughness, like R_a or R_z, do not have any significant effect on the splash threshold. The lower splash threshold from the experimental data on the rough surfaces is given by

$$We_{splash} = 10.5 \left(\frac{R_{pk}}{R_{sm}}\right)^{-0.7}$$

where R_{pk} is the average height of protruding peaks above roughness core profile and R_{sm} the mean width of a profile element. Porosity doesn't influence too much impact behavior in the case of lower splash thresholds but influences the upper deposition limit because of the penetration of the drops inside the substrate, due to the presence of porous.

.

4.3 Drop impact outcome influencing parameters, the wettability role

For the various phases of the process, the different influencing parameters change in their importance, i.e. the dimensionless numbers to be taken into account vary throughout the spreading evolution. Until the moment the lamella's diameter reaches its maximum or the plateau phase, the spreading diameter is decelerating. The maximum spreading diameter has a meaning only relevant for the case of non wettable systems. The roughness has an immediate influence on the probability of prompt splash. Surface roughness influences the phenomenon of the impact: with rough surfaces, splashing occurs for less energetic impacts than polished surfaces [24,37].

Hartley and Brunskill (1958) [38] found that a necessary condition to obtain droplet rebound was the presence of 'micro-roughness' on the leaves of the plants that were investigated. Most empirical correlations describing the influence of roughness on the splash threshold have been established with a limited number of surface and liquid variations, and, in the authors' experience, it is not difficult to find contradictions when other materials are used. This is presumably due to wettability effects. The wettability has a profound influence on the final outcome of the impact, in particular the non wettable systems result in a receding phase and, under some conditions, a receding break-up. The influence of the wettability of the system (solid– liquid–gas) had been widely visualized already. They showed the importance of this parameter to obtain a rebound of the droplets after impact onto leaves. They included in the lamella energy balance, the spreading energy, which includes the usual wetting parameter, the static contact angle.

Podvysotskii and Shraiber (1993) [273] found that at high impact velocities the wettability has much less of an influence on the deposition rate than the roughness.

A map of impact behavior according to surface roughness and impact energy was built from experimental investigations on artificial superhydrophobic porous surfaces (Figure 4.3) [40].

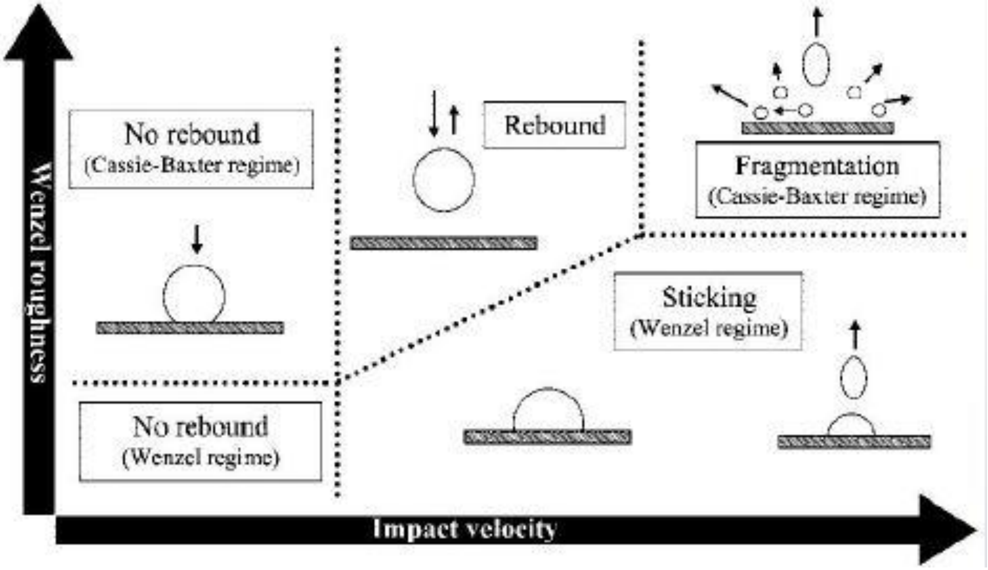

Figure 4.3: Possible impact outcomes of a drop hitting a superhydrophobic surface, depending on Wenzel roughness and drop impact velocity [40].

Tsai et al. (2009) [41] compared the dynamics of drops impact on superhydrophobic structure of control roughness and on CNF (carbon nanofiber).The CNF used for the experiment was produced using a CVD technique, from carbon containing gases using a metallic catalyst. They concluded that roughness can influence the transitional boundary of impact event.

Deng et al. (2013) [42] studied the dynamics of liquid drops impacting superamphiphobic coatings. Mixtures of ethanol–water and glycerin–water are chosen to investigate the influence of interfacial tension and viscosity on spreading and retraction dynamics. Drop spreading is dominated by inertia. At low impact velocity, the drops completely rebound. However, the contact time increases with impact velocity, whereas the restitution coefficient decreases. They suggest that the drop temporarily impales the superamphiphobic coating, although the drop completely rebound, and concluded that impalement is dominated by depinning rather than sagging. With increasing velocity, the drop partially pin, and an increasing amount of liquid remains on the coating. A time-resolved study of the retraction dynamics reveals two well-separated phases: a fast inertia-dominated phase followed by a slow decrease of the contact diameter of the drop. The crossover occurs when the diameter of the retracting drop matches the diameter of the drop before impact. The depth of impalement increases with impact velocity, where impalement is confined to the initial impact zone of the drop. If the drop partially pins on the coating, the depth of impalement exceeds a depth, preventing the whole drop from being removed during the retraction phase. Impalement hardly affects the spreading dynamics but alters the retraction dynamics and the mechanisms of energy dissipation. On a flat surface, the maximum retraction rate depends on viscosity and is independent of impact velocity. Contrary, on rough fractal-like surface, the maximum retraction rate depends on the impact velocity but is independent of viscosity and interfacial tension. The lower surface tension favors partial impalement, therefore ethanol drops pin at lower impact velocities on the surface compared to glycerin-rich drops.

Antonini et al. (2013) [277] analyzed the drop impact on horizontal surfaces and highlighted the role of the θ_R on the drop rebound. Accordingly, the rebound can be observed only on surfaces presenting θ_R greater than 100° with the rebound time decreasing as θ_R increases. However, they only refer to water as impacting liquid.

Lee et al. (2014) [44] focused their study on droplet impact on oil infused nanostructured surfaces in order to avoid Cassie-Wenzel transition (CWT). They analyzed five different situations comparing four substrates covered by a layer of oil with a normal SHP substrate and they found that retraction rate and velocity decrease as the oil viscosity increase.

Antonini et al. (2014) [45] performed an experimental study on water drops oblique impacts in order to analyse the droplet outcome in case of hydrophobic and superhydrophobic substrates, varying the substrate tilt angle. They observed six different outcomes reported in Figure 4.4. (a) Deposition, when the whole drop remains stuck close to the impact point. This regime corresponds to the so-called “spread” in Sikalo et al. [46]. (b) Rivulet, when the drop slides downhill while spreading, recoil does not occur. (c) Sliding, when the entire drop (thus, including both uphill and downhill contact point edge) moves downhill and, at the end of the recoil phase, the entire liquid mass (i.e., the main part plus possible tiny secondary droplets) remains attached to the surface. (d) Rolling, when the drop rolls downhill, typically preserving high contact angles and thus a reduced contact area. (e) Partial rebound, when a part of the drop pinches off from the surface, while the other remains stuck (and eventually flows downhill afterward). (f) Rebound (or complete rebound), when the entire drop detaches from the surface.

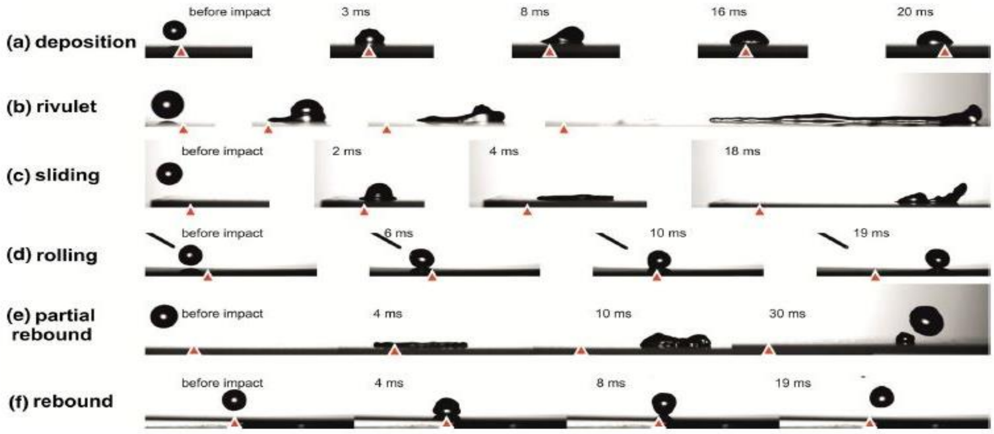

Figure 4.4: Outcomes of water drop impact onto various tilted surfaces observed by Antonini et al. [45]: (a) deposition on A1-Teflon (V = 0.1m/s, a = 45°); (b) rivulet on A1Teflon (V = 2.36m/s, a = 80°); (c) sliding on A1-Teflon (V = 2.36m/s, a = 60°); (d) rolling on SHS-1 (V = 0.1m/s, a = 60°); (e) partial rebound on A1-Teflon (V = 2.36m/s, a = 45°); (f) rebound on SHS-1 (V = 0.1m/s, a = 10°). The triangle in each image indicates the location of the impact point. a represents the surface tilt angle.

For drop impact on SHS, surface inclination facilitates drop shedding and allows reducing rebound time up to 30%; on hydrophobic surfaces, increasing surface inclination leads to a transition from drop rebound to partial rebound and sliding, and finally to slug (at high We and surface inclination). They reported also the obtained results in a regime map in the case of the hydrophobic and superhydrophobic substrate (Figure 4.5).

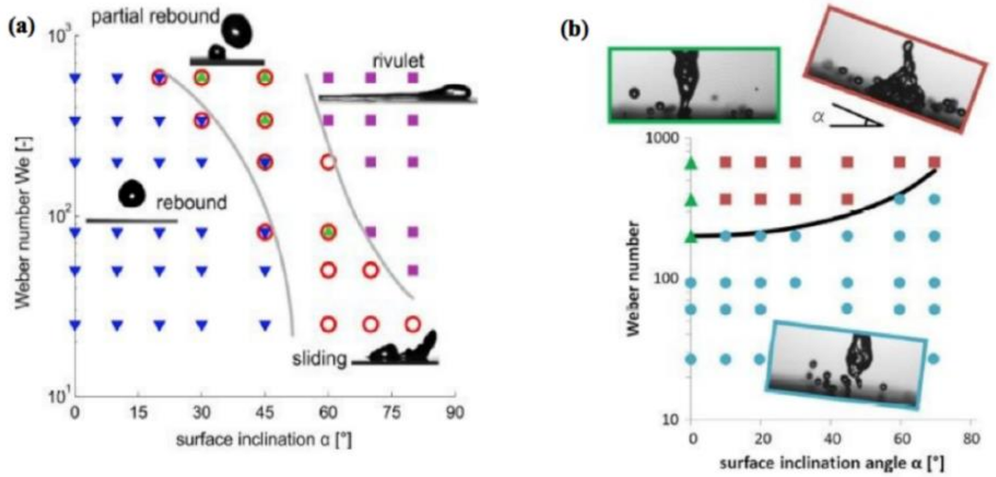

Figure 4.5: (a) Drop impact outcome map for the hydrophobic surface A1Teflon observed by Antonini et al. [45]. The outcomes observed on hydrophobic surfaces are rebound (blue triangles), partial rebound (green triangles), sliding (red open circles), and rivulets (violet squares). Gray lines are used to indicate the transition between different regimes. (b) Drop impact outcome map for the superhydrophobic surface SHS-2 observed by Antonini et al. [45]. The outcomes observed on SHS-2 surfaces are: rebound (blue circles), impalement on surface with partial rebound and sticky drop on the surface (green triangles), and impalement on surface with rebound and no sticky drop on the surface (red squares). For a = 0° (normal impact), complete rebound occurred up to We = 200; for higher We, impalement occurred and part of the drop remained attached to the substrate. The black line corresponds to drop impacts with normal Weber number $We_N = 200$.

Maitra et al. (2014) [281] show that the outcome of rebound or impalement on a textured surface is affected by air compression underneath the impacting drop and the time scale allowing this air to escape. Remarkably, drop impalement occurred at identical impact velocities, both at room and at very low temperatures (−30°C) and featured a ring like liquid meniscus penetration into the surface texture with an entrapped air bubble in the middle (Figure 4.6). At low temperatures, the drop contact time and receding dynamics of hierarchical surfaces were profoundly influenced by both an increase in the liquid viscosity due to cooling and a partial meniscus penetration into the texture. For hierarchical surfaces with the same solid fraction in their roughness, minimizing the gap between the asperities (both at micro- and nanoscales) yielded the largest resistance to millimetric drop impalement. The dynamics of meniscus penetration in the We range 10^2−10^3 or lower is controlled by compressibility of air between the impacting drop and the substrate [29,48] and not by the water hammer effect, [29,49] which originates from liquid compressibility.

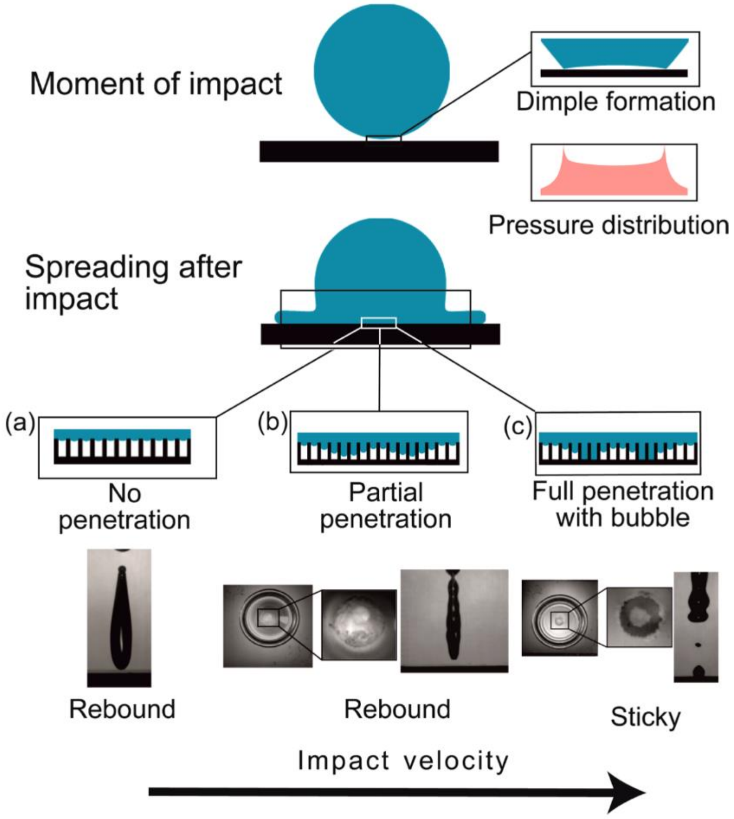

Figure 4.6: Mechanism of dimple formation and droplet deformation by draining air [281]. The dimple formation and associated rise in pressure near the impact point explain the meniscus penetration. On top the droplet impact, dimple formation and the resulting pressure profiles are shown schematically. At lower impact velocity (We) the meniscus penetrates partially, whereas beyond a critical velocity the ring like peak in the pressure profile engenders ring like penetration of the meniscus. Schematics in (a−c) show the difference impalement conditions. Below these schematics the high-speed snapshots show the corresponding experimental repercussions. The partial impalement

is visible as bright spots top view images shown (the zoom in images are used to highlight them). Above a critical impact velocity, the ring like penetration of the meniscus into the texture is obvious in the top view image under the schematic in (c), which clearly shows a dark impaled ring surrounding a centrally trapped air bubble.

Milionis et all. (2015) [50] compared the behaviour of droplet impact in the case of water and hemolymph. Insects are characterized by hemolymph, composed by water (90%) and other substances like inorganic ions, carbohydrates, nitrogenous wastes, lipids, proteins and enzymes, pigments and hormones. Because of the fact that hemolymph is principally composed by water, they first investigated the possibility of finding an analogy between water and hemolymph behaviour by using four different kinds of substrates: hydrophilic, superhydrophilic, hydrophobic and superhydrophobic. In the case of hydrophilic substrate, hemolymph spreads on the entire substrate while in the case of superhydrophobic substrate it is possible to obtain a Cassie-Bexter state that can turn in Wenzel state if the surface is not hydrophobic enough. This means that in the first case, hemolymph droplet will detach from the substrate after evaporation whereas in the second case they will remain on the surface. For this reason it is possible to obtain different result by changing the wettability of the substrate. The different behaviour respect water can be due to the fact that hemolymph is a coagulant substance and for this reason becomes solid faster than water.

In order to analyze droplet impact phenomenon, different approaches can be used, i.e. not only experimental (high speed camera), but also analytical and numerical (VOF methods). Brambilla et al. (2014) [51] analyzed oblique droplet impact onto liquid film by using a numerical simulation based on a multi-phase solver capable to capture the drop film interaction, the occurrence of secondary droplets and the formation of dry regions over the solid surface. The numerical simulation is based on spatial and temporal integration scheme, it is necessary to use a fine grid spacing considering the possibility of capturing second droplets formation and impact outcome. The outcome of the impact can be extremely different in the case of non-Newtonian liquid, that is one of the reason because of it is difficult to find a model capable to predict all the possible results. Malgarinos et al. (2014) [284] developed a VOF numerical model based on a different approach in which the dynamical contact angle is not consider like a boundary condition but as an input data. They assumed that the adhesion force acts like the contact line and inserted the effect of the force in Navier-Stokes momentum equation like an additional stress therm. Because of the dependency of contact angle on heat transfer, it can be consider a thermodynamic factor. In order to estimate his value it is important to consider the interaction between solid-liquid-gas that are gathered in the contact line.

4.4 Experiments

The wetting behavior of sandblasted aluminum foils before (TQ sample) and after the deposition of: i) organic-inorganic hybrid coatings (S samples), ii) infused hybrid coatings (SI samples), iii) grafting fatty acid treatments (LAU) and iv) grafting FAS (FAS) has been analyzed. A typical experimental apparatus for drop impact studies was used: a drop was generated at the tip of a hydrophobic needle, and then was accelerated by gravity and impacted onto a dry, solid surface.

Experimental conditions were the following: impact speed in the $0.05< V <4.2$ m/s range, drop diameter in the $1.5< D_0< 2.6$ mm range, Weber numbers in the $0.1< We < 635$ range, and Ohnesorge number in the $0.0023< Oh < 0.0186$ range. Images of drop impacts were recorded using a high-speed camera (PCO 1200-HS) with typical frame rates of 1568 and 2477 fps and a pixel resolution of 31µm/pixel. Tests were repeated at least 10 times for each condition to assess experimental reproducibility. Images were manually analyzed to identify the drop impact outcome and eventually to measure the time of the drop rebound when occurring.

4.4.1 Drop impact experimental setup

Apparatus structure

A typical experimental apparatus for drop impact studies was used: a drop was generated at the tip of a hydrophobic needle, and then was accelerated by gravity and impacted onto a dry, solid surface. A high-speed camera, which allows to record all the drop impact phases at high frame rate was used. In Figure 4.7 a representation of the experimental apparatus. The apparatus structure consists of: an impact tower, a target surface support, the drop generation system, the drop impact recording system.

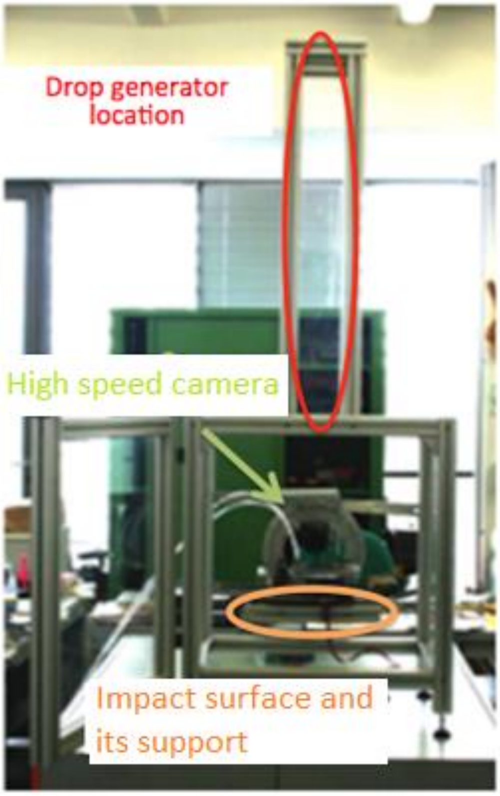

Figure 4.7: Drop impact experimental apparatus.

The liquid drop is generated at the needle tip and is positioned in the so called fall tower, built using ITEM® bars. When the drop detaches from the needle, it accelerates under gravity effect and impacts on the target surface. The height of the tower has therefore an influence on the maximum drop impact velocities. For a free falling drop, if drag is neglected, the impact velocity v is equal to $(2gh)^{1/2}$, where g is the gravity acceleration and h is the fall height. Since the drag forces act as decelerating forces, the real v is lower than the one found using the formula. Practically, if the height is excessive, even small perturbation to the drop path may cause the drop to fall far away from the expected impact point, the impact may be out of the camera focus plane or even outside the camera observation window. For this reason the maximum height was 1m, corresponding to an impact velocity of approximately 4m/s. Transparent Plexiglass® panels are mounted on the tower walls to avoid disturbance from the fluctuation of the surrounding air. The surface rests on a surface support, and it can move so that the same surface can be used for several impacts with no need for cleaning it after each impact. To study the drop impact dynamics, the drop impact is recorded using a high speed 10 bit CMOS camera, model pco.1200hs, whose frame rate is 486fps (frame per second) at full frame (1280X1024).

Drop generation

The drop generation system consists of a drop reservoir and a needle. Drops are produced using a precision needle, and detah by gravity: the drop is grown slowly, quasi-statically, and it detaches when gravity force overcomes needle adhesion force. Their initial diameter D_0 was systematically measured on the images ($1.5< D_0< 2.6$ mm range). From the high-speed sequence images, we follow the contact diameter D in time.

High speed camera and image analysis

A schematic of the high speed camera system is reported in Figure 4.8. A high speed camera pco.1200hs was used to record the drop impact dynamics.

As a drop falls towards the surface, it passes through a fork sensor (model GLS10, STM), which can detect the drop passage. The drop detection signal is used to activate the camera image acquisition. A dedicated hardware controls the delay time between sensor detection and the beginning of the image acquisition, and the duration of images acquisition. The camera parameters and the record window are controlled through a specific software, supplied with the camera, pco.camware. The frame rate and exposure time can be set according to the requirements. A Sigma macro lens (MACRO 105mm F2.8 EX DG) was used to obtain a good spatial resolution: pixel size 12μm, that is sufficient to observe the deformation of a millimetric drop. A 1KW backlight lamp is required to provide a sufficient illumination with such a reduced exposure time. Due to the high heat radiation produced by the lamp and to avoid undesired heating of the impact surface, an infrared filter was positioned between the lamp and the impact chamber. To provide a more regular illumination of the impact area, a second filter was used to diffuse lamp light.

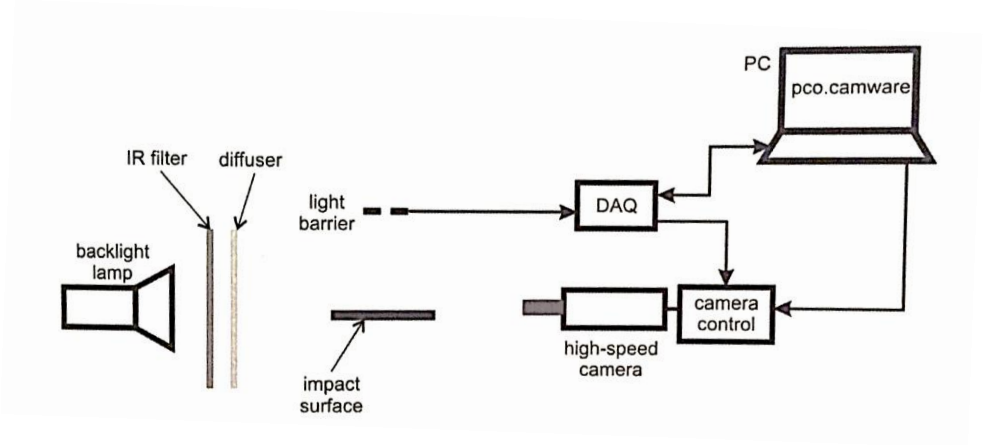

Figure 4.8: Schematic of the high speed camera system.

4.4.2 Materials and preparation of the test surfaces

Four kinds of SHS have been prepared: S, SI, LAU and FAS. TQ is the uncoated sandblasted aluminum surface taken as reference.

S and SI sample were provided by CNR-ISTEC Institute of Science and Technology for Ceramics.

S samples were prepared by dip-coating aluminum foils in an aqueous alumina sol with average particle size of about 30nm. After thermal treatments, also including boiling in deionized water, a nanostructured inorganic coating was obtained, which was then further functionalized by dipping in a commercial solution of fluoroalkylsilane in isopropanol (Dynasylan® SIVO CLEAR EC, Evonik), resulting into a hybrid organic-inorganic coating. More details on the fabrication of S samples are reported by Raimondo et al. in a previous work [285] .

SI samples were obtained by the same route, with an additional step of immersion into a fluorinated lubricant (Fluorinert™ FC-43, 3M™), allowing the formation of a continuous liquid film on the materials surface with the aim of changing the physical nature of the interface in contact with the liquid droplets (from the solid-liquid-air of S samples to the liquid-liquid-air of SI ones, according to the so-called SLIPS approach [286,287]).

LAU and FAS surfaces were prepared in our chemistry laboratory.

LAU samples are prepared using a two-step wet chemistry approach on aluminum samples: the samples are first etched, to enhance surface roughness, and then functionalized by grafting of fatty acid molecules to impart hydrophobicity. The use of fatty acid molecules is favorable due to their reduced cost compared to fluorinated molecules, and has been used in the past, e.g. by Sirong et al. [56] for hydrophobic functionalization of steel with myristic acid ($CH_3(CH_2)_{12}COOH$). Aluminum alloy plates (Al 1015), with a thickness of 0.6mm and of typical dimensions of 30x60mm, are purchased from Agnelli Metalli (Italy). Samples are initially etched with hydrochloric acid at 37% (Sigma-Aldrich) diluted 1:2 v/v with water. The samples are inserted in the acid solution, at room temperature, for two minutes and then rinsed with pure water and dried in air. Subsequently, the samples are immersed in an ethanol and lauric acid (LAU) ($CH_3(CH_2)_{10}COOH$) solution at room temperature, where LAU concentration is 12.7% by weight, with respect to ethanol concentration (i.e. 1l of ethanol and 100g of LAU). Sigma-Aldrich ethanol ≥ 98% and Sigma-Aldrich lauric acid ≥ 98% are used. The samples are inserted into the solution for two hours to allow lauric acid molecules grafting on the substrate, then rinsed with ethanol and dried in air. A schematic representation of the surfaces fabrication process is shown in Figure 4.9. At the end of the second step, the advancing contact angle of these surfaces is typically 157°±2°, the receding contact angle 155°±2° and the hysteresis about 2°±3°. The process is facile and can be used to functionalize several aluminum samples in sequence, using the same reaction batch. In addition, the process can be easily scaled up to large area treatments, which is an important factor in view of industrial applications; moreover it is a low cost process compared to other approaches, based on the use of fluorinated molecules.

FAS samples are prepared using a two-step wet chemistry approach on aluminum samples: the samples are first etched, to enhance surface roughness, and then functionalized in a water solution of perfluoroctyltriethoxysilane (FAS), optimizing the process reported in [289]. Aluminum alloy plates (Al 1015), with a thickness of 0.6mm and of typical dimensions of 30x60mm, are purchased from Agnelli Metalli (Italy). Samples are initially etched with hydrochloric acid at 37% (Sigma-Aldrich) diluted 1:2 v/v with water. The samples are inserted in the acid solution, at room temperature, for two minutes and then rinsed with pure water and dried in air. Subsequently, the samples are immersed in a pure water and FAS solution (1H,1H,2H,2H-Perfluorooctyltriethoxysilane (FAS), 97% purity, purchased from Alfa Aesar®) 0.1M at room temperature. Each sample remained immersed in the batch, inside the ultrasonic bath, for 30 min, and finally rinsed with pure water and dried in air. For optimal FAS activation, before sample immersion, the batch was heated up to 40°C and exposed to ultrasounds for 30 min. FAS is completely immiscible with water, and floats on the top of the batch. The ultrasounds hydrolysis process removes ethyl groups, leading to an improved solubility of FAS in water, making the silane group able to react with aluminum samples that are immersed in the solution. Moreover, ultrasounds provide effective agitation and simultaneous heating of the solution and also provide additional erosion of the material [58], enhancing the actual active surface of the metal able to react with hydrophobizing FAS.

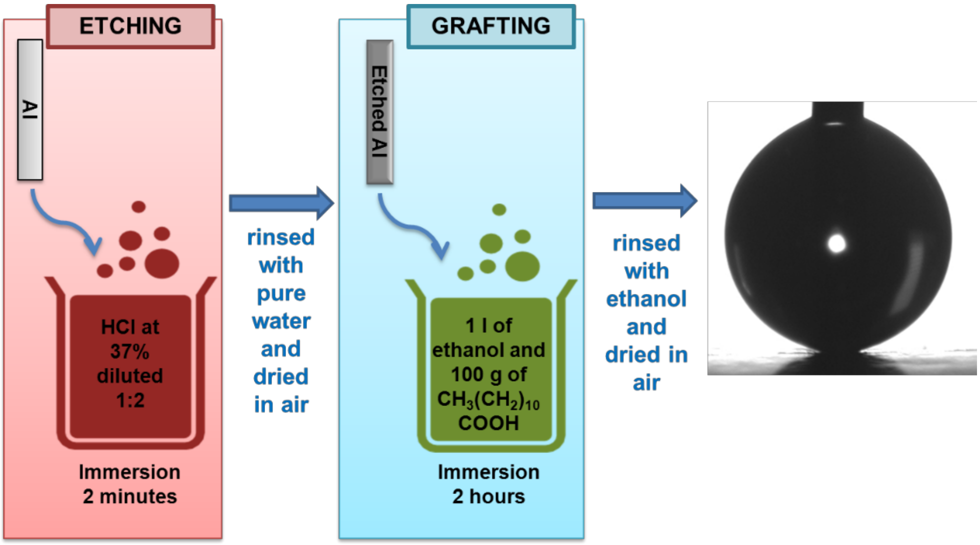

Figure 4.9: Schematic representation of the LAU surfaces fabrication process.

4.4.3 Surface characterization

The average values of θ_A, θ_R and CAH, with both water and hexadecane, are reported in Figure 4.10. The contact angle θ was computed from the slope of the circle at the surface [59,277] and it was calculated automatically from drop images by measuring the tangent of a circle fitting the drop profile at the contact point (OCA 15, Data Physics Instr.). Typical drop volume was about 2μl.

Surfaces have also been characterized in terms of topography and roughness. SEM images were obtained with a Tescan MIRA3 equipment, while roughness measurements were performed with a ContourGT-K (Bruker Nano GmbH) optical profilometer. SEM images of S and SI surfaces (Figure 4.11) show a flower-like nanostructure made up of crossed, 200nm long flakes and nanometric cavities. Previous results [285] proved that such structure is due to the γ-alumina coating obtained by deposition of Al_2O_3 nanoparticles and to the subsequent boiling in water. LAU and FAS samples display a terrace-like structure with sub-micrometric edges, as expected from the similar etching conditions held for both samples. On the sandblasted TQ surface taken as a reference, microabrasion by sand grains produced an irregular microstructure with asperities and cavities.

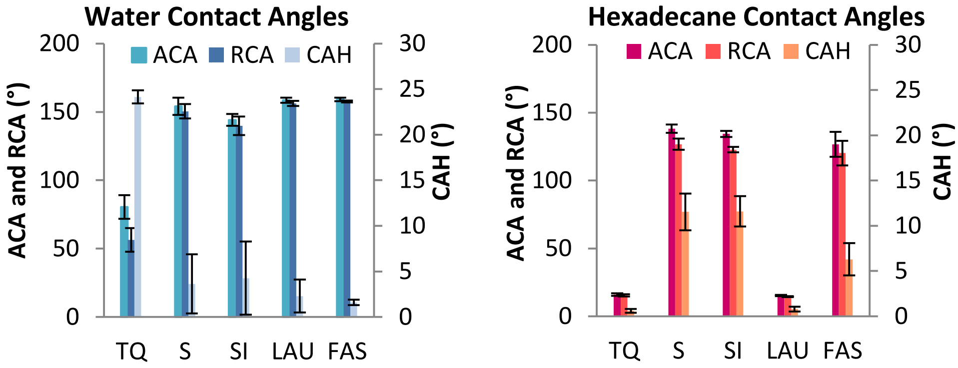

Figure 4.10: Average advancing contact angles (ACA), average receding contact angles (RCA) and average contact angle hysteresis (CAH) with water (left) and hexadecane (right).

Roughness data (S_a, S_q, S_v and S_z) are shown in
Figure 4.12. S_a defines the average of the absolute values of the profile heights Z (x,y) in the measured area, while S_q is the root mean squared of Z (x,y) in the measured area. S_v expresses the maximum value "valley" depth of the surface in the measured area and S_z expresses the sum of the maximum value of peak height and the maximum value of valley depth on the surface within the measured area. A 15x15µm^2 area was analyzed for every measure, and a minimum of three measurements were done on the same sample for repeatability reason.

The difference between coated (S, SI) and etched (LAU, FAS) samples can be remarked: the former have lower average roughness (S_a, S_q) but higher peaks (S_v, S_z). A comparison with the data obtained for a TQ surface led us to conclude that the hybrid nanostructured coating has a small influence on the micrometric roughness of S and SI, while the main contribution belongs to the microstructure provided by sandblasting. On LAU and FAS surfaces, etching provided a rougher structure, but with less pronounced asperities and cavities.

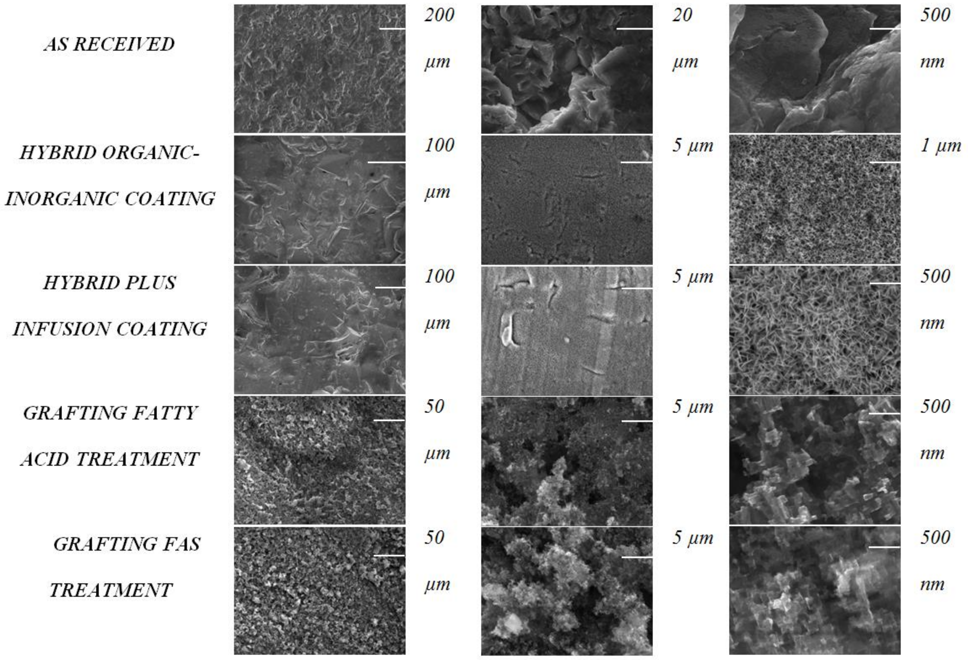

Figure 4.11: SEM images of the sample surfaces: as received sandblasted (TQ), hybrid organic-inorganic coating (S), hybrid plus infusion coating (SI), grafting fatty acid treatment (LAU) and grafting FAS treatment (FAS).

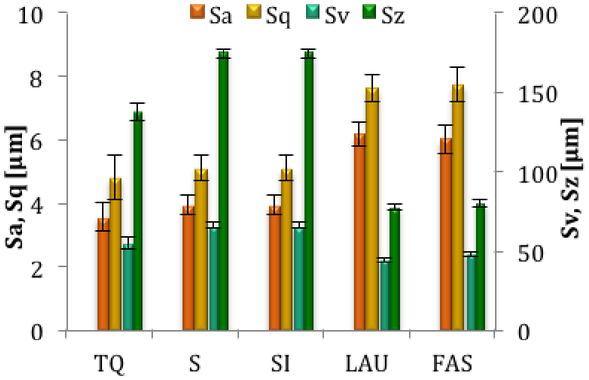

Figure 4.12: Surface roughness data obtained on TQ, S, SI, LAU and FAS samples. S_a and S_q values are referred to the left vertical axis, while S_v and S_z are referred to the right vertical axis.

4.4.4 Results and discussion

In Table 1 the summary of all the outcomes of the drop impact tests is reported. Five main regimes stand out: complete rebound, partial rebound, prompt splash, receding breakup, and deposition. All the functionalized surfaces are able to generate a complete or partial rebound of water drops, while TQ surface promotes drop deposition for We up to about 200 and receding break-up for higher Weber numbers. Remarkably surfaces S and SI are able to repel the water drops up to the maximum We value of 620. No splash is observed for the overall range of the We, confirming the previous literature results [60]. In the case of hexadecane, no rebound was observed for any of the surfaces, even if the contact angles and the hysteresis reached, respectively, very high and very low values (i.e. FAS surface). The prompt splash appears to be an important outcome for We > 200. FAS sample shows a peculiar behavior, since it produces a partial rebound with water even for moderate values of We, while with hexadecane it is able to allow the generation of a singular jet [293] for very low We, and allow the receding breakup behavior for the higher analyzed We.

Image sequences of water and hexadecane liquid drops normally impacting on the tested surfaces are shown in Figure 4.13 and in Figure 4.14, respectively. Interestingly, when a water drop impacts on TQ at We≈21, deposition occurs with the generation of a singular jet [293], as shown in Figure 4.15. The same behavior can be observed in the case of hexadecane drop impacting on FAS surface at We≈15.

	We *(WATER)*							We *(HEXADECANE)*						
Surface type	< 1.5	16 ÷35	40 ÷75	65 ÷100	150 ÷215	270 ÷360	500 ÷620	10 ÷20	30 ÷40	60 ÷75	85 ÷125	205 ÷275	325 ÷485	545 ÷635
TQ	D	D*	D	D	D	RB	RB	D	D	D	D	D	PS	PS
S	R	R	R	R	R	R	R	D	D	D	D	PS	PS	PS
SI	R	R	R	R	R	R	R	D	D	D	D	PS	PS	PS
LAU	R	R	R	R	R	R	PR	D	D	D	D	D	PS	PS
FAS	R	R	R	R	PR/R	PR	PR	D*	D	D**	D**	D**	RB	RB

Table 4.1: Summary of the outcomes of the drop impact tests. R = rebound, PR = partial rebound, PS = prompt splash, RB = receding breakup, D = deposition. *Secondary drop. ** Transition region.

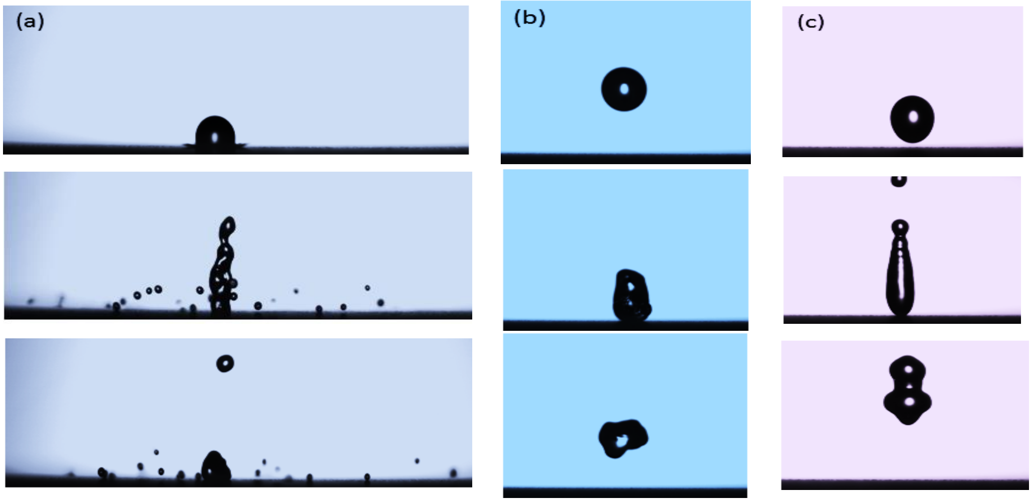

Figure 4.13: Image sequences of water drops (average diameter D_0 = 2.45mm) impacting on three functionalized surfaces: (a) partial rebound with fragmentation on FAS sample at We = 312 at t = 0, 14.6ms and 31.2ms after impact; (b) rebound on SI sample at We = 54 at t = 0, 17.8ms and 19.7ms after impact; (c) rebound on S sample at We = 21 at t = 0, 14.0ms and 21.6ms after impact.

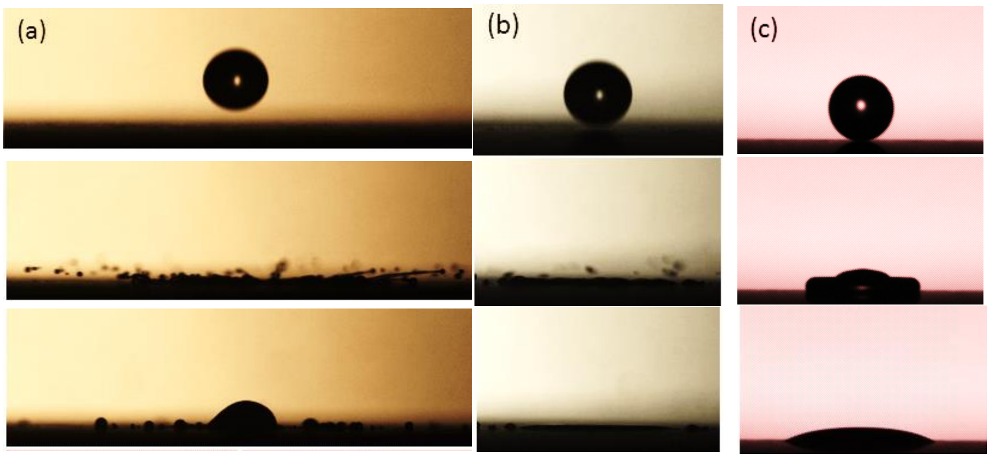

Figure 4.14: Image sequences of hexadecane drops (average diameter D_0 = 1.66mm) impacting on three functionalized surfaces displaying different behavior: (a) receding breakup on FAS sample at We = 560; (b) splash on SI

sample at We = 580; (c) deposition on LAU sample at We = 17. For every surface, images at t = 0, 2.0ms and 17.6ms after impact are reported.

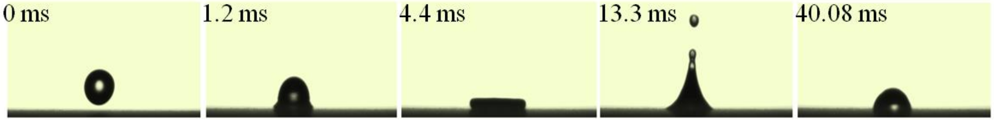

Figure 4.15: Image sequence of water drop (average diameter D_0 = 2.35mm) impacting on TQ surface at We = 21. A deposition occurs with the generation of a secondary drop.

The evolution of the spreading film diameter of water and hexadecane after the instant of impact is shown in Figure 4.16. The dimensionless diameter of the spreading film $\xi(t) = D(t)/D_0$ (i.e., the contact diameter at time t, made dimensionless by dividing it for the initial drop diameter) is shown in function of the time. Different outcomes were observed from deposition to rebound (occurring for t>0 when $\xi = 0$). In dynamic SHS cases, drops do not stick on the surface and the rebounds of the droplets can be observed. When the drop is detached from the surface, the contact diameter is zero, therefore the spread factor is zero. The time evolution of the spread factor suggests that the drop impact dynamics depends not only on the θ_R value, since, contrary to what is reported by Antonini et al. [277], even when θ_R reaches 120° indicating a very low wettability, complete drop rebound does not occur (see tests with hexadecane on FAS surfaces).

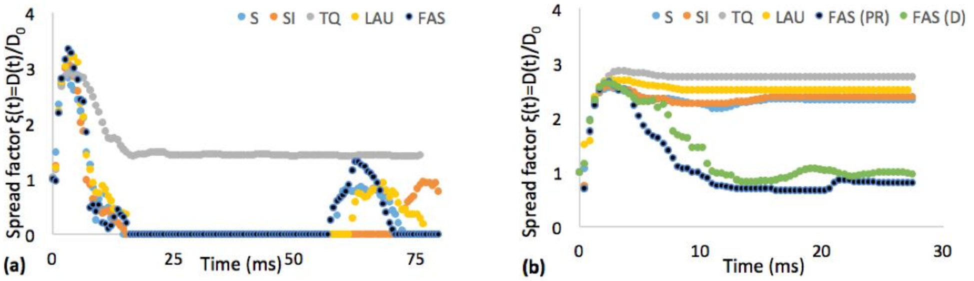

Figure 4.16: Spread factor time evolution, $\xi(t)=D(t)/D_0$, for the tested samples single runs).(a) Water test conditions: V = 1.6m/s, D_0 = 2.5mm, and We ≈ 90. (b) Hexadecane test conditions: V = 1.5m/s, D_0 = 1.7mm, and We ≈110.

According with [18,28,42], as previously reported, in the contact stage the initial impact of the droplet onto the surfaces generates a water hammer pressure P_{WH} due to the compression of liquid behind the shock wave envelope. At the spreading stage, the shock wave overtakes the outward moving contact line. At this stage, this high pressure is converted in the dynamic pressure P_D. For having a rebound as outcome of the drop impact is necessary that the liquid lamella is stretched enough to have sufficient energy at the end of the recoiling phase, thus promoting the drop detachment from the surface, i.e. it is necessary to have enough impact kinetic energy (the kinetic energy of the impinging droplet has to be larger than the surface energy dissipated during the retraction stage [16,17]). Moreover, for having a rebound as outcome of the drop impact, or the antiwetting pressure, equal to the capillary pressure P_C for a textured surface, is higher than the wetting pressure ($P_C>P_{WH}>P_D$), or $P_{WH}>P_C>P_D$. In the first case the structure resist wetting in both stages, in the second case the fluid penetrates only during the contact stage. Anyway, in both cases, if the impacting droplet has enough kinetic energy, the impalement process (called also Cassie-to-Wenzel transition, CWT) can occur and the drop does not rebound: in the first case it is called non-bouncing fakir (NB) state, in the second case it is called second non-bouncing droplet (2NB) state. In fact, the liquid meniscus can penetrate the surface topology for a given critical velocity $U_{c,p}$ (in the case of Wenzel - $P_{WH}>P_D>P_C$ - state the liquid penetrates in both contact and spreading stage for any impact velocity), while the rebound may happen for the given impact velocity range $U_{r,min}< U <U_{r,max}$. Therefore if $U < U_{c,p}$, the rebound will occur and the surface can be considered “dynamically amphiphobic”, while when $U > U_{c,p}$ the rebound will be limited by the impalement phenomenon, even if the surface is statically able to repel the liquid as indicated by the high values of θ_R and the very low CAH. Maitra et al. [281] reported as critical Weber number, the condition $P_c=P_{max}$, where P_C is the capillary pressure ($P_C \approx - \sigma\cos\theta_a/r_p$, where σ is the surface tension, θ_A is the advancing contact angle of the corresponding smooth surface and r_p is a length scale for the cavity radius) and $P_{max}=0.88R\mu_g^{-1}U^7 \rho_l^4 C_a^{1/3}/P_0 R^{1/2} St^{7/9}$ (R is the droplet radius, μ_g the air viscosity, C_a the Capillary number, P_0 the ambient pressure, St the Stokes number). The smaller the cavity size, the higher must be the impact velocity above which CWT will occur. This is in agreement with the different output observed at high We on surfaces with different morphologies: S and SI samples have nanoscale cavities on their surfaces, hence a U_p higher than the maximum U investigated in these experiments. Instead, LAU and FAS surfaces displayed only sub-micrometric voids which originated a smaller $U_{cr,imp}$ and the CWT can be observed at We > 500. Furthermore, the critical impact velocity for having a dynamical amphiphobic surface is increasing with the surface tension, i.e., for the same advancing contact angle, a low surface tension fluid will have a lower threshold for impalement. Hence for a given impact velocity, a drop tends to deposit rather than to rebound when a lower surface tension fluid is involved. Such impalement velocity can be so low that it is under the minimum energy threshold for rebound, meaning that a statically amphiphobic surface may never be a dynamically amphiphobic surface. To be noticed, the critical We for impalement on non-wetting surfaces still depends on surface tension. Considering that for a low surface tension liquid and for the same chemistry of the surface, θ_A is smaller and even lower than 90°, $We_{cr,imp}$ will therefore annihilate. This is in agreement with the fact that, for the same We, the low surface tension liquid causes the drop deposition while for water drops a rebound is observed, even if statically the surface is non-wettable by both liquids. It is important to stress that another important dimensionless number, the Ohnesorge number, i.e. the viscous dissipation, is having a part for the drop impact outcomes. For water, the Ohnesorge number is about 0.0024, while for hexadecane is 7 times higher ($Oh_{Hex} \approx 0.0177$). In fact the viscous dissipation may prevent the liquid to rise back from the partial penetration to a Cassie-Baxter regime, while this may still happen for low viscosity fluids like water.

In all the work published until now, the chemistry of the surface and of the liquid is never considered a crucial factor for determining the CWT. However, with this work it is shown, for the first time, that also the chemistry of the surface and the physico-chemical interactions with the liquid drops play an important role in determining $We_{cr,imp}$. For water drops with We = 150÷360, different outputs are observed for LAU and FAS surfaces notwithstanding their identical morphology. The former surface is rich in apolar C-H bonds (dipole moment μ = 0.3 D), which do not interact with polar water molecules (μ = 1.85 D), favoring total rebound. Meanwhile on FAS surfaces, polar C-F bonds (μ = 1.5 D) can have a dipolar interaction with water molecules, causing a partial retention of the drop on the surface and thus a partial rebound. At We < 150, rebound is observed on all functionalized surfaces due to the high surface tension of water, which causes recoil of the drop. Instead, for hexadecane drops, no influence of the surface chemistry can be yet recognized: the very low surface tension makes more probable to either splash at high We or deposit at low We, when the kinetic energy is insufficient to break the drop. Only a small influence of the surface structure is observed, causing the splash-deposition transition to shift to lower We values for the S and SI samples with a flower-like surface morphology.

4.5 Conclusions

After an overview on the drop impact phenomenon and on the state of the art of the wettability effect on interface dynamics, the normal impact of water and hexadecane liquid drops onto dry, rigid surfaces with different wettabilities has been studied experimentally using a high-speed camera.

The results highlighted that it is not possible to easily correlate contact angles (receding, advancing and hysteresis) and drop impact dynamics on different surfaces. The Cassie-to-Wenzel transition can be observed even on statically repellent surfaces. In order to explain the observed phenomena, physical and chemical characteristics of both the liquid drops and the surface have to be taken into account. Surface morphology is crucial in defining the critical velocity over which impalement occurs: the smaller the surface cavities, the higher $U_{cr,imp}$. Also, for the first time, it is proved that surface chemistry is relevant in determining $Uc_{r,imp}$, as dipolar interactions between surface functional groups and molecules in the liquid phase can lower $U_{cr,imp}$ and favor impalement. As far as the liquid properties are concerned, in agreement with Butt [42], with increasing viscosity and lower fluid surface tension the CWT shifts to smaller We. In the case of hexadecane drops, the CWT threshold is so low that no rebound has been observed, even if the contact angles are well above the expected critical values obtained from previous works focusing on water drops. Numerical simulations of drop impacts onto rigid and dry surfaces consider the advancing and receding contact angles and surface tension in order to represent the impact outcomes [284]. Therefore a direct and important consequence of this study is that all the numerical simulations of drop impact onto solid, dry surfaces will never be able to capture the final outcome of the impact for all the possible fluids, if the surface topology and chemistry is not properly considered. Furthermore the present results emphasize how an accurate design of the surface properties must be pursued in the future research towards dynamically amphiphobic surfaces.

Bibliography Chapter 4

[1] V. Bertola. Some application of controlled deposition on solid surfaces. Recent Patents on Mechanical Engineering 3 (2008) 167-174.

[2] C. Guiot, P.P. Delsanto, T.S. Deisboeck. Morphological instability and cancer invasion: a 'splashing water drop' analogy. Theoretical Biology and Medical Modelling 4 (2007) 1-6.

[3] R. Rioboo, M. Marengo, C. Tropea. Outcomes from a drop impact on solid surfaces. Atomization and Sprays 11 (2001) 155-165.

[4] M. Marengo, C. Antonini, I.V. Roisman, C. Tropea. Drop collisions with simple and complex surfaces. Current Opinion in Colloid & Interface Science 16 (2011) 292-302.

[5] I. Malavasi, I. Bernagozzi, C. Antonini, M. Marengo. Towards a standard protocol for assessing durability of superhydrophobic surfaces. Surface Innovations 3 (2014) 49-60.

[6] X.J. Feng, L. Jiang. Design and Creation of Superwetting/Antiwetting Surfaces. Advanced Materials 18 (2006) 3063-3078.

[7] D. Quéré. Non-sticking drops. Reports on Progress in Physics 68 (2005) 2495-2532.

[8] S.N.J. Shirtcliffe, G. McHale, S. Atherton, M.I. Newton. An introduction to superhydrophobicity. Advances in Colloid and Interface Science 161 (2010) 124-138.

[9] N. Saleema, D.K. Sarkar, R.W. Paynter, X.G. Chen. Superhydrophobic Aluminum Alloy Surfaces by a Novel One-Step Process. Applied Materials & Interfaces 2 (2010) 2500-2502.

[10] H. Zhanga, W. Lia, G. Fang. A new model for thermodynamic analysis on wetting behavior of superhydrophobic surfaces. Applied Surface Science 258 (2012) 2707-2716.

[11] F.Z. Zhang, L.L. Zhao, H.Y. Chen, S.L. Xu, D.G. Evans, X. Duan. Corrosion resistance of superhydrophobic layered double hydroxide films on aluminum. Angewandte Chemie International Edition 47 (2008) 2500-2503.

[12] C.Y. Lee, C.J. Kim. Underwater restoration and retention of gases on superhydrophobic surfaces for drag reduction. Physical Review Letters 106 (2011) 14502.

[13] F. Guo, X. Su, G. Hou, P. Li. Bioinspired fabrication of stable and robust superhydrophobic steel surface with hierarchical flowerlike structure. Colloids and Surfaces A 401 (2012) 61-67.

[14] C. Antonini, M. Innocenti, T. Horn, M. Marengo, A. Amirfazli. Understanding the effect of superhydrophobic coatings on energy reduction in anti-icing systems. Cold Regions Science and Technology 67 (2011) 58-67.

[15] J. Genzer, K. Efimenko. Recent developments in superhydrophobic surfaces and their relevance to marine fouling: a review. Biofouling 22 (2006) 339-360.

[16] M. Reyssat, A. Péin, F. Marty, Y. Chen, D. Quéré. Bouncing transitions on microtextured materials. Europhysics Letters 74(2) (2006) 306-312.

[17] D. Bartolo, F. Bouamrirene, E. Verneuil, A. Buguin, P. Silberzan, S. Moulinet. Bouncing or sticky droplets: Impalement transitions on superhydrophobic micropatterned surfaces. Europhysics Letters 74(2) (2006) 299-305.

[18] T. Deng, K.K. Varanasi, H. Hsu, N. Bhate, C. Keimel, J. Stein, M. Blohm. Nonwetting of impinging droplets on textured surfaces. Applied Physics Letters 94 (2009) 133109.

[19] A.J.B. Milne, A. Amirfazli. The Cassie equation: How it is mean to be used. Advances in Colloid and Interface Science 170(1-2) (2012) 48-55.

[20] A.V. Mahulkar, G.B. Marin, G.J. Heynderickx. Droplet-wall interaction upon impingement of heavy Hydrocarbon droplets on a heated wall. Chemical Engineering Science 130(7) (2015) 275-289.

[21] C. Mundo, M. Sommerfeld, C. Tropea. Droplet-wall collisions: experimental studies of the deformation and breakup process. International Journal of Multiphase Flow 21(2) (1995) 151-173.

[22] R. Rioboo, M. Marengo, C. Tropea. Time evolution of liquid drop impact onto solid, dry surfaces. Experiments in Fluids 33 (2002) 112–124.

[23] J. Fukai, Y. Shiiba, T. Yamamoto, O. Mitayake, D. Poulikakos, C.M. Megaridis, Z. Zhao. Wetting: effects on the spreading of a liquid droplet colliding with a flat surface: experiments and modeling. Physics of Fluids A 7 (1995) 236-247.

[24] Z. Levin, P.V. Hobbs. Splashing of water drops on solid and wetted surfaces: hydrodynamics and charge separation. Philosophical Transactions of the Royal Society A 269 (1971) 555-585.

[25] A. Gipperich, A.N. Lembach, I.V. Roisman, C. Tropea. On the splashing threshold of a single droplet impacting onto rough and porous surfaces. In: Proc. ILASS Europe, Brno, Czech Republic (2010).

[26] D. Bartolo, C. Josserand, D. Bonn. Retraction dynamics of aqueous drops upon impact on non-wetting surfaces. Journal of Fluid Mechanics 545 (2005) 329-338.

[27] D.H. Kwon, S.J. Lee. Impact and wetting behaviors of impinging microdroplets on superhydrophobic textured surfaces. Applied Physics Letters 100 (2012) 171601.

[28] S. Moulinet, D. Bartolo. Life and death of a fakir droplet: Impalement transitions on superhydrophobic surfaces. The European Physical Journal E 24 (2007) 251-260.

[29] H.M. Kwon, A.T. Paxon, K.K. Varanasi, N.A. Patankar. Rapid Deceleration-Driven Wetting Transition during Pendant Drop Deposition on Superhydrophobic Surfaces. Physical Review Letters 106 (2011) 036102.

[30] N.A. Patankar. Consolidation of Hydrophobic Transition Criteria by Using an Approximate Energy Minimization Approach. Langmuir 26 (2010) 8941-8945.

[31] Y.C. Jung, B. Bhushan. Dynamic Effects of Bouncing Water Droplets on Superhydrophobic Surfaces. Langmuir 24 (2008) 6262-6269.

[32] Y. Liu, L. Moevius, X. Xu, T. Qian, J.M. Yeomans , Z. Wang. Pancake bouncing on superhydrophobic surfaces. Nature Physics 10 (2014) 515-519.

[33] Z. Romdhani, A. Baffoun, M. Hamdaoui, S. Roudesli. Drop Impact on textile material: effect of fabric properties. Autex Research Journal 14(3) (2014) 145-151.

[34] G.E. Cossali, A. Coghe, M. Marengo. The impact of a single drop on a wetted solid surface. Experiments in Fluids 22 (1997) 463-472.

[35] J. Palacios, P. Gómez, C. Zanzi, J. López , J. Hernández. Experimental study on the splash/deposition limit in drop impact onto solid surfaces.

LASS – Europe 2010, 23rd Annual Conference on Liquid Atomization and Spray Systems, Brno, Czech Republic (2010).

[36] I.V. Roisman, A. Lembach, C. Tropea. Drop splashing induced by target roughness and porosity: The size plays no role. Advances in Colloid and interface Science 222 (2015) 615-621.

[37] O. Engel. A water drop collision with solid surfaces. Journal of research of the National Bureau of Standards 54 (1955) 281-298.

[38] G.S. Hartley, R.T. Brunskill. Reflection of water drop from surfaces. In: Surface phenomena in chemistry and biology. Pergamon, Oxford (1958) 214–223.

[39] A.M. Podvysotskii, A.A. Shraiber. Experimental investigation of mass and momentum transfer in drop-wall interaction. Izvestiya: Mathematics 2 (1993) 203-208.

[40] R. Rioboo, M. Voué, A. Vaillant, J. De Coninck. Drop impact on porous superhydrophobic polymer surfaces. Langmuir 24(24) (2008) 14074-14077.

[41] P. Tsai, S. Pacheco, C. Pirat, L. Lefferts, D. Lohse. Drop impact upon micro and nanostructured superhydrophobic surface. Langmuir 25(20) (2009) 12293-12298.

[42] X. Deng, F. Schellenberger, P. Papadopoulos, D. Vollmer, H.J. Butt. Liquid Drops Impacting Superamphiphobic Coatings. Langmuir 29 (2013) 7847-7856.

[43] C. Antonini, F. Villa, I. Bernagozzi, A. Amirfazli, M. Marengo. Drop Rebound after Impact: The Role of the Receding Contact Angle. Langmuir 29 (2013) 16045-16050.

[44] C. Lee, H. Kim, Y. Nam. Drop Impact Dynamics on Oil-Infused Nanostructured Surfaces. Langmuir 30(28) (2014) 8400-8407.

[45] C. Antonini, F. Villa, M. Marengo. Oblique impacts of water drops onto hydrophobic and superhydrophobic surfaces: outcomes, timing, and rebound maps. Experiments in Fluids 55 (2014) 1713.

[46] S. Sikalo, C. Tropea, E.N. Ganic. Impact of droplets onto inclined surfaces. Journal of Colloid and Interface Science 286(2) (2005) 661-669.

[47] T. Maitra, M.K. Tiwari, C. Antonini, P. Schoch, S. Jung, P. Eberle, D. Poulikakos. On the Nanoengineering of Superhydrophobic and Impalement Resistant Surface Textures below the Freezing Temperature. Nano Letters 14 (2014) 172-182.

[48] A. Alizadeh, V. Bahadur, S. Zhong, W. Shang, R. Li, J. Ruud, M. Yamada, L.H. Ge, A. Dhinojwala, M. Sohal. Temperature dependent droplet impact dynamics on flat and textured surfaces. Applied Physics Letters 100 (2012) 111601.

[49] S. Dash, M.T. Alt, S.V. Garimella. Hybrid Surface Design for Robust Superhydrophobicity. Langmuir 28(25) (2012) 9606-9615.

[50] A. Milionis, K.G. Krishnan, E. Loth. Hemolymph drop impact outcomes on surfaces with varying wettability. Applied Surface Science 345 (2015) 36-43.

[51] P. Brambilla, A. Guardone. Assessment of dynamic adaptive grids in Volume-Of-Fluid simula. Journal of Computational and Applied Mathematics 281 (2015) 277-283.

[52] I. Malgarinos, N. Nikolopoulos, M. Marengo, C. Antonini, M. Gavaises. VOF simulations of the contact angle dynamic during the drop spreading: standard models and a novel wetting force model. Advances in Colloid and Interface Science 212 (2014) 1-20.

[53] M. Raimondo, M. Blosi, A. Caldarelli, G. Guarini, F. Veronesi. Wetting behavior and remarkable durability of amphiphobic aluminum. Chemical Engineering Journal 258 (2014) 101-109.

[54] S. Yang, R. Qiu, H. Song, P. Wang, Z. Shi, Y. Wang. Slippery liquid-infused porous surface based on perfluorinatedlubricant/iron tetradecanoate: Preparation and corrosion protectionapplication. Applied Surface Science 328 (2015) 491-500.

[55] T.V.J. Charpentier, A. Neville, S. Baudin, M.J. Smith, M. Euvrard, A. Bell, C. Wang, R. Barker. Liquid infused porous surfaces for mineral fouling mitigation. Journal of Colloid and Interface Science 444 (2015) 81-86.

[56] Y. Sirong, W. Xiaolong, W. Wei, Y. Qiang, X. Jun, X. Wei. A new method for preparing bionic multi scale superhydrophobic functional surface on X70 pipeline steel. Applied Surface Science 271 (2013) 149-155.

[57] I. Bernagozzi, C. Antonini, F. Villa, M. Marengo. Fabricating superhydrophobic aluminum: an optimized one-step wet synthesis using fluoroalkyl silane. Colloids and Surfaces A 441 (2014) 919-924.

[58] E.V. Anslyn, D.A. Dougherty. Modern Physical Organic Chemistry. University Science Books, Herndon, VA, USA (2005).

[59] C. Antonini, A. Amirfazli, M. Marengo. Drop impact and wettability: from hydrophilic to superhydrophobic surfaces. Physics of Fluids 24 (2012) 102104.

[60] F. Villa, C. Antonini, I.V. Roisman, M. Marengo. Experimental Analysis of High Weber Number Drop Impact onto Super-Hydrophobic and Hydrophobic Surfaces. In: Proc. of the 15th International Heat Transfer Conference, Kyoto (2014).

[61] D. Bartolo, C. Josserand, D. Bonn. Singular Jets and Bubbles in Drop Impact. Physical Review Letters 96 (2006) 124501.

Chapter 5

5 Conclusions

Two parallel paths were followed during the research program. On one hand, basic research was performed to evaluate the wettability influence on pool boiling heat transfer, with particular focus in understanding the effect of the surface wettability alone. On the other hand, basic research was performed to evaluate how the drop mobility is related to a sort of “dynamic superamphiphobicity”.

A considerable part of the work has been devoted to the literature review on the role of wettability on pool boiling heat transfer. Numerous theoretical and experimental studies have focused on the enhancement of pool boiling heat transfer, using strategies that alter the liquid and/or the surface properties. In this context, nanofluids and surface micro-and-nano coatings have shown great potential in improving the heat transfer coefficients and enhancing the Critical Heat Flux, although much research is still required to optimize these strategies. Such optimization involves a deeper understanding on how these strategies act on the pool boiling phenomena, so that significant fundamental research is of major importance. Additionally, there is still room for more specific studies related to the composition (chemistry) and morphology of the coatings. Similar exercise is required to quantify the effect of the chemical composition and concentration of the particles added in nanofluids. Careful analysis of the various strategies to enhance pool boiling heat transfer leads to the conclusion that all these strategies mainly act on modifying the boundary conditions at the liquid-solid-vapour interfaces, by altering the wettability and/or surface topography. These two parameters are strongly related, so it is very difficult to distinguish the effect of the surface wettability alone on most of the experimental work reported in the literature. However, it is important to isolate these effects, as much as possible, namely by separating the effect of wettability related to the chemistry form that of surface morphology. Misinterpretation of the results due to unclear boundary conditions will be passed to most of the existing correlations and models, since they have a strong empirical nature. Hence, only a systematic approach, which allows quantifying the effect of the various influencing parameters, may overtake the empirical nature of the models to describe such a complex phenomena as pool boiling heat transfer. In this context, many questions still remain open in the theoretical description of the wettability role on bubble formation and on the heat transfer fundamentals.

Wettability has a vital role, which starts at the nucleation fundamentals: at low heat fluxes, higher contact angles (hydrophobic/superhydrophobic conditions) and lower hysteresis promote the activation of the nucleation sites and the stable bubble detachment, thus triggering the nucleate boiling to start at lower superheat. The opposite trend is observed for hydrophilic conditions. This will affect bubble detachment and the interaction mechanisms: the hydrophobic conditions favor the regular departure of larger bubbles, which are more likely to coalesce. This is particularly relevant as the heat flux increases and one enters in the regime of slugs and columns, since large bubbles will actually be less beneficial, leading to a fast formation of large vapor blankets, thus decreasing the heat transfer coefficient and promoting the establishment of the Critical Heat Flux condition. Hence “optimal” wetting properties also depend on the part of the boiling curve that is covered on the working conditions. Despite it alters surface wettability, changing surface topography mainly works, according to nucleation fundamentals, as a way to increase improve capillary pumping, increase liquid solid surface area and increase the number of nucleation sites. In particular, altering surface topography will mainly act on the nucleation sites density and consequently on interaction mechanisms such as bubble coalescence, which, in turn, should improve the heat transfer coefficients, but may promote the Critical Heat Flux condition to occur at lower degrees of superheat. On the basis of the reviewed literature and considering the importance in understanding the effect of the surface wettability alone on pool boiling heat transfer mechanisms, pool boiling experiments were carried out with degassed water on stainless steel substrates with different surface topography and wettability. Boiling curves have been measured together with visual high-speed observations of the boiling process. The onset temperature of nucleate boiling (ONB) has been measured and the influence of surface roughness and wettability has been quantified for different surfaces, with the aim to better understand the effect of superhydrophobicity on pool boiling. The original finding is that the boiling curve shape is rather different between hydrophilic and superhydrophobic case, keeping the same surface roughness. Superhydrophobic surfaces show a peculiar behavior similar to an early “quasi-Leidenfrost” regime for low superheat. The ONB appears after less than 5K of superheat on superhydrophobic surfaces, while, for the hydrophilic cases the ONB appears at more than 7K of superheat, which is a standard value using water on steel with a mean surface roughness above 2μm. Bubble nucleation on SHS builds up a large and stable vapour film with a very long departure time of the order of one minute. Only when the superheat is about 15/20K the departure time starts decreasing and it get down to the more standard value of one second. Regardless of the surface roughness and topology, the boiling curves obtained with the superhydrophobic surfaces having different roughness are very similar. This means that the wettability has a predominant effect with respect to the roughness, when the contact angle exceeds the typical value for superhydrophobic surfaces (receding contact angle $\theta_{rec} > 135°$).

The other part of the work deal with the wettability effect on interface dynamics. The normal impact of water and hexadecane liquid drops onto dry, rigid surfaces with different wettabilities has been studied experimentally using a high-speed camera. The results highlighted that it is not possible to easily correlate contact angles (receding, advancing and hysteresis) and drop impact dynamics on different surfaces. The Cassie-to-Wenzel transition can be observed even on statically repellent surfaces. In order to explain the observed phenomena, physical and chemical characteristics of both the liquid drops and the surface have to be taken into account. Surface morphology is crucial in defining the critical velocity over which impalement occurs: the smaller the surface cavities, the higher $U_{cr,imp}$. Also surface chemistry is relevant, as dipolar interactions between surface functional groups and molecules in the liquid phase can lower $U_{cr,imp}$ and favor impalement. As far as the liquid properties are concerned, with increasing viscosity and lower fluid surface tension the Cassie-to-Wenzel transition shifts to smaller Weber numbers. In the case of hexadecane drops, the Cassie-to-Wenzel transition threshold is so low that no rebound has been observed, even if the contact angles are well above the expected critical values obtained from previous works focusing on water drops. Generally, numerical simulations of drop impacts onto rigid and dry surfaces consider the advancing and receding contact angles and surface tension in order to represent the impact outcomes. Therefore a direct and important consequence of this study is that all the numerical simulations of drop impact onto solid, dry surfaces will never be able to capture the final outcome of the impact for all the possible fluids, if the surface topology and chemistry is not properly considered.

The combination of results from the two research paths emphasize how an accurate design of the surface properties must be pursued in the future research in function of the purpose to which the surface is intended. In particular, high hydrophilicity is recommended for applications deputed to heat source to promote the evaporation, and high hydrophobicity for applications that need the regular departure of larger bubbles, which are more likely to coalesce, thus decreasing the heat transfer coefficient and promoting the establishment of the Critical Heat Flux condition. Moreover, it is not possible to easily correlate the surface wettability with the drop impact dynamics and outcome; also surface chemistry play a relevant role.

The fact that superhydrophobicity and amphiphobicity have many potential applications opens new technological issues, the major of which to be tackled is the coating durability. Furthermore, the present results emphasize how an accurate design of the surface properties must be pursued in the future research towards dynamically amphiphobic surfaces. Further test should be performed to better understand the correlation existing between chemistry and impact behavior, in order to consider all the parameters necessary to run a numerical simulations of drop impact onto solid, dry surfaces able to capture the final outcome of the impact for all the possible fluids.

List of Publications

1. **I. Malavasi**, I. Bernagozzi, C. Antonini, M. Marengo, "How to choose among different kinds of superhydrophobic surfaces? Innovative test protocol on ageing of superhydrophobic surfaces". Workshop “Smart and Green Interfaces 2013”, COST Action MP1106, 21-22 March 2013, Prague, Czech Republic.

2. **I. Malavasi**, E. Teodori, M. Marengo, A. S. Moita, A.L.N Moreira, "Pool boiling over enhanced surfaces over a wide range of wettability conditions". 8th World Conference on Experimental Heat Transfer, Fluid Mechanics, and Thermodynamics, 16-20 June 2013, Lisbon, Portugal.

3. C. Antonini, D. Mangini, I. Bernagozzi, **I. Malavasi**, A. Amirfazli, M. Marengo, "IR investigation of ice formation mechanisms from hydrophilic to superhydrophobic surfaces". 8th World Conference on Experimental Heat Transfer, Fluid Mechanics, and Thermodynamics, 16-20 June 2013, Lisbon, Portugal.

4. **I. Malavasi**, I. Bernagozzi, C. Antonini, M. Marengo, "Why superhydrophobic surfaces are smart? A method to prepare a type of SHS and how to test them”. Smart & Functional Coatings Conference, 26-27 September 2013, Torino, Italy.

5. **I. Malavasi**, I. Bernagozzi, C. Antonini, M. Marengo, "Why superhydrophobic surfaces are smart? A method to prepare a type of SHS and how to test them". Workshop "Smart and Green Interfaces: multiphase flows with/without phase change", COST Action MP1106, 3-4 October 2013, Saragossa, Spain.

6. **I. Malavasi**, I. Bernagozzi, C. Antonini, M. Marengo,"Assessing durability of superhydrophobic surfaces". Surface Innovations Journal 3 (1) (2014), pp. 49-60.

7. **I. Malavasi**, B. Bourdon, P. Di Marco, J. de Coninck, M. Marengo,"Appearance of a low superheat quasi- Leidenfrost regime for boiling on superhydrophobic surfaces". International Communications in Heat and Mass Transfer 63 (2015), pp. 1-7.

8. **I. Malavasi**, B. Bourdon, P. Di Marco, J. de Coninck, M. Marengo,"Appearance of a low superheat quasi- Leidenfrost regime for boiling on superhydrophobic surfaces". Smart and Green Interfaces Conference 2015, 30 March – 1 April 2015, Belgrade, Serbia.

9. **I. Malavasi**, F. Veronesi, A. Caldarelli, M. Zani, M. Raimondo, M. Marengo, "Dynamic amphiphobicity with hexadecane and water droplets". 6th International Conference on Bubble and Drop Interfaces 2015, 5-10 July 2015, Potsdam/Golm, Germany.

10. T. Valente, **I. Malavasi,** E. Teodori, A. S. Moita, M. Marengo, A.L.N Moreira, "Effect Of Extreme Wetting Scenarios On Pool Boiling". UK Heat Transfer Conference 2015, 7-8 September 2015, Edinburgh, United Kingdom.

11. **I. Malavasi**, M. Negrin, F. Giacobbo, M. Mariani, G. Consolati, F. Quasso, M. Soccio, M. Gigli, N. Lotti, A. Munari, "Effect Of Gamma Irradiation on Poly(butylene Naphthalate)-based Polyesters". 13th Tihany Symposium on Radiation Chemistry, 29 August – 3 September 2015, Balatonalmádi, Hungary.

12. **I. Malavasi**, G. Consolati, F. Quasso, M. Soccio, M. Gigli, M. Negrin, F. Giacobbo, N. Lotti, A. Munari, M. Mariani, "Effect Of Gamma Irradiation On Poly(Butylene Naphthalate) Based Polyesters". Radiation Physics and Chemistry, In Press.

13. **I. Malavasi**, F. Veronesi, A. Caldarelli, M. Zani, M. Raimondo, M. Marengo, “Dynamic Amphiphobicity with Hexadecane and Water Droplets”. To be submitted to Langmuir.
14. **I. Malavasi**, M. Marengo, E. Teodori, A. S. Moita, A.L.N Moreira, “Wettability Effect On Pool Boiling: A Review”. To be submitted to Progress in Energy and Combustion Science.
15. E. Teodori, T. Valente, **I. Malavasi**, A.S. Moita, M. Marengo, A.L.N. Moreira, “Effect of extreme wetting scenarios on pool boiling conditions in a quiescent medium”. To be submitted to Experimental Thermal and Fluid Sciences.

Appendices: CONSTRUCTION OF AN EXPERIMENTAL APPARATUS FOR THE EVALUATION OF THE HEAT EXCHANGE COEFFICIENTS OF AN OSCILLATING INTERFACE

Appendix A

A. Investigation of oscillating two-phase flows in mini-tubes with different wettability

A.1 Introduction

This phase of the Research Work deals with heat transfer coefficient (HTC) experimental estimation in a two-phase fluid flow confined in capillary tubes with different wettability levels. The aim of this research branch is to define the effect of wettability on HTC in a system that can be defined as a “unit-cell” of a totally passive device with no moving parts able to transfer heat from a heat source to a heat sink with minimal temperature gradients or to isothermalize surfaces.

The process involves then evaporation and condensation, addition of heat to a flowing liquid in such a way to generate vapour and subtraction of heat to the vapour to obtain again fluid. In evaporation and condensation the hydrodynamic and the heat transfer process are very closely linked each other. This coupling is much closer than the one existing in single phase flows because the addition/removal of heat cause a variation in the amount and distribution of each phase and the flow pattern or topology of the fluid flow. It is very important to understand the difference between physical mechanisms involved in a macro-scale two phase flow rather than in a micro-scale. For very small channels, capillary force become stronger while inertia and viscous forces effect are attenuated. As the channel diameter become smaller, like in micro-channels, surface tension become non-negligible and start to play an important role. This means effects on the flow pattern transition and in particular on the presence and thickness of a thin liquid film on the tube internal wall laid down by the meniscus during the downward motion from the Heat Source to the Heat Sink. It is responsible of a large vapour generation and this mass contributes to increase the vapour pressure in the system. Depending on the temperature difference between Heat Source and Heat Sink, a quasi-periodic and nicely repeatable meniscus movement and pressure oscillation have been observed. This cyclic process is repeated with regular repeatable oscillations. Is thus clear the importance of investigating the thin liquid film and the evaporation phenomena of thermal auto-oscillation of the meniscus with the aim of define wheter a combination of different wettability conditions, in particular high hydrophilicity for the section deputed to the heat source to promote the film evaporation, and high hydrophobicity in the section deputed to the heat sink to promote the drop-wise condensation.

A.2 Two-phase flows

Two-phase flow is usually referred to the simultaneous flow of the gas and liquid phases of a single fluid component through a duct. Such a flow occurs when a vapor is being condenser or a liquid is being vaporized. The flow of two immiscible liquids, such as oil and water, is commonly referred to as two-component flow. The two-phase flow configuration, or regime, existing in a tube in a given case depends mainly upon the relative and absolute quantities and physical properties of the fluids flowing, the geometric configuration and the material of the conduit, and the kind of heat transfer process involved.

Historically, the most commonly studied cases of two-phase flow are in large-scale power systems. Coal and gas-fired power stations used very large boilers to produce steam for use in turbines. In such cases, pressurized water is passed through heated pipes and it changes to steam as it moves through the pipe. The design of boilers requires a detailed understanding of two-phase flow heat-transfer and pressure drop behavior, which is significantly different from the single-phase case. Even more critically, nuclear reactors use water to remove heat from the reactor core using two-phase flow. A great deal of study has been performed on the nature of two-phase flow in such cases, so that engineers can design against possible failures in pipework, loss of pressure, and so on [1]. Another case where two-phase flow can occur is in pump cavitation. Here a pump is operating close to the vapor pressure of the fluid being pumped. If pressure drops further, which can happen locally near the vanes for the pump, for example, then a phase change can occur and gas will be present in the pump. Similar effects can also occur on marine propellers; wherever it occurs, it is a serious problem for designers. When the vapor bubble collapses, it can produce very large pressure spikes, which over time will cause damage on the propeller or turbine.

Several features make two-phase flow an interesting and challenging branch of fluid mechanics:

- surface tension makes all dynamical problems nonlinear;
- in the case of air and water at standard temperature and pressure, the density of the two phases differs by a factor of about 1000. Similar differences are typical of water liquid / water vapor densities;
- the sound speed changes dramatically for materials undergoing phase change, and can be orders of magnitude different, and this introduces compressible effects into the problem;
- the phase changes are not instantaneous, and the liquid vapor system will not necessarily be in phase equilibrium;
- it can give rise to other counter-intuitive, negative resistance-type instabilities, like Ledinegg instability, Geysering, Chugging, relaxation instability, and flow maldistribution instabilities as examples of static instabilities, and other dynamic instabilities [2].

In most single-phase flow problems it is important to distinguish whether the flow is laminar or turbulent, and whether separation flow or secondary flows exist. These distinctions provide useful information about the behavior of the flow and help select the most appropriate models to analyze the flow. Although these distinctions are equally useful in the study of two-phase flow systems, the two phase flow in a pipe can exhibit a variety of shapes and distributions of the interfacial spaces of the phases. The configurations of these interfacial surfaces are of critical importance in determining the characteristics of the flow. Since it is impossible to specify the spatial and temporal distribution of the phases, the internal structure of the flow is usually classified in a number of characteristic patterns or regimes. The conditions under which these patterns are expected to occur are usually presented as diagrams called flow regime maps.

The identification of flow patterns and the definitions of the transitions between them were the subject of numerous investigations. Govier and Aziz [3], Delhaye et al. [4], and Hewitt [5] published detailed reviews of the earlier work on two-phase flow patterns and pattern transitions. Rogers [6] provided a comprehensive assessment of the regime boundaries and interphase drag models used in advanced thermal hydraulics codes for two-phase vertical up-flow. Collier and Thome [7] provided reviews of more recent experimental and semitheorehcal studies.

When multiple phases passes through a cross-section of the pipe, each phase can obviously not cover more than a fraction of the area. The void fraction ε is one of the most important parameters used to characterize two-phase flows. It is the key physical value for determining numerous other important parameters, such as the two-phase density and the two-phase viscosity, for obtaining the relative average velocity of the two phases, and is of fundamental importance in models for predicting flow pattern transitions, heat transfer and pressure drop. Various geometric definitions are used for specifying the void fraction: local, chordal, cross-sectional and volumetric. The local void fraction ε_{local} refers to that at a point (or very small volume when measured experimentally) and thus $\varepsilon_{local} = 0$ when liquid is present and $\varepsilon_{local} = 1$ when vapor is present. Typically, the local time-averaged void fraction is cited, or measured using a miniature probe, which represents the fraction of time vapor that was present at that location in the two-phase flow. If $P_k(r,t)$ represents the local instantaneous presence of vapor or not at some radius r from the channel center at time t, then $P_k(r,t) = 1$ when vapor is present and $P_k(r,t) = 0$ when liquid is present. Thus, the local time-averaged void fraction is defined as $\varepsilon_{local}(r,t) = (1/t) * \int P_k(r,t)\, dt$. The chordal void fraction $\varepsilon_{chordal}$ is typically measured by shining a narrow radioactive beam through a channel with a two-phase flow inside, calibrating its different absorptions by the vapor and liquid phases, and then measuring the intensity of the beam on the opposite side, from which the fractional length of the path through the channel occupied by the vapor phase can be determined. The chordal void fraction is defined as $\varepsilon_{chordal} = L_G/(L_G + L_L)$, where L_G is the length of the line through the vapor phase and L_L is the length through the liquid phase. The cross-sectional void fraction $\varepsilon_{c\text{-}s}$ is typically measured using either an optical means or by an indirect approach, such the electrical capacitance of a conducting liquid phase. The cross-sectional void fraction is defined as $\varepsilon_{c\text{-}s} = A_G/(A_G + A_L)$, where A_G is the area of the cross-section of the channel occupied by the vapor phase and A_L is that of the liquid phase. The volumetric void fraction ε_{vol} is typically measured using a pair of quick-closing values installed along a channel to trap the two-phase fluid, whose respective vapor and liquid volumes are then determined. The volumetric void fraction is defined as $\varepsilon_{vol} = V_G/(V_G + V_L)$, where V_G is the volume of the channel occupied by the vapor phase and V_L is that of the liquid phase. It is important to distinguish the difference between void fraction of the vapor phase and the thermodynamic vapor quality x; they do not mean the same thing. The vapor quality is the ratio of the mass of vapor in the considered volume to the total mass of liquid plus vapor.

A.2.1 Patterns in vertical co-current up-flow

A number of flow patterns have been identified in upward co-current (when both phases are flowing in the same direction) flow in a vertical pipe. These patterns are usually grouped in the major regimes described below and are illustrated in Figure A.1.

(a) Bubble flow: regime characterized by a dispersion of discrete bubbles flowing in a continuous liquid phase. The number of bubbles increases with increasing the gas flow rate.

(b) Plug slug flow: pattern composed of a series of large elongated bubbles separated by aerated slugs of water. The bubbles usually have nearly the same diameter as that of the pipe.

(c) Foam flow (or churn flow): regime similar to slug flow, but much more chaotic and unstable. At relatively higher flow rates, structures of the large bubbles in the slug flow pattern become unstable and eventually break down, leading to an oscillatory motion of the liquid. This regime is often considered as a transitional regime because of its unstable behavior. The churn flow pattern is sometimes referred to as semi-annular flow.

(d) Wispy-annular flow: under certain annular flow conditions, as the liquid flow rate is increased, the droplets entrained in the gas core coalesce into large lumps or "wisps" of liquid. Hewitt et al. [8] considered this type of flow as a separate regime.

(e) Annular flow: liquid swept up around the entire wall of the pipe in an annular form, while the faster moving air occupies the core of the tube and entrains small droplets of liquid dispersed in the form of a mist. The liquid film has a wavy and irregular surface and may contain gas bubbles. This regime is encountered at relatively high mass velocities. Annular droplet flow can be relatively difficult to model accurately since the model needs to incorporate such effects as how fast the droplets are torn from the liquid film, how fast droplets settle on the liquid film, and how the liquid film affects the surface roughness between gas and liquid.

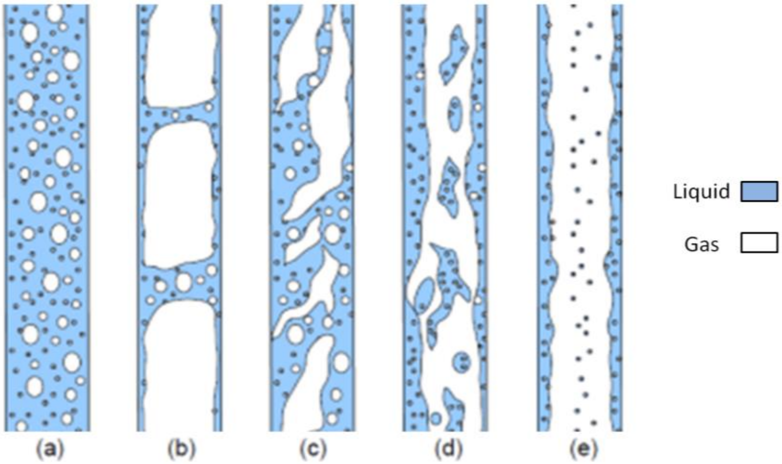

Figure A.1: Gas-liquid flow patterns in vertical co-current up-flow: (a) bubble flow, (b) plug slug flow, (c) foam flow, (d) wispy-annular flow, (e) annular flow.

A.2.2 Patterns in horizontal flow

In horizontal two-phase flow, because of the density differences of the gas and liquid phases, gravity causes the gas, the less dense phase, to migrate to the top of the channel. As a result, horizontal two-phase flow has flow patterns that are not axisymmetrical.

For very low superficial gas and liquid velocities the flow is stratified. As the velocities approach zero, we expect the pipe to act as a long, horizontal tank with liquid at the bottom and gas on top. If the gas velocity increases, waves start forming on the liquid surface. Due to the friction between gas and liquid, increasing the gas flow will also affect the liquid by dragging it faster towards the outlet and thereby reducing the liquid level. If the gas flow increases further, the gas turbulence intensifies until it rips liquid from the liquid surface so droplets become entrained in the gas stream, while the previously horizontal surface bends around the inside of the pipe until it covers the whole circumference with a liquid film. The droplets are carried by the gas until they occasionally hit the pipe wall and are deposited back into the liquid film on the wall. If the liquid flow is very high, the turbulence will be strong, and any gas tends to be mixed into the liquid as fine bubbles. For somewhat lower liquid flows, the bubbles float towards the top-side of the pipe and cluster. The appropriate mix of gas and liquid can then form Taylor-bubbles, which is the name used for the large gas bubbles separating liquid slugs. If the gas flow is constantly kept high enough, liquid is swept up around the perimeter of the tube, while the faster moving air flows in the core.

The following descriptions are based on the most widely accepted classifications of the gas-liquid flow patterns in horizontal flow, i.e. Alves [302], Baker [10], Govier and Omer [304], Mandhane et al. [305]. These patterns are shown in Figure A.2.

(a) Dispersed bubble flow: flow pattern characterized by bubbles of gas randomly dispersed in a continuous liquid phase. The bubbles are relatively small in comparison with the diameter of the tube. Because of gravity, the gas bubbles tend to travel in the upper half of the tube.

(b) Plug flow: gas phase is present in the form of elongated bubbles transported in an aerated continuous liquid phase in the upper half of the tube. This flow is also referred to as elongated bubble flow by Govier and Aziz [3] and Mandhane et al. [305].

(c) Stratified smooth flow: gas phase travels along the upper half of the tube while the liquid flows along the bottom with no significant interfacial waves. The gravity separation is complete, and the stratified flow regime occurs at relatively low gas and liquid mass flow rates.

(d) Stratified wavy flow: as the gas velocity increases, the faster moving gas causes waves at the gas-liquid interfaces, resulting in a wavy flow pattern. The gas phase might contain some liquid droplets, and at the same time the liquid waves might be aerated.

(e) Slug flow: with increased gas velocity, the magnitude of the waves increases. Ultimately, the waves build up and reach the upper wall of the tube to form some liquid packets, also liquid slugs. These liquid slugs are then transported at the higher velocity of the gas. Unlike plug flow, in which the elongated bubbles of gas are transported by the liquid phase, in slug flow the liquid slugs are carried by the faster moving gas flow. The slug flow regime is highly undesirable in practical applications. The faster moving liquid slugs are usually associated with sudden pressure pulses and severe pressure oscillations that can cause damage to downstream equipment. Prediction of the onset of slugging has been the focus of many theoretical and experimental studies, e.g. Kordyban [306], Hubbard and Dukler [14], Wallis and Dorbson [15], Taitel and Dukler [309], Kubie [17], Lin and Hanratty [18], Barnea and Taitel [312], Jepson and Taylor [20]. It is generally accepted that slugs form in horizontal gas-liquid flow as a consequence of local Kelvin-Helmholtz instability at the wave crest, rather than the instability of the whole wave. The Kelvin-Helmholtz instability may be interpreted physically as the instability of the wave which occurs when the low pressure at the crest, resulting from higher gas velocity there, overcomes the stabilizing effect of gravity. Prior to slug formation small waves always appear on the crest of the large waves, and slug result from rapid growth of one of these wavelets. The appearance of these wavelets represents the onset of the Kelvin-Helmholtz instability. The slug initiation depends mainly on the superficial gas velocity, and as the pipe diameter is increased, an increase in the superficial liquid velocity is needed to attain slug flow.

(f) Annular flow regime: liquid is swept up around the perimeter of the tube in an annular form, while the faster moving air flows in the core of the tube and entrain small droplets of liquid dispersed in the form of a mist. Small bubbles of gas may also be entrained in the liquid film. Because of gravity, the thickness of the liquid film is higher at the bottom of the tube that at top. This regime occurs at a relatively high mass flow rate of the gas phase.

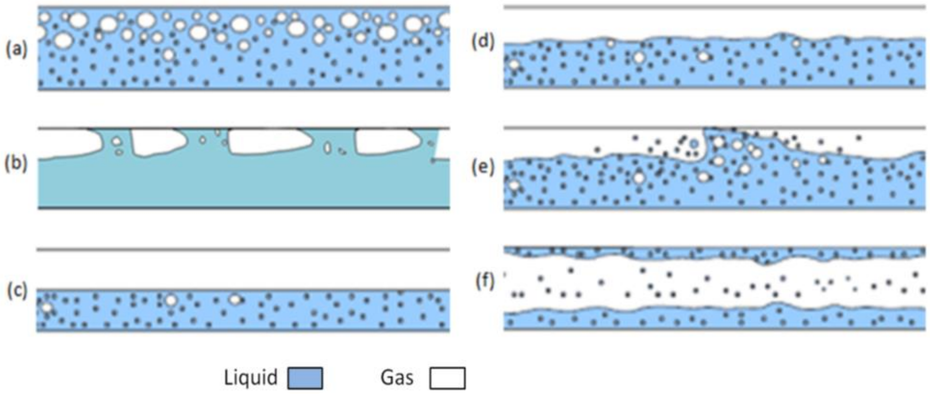

Figure A.2: Gas-liquid flow patterns in horizontal flow: (a) dispersed bubble flow, (b) plug flow, (c) stratified smooth flow, (d) stratified wavy flow, (e) slug flow, (f) annular flow.

A.2.3 Flow regime maps

The rate of exchange of mass, momentum and energy between gas and liquid phases as well as between any multiphase mixture and the external boundaries is closely related on these internal flow geometries and interfacial area; hence it is strictly correlated on flow-pattern. For instance, the relationships for pressure drop and heat transfer are likely to be different for a dispersed flow consisting of bubbles in a liquid (bubbly flow) than for a separated flow consisting of a liquid film on a channel wall with a central gas core (annular flow). This leads to the use of flow-pattern dependent models for mass, momentum and energy transfer, together with appropriate flow-pattern transition criteria. The usual way of presenting results of observations of flow patterns is to plot them on a graph whose axes represent the flow rates of the two phases; an alternative is to plot total mass flux on one axis and the mass fraction of the flow which is vapor or gas on the other axis. When all the observations have been recorded, lines are drawn on the graph to represent the boundaries between the various flow regimes. The resultant diagram is called “flow regime map”. Flow pattern maps are an attempt, on a two-dimensional graph, to separate the space into areas corresponding to the different flow patterns. Examples of flow regime maps are shown in Figure A.3.

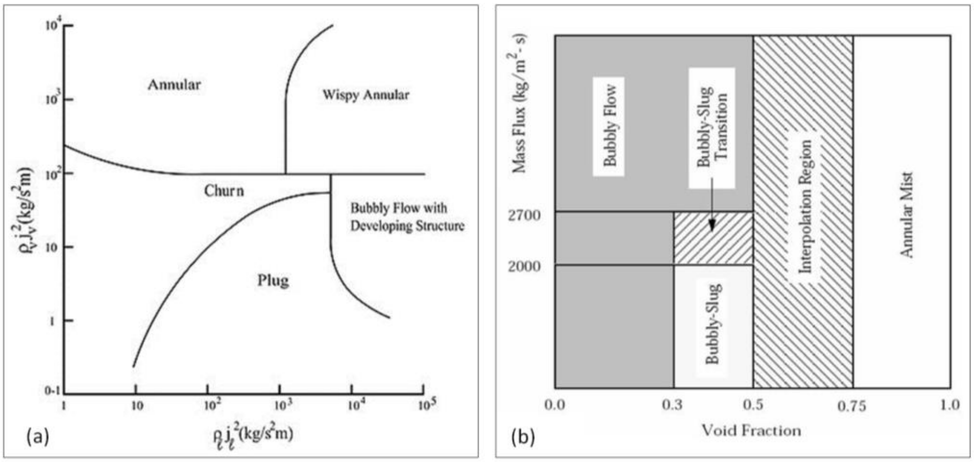

Figure A.3: (a) Example of flow regime map for vertical upward two-phase flow [21,22]. (b) Flow regimes plotted on void fraction vs. mass flux (kg/m^{2}s) axes [29].

Notice that even if such maps can be made dimensionless under certain conditions, no one has succeeded in drawing any general maps valid for all diameters, inclinations and fluid properties. Therefore a diagram valid for one particular situation (one point in one pipeline with one set of fluid data) is of little help when determining the flow regime for any other data set. That is why we need more general flow regime criteria rather than measured flow regime maps. Characterizing flow regimes from visual observations in the laboratory is complicated as well, and the transitions are difficult to define accurately. Different researchers define different number of flow regimes during

laboratory categorization and the number of regimes implemented in simulations models is sometimes kept lower for simplicity. Another difficulty comes from the fact that measurements, which are most abundant for small diameter pipes, are hard to scale up to larger diameters. This problem effects both flow regime determination and the modeling of each specific regime.
In order to better evaluate heat transfer coefficients it is desirable to develop a flow pattern map to predict the flow regimes; flow pattern maps are used to determine the flow patterns that exist under different operating conditions and to predict the transition from one type of two-phase flow pattern to another type.

A.2.4 Non-dimensional numbers relevant to two-phase flow studies in microchannels

The non-dimensional numbers relevant to two-phase studies in micro-/mini-channels are summarized in the following table. In the following definitions, the velocity is considered as the superficial velocity that is, for the phase i: $j_i = q_i/\rho_i A$ [23], where q is the mass flow rate (kg/s), ρ the density (kg/m^3) of the phase i and A the cross sectional area (m^2) of the pipe. The superficial velocity of the liquid, j_L, is defined as the ratio of the volumetric flow rate of the liquid phase and the total cross sectional area of the two-phase flow, obtaining $j_L = G(1-x)/\rho_L$, where G is the mass flux (kg/m^{2}s) and x the vapor mass fraction. In the same way, the superficial velocity of the vapor, j_V, is $j_V = G_v x/\rho_V$.

Boiling number	$Bl = q''/Gh_{LV}$	It represents the ratio of the evaporation mass flux to the total mass flux flowing in a channel [24].
Bond number	$Bo = g(\rho_L - \rho_V)d^2{}_h/\sigma$	Ratio between gravity and surface tension forces[1].
Capillarity number	$Ca = \mu_L j_L/\sigma = \mu_L G(1-x)/\rho_L\sigma$ $Ca_{LO} = \mu_L G/\rho_L\sigma$	Ratio of viscous to surface tension forces.
Confinement number	$Co = [\sigma/g(\rho_L - \rho_V)d^2{}_h]^{1/2}$	Ratio between surface tension forces and gravity.

---

[1] The practical difference between Bo and Eo is that in the definition of Bo the hydraulic diameter, d_h, is used, while in the definition of Eo, L is d_h but also another relevant physical dimension.

Convection number	$Cn = [(1\text{-}x)/x]^{0.9}[\rho_V/\rho_L]^{0.5}$	Modified Martinelli parameter, introduced by Shah [25] in correlating flow boiling data.
Eötvös number	$Eo = g(\rho_L - \rho_V)L^2/\sigma$	Ratio between gravity and surface tension forces.
Garimella number - convective confinement number	$Ga = Bo^{0.5}\, Re_{LO}$	Weighted ratio between gravity dot inertia forces and surface tension dot viscous forces.
Jakob number	$Ja = c_p(T_s - T_{sat})/h_{LV}$	Ratio of sensible to latent energy absorbed during liquid-vapor phase change.
Kandlikar first number	$K_1 = ((q''/h_{LV})(d_h/\rho_V))/(G^2 d_h/\rho_L) = ((q''/Gh_{LV})^2(\rho_L/\rho_V)) = Bl_2\rho_L/\rho_V$	It represents the ratio of the evaporation momentum force and the inertia force [24].
Kandlikar second number	$K_2 = ((q''/h_{LV})^2(d_h/\rho_V))/\sigma = ((q''/h_{LV})^2(d_h/\rho_V\sigma)$	It represents the ratio of the evaporation momentum force and the surface tension force [24].
Prandtl number	$Pr = v/\alpha$	Ratio between kinematic viscosity and thermal diffusivity.
Reynolds number	$Re_L = \rho_L j_L d_h/\mu_L = G(1 - x)d_h/\mu_L Re_{LO} = Gd_h/\mu_L Re_V = \rho_L j_L d_h/\mu_V = Gxd_h/\mu_V$ $Re_{VO} = Gd_h/\ \mu_V$	Ratio of inertia and viscous forces.
Weber number	$We_L = \rho_L j_L^2 d_h/\sigma = G^2(1 - x)^2 d_h/\rho_L\sigma We_V = \rho_V j_V^2 d_h/\sigma = G^2x^2d_h/\rho_V\sigma We_{LO} = G^2d_h/\rho_L\sigma We_{VO} = G^2d_h/\rho_L\sigma$	Ratio between inertia and capillary forces, it aims to represent the interaction between vapor and liquid phases.

Table A.1: Non-dimensional numbers relevant to two-phase studies in microchannels [26].

A.2.5 Macro to microscale transition in two-phase flows

In space applications the use of passive thermal components, such as heat pipes, loop heat pipes, pulsating heat pipes and active components such as miniaturized pumped systems, underline the importance in understanding the flow boiling mechanisms, in order to simulate precisely the heat transfer conditions in satellites and in thermal components for extraplanetary exploration. The main question is if for very small tubes the flow behavior changes, since physics mechanisms alter passing from macroscale to microscale two-phase flows, as capillary forces become stronger, while buoyancy force effects are weakened. Unlike in conventionally-sized passages, in which surface tension effects are limited, surface tension in miniature/micro channels can have significant effects on flow pattern transitions, on overall hydrodynamics and, in particular, on the thin films that are believed to be the dominant mechanism controlling the heat transfer characteristics.

It is very chancy to extrapolate macroscale two-phase flow boiling methods to microchannels. While in single-phase heat transfer the threshold between microscale and macroscale can be determined on the basis of scaling effects[2], in flow boiling the transition between micro and macroscale has not been well defined yet. The current knowledge of flow boiling heat transfer in macroscale cannot be extended tout-court to microscale, where bubble confinement plays a more relevant role with the decreasing of the channel size. It is then necessary to use a new heat transfer method that incorporates features of the physical process of microchannel flow and evaporation.

In general, the scales of two-phase flow and heat transfer in channels can be classified according to the hydraulic diameter of the channels, although it also depends on the properties of the fluid and flow conditions. One recent

---

[2] In single-phase heat transfer, after a period of uncertain results (1990-2007), it is nowadays clear that no peculiar physics has been detected in microscale, even if some phenomena are not negligible as the scale reduces; these are, for example, the so-called scaling effects in the thermal entrance length, axial conduction and viscous heating. In recent works, such as in [26], it has been found that, taking into account the scaling effects, there is a general agreement with macroscale phenomena. Hence in most of the engineer applications, the use of empirical correlations well known in macroscale is still possible, when the proper channel size and surface roughness are used.

classification based on the hydraulic diameter D_h of the channels [318] (2005) provides:

- macrochannels: $D_h > 6mm$;
- minichannels: $200\mu m < D_h < 6mm$;
- microchannels: $10\mu m < D_h < 200\mu m$;
- transitional channels: $100nm < D_h < 10\mu m$;
- nanochannels: $D_h < 100nm$.

Anyway, the classifications based on the channel size do not necessarily address the threshold where the characteristics of two-phase flow and heat transfer depart from the macroscale descriptions.

Kew and Cornwell [28] (1997) recommend a confinement number, Co, to distinguish between micro and macroscale. Co is the ratio between the capillary length l_c and the hydraulic diameter. They find deviations in the flow regimes from those observed in large channels and that the existing flow boiling heat transfer correlations do not perform well when applied to narrow channels having $Co > 0.5$; therefore they set $Co = 0.5$ as the threshold for microscale flows.

Li and Wang [29] (2003) recommend using the capillary length, l_c, to distinguish between micro and macroscale and give the following condensation flow regimes based on the tube diameter d:

- $d > d_{th}$: gravity forces are dominant and the flow regimes are typical of macroscale;
- $d < d_c$: gravity effect on the flow regime can be ignored completely, the flow is symmetric with respect to bulk forces and it is a microscale flow;
- $d_c < d < d_{th}$: gravity and surface tension forces are equally dominant, a slight stratification of the flow distribution was observed.

The values of d_c and d_{th}, in terms of l_c, are: $d_c = 0.224l_c$ and $d_{th} = 1.75l_c$. The capillary length l_c is defined as

$$l_c = \left[\frac{\sigma}{g(\rho_L - \rho_V)}\right]^{1/2} \qquad \text{(I)}$$

where σ, g, ρ_L and ρ_V are the surface tension, gravitational acceleration and densities of the liquid and vapor at the saturated pressure, respectively.

Kawaji and Chung [30] (2004) present a thorough review of adiabatic two-phase flow in minichannels and microchannels. They suggested that the transition from minichannels to microchannels occurred between 100 and 250μm.

Thome [31] (2004) underlines that the hydraulic diameter criterion does not reflect the influence of channel size on the physical mechanisms, as the effect of reduced pressure on bubble sizes and flow transitions. Furthermore, the hydraulic diameter criterion does not take in consideration the test fluid properties and should be rejected as too rough. Thome asserts that a macro to microscale transition criterion might be related to the bubble departure diameter, which is defined as the point at which the bubble departure size reaches the channel diameter. If the diameter of a growing bubble reaches the internal diameter of the tube before detachment, then the bubble can only grow in length as it flows downstream and the result is that only one bubble can exist in the channel cross-section at a time. Hence, this condition of confined bubble flow is suggested by Thome et al. [32] to be the threshold beyond which macroscale theory is no longer applicable. In few words the best threshold criterion for distinguishing the microscale from the macroscale is bubble growth. With its diameter confined by the channel, a bubble can grow only in length rather than diameter. This criterion should be a function of geometry, size and fluid properties.

Cheng and Wu [33] (2006), based on the critical and threshold diameters obtained by Li and Whang [29], classifie phase change heat transfer in channels according to Bo as follows:

- microchannel if $Bo < 0.05$, the effect of gravity can be neglected;
- mesochannel if $0.05 < Bo < 3$, surface tension effect becomes dominant and gravitational effect is small;
- macrochannel if $Bo > 3$, the surface tension is small in comparison with gravitational force.

A criterion to identify the threshold is also proposed by Ullmann and Brauner [34] (2007) on the basis of flow pattern maps, using Eo. On the basis of flow pattern map deviation for experiments in pipes, Ullmann and Brauner proposed a microscale threshold of $Eo \leq 1.6$.

Harirchian and Garimella [35] (2010) develop a transition criterion based on the fact that bubble confinement depends on channel size and on the mass flux since the bubble diameters varies with the flow rate. $Bo^{0.5} \times Re_{LO}$ is called by Harirchian and Garimella “convective confinement number” and is denoted as Ga. When Ga is equal to 160 the threshold between micro and macroscale occurs. This criterion considers as microchannels those channels having Ga

< 160 while for larger convective confinement numbers, the vapor bubbles are not confined and the channels is considered as a macroscale channel.

Baldassari and Marengo [26] (2013) stressed that a macro to micro transition also occurs for a fixed channel diameter, when, due to bubble coalescence downstream, there is a point along a tube where the bubble diameter may reach the channel section size. When the bubbles are able to detach from the tube surface with small sizes, any bulk force (as gravity) acting normally or radially is able to drift the bubbles downstreaming combining vectors of the flow drag force and the bulk force. But when the bubbles are completely filling the tube section, the gravity and other bulk forces are playing a role in the dynamics of the flow only if they are aligned with the tube or channel axes. Therefore, due to bubble coalescence for example, it is possible that a transition from macro to microscale is occurring along the flow, during its development in the tube for the same tube diameter. Such effects can be also originated by the pressure drop. Therefore, no physical sharp distinction occurs between a macro and a micro regime, since, until an extremely low value of the channel size, the fundamental physical phenomena are simply the same, i.e. there is no “microscale” or “macroscale”, but only a change of the flow patterns, and therefore of the heat transfer mechanisms, linked to different values of flow parameters and dimensionless numbers. From the flow pattern point of view, stratified-wavy and fully stratified flows disappeared in small horizontal channels. In fact no stratified flow exists if the tube diameter is sufficiently small, and this could be an indication of the lower boundary of macroscale two phase flow. The upper boundary of microscale two-phase flow might be the point in which the effect of gravity becomes negligible, meaning that in microgravity conditions there should be only microscale features. Anyway, this was proved not to be true [26]. From the heat transfer point of view, the results in [22] seem to suggest an increase of the heat transfer coefficient passing from the macroscale to the microscale regime. Generally, the microscale has only a simple relation with the channel size, i.e. it is the maximum value of micrometers above which the physical phenomena, given the same fluid and physical flow condition such as G and x, are showing a rapid variation in terms of patterns, pressure drop and heat transfer. Under such given size, some of the usual physical phenomena in macroscale (i.e. for a larger scale) should change.

The boiling flow in minichannels is interesting and complex, and the research needs further experimental data for flow patterns, heat transfer coefficients and for the validation of the boiling models. Defining the right length scale for which a transition between macroscale to microscale phenomena should occur is only a mere exercise of categorization. Considering the definition for which the flow boiling miniscale is set when the bubbles are filling completely the channel section (the so-called “confined bubble flow”), there could be tubes of millimeters in which such condition still appears. Therefore it is better to speak about different patterns, rather than focusing on a feeble distinction linked to the channel size. Of course, like for single-phase flows, going toward very small tubes of few microns size or even nanoscale diameters, the physical phenomena can really change, since many classical hypotheses on continuum, on viscous dissipation and so on, may ceased to be completely valid. Since the micro to macroscale threshold has been practically associated with bubble confinement, a more refined correlation is still necessary to define a univocal and universal criterion for the transition from unconfined to confined bubble flow. Better characterized experimental data are necessary to improve the knowledge in this field. Some effects, like bubble confinement, the prevalence of surface tension over buoyancy and the importance of inertial forces in the force balance, have still to be investigated and analyzed in detail. Finally, it is also evident that, since the pressure drop in microchannels is very significant, a transition from an unconfined to a confined flow may appear along the tube or the channel due to the decrease of the local pressure. Such transition has not been investigated in the literature yet.

A.2.6 Two-phase flow patterns in micro and minichannels

An important aspect of two-phase flow patterns in microchannels is how to identify them, qualitatively and/or quantitatively. The difficulty of identifying flow regimes and their transitions visually comes from the difficulties both in obtaining good high-speed images and in the interpretation of the flow (subjectivity and pattern definition depending on the author), and also in choosing the channel size that determines either macro or microscale or the transition between them. The influence of surface tension forces becomes more dominant in small diameter channels, and this is reflected in the flow patterns observed in these channels. Over the years many studies have focused on two-phase flow patterns in microchannels; the following are the main works.

Thome [36] (2006) asserts that at a very low G the two-phase flow in microchannels approaches capillary flow as a natural limit, where all the liquid flow is trapped between pair of menisci with dry wall vapor flow in between; no stratified flow is observed in microchannels due to the predominance of surface tension over gravity forces so that the tube orientation has negligible influence on the flow patterns.

For Revellin et al. [37] (2006) the bubble frequency, at a fixed G, increases with q'' and x until it reaches a peak; after that the frequency decreases, first very sharply and then slightly less sharply, to a bubble frequency of zero. The first sharp fall off is due to the coalescence of all the smaller bubbles into long bubbles and the slower fall off is from the coalescence of the long bubbles into even longer and thus fewer bubbles, until the annular flow is reached.
Revellin and Thome [38] (2007) showed that the flow pattern transition depends on the coalescence rates and that the observed transitions did not compare well neither with the existing macroscale flow map for refrigerants nor with a microscale map for air-water flows. So they proposed [39] (2007) a new type of flow pattern map for evaporating flow in microchannels. The new type of diabatic map classifies flows as follows:

- isolated bubble regime (IB): bubble generation rate much larger than bubble coalescence rate and includes both bubbly and slug flows;
- coalescing bubble regime (CB): bubble coalescence rate much larger than bubble generation rate and exists up to the end of the coalescence process;
- annular regime (A): extent limited by x at the onset of CHF;
- dryout regime (PD): begins at x corresponding to the onset of CHF and PD refers to the post-dryout region, after passing through CHF at the critical vapor quality.

The passage of bubble trains, with slugs of liquid bridging neighboring bubbles, is found at low and intermediate vapor qualities in micro-channel systems. The vapor quality transition location IB/CB does not depend on the channel diameter but is a function of q''; on the other hand, the CB/A transition, corresponding to the vapor quality at which the bubble frequency reaches zero, i.e. the end of the presence of liquid slugs and distinct vapor bubbles, is not influenced by q''. Beyond a certain threshold vapor quality, the passage frequency falls sharply due to the rapid increase of coalescence among nearby bubbles (refer for example to Revellin et al., 2006 [39], 2008 [32]). In general terms, the frequency presents a maximum value, f_{max}, at the transition vapor quality between the isolate bubble and coalescing bubble flow modes, and declines to zero at the transition to annular flow [40]. During coalescence, the breakup process of the liquid slugs induces a redistribution of liquid among the remaining flow structures, including the film surrounding individual bubbles. Experimental observations have shown also that the bubble–slug passage has a cyclical nature. In Figure A.4 the flow pattern map of Revellin and Thome (2006) [39], updated by Ong and Thome (2009) [41], is shown.

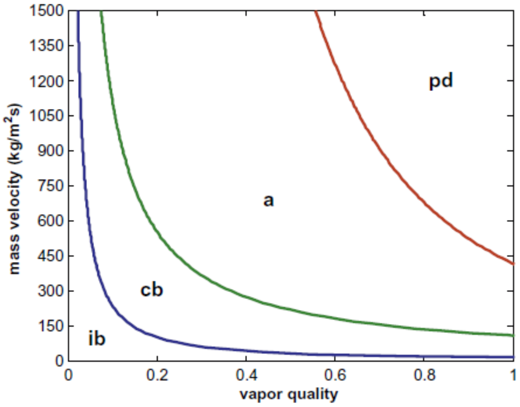

Figure A.4: The flow pattern map of Revellin and Thome (2006) [39], updated by Ong and Thome (2009) [41]: ib – isolate bubble flow, cb – coalescing bubble flow, a – annular flow, pd – post dry-out flow. Simulated for R-134a at 7 bar with a mass velocity of 500kg/m^{2}s and a heat flux of 50kW/m^2 in a 500µm diameter channel.

It is important to underline that in subcooled boiling, the bubble flow occurs with higher heat flux compared with saturated boiling at the same mass flux and, in accordance with [42] (1997), the onset of nucleate boiling (ONB) heat flux increases as the subcooling increases. The bubble size and the bubble behavior is influenced also by subcooling. Kandlikar et al. [43] (1997) conclude that the bubble growth rate strongly depended upon subcooling. In Ref. [44] (2009) it is underlined that a higher wall superheat and a higher imposed heat flux are needed to initiate the boiling for a higher subcooling and, recording the bubble motion at a given ΔT_{sub}, it emerges that the bubbles are larger at a lower liquid subcooling. This is due to the weaker vapor condensation and to the more bubble coalescence at a lower ΔT_{sub}. Recently Zhuan et al. [45] (2011) analyze the process of bubble growth, condensation, and collapse in subcooled boiling in microchannel through simulations. The degree of subcooling influences bubble growth and collapse; an annular flow seldom occurs in subcooled boiling for wide ranges of mass and heat fluxes and this is a big difference with the saturated boiling where slug and annular flows usually appear in the microchannel.

More recently, a detailed map of the flow sub-regimes in a shear-driven liquid film flow of water and FC-72 for a 2mm channel operating at room temperature is obtained by Kabov et al. (2011) [46]. While the water film can be smooth under certain liquid/gas flow rates, the surface of an intensively evaporating film of FC-72 is always distorted by a pattern of waves and structures. When heated, the shear-driven liquid films are less likely to rupture than gravity-driven liquid films. This provides a way to prevent and control a hot dry patch formation by the shear stress induced by gas flow. The performance gap associated with the deterioration of the heat transfer coefficient at high qualities, most probably due to local dryout of thin films caused by thermocapillary, Kelvin–Helmholtz, or other instability mechanism, in the microgap coolers has been identified. For shear-driven water films the critical heat flux was found of up to 10 times higher than that for a falling film, which makes shear-driven films (annular or stratified two phase flows) more suitable for cooling applications than falling liquid films.
The summary of the observations on flow patterns in mini-microchannels recently presented in literature is reported in Table A.2.

Author(s)	**Observations on flow patterns**
Chen et al. [47]	Dispersed bubble, bubbly, slug, churn and annular flow. Occasionally mist flow was observed in the bigger tubes at a very high vapor velocity, while confined bubble flow[3] was found in smaller tubes at a lower vapor and liquid velocity. It was only observed in the 1.10mm tube at all experimental pressures and in the 2.01mm tube only at 6.0 bar. This indicates that surface tension became the dominant force in the smaller tubes at the lower fluid velocities and this agrees with the confinement criterion by Kew and Cornwell [28] for which the confinement effect should be observed at tube diameter between 1.7 and 1.4mm at $6*10^{-14}$ bar. With the increase of fluid velocities, inertial force and friction gradually replace the importance of surface tension.
Harirchian and Garimella [35,48]	Five flow regimes, i.e. bubbly, slug, churn, wispy-annular and annular flow, were identified. Vapor

---

[3] It is similar to slug flow but with elongated spherical top and bottom bubbles.

	bubbles are confined within the channel cross section in slug flow and in confined annular flow.
Cornwell and Kew [49] Lin et al. [50,51]	Three flow patterns are commonly encountered during flow boiling in minichannels/microchannels: isolated bubble, confined bubble or plug/slug[4], annular flow.
Ong and Thome [41]	Isolated bubble, coalescing bubble and annular flow.
Revellin and Thome [39]	The microscale flow patterns were first classify in the 'classical' manner as follows: bubbly flow, bubbly/slug flow, slug flow, slug/semi-annular flow, semi-annular flow, wavy annular flow and smooth annular flow. Then, rather than limiting the observations into the traditional flow regimes and an adiabatic map, a novel diabatic map classifies flows into three types: isolated bubble, coalescing bubble and annular flow zones.
Revellin et al. [37,38]	Bubbly flow, slug flow, semi-annular flow and annular flow. It is evidenced that the thin film surrounding the bubbles becomes more uniform as the diameter decreases and this is the evidence that buoyancy has still a role. The higher G is, the earlier annular flow is encountered, while bubbly flow tends to disappear at high G because small bubbles quickly coalesce to form elongated ones.
Ribatski et al. [52]	Bubbly flow is seldom observed due to the fact that its lifespan is very short as bubbles coalesce or grow to the channel size very quickly.
Shiferaw et al. [53]	At low q'' confined bubble flow and then, increasing q'', elongated bubble, slug, wavy annular, annular flow respectively.
Zhang et al. [54]	No bubbly or plug flow, mostly annular flow with a very thin layer of liquid.

Table A.2: Summary of the observations on flow patterns in mini-microchannels recently presented in literature [26].

---

[4] Slug flow, is found at low and intermediate vapor qualities in microchannel systems.

A.3 Liquid–vapor phase transition in micro/mini scale flow boiling

In the next subsections the two liquid–vapor phase transitions with the bubble formation associated with the flow boiling in micro/mini channels are analyzed.

A.3.1 Flow condensation in micro and minichannels

Condensation in miniature or micro channels finds its applications in electronics cooling, microscale energy, and Micro-Electro-Mechanical Systems (MEMS). In an effort to increase system efficiency and reduce system footprint and refrigerant inventory, microchannel condensers have become increasingly common in HVAC&R (heating, ventilating, air conditioning and refrigeration) equipment. Condensers with circular and noncircular microchannel tubes are being used in applications ranging from automotive space conditioning systems to mobile refrigerated transport. Optimal design of these condensers requires a detailed understanding of condensation heat transfer and pressure drop at small hydraulic diameters [55]. Heat transfer and pressure drop for two-phase flow inside tubes are closely related to the corresponding flow mechanisms. The flow patterns formed in microchannels during condensation differ from those observed in conventional tubes.

As condensation progresses, various flow regimes are observed resulting from the changes in the relative magnitudes of forces acting upon the two phases. Examples include gravity-dominated regimes (e.g. stratified, wavy) and shear-dominated (e.g. annular) regimes. In larger diameter tubes, it has been shown that the heat transfer and pressure drop mechanisms in condensing flows are different in each flow regime. Thus, an understanding of the occurrence of, and transition between, different flow regimes as a function of fluid properties, tube size and vapor quality is necessary to accurately model condensation heat transfer and pressure drop.

Relatively few studies [55-64] have been conducted to understand two-phase flow regimes during condensation of several fluids in tubes with different geometry, pressures ranging and mass fluxes. The physical properties of refrigerants, especially the ratio of saturated liquid and vapor properties, are significantly different from those of air-water mixtures. These property differences and the condensation process are expected to affect flow regimes and transitions.

Soliman (1974) [65] identifies annular, semiannular, semiannular-wavy, spray annular, annular wavy, and spray regimes for condensation of refrigerants.

Wang et al. (1997) [66,67] find that for a condensing flows of R22, R134a and R407C in a 6.5mm diameter tube, the intermittent-wavy and wavy-annular transitions for R407C occurre at higher mass fluxes and qualities compared to those for R12 and R134a. Dobson et al. (1998) [68] report annular, wavy, wavy-annular and mist-annular regimes for condensation of refrigerants.
Tabatabai and Faghri (2001) [69] emphasize also the importance of surface tension in two-phase flow in horizontal miniature and micro channels and propose a transition boundary based on a force balance that includes shear, buoyancy and surface tension forces. The flow map obtained is compared to a number of existing experimental data and the comparison of the proposed model with previous models shows substantial improvement and accuracy in determining surface tension-dominated regimes, i.e. each regime transition boundary is affected by surface tension.
Coleman and Garimella (2000, 2003) [56,70] observe four major flow regimes during condensation of R134a in circular (D_h = 4.91mm) and rectangular ($1.0 < D_h <$ 4.8mm and $0.5 < \alpha < 2$) tubes, with mass fluxes of 150-750 kg/m^{2}s and qualities from 0 to 1:

1) annular;
2) wavy;
3) intermittent;
4) dispersed.

Each major flow regime is further subdivided into several minor flow patterns.

1) The annular flow regime is characterized by a liquid film layer at the tube wall with a vapor core inside. The flow patterns within this regime are:
   - mist: it consists of a vapor core with significant liquid entrainment and a very thin liquid film;
   - annular ring: it has a periodic appearance of liquid rings between large intervals of mist flow;
   - wave ring: it is similar to the annular ring pattern, with the exception that the liquid rings become noticeably thicker at the bottom compared to the top;
   - wave packet: it pattern consists of individual wave packets occurring periodically in the flow, with waves confined to the bottom portion of the tube;
   - annular film: a noticeably thick and approximately uniform liquid film forms on the inner periphery of the tube.

2) The wavy flow regime is characterized by separate liquid and vapor layers with liquid flowing at the bottom of the tube and vapor flowing above. As the tube diameter is decreased, the importance of this regime becomes smaller and eventually vanishes as surface tension forces overtake gravity. This flow regime is divided into two flow patterns:
   - discrete waves: the liquid-vapor wavy interface is clearly distinguishable, with the dominant wave pattern being of large wavelength and amplitude (the discrete waves were further classified by Coleman and Garimella (2003) [56] into discrete waves 0, 1 and 2 based on increasing wave intensity);
   - disperse waves: the liquid-vapor interface becomes indistinguishable because of the presence of multiple waves of a variety of typically smaller wavelengths and amplitudes along with the dominant wave.
3) The intermittent flow regime is characterized by the formation of vapor slugs or plugs surrounded by a thin liquid coating on the periphery with a liquid slug between successive vapor bubbles. This flow regime can be subdivided into two flow patterns:
   - slug flows: vapor slugs move through the liquid, often accompanied by discrete waves, these slugs are usually followed by trailing bubbles;
   - plug flows: solitary plugs are formed without trailing bubbles.

For smaller diameter tubes, slugs or plugs are located in the center of the tube, but for the large diameter tubes, they are located closer to the top of the tube, implying that the effect of buoyancy is discernible in the larger diameter tubes.

4) The dispersed flow regime is characterized by the flow of small vapor bubbles in the liquid. This flow regime is usually observed at low quality and high mass flux. However, the mass fluxes and qualities necessary for such flows are not particularly common in most refrigeration and air-conditioning applications and this flow regime is usually not observed in isolation. In other words, it is always found to coexist with some other flow regime. This flow regime can be divided in to two flow patterns:
   - bubble flow: bubbles are usually found at the top of the tube due to the influence of buoyancy;
   - dispersed flow: usually found at higher velocities, when the small bubbles span the entire cross-section.

As the tube diameter is reduced, the intermittent and annular regimes span a larger quality range, and the wavy flow regime range decreases. In fact, the disperse-wave flow pattern is almost completely absent for the 2mm tube. This indicates the diminishing effect of gravity versus surface tension at smaller hydraulic diameters. The dispersed flow regime is not observed for either tube at the mass fluxes of interest. The primary fluid properties that govern flow transitions are surface tension and liquid and vapor density and viscosity.

The transition criteria developed by Nema et al. [55] can be used to determine the flow regime/pattern at a particular condition if the hydraulic diameter (D_h), quality (x), mass flux (G), saturated liquid and vapor density (ρ_L, ρ_G), dynamic viscosity (μ_L, μ_G), and surface tension (σ) are known. The annular flow data were divided into three categories: annular film, annular film with mist, and mist flow. To model the transitions, annular film and annular film with mist were considered as one region (annular film), while mist flow as treated as the other region. The transition to the annular-film regime from intermittent flow was established based on the vapor-phase Weber number and Martinelli parameter. To model the wavy-annular film transition, it is suggested that the Bond number should be included along with the vapor-phase Weber number to account for the effect of gravity. A simplified criterion for mist flow transition using the vapor-phase Weber number was developed. It is also found that most of the mist flow data exist only for liquid volume fractions (represented by the Martinelli parameter) less than a critical value. If $Bo \leq Bo_{critical}$, then small tube effects are important. The possible flow regimes for this tube size are dispersed (D), annular film (AF), intermittent/annular film (I-AF) or intermittent (I). The wavy flow regime is not present. If $Bo > Bo_{critical}$, confinement effects are less important. The possible flow regimes in this case are dispersed (D), annular film (AF), dispersed wave (DpW), discrete wave (DcW) intermittent/discrete wave (I-DcW) or intermittent (I).

Moreover, film or interface instability can be used as a criterion for flow transitions and Rabas and Minard [71] suggested two forms of flow instabilities occurring inside horizontal tubes with complete condensation. The two forms are distinguished by a transition Froude number. It is suggested that the first instability results from the low vapor flow rate associated with a stratified exit condition and from vapor flowing into the tube exit, which causes condensate chugging or water hammer instability. The second instability results from a high vapor flow rate, which produces an inadequate distribution of the vapor and blockage of the tube exit, in turn causing large subcooled condensate temperature variations. Instability can also occur in small-diameter tubes, due mainly to capillary blocking where the liquid film bridges the tube to form a plug. In an integro-differential approach by Teng et al. [72], capillary blocking was investigated in a thermosyphon condenser tube with an axisymmetric viscous annular condensate film with a vapor core. It was found that at low relative vapor velocities, surface tension was responsible for film instability in capillary tubes. At high relative vapor velocities, on the other hand, hydrodynamic force was responsible for the instability.

As already mentioned, lightweight and compact condensers for vapor compression cycles have a variety of applications from electronics' cooling to transportation. However, as reported in the literature [73], uncertainties in measured condensation heat transfer coefficients can be as high as ±20% to ±40% due to the challenges of measuring condensation heat fluxes and wall temperatures at the micro- and mini-scales. It is very difficult to measure the local heat transfer coefficient of flow condensation in a single small-diameter tube, because of complexities involved in controlling the flow conditions, heat flux and vapor quality. Large uncertainties encourage condenser over-design. Typical approaches to measure condensation heat transfer coefficients in the micro and miniscale utilize fluid-to-fluid heat exchangers, which can have high experimental uncertainties at the low heat duties encountered in micro and miniscale condensation. Several approaches to measure condensation heat transfer coefficients at the macroscale have been later applied to the mini and microscale. Akers et al. [74] and Dobson and Chato [68] used fluid-to-fluid heat exchangers, where one fluid was condensing and the other was the coolant. Condensation heat transfer rates can also be found by conducting an energy balance before and after the test section on a pre- and post-heater [75,76]. Another common macroscale condensation heat transfer coefficient measurement approach applied to mini and microscale condensation is the Wilson plot method, reviewed by Fernandez-Seara et al. [56]. The Wilson plot is a graphical method that determines heat transfer coefficients without direct measurement of wall temperatures. The Wilson plot and modified Wilson plot have several limitations at the mini and microscale. A functional form of the coolant heat transfer coefficient must be assumed, and the condensation heat transfer resistance must be the dominant resistance.

Although measurement of mini and microscale condensation heat fluxes and wall temperatures (and, thus, heat transfer coefficients) has been difficult, researchers have identified several important parameters. Of prime importance is the increase of condensation heat transfer coefficients with decreasing channel diameter, which makes mini and microscale condensation attractive. In addition to channel diameter, several studies investigated the dependency of the condensation heat transfer coefficient on the channel shape, which modified surface tension forces. Shin and Kim [77] find the length-averaged condensation heat transfer coefficients to be higher in rectangular channels at lower mass fluxes, and higher in circular channels at higher mass fluxes. Wang and Rose [78] argue that in non-circular channels condensate gathers at the corners, thins the liquid film and lowers thermal resistance compared to the uniform film of a circular channel. In virtually all studies, mass flux and quality exert the largest effects on condensation heat transfer coefficients [73]. Other variables influencing condensation heat transfer included heat flux and system pressure. Few researchers have observed a dependence of heat transfer coefficient on condensation heat flux, possibly because the fluid-to-fluid heat exchanger test sections did not allow for variation of heat flux. Baird et al. [79] report a ‘‘significant’’ impact of condensation heat flux on heat transfer coefficients, especially at higher qualities, and also noted higher heat transfer coefficients, in general, at lower system pressures. However, Agarwal and Garimella [76] varying saturation temperature of R134a between 30°C and 60°C do not find any significant dependence on pressure. Derby et al. [73], in order to obtain condensation heat transfer coefficients with low uncertainties, develop a measurement method that utilized conduction in a copper block to measure condensation heat fluxes and wall temperatures. Three channel geometries (square, triangle, semi-circle) with hydraulic diameters of 1mm were machined to facilitate comparison of channel shape and condensation physics due to surface tension. They observe that condensation heat transfer coefficients are strongly dependent on mass flux and quality but not on heat flux and saturation pressure. Other researchers find no quality dependence at low mass fluxes, which may be an artifact of high heat transfer coefficient uncertainties at low flow rates in their experimental setups. Generally, no appreciable differences are found between channel shapes in this study. The lack of surface tension effect is perhaps in part influenced by the three-sided cooling boundary conditions. On the other hand, numerical studies by Wang and Rose [78,80] find significant condensation heat transfer enhancement through surface tension at the millimeter scale.

A.3.2 Flow evaporation, boiling and onset of nucleate boiling in micro and minichannels flow

Boiling is defined as the process of phase changing of a substance from liquid to gas by heating and it past its boiling point. Different types of boiling can be defined according to the geometric situation and to the mechanism occurring. Regarding the geometry, it is possible to distinguish between pool boiling, where the heat is transferred to a stagnant fluid, and flow boiling, where the fluid has a velocity relative to the heating surface. The three different boiling heat transfer mechanisms are nucleate boiling, where heat is transferred by means of vapor bubbles nucleating, growing and finally detaching from the surface; convective boiling, where heat is conducted through the liquid and evaporates at the liquid–vapor interface without bubble formation; and film boiling, where the heat is transferred by conduction and radiation through a film of vapor that covers the heated surface and the liquid vaporizes at the vapor–liquid interface. Nucleate boiling and film boiling may occur in both pool boiling and flow boiling, while forced convective boiling occurs only in flow boiling. In addition, if the temperature of the liquid is below the saturation temperature, the process is called subcooled boiling, whereas if the liquid is maintained at the saturation temperature, the process is known as saturated boiling [81].

Utilizing the latent heat of the coolant, two-phase microchannel heat sinks can dissipate much higher heat fluxes while requiring smaller rates of coolant flow than in the single-phase counterpart. Better temperature uniformity across the heat sink is also achievable. In spite of these attributes, the complex nature of convective flow boiling in microchannel heat sinks is still not well-understood, hindering their application in industry practice [31,82-84]. One subject of particular importance is the prediction of the onset of nucleate boiling (ONB) in microchannels. The first occurrence of vapor bubbles demarcates the transition from a single-phase to a two-phase flow regime, with the accompanying dramatic change in heat transfer and pressure drop, and for this reason, the prediction of onset of nucleate boiling is very important. In addition, a prediction of the ONB is necessary for understanding other flow boiling phenomena such as the onset of significant void (OSV) and departure from nucleate boiling (DNB) [85].

Hsu (1962) [360] is the first to postulate a minimum superheat criterion for the ONB in pool boiling. He proposes that the bubble nucleus would grow only if the minimum temperature surrounding the bubble (the temperature at the tip of the bubble) is at least equal to the saturation temperature of the vapor inside the bubble. The ONB heat flux correlation based on the minimum superheat criterion for pool boiling proposed by Hsu is:

$$q''_{ONB}=\frac{k_l h_{lv} \rho_v (T_w-T_{sat})^2}{12.8\sigma T_{sat}} \qquad \text{(II)}$$

where q'' is the heat flux [W/cm^2], k the thermal conductivity [W/m°C], h the latent heat [J/kg], ρ the density [kg/m^3] and σ the surface tension [N/m].

The effect of contact angle on the ONB heat flux was introduced by Davis and Anderson (1966) [87], who proposed the following correlation:

$$q''_{ONB} = \frac{k_l h_{lv} \rho_v (T_w - T_{sat})^2}{8(1+\cos\vartheta)\sigma T_{sat}} \quad \text{(III)}$$

where θ is the contact angle [deg].

Both eqs. (II) and (III) are obtained based on pool boiling, but they are also used to predict ONB in conventional channels.

Liu et al. (2005) [88] thoroughly review the existing works on ONB and propose an analytical model for ONB in microchannels (grooves). It is assumed that (i) the bubble shape is a truncated sphere, (ii) the liquid temperature is not affected by the bubble nucleus due to its small size, and (iii) the vapor and liquid are in equilibrium under saturation. The condition required for the bubble nucleus to grow is that the fluid temperature at a distance from the wall equal to the bubble height is greater than the superheat requirement.

A.3.3 Heat transfer in micro/mini scale flow boiling

In the microchannel flow boiling, there is a liquid layer between the elongated bubble and the channel, which is formed when the anterior liquid slug is jostled and squeezed by the high-speed proceeding cap-like meniscus of an elongated bubble and extends evenly backward along the channel. The liquid layer persists to evaporate and becomes the main source of the generated vapor which contributes to the bubble expansion or elongation if there is continued heat flux at the channel wall. A fictitious liquid passage with a dimension of the liquid layer thickness δ is assumed to exist near the meniscus which can replenish the liquid for evaporation in the liquid layer interface and the effective evaporation region of the meniscus continuously, and the liquid velocity in this supplemental liquid passage takes a linear distribution.

Flow boiling heat transfer consists of a nucleate boiling component, resulting from the nucleating bubbles and their subsequent growth and departure from the heated surface, and a convective boiling component, resulting from the convective dynamic effect. Nucleate boiling is characterized by the liquid–vapor phase change associated with the bubble formation, and it takes place when the surface temperature is hotter than the saturated fluid temperature by a certain amount but where the heat flux is below the critical heat flux, i.e. the thermal limit of a phenomenon where a phase change occurs during heating, which suddenly decreases the efficiency of heat transfer, thus causing localized overheating of the heating surface. Compared to single-phase, nucleate boiling involves heat transfer coefficients (HTC) typically one order of magnitude higher than single-phase forced convection and two orders of magnitude higher than single-phase natural convection [363], thus enabling to exchange more energy with a relatively lower temperature difference at the wall. In Kandlikar's opinion [90] these two mechanisms are closely interrelated. Several studies try to shed light on flow boiling heat transfer debate [26,52,91,92], but until now the dominant heat transfer mechanism inside mini and microchannels is still an open question.

In most of the papers nucleate boiling has been suggested to be the dominant heat transfer mechanism in microscale channels. Experimental heat transfer coefficient for deionized water in a single microchannel (d_h = 100mm) is found to be independent on G and vapor quality [93]. Though this behavior seems to suggest nucleate boiling as the dominant heat transfer mechanism, the major flow pattern is similar to annular flow, which does not present h independent of G and x. This discrepancy is attributed to the fast and long elongated bubbles that grow from single bubbles in a microchannel; the continuous supply of heat through the thin liquid film speeds up the continual growth of elongated bubbles and finally creates an annular flow. Anyway, Thome [22] (2004) asserts that the nucleate boiling is not the dominant heat transfer mechanism in microscale channels and that this error originates from the misconception that an evaporation process depending on the heat flux necessarily means that nucleate boiling is the controlling mechanism. Thome underlines also that another diffuse inaccuracy is to simple label microchannel flow boiling data as being nucleate boiling dominated, only because this seems to be the case for the bubbly flow regime, which occurs at very low vapor qualities. Furthermore, experimental flow boiling studies reporting that nucleate boiling was dominant at low x, equally show that the flow regime observed at such conditions was elongated bubble flow and such two conclusions are then contradictory. Many empirical prediction methods for boiling in microchannels are essentially modifications of macroscale flow boiling methods and thus assume that nucleate boiling is an important heat transfer mechanism without proof of its existence as the two principal microchannel flow regimes are in fact slug and annular flow [22].

The summary of heat transfer mechanisms in microscale flow boiling as described in literature is reported in the following table.

Author(s)	**Heat transfer mechanisms active during boiling in microchannels**
Kandlikar [24]	Nucleate boiling dominates heat transfer during flow boiling, the role of the convective boiling mechanism is diminished.
Bao et al. [94]	Nucleate boiling.

Lin et al. [95]	Nucleate boiling dominated at low x, convective boiling at high x.
Yen et al. [96]	Bubble nucleation only occurred when x < 0.4. x = 0.4 is considered to be the x critical for nucleate and convective boiling dominance in microchannels.
Jacobi and Thome [97]	Transient evaporation of a thin liquid films in slug flow.
Thome [22]	- In bubbly flow, nucleate boiling and liquid convection. - In slug flow, the thin film evaporation of the liquid film trapped between the bubble and the wall. Liquid convection to slug and vapor convection, when there is a dry zone present, are also important, depending on their relative residence times. - In annular flow, convective evaporation across the liquid film. - In mist flow, vapor phase heat transfer with droplet impingement.
Cheng et al. [98]	- Nucleation mechanism near the onset of boiling at upstream of the microchannels. - Film vaporization (convective boiling) in the Taylor bubble and annular flow at downstream.
Lee et al. [91]	- Heat transfer is associated to different mechanisms depending on the vapor quality. - Nucleate boiling occurs at low qualities (x < 0.05). - Annular film evaporation dominates at medium quality (0.05 < x < 0.55) and at high quality (x > 0.55).
Harirchian and Garimella [99]	- Nucleate boiling for unconfined flow. - Evaporation of the thin liquid film dominate in the confined flow.

Table A.3: Summary of heat transfer mechanisms in microscale flow boiling as described in literature [26].

The experimental data observation is used to try to explain the physical phenomenon through simplified models. The simplified heat transfer models in micro/mini scale flow boiling are shown below.

For Jacobi and Thome [97] (2002) the nucleate boiling is not the dominant heat transfer mechanism and the heat flux effect can be explained and predicted by the thin film evaporation process occurring around elongated bubbles in the slug flow regime without any nucleation sites. They propose an analytical two-zone model to describe evaporation in microchannels in the elongated bubble (slug) flow regime and they show that the thin film heat transfer mechanism along the length of the bubbles is very dominant compared to the liquid convection occurring in the liquid slugs. Their model predict that the two-phase flow boiling heat transfer coefficient is proportional to q^n, where q is the heat flux and n depended on the elongated bubble frequency and initial liquid film thickness laid down by the passing bubble. So the thin film evaporation heat transfer mechanism, without any local nucleation sites in slug flows, yields the same type of functional dependency as the boiling curve.

Afterwards, Thome et al. [32] (2004) and Dupont et al. [100] (2004) develop a three-zone elongated bubble flow boiling model for slug flow (Figure A.5), that describes the transient variation in the local heat transfer coefficient during sequential and cyclic passage of (i) a liquid slug, (ii) an evaporating elongated bubble and (iii) a vapor slug when film dryout has occurred at the end of the elongated bubble. The local flow characteristics are modeled as a cyclical passage, with constant frequency, of a saturated liquid slug, an elongated bubble with an evaporating thin film at the heated wall, and a dry vapor zone that develops once the liquid film is depleted. The local heat transfer coefficient thus results as a time-averaged value, over the total passage period θ, of these successive heat transfer mechanisms. Heat transfer in the film evaporation zone is postulated as pure conduction through the film's thickness with no presence of bubble nucleation. The authors claime that a slug flow heat transfer coefficient, which may have the same features as in nucleate boiling (for example, by displaying a strong heat flux dependency), is governed by thin film evaporation, i.e. the transient evaporation of a thin liquid film surrounding elongated bubbles is the dominant heat transfer mechanism in slug flow and the model described in [32] (2004) is able to predict the heat transfer data for different liquids without including nucleate boiling. The input parameters required by the model are: the local vapor quality, the heat flux, the internal diameter, the mass flow rate and the fluid physical properties at the local saturation pressure. The main assumptions that have been made in developing the model for the elongated bubble flow are:

- δ_0, the initial thickness of the liquid film, is very small if compared with the inner radius of the channel;
- vapor and liquid travel at the same velocity;

- the heat flux is uniform and constant;
- the fluid is saturated liquid at the entrance of the channel;
- vapor and liquid remain at saturation temperature, neither the liquid nor the vapor is superheated.

This model so far only covers heat transfer in the elongated bubble (slug) flow regime with and without intermittent dryout; even if this is the most dominant flow regime in microchannels, there are other patterns, such as the annular flow, and so further extensions of the model at least to annular flow are necessary.

For Kandlikar (2004) [24] the change of phase from liquid to vapor is associated with a large momentum change due to the higher specific volume of the vapor phase. Evaporation momentum force arises due to the difference in liquid and vapor densities at an evaporating interface. This force caused by the momentum change, namely the evaporating momentum force, is given by the product of evaporation mass flow rate and the vapor velocity leaving to bubble from interface [101], whose direction is opposite to that of vapor leaving into the bubble. The resulting rapid interface motion increases the microconvection heat transfer around the bubble and the resulting force is used in deriving two non-dimensional groups K_1 and K_2.

The evaporation momentum force, the inertia force and the surface tension forces are primarily responsible for the two-phase flow characteristics and the interface shape and its motion during flow boiling in microchannels and minichannels. Figure A.6 shows an evaporating interface occupying the entire channel. For the elongating bubble in microchannel, the evaporating momentum force acting on the meniscus is traditionally deemed to be important to the meniscus motion, as shown in Figure A.7. The magnitude of this force is the highest near the heater surface due to a higher evaporation rate in contact line region between the evaporating and moving meniscus and the heater surface, which has been verified by Wang et al. (2007) [102] and Dhavaleswarapu et al. (2007) [103] independently, they found that “almost 95% of the total heat transfer takes place from 30% of the meniscus region that is close to the contact line”.

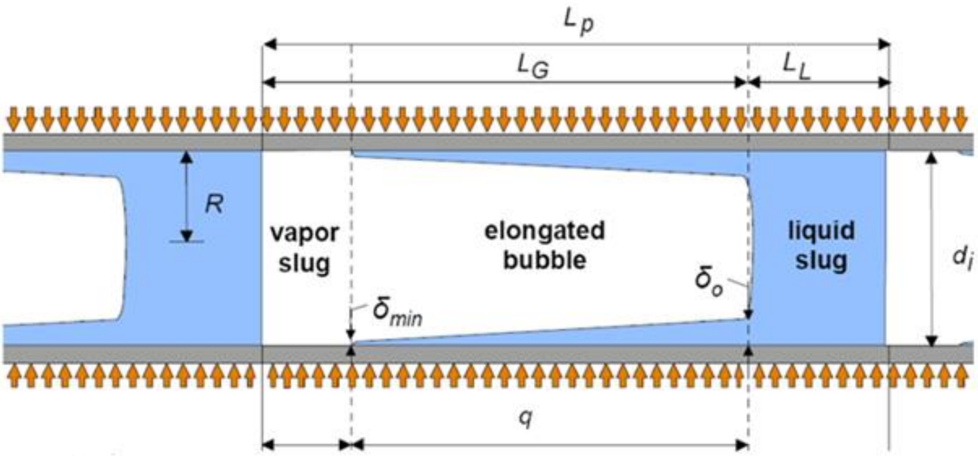

Figure A.5: Three-zone heat transfer model for elongated bubble flow regime in microchannels: diagram illustrating a triplet comprised of a liquid slug, an elongated bubble and a vapor slug [32]. δ_{min} is the film dryout thickness and δ_0 is the initial film thickness.

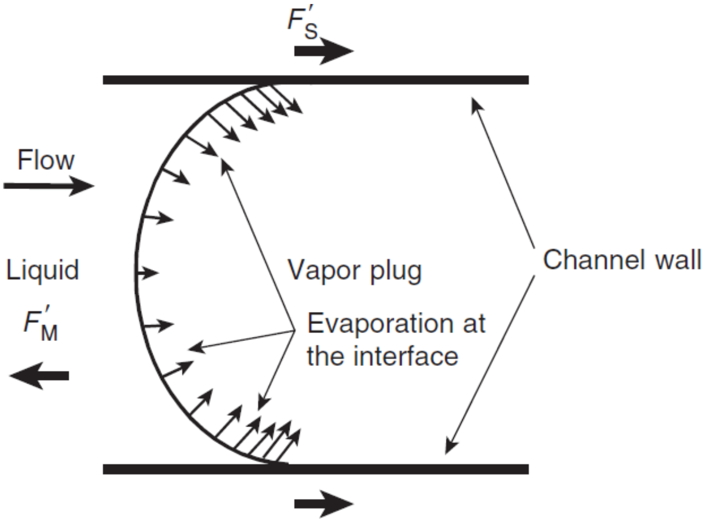

Figure A.6: Schematic representation of evaporation momentum and surface tension forces on an evaporating interface in a microchannel or a minichannel (Kandlikar, 2004 [24]). F'_S is the interfacial force created by surface tension and F'_M is the interfacial force created by evaporation momentum.

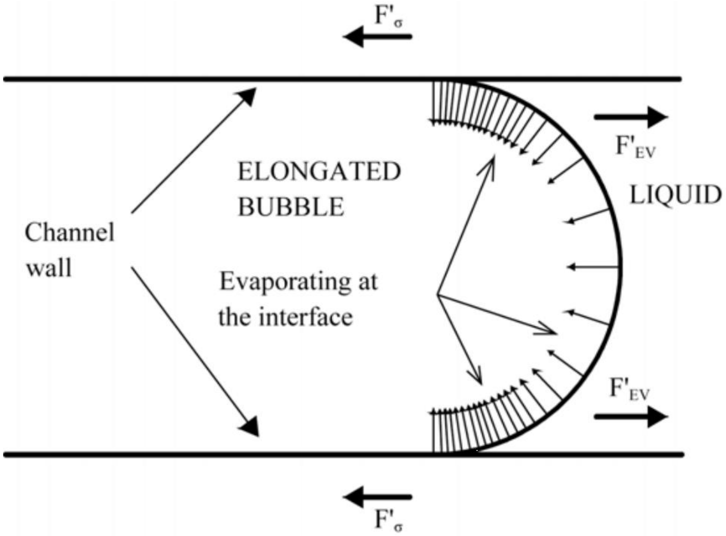

Figure A.7: Forces due to evaporation momentum and surface tension acting on a liquid-vapor interface of an elongated bubble filling the microchannel cross-section [104].

Moreover, a one-dimensional model [40], maintaining the purely convective boiling nature suggest in the three-zone model and including coalescence in the description of the thin evaporating film and thus account for its influence on heat transfer, is proposed by Consolini and Thome [40] (2010). The comparisons for three different fluids (R-134a, R-236fa and R-245fa) gave encouraging results with 83% of the database predicted within a ±30% error band. Some other comparisons between experimental data and three zone model prediction are reported in [36,53,94]. The three-zone evaporation model [32] suggests that, for small channels, the same behavior can be explained if transient evaporation of the thin liquid film surrounding elongated bubbles, without nucleate boiling contribution, is the dominant heat transfer mechanism. Although the three zone model [32] should only be used in the slug flow regime for which it was developed, it was found [94] that the model [32] can make satisfactory predictions at qualities expected to be in the annular flow regime, up to the onset of partial dryout. Anyway, the effect of q'' on the experimental h gets smaller as q'' is increased and this is not well predicted by the model. Cioncolini and Thome are also working on the development of the heat transfer model in annular flow, they presented a turbulence model [105] (2011) that is part of a unified annular flow modeling suite that includes methods to predict the entrained liquid fraction [106] (2010) and the axial frictional pressure gradient [107] (2009).

More recently, Liaofei et al. (2014) [104] investigate the evaporating momentum force and the shear force acting on the meniscus of an elongated bubble in flow boiling in microchannels, whose analytical expressions have been obtained by exploring the nature of the evaporation of meniscus and thin liquid film. The shear force exerted at the meniscus is caused by the liquid supplement to evaporation, in order to take account of the difference between the effective evaporation region and the non-effective evaporation region, the determination of the shear force also needs to be distinguished in two zones. Only the axial component of the shear force needs to be investigated due to the symmetrical characteristic of the meniscus of elongated bubble. For the non-effective evaporation region of the meniscus, there is no vaporization on its interface, thus the liquid flow rate in supplemental liquid passage corresponding to this region can be classified to two parts: one part is to supply the effective evaporation region, while the other part is to provide liquid to the thin liquid layer between the elongated bubble and the channel (Figure A.8).

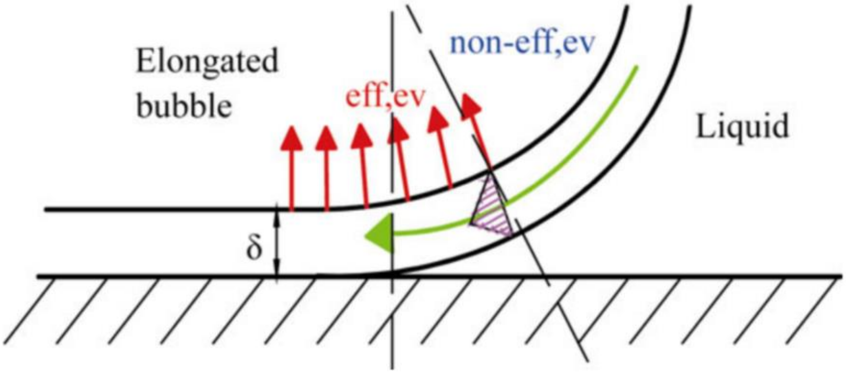

Figure A.8: The liquid supplemental passage and the shear force acting on the meniscus [104].

Magnitude analysis and numerical simulation have been employed to determine the relative importance of the evaporating momentum force and shear force compared to other forces on the meniscus, such as the surface tension force and the gravity force, which is fundamental for the dynamic analysis of the motion of the elongated bubble in microchannel flow boiling. They found that the evaporating momentum force acting on the meniscus can be ignored in analyzing the process of confined bubble elongation and the motion of the meniscus of elongated bubble in microchannel flow boiling, which is contrary to the idea of Kandlikar who claimed that this force plays a major role in the motion of evaporating interface and can cause the reversed flow. Whether the shear force acting on the elongated bubble meniscus should be considered in analyzing confined bubble elongation process, the motion of the meniscus in microchannel flow boiling should be determined according to the applied particular microchannel dimensions, when the hydraulic diameter of the channel is in the range of 10μm to 100μm, it is necessary to take consideration, when in the range of 100μm to 1mm, it is not necessary to consider the shear force generally.

The debate about which mechanism dominates the two-phase flow heat transfer is still open, but it is standardly accepted that the transition from nucleate boiling to convective boiling is linked also to vapor quality [26].

A.3.4 Heat transfer coefficient in micro-/mini- scale flow boiling

The heat transfer coefficient or convective coefficient h is the proportionality coefficient between the heat flux and the thermodynamic driving force for the flow of heat (i.e., the temperature difference, ΔT) and it is used in calculating the heat transfer, typically by convection or phase transition between a fluid and a solid. It is determined from the following equation:

$$h=\frac{q''}{T_W-T_F} \qquad [W/(m^2K)] \qquad \text{(IV)}$$

where $q'' = d\dot{Q}/dA$ is the heat flux (W/m^2), T_W is the wall temperature and T_F is the fluid temperature (K).

The dependency of h on q'' and on x in micro-/mini- scale flow boiling is complex [95,108]. In the nucleate boiling regime the heat transfer coefficient is a function of the heat flux and system pressure, but is independent of vapor quality and mass flux. In the convective boiling regime the heat transfer coefficient depends on vapor quality and mass flux, but is not a function of heat flux. The three-zone heat transfer model proposed by Thome et al. [32] (2004) illustrates the strong dependency of heat transfer on the bubble frequency, the length of the bubbles and liquid slugs and the liquid film thickness.

An increasing in q'' tends to increase h but this is not more true at high x, moreover, the effect of G varies from no effect to an increasing or a decreasing effect [109]. For $x < 0.5$, h increases with q'' and decreases, or is relatively constant, with respect to x; for $x > 0.5$, h decreases sharply with x and it does not depend on q'' or G. The average heat transfer coefficient of R-410A flowing through a horizontal aluminium rectangular multiport mini-channel having 3.48mm hydraulic diameter during evaporation tend to increase with increasing average quality, mass flux, and heat flux, but tended to decrease with increasing saturation temperature [110]. The pressure drop increased with increasing the mass flux, but decreased with increasing the saturation temperature, and the heat flux has no significant effect on the pressure drop. The summary of the behavior of heat transfer coefficient recently presented in literature is reported in the following table.

Authors, test fluid and test section diameter	**Heat transfer coefficient depends on**
Bao et al. [94] R-11 and R-123 d = 1.95mm	- q'' - independent of G - independent of x
Bertsch et al. [109]	- on x, h decreases for x > 0.5 - slightly on G, h increases weakly with G - on q'', h increases with it
Consolini et al. [111] R134a, R236fa, R245fa d = 510μm and d = 790μm	- minimal effect of G and x on h
Dupont et al. [112] d = 0.5-2 mm in increments of 0.166mm	- h decreases with diameter for x < 0.04 - for 0.04 < x < 0.18 h increases, reaching a peak, and then it decreases with the diameter - h increases with diameter for x > 0.18 Depending on the thermophysical properties of the fluid and the operating conditions, each zone can disappear or move as a function of quality x
Harirchian and Garimella [99]	- the microchannel cross sectional area, h increases with decreasing cross sectional area for microchannel smaller than 0.089 mm^2 while for microchannel area > 0.089 mm^2 h is independent of channel dimensions - on q'', h increases with it
Harirchian and Garimella [113]	- on x for R-134a, h increases with increasing of x till vapor quality of 20% after which it drops for further increases in x

	- on x for FC-77, h increases with increasing exit vapor quality until the point of dryout after which h decreases
Huo et al. [114] R-134a d = 2.01 and d = 4.26mm	- h has a complex behavior especially for x > 0.2. The trends of h versus x are the same as in [94], but the values of h are different.
Lee et al. [91]	- on x, h decreases with it - on q’’, h increases with it
Lin et al. [95] [108] R-141b d = 1.1mm	- strongly on x at low and high q’’. At low q’’ h has a peak at about x ¼ 0.6. At high q’’ h has a peak for small x and then fell with x and becomes independent from q’’ - at intermediate q’’ is independent on x
Ong et al. [41] R134a, R236fa, R245fa d = 1.030mm	- on q’’ at low x R245fa - h increases with q’’ for a wide range of x for R134a and R236fa at low G - the fluid properties. In fact for low x, h for R134a is the highest followed by R236fa and R245fa reflecting their values of reduced pressure - on G for R134a and R236fa. It appears that the transition to annular flow occurs at lower x with increasing G. h increases after the transition occurrence for both fluids
Shiferaw et al. [94] R134a d = 2.01mm and d = 4.26mm	- on q’’ till x = 0.5 for the 4.26mm tube and till x = 0.3 for the 2.01mm tube. - on system pressure (h increases with the pressure) - independent on x for x < 0.5 for the 4.26mm tube and for x < 0.3 for the 2.01mm tube - independent on G for low quality
Shiferaw et al. [53] R134a d = 1.1mm	- h increases with the pressure (probably due to the fact that bubble departure diameter decreases as the system pressure increases) - on q’’ - for low q’’ and G and for x < 0.5, h is independent on x
Yen et al. [96]	- on x

HCFC123 $d = 210\mu m$, $d_h = 214\mu m$	- on the shaped cross-sections for $x < 0.4$. In this range h is higher for the square microchannel because corners in the square microchannel acted as effective active nucleation sites

Table A.4: Summary of the behavior of heat transfer coefficient recently presented in literature [26].

Recently, Harirchian and Garimella [388] (2012) proposed flow regime-based models for predictions of heat transfer coefficient in the annular and annular/wispy-annular regions while they suggest the empirical correlation of Cooper [116] (1984) for the bubbly flow and a modified three zone model of Thome et al. [32] (2004) for the slug flow region. Farahani et al. [81] (2014) used an inverse heat conduction method for determining the local convective boiling heat transfer coefficient in mini-channel for pure water, copper nanofluid by using three different concentrations of nanoparticles: 5mg/L, 10mg/L and 50mg/L. Conjugated gradient method with adjoint equation is used to solve the IHCP and estimate directly the space-variable convective heat transfer coefficient. Direct estimation local convective boiling heat transfer coefficient is a nonlinear inverse heat problem. The uncertainties in the estimated in heat transfer coefficient are calculated using bias and variance errors.

Since the two-phase flows are often in non-equilibrium conditions (oscillations, regime variations, lack of fully developed conditions) it would be better to define a time and space averaged heat transfer coefficient, called HTC, rather than a convection coefficient, which is directly linked to the Newton laws, i.e. to equilibrium, stationary conditions. The overall heat transfer coefficient HTC is determined from the following equation:

$$HTC= \frac{q}{A \cdot \Delta T_{ML}} \qquad [W/(m^2K)] \qquad (V)$$

where q is the heat transfer rate (W), A the heat transfer surface area (m^2) and ΔT_{ML} the log mean temperature difference (K). However many papers are referring in any case to a convection coefficient h, even if for Baldassari and Marengo [26] it is, for flow boiling, not appropriate.

A.4 Heat exchange with oscillating liquid-vapor interfaces

As repeatedly mentioned previously, the recent marked increase in power dissipation of electronic devices has drawn a great deal of attention for developing highly efficient miniature heat transport devices. Computer chips in compact information devices for personal use may dissipate more than 100W of power, with a surface heat flux on the order of 100W/cm^2, which must be transported to the heat radiation part (including fins and fans) through the narrow space between electronic components so that the chip temperature does not exceed the allowable limit. A conventional heat pipe, for example, having a diameter of 3mm and a length of 300mm transports 12–13W with an effective thermal conductivity of approximately 40 times the thermal conductivity of copper in the horizontal orientation. However, the limit of the heat transport rate for this type of heat pipe, which uses capillary action for the return flow of liquid, decreases markedly as the tube diameter is decreased. Therefore, the heat pipes based on different principles have been proposed, which may be applicable to smaller tubes, and a number of studies on heat pipes are conducted [117-121]. Heat transport tubes using the oscillating flow of the working fluid, particularly due to the self-excited oscillation caused by evaporation and condensation of the working fluid, are capable of realizing high heat transport performance. This type of heat pipe is referred to as pulsating (or oscillating) heat pipe (PHP or OHP). A pulsating heat pipe (PHP) is an apparently simple looking heat transfer device, however with complex internal thermo-hydrodynamic transport processes, responsible for the self-sustained thermally driven oscillating two-phase Taylor bubble flow, which in turn, leads to its unique heat transfer characteristics. Research on PHP has received substantial attention in the recent past, due to its unique operating characteristics and potential applications in many passive heat transport situations [122-124]: its effective thermal conductivity can sometimes reach as much as 200 times (for bottom heating in vertical orientation) the thermal conductivity of copper without any supply of oscillation work. A PHP consists of a simple capillary tube, with no wick structure, bent into many turns, and partially filled with a working fluid (for constructional details, refer to [390]). A schematic representation of the PHP is show in Figure A.9.

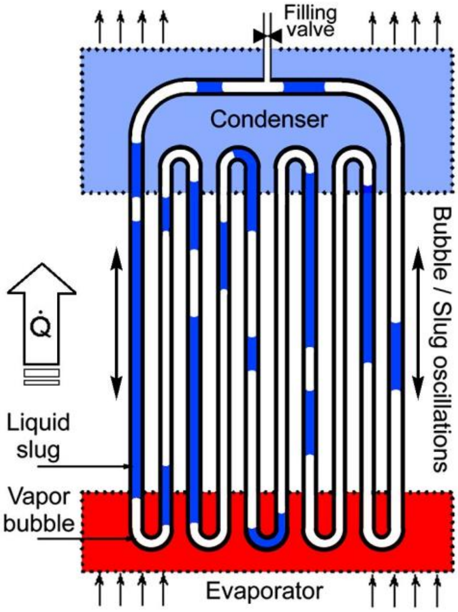

Figure A.9: Schematic representation of the PHP [135].

When the temperature difference between the heat source and the heat sink exceeds a certain threshold, the vapor bubbles and liquid plugs present inside the capillary tube begin to auto-oscillate back and forth. Heat is thus passively transferred, not only by latent heat exchange like in conventional wicked heat pipes, but also by sensible heat transfer between the wall and the fluid [125,126]. No external power is required to drive the device, internal oscillations being fully driven by the existing thermal non-equilibrium which is sustained inside the system due to external heating and cooling. Compared to other passive heat transfer solutions, PHPs are quite simple in construction, and thus, more reliable and cheap. The meandering PHP, however, must be bent into many turns for stable operation, and the oscillation behavior is very complex. Moreover, in the case of a horizontal orientation, the oscillation becomes sometimes unstable or almost stops due to the accumulation of the generated vapor in the heating section [127]. At present there are no theoretical models or correlations available that can predict the thermo-hydrodynamic transport behavior of PHPs. This prevents the widespread use of PHPs in industrial applications. Comprehensive and reliable mathematical design tools can only be formulated if the nuances of its operating principles are well understood, which, at present, remain rather inadequate. In this context, several authors have focused their efforts on understanding the simplest possible PHP structure, consisting of one liquid plug and one vapor bubble, also termed as a ‘unit-cell’. Simplistic mathematical models based on the balance equations for such a simple unit-cell system are presented [126,128,129]. The vapor-phase was considered as an ideal gas. The pressure fluctuations inside the system was introduced by modeling the evaporation of a thin liquid film left on the wall when the liquid plug leaves the evaporator. Many investigations have been conducted concerning on the oscillation in a pulsating heat pipe with open end [130-133]. Effort has been devoted primarily to the modeling of the system that causes self-sustained thermally driven oscillations. It has been shown that a single vapor slug occupies the closed end side on which the heating section (maintained at a constant temperature) is located, and the evaporation and condensation over a liquid film left on the tube wall during the growth of the vapor slug toward the open end plays an important role in the oscillation of the liquid plug. However, the occurrence and stagnation of the dry-out region in the heating section may cause a fatal increase in the tube wall temperature under the imposed heat flux conditions. The structure of the heating section to ensure the stable oscillation with large amplitude leading to high heat transport performance without any dry-out, and the heat transport mechanism of the resulting oscillation with such large amplitudes as significant portion of the liquid plug will be pushed out from the open end to be exchanged with the liquid of the cooling section have not been clarified yet. Firsts experimental results of such a system consisting of a 2.0mm ID capillary tube, heated on one hand and cooled on the other end, are presented by Das et al. [392] and Rao et al. [134]. They obtain thermally driven auto-oscillations in such a ‘unit-cell’ system under a definite range of operating experimental conditions. The dynamic contact angle of the meniscus is totally different in the downward and the upward stroke. In the upward stroke, the receding dynamic contact angle of the moving meniscus is close to 90° and the vapor space gets compressed once the meniscus leaves the condenser. There is no thin film seen and no phase change. In the downward stroke, the meniscus shows strong curvatures and lays a thin liquid film along the tube inner wall. As the meniscus goes down the evaporator, there is a strong presence of evaporation.

Thus, contrary to obvious but erroneous interpretation (which will come if the vapor space is modeled as an ideal gas), downward stroke of the meniscus (leading to an increase of internal volume of the vapor bubble) actually leads to an increase of the pressure inside the vapor space, due to rapid evaporation. The evaporation mass flux experienced in the vapor space is not only due to the heat flow by conduction from the wall to the interface, but also to the thermal non-equilibrium between the vapor and the liquid. If the vapor temperature is greater than the liquid temperature, the net mass flux of evaporation will be lower than conduction–induced evaporation mass flux, as the thermal non-equilibrium leads to condensation. Otherwise, the mass flux is due to both conduction through the film and thermal non-equilibrium. The simplified analysis of unsteady heat transfer in the liquid thin film shows the importance of measuring the time-evolution of the temperature of the vapor with a high time-resolution and a good accuracy which remains a challenge today under such experimental conditions.

A.5 Wettability effect in minichannels

Mini/micro/nanostructures have been extensively studied to amplify the intrinsic wettability of materials to create superhydrophilic or superhydrophobic surfaces. Such extreme wetting properties can influence the heat transfer performance during phase-change which is of great importance in a wide range of applications, including thermal management, building environment, water harvesting and power production. Kandlikar [136] investigated the scale effect of various forces during flow boiling in microchannels. Using scale analysis, he explained that the relative magnitude of the surface force is larger than that of the volume force as the channel diameter decreases. Coleman and Garimella [70] reported that the slug flow regime in mini-microchannels has broader coverage than that in macrochannels at the two-phase flow map. These studies showed that as the tube diameter becomes smaller, the capillary effect starts to play an important role in changing of two-phase flow patterns. In such a case, the surface property of the tube wall as well as the combinations of the gas and liquid is another important factor to be considered in determining the flow pattern of two-phase mixtures. The surface tension force tends to maintain the bubbles at the solid wall, increasing the frictional pressure drop of the moving fluid. In mini and microchannels, the flow regime of a two-phase flow is also influenced by surface wettability. In particular, slug flow in a two-phase flow regime varies according to surface wettability. In hydrophilic microchannels, slugs are generated with liquid films, but in hydrophobic microchannels, they are generated with triple-lines instead of liquid films. Moreover, a slug with a triple-line exhibits a higher pressure drop than a slug with a liquid film, due to the motion of the triple line. The pressure drop of a triple-line is affected by the dynamic contact angle, channel diameter, and fluid properties. Therefore, superhydrophilic surfaces have been of interest to achieve thin film evaporation with high heat fluxes. Meanwhile, superhydrophobic surfaces with dropwise condensation promises higher heat transfer coefficients than typical filmwise condensation. It is possible to say that the surface wettability affects the flow patterns [137,138], the pressure drop [139-142] and flow boiling [143,144] in a two-phase flow, especially with capillary dimensions. The wettability certainly affects a two-phase flow passive device like the Pulsating Heat Pipe, were the fluid motion and the heat exchange are linked together. There are several works reported on the effect of the tube materials on two-phase flow behavior, the following are the major works.

A.5.1 Flow patterns

Barajas and Panton (1993) [145] supplied air–water mixtures through the four different circular minichannel materials having different liquid contact angles such as pyrex, polyethylene, polyurethane and FEP (Fluorinated Ethylene Propylene, a kind of Teflon). The inner diameter of the tubes was 1.6 mm, and the liquid contact angles were 34°, 61°, 74° and 106°, respectively. The rivulet flow was reported as a new flow pattern that replaced the wavy annular flow with the larger contact angle. Except for the plug-slug flow transition, the transition boundaries between the two-phase flow patterns in the FEP tube (poorly wetting tube) appeared substantially different from those in other tubes. In other words, there is a considerable increase in the rivulet flow region by reduction of the annular flow region, and the transition boundaries between slug and rivulet flows and between slug and annular flows move to the lower range of the gas superficial velocity. Nevertheless, the influence of the contact angles on the transition of the flow patterns was not analyzed quantitatively.

Iguchi and Terauchi (2001) [146,147] evaluated the influence of wall surface wettability on flow regime transition in vertical air–water two-phase flows in 5–15mm diameter pipes, and proposed a bubbly-to-slug flow transition criterion for hydrophobic pipes with the contact angle higher than 100°.

Cubaud et al. (2004-2006) [148,149] investigated flow patterns in rectangular microchannels with different modified surfaces. They used water and air as working fluids and Teflon, glass and silicon as the surfaces of microchannels. Their mixer was cross shaped, consisting of two liquid ports and one gas port. They compared flow regimes for hydrophilic and hydrophobic surfaces. A new flow pattern was observed in the hydrophilic microchannel, and they called it wedging flow. They explained that the new flow pattern was metastable and could be broken by nucleation of dewetting patches. Also, they observed unstable flow patterns in the hydrophobic microchannel, and bubbles were not lubricated, with their motion subject to contact line friction. However, their microchannel was not fabricated from a single material in order to allow visualization, and the microchannel was not straight but serpentine.

Allen and Son [150] (2007) carried out visualization of adiabatic water/nitrogen two-phase flow patterns in microchannels with different wettabilities. They used conventional 330μm circular microtube and 500μm rectangular microchannels. Their hydrophobic and hydrophilic microchannels had static contact angles of approximately 120° and 20°, respectively. Adiabatic conditions were achieved using water and nitrogen as liquid and gas phase, respectively. They used a converging-nozzle-type mixing region to minimize the entrance effect on the flow downstream of the microchannel. They observed that liquid may be isolated in a corner or cover an entire wall of the rectangular microchannel; they called this separated flow. In their results, the pressure drop in the hydrophobic microchannel was higher than that in the hydrophilic microchannel except for separated flow regime. They observed bubbles which were not surrounded by liquid film in the hydrophobic microchannel. Also, new flow pattern similar to stratified flow was observed, where the phase separation was not governed by gravity. This flow pattern was found in only the hydrophobic rectangular microchannel.

Ide et al. (2008) [151] conducted experiments on adiabatic two phase flow in different wetting circular conventional microtubes. A 100μm fused silica microtube and a silane-treated microtube were used. And a conventional Tee connector was used as the mixer. Their results indicated that the slug regime was wider and that the pressure drop was higher with the hydrophobic surface than with the hydrophilic surface.

Lee and Lee (2008) [137] experimentally evaluated the influence of the surface wettability on the transition of two-phase flow pattern in round mini-channels. They tested three capillary tubes: an highly wetting tube (normal glass tube with a θ<50°, ID=1,46mm), a marginally wetting tube (50°<θ<90°, ID=1,59mm) and a low wetting tube (Teflon, θ>90°, ID=2mm). They visualized the flow patterns with a high-speed camera using different liquid velocity (from 0.004m/s to 0.4m/s) and gas velocity (from 0.5m/s to 50m/s). The flow patterns differed between the hydrophilic case and the hydrophobic case, especially when the gas velocity was high. Through a series of experiments, all the flow patterns were classified into two groups, i.e. the wet- and dry-flow regimes. The wet-flow regime includes the wet-plug, wet-slug and annular flows as well as the bubbly flow. The dry-flow regime includes the dry-plug, dry-slug and the rivulet flows as well as the wavy flow. For the highly wettable case, the flow pattern map for air–water flow in the glass tubes (A+W+G, θ = 30°), with ranges of the superficial velocities of water and air of 0.004–0.4m/s and 0.5–50m/s respectively, cover the regimes of plug, slug, annular and wavy flows (Figure A.10a). In the plug flow regime (point A Figure A.11a), the elongated bubbles with a liquid film along the periphery were seen. As the gas flow velocity was increased, slug flows appeared (point B Figure A.11a, Figure A.11b), and finally, the annular velocity was visualized (point C Figure A.11a, Figure A.11c). The liquid film always exists at the inner wall because the glass surface is highly wettable due to the high surface energy of the glass [152]. Nevertheless, as the water flow rate becomes very small (below the liquid superficial velocity of about 0.018m/s), the wavy flow is observed with the upper surface remains dry (point D Figure A.11a, Figure A.11d).

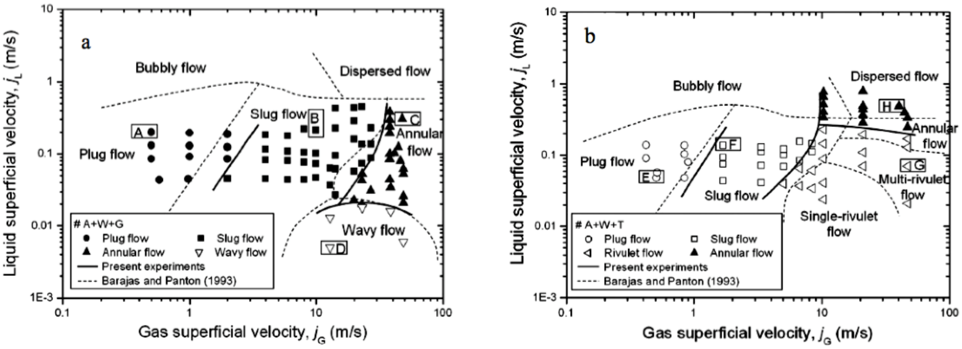

Figure A.10: Flow pattern maps: (a) air–water flow in the glass tube (A +W + G, θ = 30°); (b) air–water flow in the Teflon tube (A +W + T, θ = 110°) [137].

The flow patterns appeared different for the hydrophobic case: air–water mixture in Teflon tube (A+W+T, θ = 110°) (Figure A.12b). The superficial velocities of air and water cover 0.4–47m/s and 0.02–0.8m/s respectively, and the flow regimes at large gas flow rates appear different from those with the highly wetting cases. That is, the rivulet flow regime covers a large portion of the map. In the plug flow regime (point E Figure A.12b), the liquid film around the vapor bubble did not exist because of the low Teflon surface energy. As the flow rate increased, the slug flow regime appeared (point F Figure A.12b), in this case the liquid slugs were formed at the bottom of the tube, while the upper wall still remained dry. When the gas velocity further increased, it was observed a rivulet flow (point G Figure A.12b). If the liquid superficial velocity becomes higher than about 0.28m/s, the small rivulets are merged to form a liquid film with some dry spots (point H Figure A.12b). It should be noted that, unlike the highly wetting cases, a continuous liquid film is not observed for the plug, slug and rivulet flows.

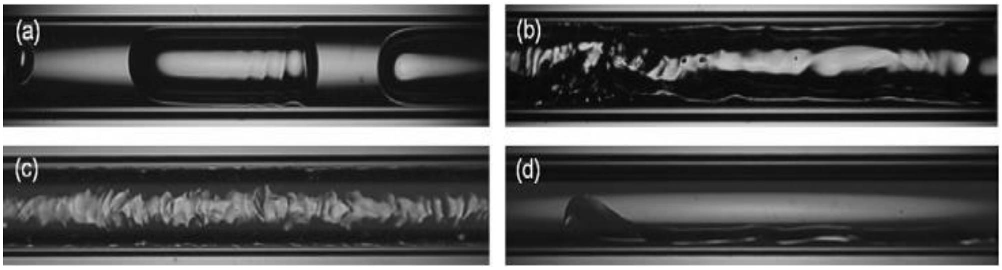

Figure A.11: Hydrophilic case (A+W+G, θ = 30°): visualization of flow patterns at points A–D shown in Figure A.10a: (a) plug flow with the wetted wall (point A); (b) slug flow with the wetted wall (point B); (c) annular flow (point C) and (d) wavy flow with the upper wall in dry condition (point D) [137].

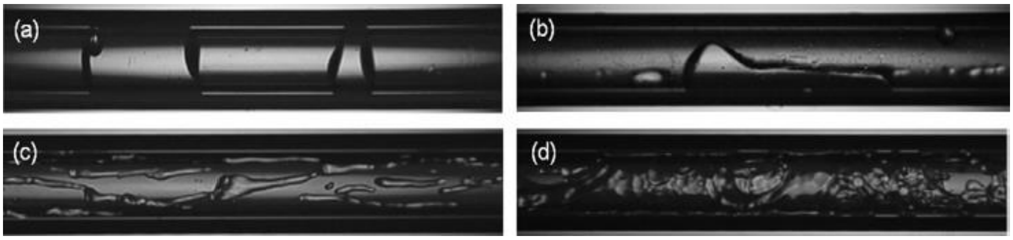

Figure A.12: Hydrophobic case (A+W+ T, θ = 110°): visualization of flow patterns at points E–H shown in Figure A.10b: (a) plug flow with the gas–wall contact area in dry condition (point E); (b) slug flow with the gas–wall contact area in dry condition (point F); (c) rivulet flow (point G) and (d) annular flow with dry spots (point H) [137].

The Figure A.13 shows visualization and illustration of the flow patterns in the three tubes. It is clearly possible to see the liquid film surrounded the vapor bubble in the hydrophilic case, while the surfaces having low wettability had the inner surface completely dry. In Figure A.14 a schematic illustration of the two-phase flow patterns based on Lee and Lee [206] is shown.

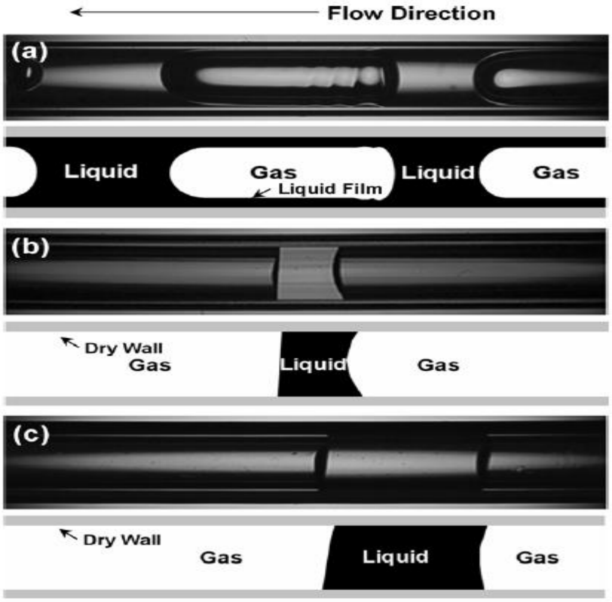

Figure A.13: Visualization and illustration of plug flows of air–water mixture. (a) Glass tube (wet-plug flow, j_G = 0.498m/s, j_L = 0.200m/s), (b) polyurethane tube (dry-plug flow, j_G = 0.451m/s, j_L = 0.024m/s) and (c) Teflon tube (dry-plug flow, j_G = 0.504m/s, j_L = 0.0478m/s) [140].

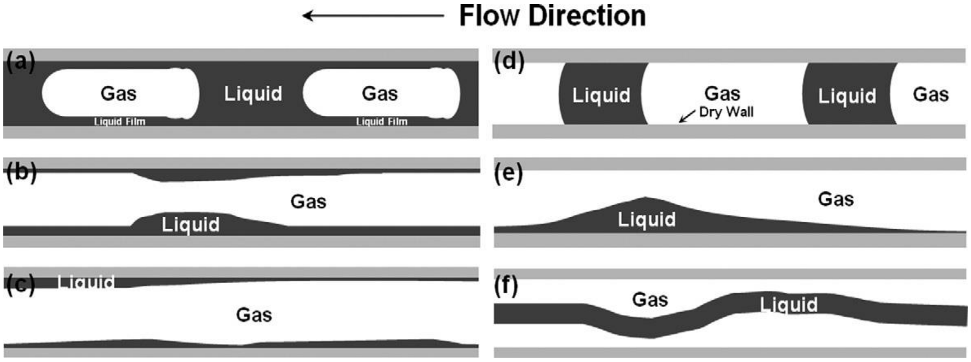

Figure A.14: Illustration of two-phase flow patterns based on Lee and Lee [137]. In the wet-plug flow regime (a), the gas plugs with a liquid film along the periphery are seen. As the gas flow rate is increased, the wet-slug flow (b) appears, and eventually, the flow pattern is changed to the annular flow (c).

In other words, in the wet flow regime, the liquid film exists at the inner wall. On the other hand, in the dry-flow regime, the gas portion was dry wall condition. In the dry-plug flow regime (d), the tube wall is dry at the portion of gas plug. As the air flow rate is increased, the dry slug flow (e) appears. In this case, the liquid slugs are formed at the bottom of the tube while the upper wall still remains dry. When the air flow rate is further increased, the flow pattern is changed to the rivulet flow (f) [404].

Different flow patterns were evaluated also for non-capillary tubes (2008) [138] (inner diameter of 20mm and length of the test pipes 2800mm, with a purified water as working fluid). The effect of wall surface wettability was evaluated on flow characteristics in a vertical upward gas–liquid two-phase flow using three pipes with different wettability; one with an acrylic inner surface (43°<θ<47°), one with a hydrophilic inner surface (a glass pipe coated with hydrophilic coating material, θ<7°) and one with a hydrophobic inner surface (synthetic resin material, provided by NTT-AT applied to the inner surface of an acrylic pipe, 135°<θ<150°). It was measured flow regime, frictional pressure loss and void fraction (the ratio between the vapor phase and the liquid phase; higher the void fraction, higher the vapor phase) in these pipes and discussed the wettability effect on the flow parameters. The flow patterns in the tubes were different for the different wettability. They observed that in the hydrophilic pipe, the slug flow to churn flow transition boundary was shifted to a higher gas velocity at a given liquid velocity, whereas the churn flow to annular flow transition boundary was shifted to a lower gas velocity at a given liquid velocity. In the hydrophobic pipe, an inverted-churn flow regime was observed in the region where the churn flow regime was observed in the acrylic pipe, while a droplet flow regime was observed in the region where an annular flow regime was observed in the acrylic pipe. At a high gas flow rate, the mean void fraction in the hydrophobic pipe was higher than in the acrylic pipe. Also, in the hydrophobic case, in the so called bubbly flow region (lowest fluid velocity), some vapor bubble remained attached on the tube. Figure A.15 shows images taken at superficial gas and liquid velocities respectively of 10m/s and 0.1m/s. An annular flow was observed in the acrylic and hydrophilic pipes, with a thin liquid film on the pipe wall and a continuous gas flow in the pipe core region. In contrast, no liquid film was observed on the wall of the hydrophobic pipe. The liquid phase flowed upward as droplets in a continuous gas phase.

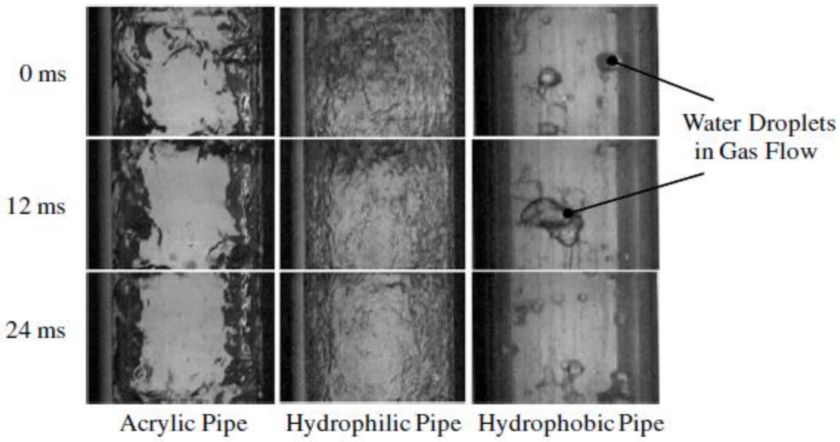

Figure A.15: Different flow patterns in the 3 tubes (Liquid velocity was equal to 0,1m/s, gas velocity=10m/s) [138].

In addition to these studies, it should be mentioned that some studies on the effect of wettability on oil–water flows have been carried out in the field of petroleum engineering. Govier et al. (1961) [154] obtained a flow regime map in an oil–water two-phase flow and Charles et al. (1961) [155] developed the drift-flux correlation in a horizontal oil–water two-phase flow.

A.5.2 Pressure drop and heat transfer

Son and Allen (2005) [141] have reported that the moving contact lines dissipate much more energy than the inertia force or the viscous force does. Consequently, the pressure drop in hydrophobic case appeared larger than in hydrophilic case. In other words, the surface wettability affected the morphologies of two phase flow patterns, and eventually resulted in large difference in pressure drop. That is, the pressure drop of the dry-plug flow having the moving contact lines appeared much larger than the wet-plug flow. Rapolu and Son (2007) [139] investigated the effect of the surface wettability on the pressure drop of two-phase plug flow. They performed experiments of adiabatic co-current flow of air-water mixtures in horizontal microchannels of both square and circular geometries of 700mm hydraulic diameter, for various liquid volumetric flow ratios. They observed for the hydrophilic case that a liquid film covers the wall surface and the gas bubbles slide over the liquid film; thus, the energy dissipation becomes small. On the other hand, for the hydrophobic case, the contact lines (between the gas, liquid and solid wall) play an important role in energy dissipation as the liquid plugs move along the dry surface (in accordance with the flow visualization done by Lee and Lee [137]). Consequently, the pressure drop in hydrophobic case appears larger than in hydrophilic case. In other words, the surface wettability affects the morphologies of two-phase flow patterns, and eventually results in large difference in pressure drop. That is, the pressure drop of the dry-plug flow (having the moving contact lines) appears much larger than the wet-plug flow. However, dependence of the pressure drop of the two-phase plug flow on the surface wettability has not been reported quantitatively.

Lee and Lee (2008) [140] investigated the pressure drop of the two-phase plug flow for round mini-channels made of three kinds of tube materials such as glass, polyurethane and Teflon. The inner diameters of tubes were 1.78mm for the glass tube, 2.16mm for the polyurethane tube and 1.62mm for the Teflon tube. Air and water were used as test fluids. The ranges of the superficial velocities of air and water were 0.134–0.536 and 0.060–0.154m/s for the glass tube, 0.041–0.250 and 0.006–0.021m/s for the polyurethane tube and 0.089–0.243 and 0.022–0.055m/s for the Teflon tube, respectively. They measured the pressure drop using a differential pressure transducer in the range of 0.5-2.5kPa. In the wet-plug flow regime (with the glass tube), the pressure drop became larger with the increases of the superficial velocities of gas and liquid, due to the increase in the frictional pressure drop (Figure A.16a). In the dry-plug flow regime (with the polyurethane and Teflon tubes), the pressure drop become larger either by increasing the liquid superficial velocity or by decreasing the gas superficial velocity (Figure A.16b) due to the increase of the number of the moving contact lines in the tubes: in this flow regime, the energy dissipation by the moving contact lines played an important role in determining the pressure drop. The pressure drop reaches the highest value in the dry-plug flow, i.e. inside the tubes with low wettability, and higher the pressure drop, lower the gas superficial velocity. This is explainable as follows: the moving contact lines dissipate much more energy than the inertia force or the viscous force does [141]. From flow visualization analysis, lower the gas velocity, higher the number of the moving contact lines higher the pressure drop. The energy dissipation by the moving contact lines plays an important role in determining the pressure drop for the low-wettability case. This implies the pressure drop by the moving contact lines is an important parameter to be considered in predicting the pressure drop in the dry-plug flow regime [404]. At two-phase flow in microchannels, slug flow regime is different for wettability of surface. A slug in a hydrophilic microchannel has liquid film. However, a slug in a hydrophobic microchannel has no liquid film instead, the slug makes higher pressure drop. It is however to specify that in this work, the different tubes with different wettability had no the same ID dimensions. The ID dimensions should be the same, since the pressure drops and the capillary forces are dependent with the ID^2.

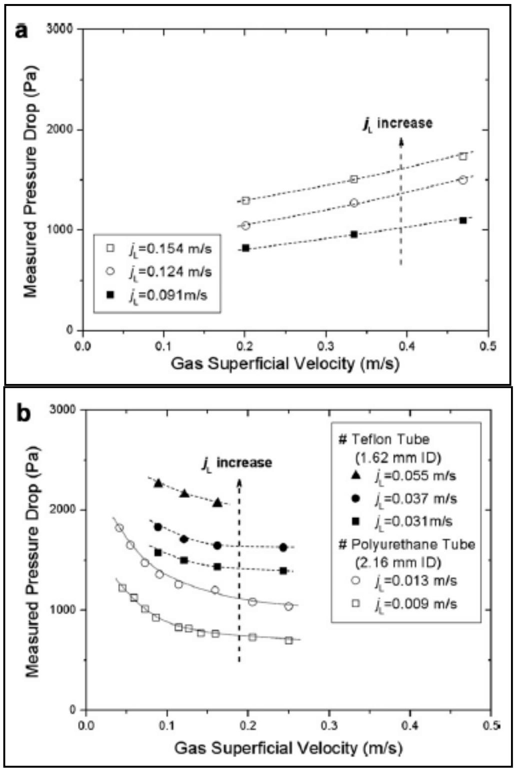

Figure A.16: Measured pressure drop. (a) Wet-plug flow (glass tube (1.78mm ID)) and (b) dry-plug flow (polyurethane (2.16mm ID) and Teflon (1.62mm ID) tubes). j_L is the liquid flow velocity [140].

Yu et al. (2010) [142] conducted experiments in adiabatic conditions with round channels of various diameters (0.546, 0.763, 1.018, 1.555, 2.075mm). To modify the wettability, they utilized mixtures of air and various fluids such as water or ethanol. In order to understand the pressure drop of motion of triple-lines, they utilized various superficial velocity (liquid velocity = 0.01~0.4m/s). Using experimental data, they calculated the pressure drop due to displacement of the contact lines and observed that this pressure drop increases with the static contact angle.

Liu et al. (2011) [156] investigated the flow boiling modes in three microchannels with identical sizes at 105x1000x30000μm but at different wettability. The authors tested two different contact angles, 36°and 103°. They observed cyclic flow process which leads to cyclic temperature and pressure fluctuation when the channel is hydrophilic.

Choi et al. (2011) [143] studied the surface wettability effect on flow boiling in rectangular microchannels fabricated with a photosensitive glass to visualize flow pattern. The hydraulic diameter and length of the microchannel were approximately 500μm and 50mm, respectively. The authors observed that the pressure drop in the hydrophobic (contact angles of 105°) rectangular microchannel was higher than that in the hydrophilic (contact angles of 25°) rectangular microchannel, which is highly related with unstable motions of bubble and liquid film. The effect of wettability on two-phase pressure drop is strong in the lower quality region, which included relatively short elongated bubbles. The main reason for the higher pressure drop in the hydrophobic microchannel is the dissipation of moving triple-lines. The boiling heat transfer coefficient in the hydrophobic rectangular microchannel was higher than that in the hydrophilic rectangular microchannel, which is highly related with nucleation site density and liquid film motion. The main heat transfer considerations are the nucleation density and departure frequency of bubbles. The number of bubble in the hydrophobic rectangular microchannel was higher. Bubble was not lubricated by liquid film, so the motion of bubbles was unstable. Also, bubble departure at a mass flux of 25kg/m^2 s was more difficult than at mass flux of 75kg/m^2 s. Sometimes the bubbles were trapped on the hydrophobic surface. Therefore, the heat transfer in the hydrophobic microchannel was enhanced due to higher number of bubble, except at the lower mass flux condition. In the higher quality region, the main flow pattern is long elongated bubbles, which is similar to annular due to their long length. The main heat transfer mechanism is film evaporation. The motion of the liquid film surrounding bubbles in the hydrophobic microchannel was unstable. Moreover, nucleation was observed in the liquid film. This motion is associated with enhancement of the heat transfer in the hydrophobic microchannel. A delay of local dryout on the hydrophobic microchannel was observed, which also contributes the enhancement of heat transfer at the same quality.

Choi et al. (2011) [157] studied water liquid and nitrogen gas flows with T-junction mixer in rectangular microchannels with different wettabilities. The rectangular glass microchannels were fabricated using MEMS (Micro-Electro-Mechanical System) fabrication techniques from photosensitive glass (most experiments have used conventional microtube due to limitations of visualization and fabrication, however, conventional microtube has higher uncertainty, especially rectangular shape, for this reason they used MEMS fabrication techniques to visualize two phase flow pattern in well controlled rectangular channel), whose surface is hydrophilic. The surface of one was silanized using octadecyl-trichloro-silane (OTS) to prepare a hydrophobic microchannel. The two-phase flow pattern was visualized with a high-speed camera and a long distance microscope. The frictional pressure drop in the microchannel was measured directly with embedded pressure ports. The flow pattern and the pressure drop were both considered in adiabatic flow in the rectangular microchannels with different wettabilities. The flow pattern and pressure drop in the hydrophobic microchannel were totally different from those in the hydrophilic microchannel. The two-phase flow patterns were highly affected by surface wettability. In the hydrophilic microchannel, the major flow patterns were bubbly, elongated bubble and liquid ring flow. In the hydrophobic microchannel, the major flow pattern was stratified flow, which was governed by capillary force and hydrophobicity. The void fraction of stratified flow in the hydrophobic microchannel was lower than that in the hydrophilic microchannel. The pressure drop was higher in the hydrophilic microchannel than in hydrophobic microchannel. The pressure drop of stratified flow regime in the hydrophobic microchannel has monotonic behavior and has less interactional effect than bubble behaviors in the hydrophilic microchannel. The surface wettability is a critical parameter in determining flow pattern, especially in microchannels, and the two-phase flow pattern is closely related with the pressure drop.

Phan et al. (2011) [144] performed an experimental analysis to study the effects of surface wettability on two-phase pressure drop of flow boiling of water at atmospheric pressure. The test channel is a single rectangular channel 0.5mm high, 5mm wide and 180mm long. The mass flux was set at 100kg/m^{2}s and 120kg/m^{2}s, respectively. The base heat flux varied from 30 to 80kW/m^2. Water enters the test channel under subcooled conditions. The study has been performed at low exit vapour quality (less than 0.1). The samples are either hydrophilic like Polydimethylsiloxane (SiOx), Titanium (Ti), Diamond-Like Carbon (DLC) or hydrophobic like Polydimethylsiloxane (SiOC). These surfaces have static contact angles of 26°, 49°, 63°and 104° (see Table A.5), respectively. It was observed that the total two-phase pressure drop significantly increases with the static contact angle. In particular, the average deviation between the highly-wetted and the unwetted surfaces is about 170% (Figure A.17). To explain this observation, the "wetting pressure drop", caused by the surface tension forces generated at the triple contact lines, is introduced. The wetting pressure drop is calculated as a difference between the experimental two-phase pressure drop and the frictional and momentum pressure drops given by the model of Lockhart and Martinelli [158]. It was shown that the wetting pressure drop is proportional to (1 - cosθ). A correlation is thereby suggested to predict the wetting pressure as a function of the static contact angle.

Surface	θ[°]	θa[°]	θr[°]	Δθ[°]
SiOx	26	38	15	23
Ti	49	82	36	46
DLC	63	94	51	43
SiOC	104	108	96	12

Table A.5: Static, advancing, receding and hysteresis contact angle measured for the four surfaces tested using the sessile drop method [144].

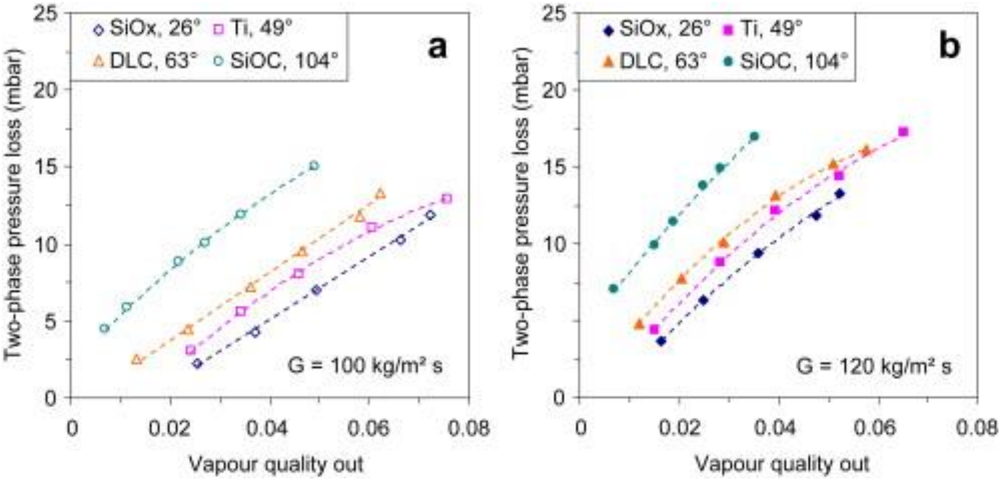

Figure A.17: Two-phase pressure drops: a) at 100kg/m² s and b) at 120kg/m²s [144].

Yu et al. (2012) [159] measured the pressure drops of slugs (this region is based on the flow regime map of hydrophobic (Teflon SCA = 110°) minitubes (D = 1.62, 2.06mm) and can be defined in the range of $0.050 < j_G < 0.243$m/s and $0.010 < j_L < 0.055$m/s [404]) with triple-lines for various diameters (0.546, 0.763, 1.018, 1555 and 2.075mm), several fluids (DI water, DI water-1%, 5%, 10% ethanol), and a range of velocities (0.01–0.4m/s). Triple-line (TL) pressure drop increased as increasing velocity and decreasing diameter. However, TL pressure drop is independent of the length of a liquid slug. In addition, advancing dynamic contact angle (A-DCA) increased as velocity increased, independent of the channel diameter. Dynamic contact angles were calculated from an equation describing the pressure drop of a triple-line. Over the given experimental range, previous correlations have underestimated the dynamic contact angles in comparison with the experimental values. They suggested that the reason for this underestimation is that previous correlations were developed solely in a dynamic contact angle regime in which inertial forces were not considered. Accordingly, they proposed a new dynamic contact angle correlation for a regime in which inertial forces are considered.

Most previous studies on TL motion have focused on the advancing dynamic contact angle (A-DCA) [160-166]. Rose and Heins [160] confirmed that the advancing dynamic contact angle (A-DCA) and receding dynamic contact angle (R-DCA) are dependent on velocity in experiments using the Nujol–air–glass system and oleic acid–air–glass system. In an experiment with parallel solid plates, Elliott and Riddiford [417] showed that A-DCA and R-DCA are dependent on velocity, except at very low rates. Schwartz and Tejada [162] measured A-DCA by placing a wire in various fluids, finding different A-DCA modes according to different velocity regions. Hoffman [163] measured A-DCA in a horizontal capillary tube and reported that A-DCA depends on the capillary number (the ratio between viscous force and surface tension force) and a shift factor that compensates for the static contact angles (SCA) of variable fluids. Jiang et al. [164] proposed a universal correlation (H) that depends on the capillary number and the SCA, and thus does not require an a priori shift factor. Subsequently, Bracke et al. [165] measured A-DCA by drawing a strip or a plate into a large liquid pool and then modifying the universal correlation. In addition, Seebergh et al. [422] measured A-DCA to immerse a solid sample in a liquid and then modified the universal correlation in the low capillary number range ($10^{-16} < Ca < 10^{-6}$) and the high capillary number range ($10^{-6} < Ca < 10^{-3}$). However, these previous researches generally experimented with very viscous fluids such as oil. In this case, the velocity of the A-DCA of a viscous fluid is much lower than that of an aqueous fluid in terms of the equivalent capillary number. These researchers did not study the slug flow regime region of an aqueous fluid ($10^{-4} < Ca < 10^{-3}$ and $10^{-3} < We < 1$). Therefore, this correlation does not consider the inertial force among the dominant forces that effect TL movement. Thus, this correlation is limited to the low Weber number region (We < 10^{-3}).

To understand the wettability effect on the condensation in mini-channels Derby et al. (2014) [167] examined the steam flow condensation enhancement on hydrophobic and hydrophilic surfaces. The study examined the enhancement of flow condensation of steam on hydrophobic and hydrophilic surfaces. In order to achieve dropwise condensation in an internal flow, patterned hydrophobic/hydrophilic surfaces were fabricated in a 1.06mm mini-gap. Six 1.06mm mini-gaps were tested at pressures of 350–400kPa, average qualities X of 0.2–0.95 and mass fluxes of 50–200kg/m^{2}s The surfaces included hydrophilic copper, hydrophobic Teflon AF™, and four surfaces with combined Teflon and hydrophilic patterns, as seen in the

Table A.6. Condensing heat transfer coefficients on hydrophobic and an alternated hydrophobic/hydrophilic patterned surfaces are an order of magnitude bigger than the hydrophilic surface one, as seen on the

Figure A.18. The wettability plays also an important role in the condensation heat transfer coefficient.

Surface	**Hydrophilic area/Total area (%)**
Copper, N=0	100
N=7	33
N=3	33
N=2	31
N=1	13
Teflon, N→∞	0

Table A.6: Percent hydrophilic area for different surfaces [167].

Hao et al. (2014) [168] experimentally investigated the wettability effects on the heat transfer performance and slug motion for oscillating heat pipes (OHPs). Deionized water was used as the working fluid. The surfaces of the OHPs were copper, superhydrophilic, hydrophilic and hydrophobic surfaces with contact angles of 73.4°, 0°, 12.9° and 141.5°, respectively (Figure A.19). The OHP had the upper part transparent to visualize the flow patterns. The heat transfer performance in six-turn OHPs was higher than in four-turn OHPs because of the increased perturbations. Experimental results showed that the surface wettability remarkably influenced the slug motion and thermal performance of OHPs. The liquid slug movements became stronger both in superhydrophilic and hydrophilic OHPs as opposed to the copper OHP, while the global heat transfer performance of the superhydrophilic and hydrophilic

OHPs increased in the six-turn OHP. For six-turn OHPs, the maximum displacement of the liquid slug in the hydrophilic OHPs and superhydrophilic OHPs increased by 5–60% and 25–60%, respectively, in comparison with that of copper OHPs. The thermal resistance in the evaporator section is less in the hydrophilic surface. The superhydrophilic surface however presents a higher thermal resistance with respect to the copper tube for the six turns OHP. The lowest thermal resistance, approximately 0.03°C/W, was achieved in the six-turn OHP with a hydrophilic surface, and the startup temperature of the hydrophilic OHP was reduced by 5°C when compared to the copper OHP. The thermal resistance and the evaporation temperature were significantly increased in the hydrophobic OHP due to the motionless of the liquid slug. The heat transfer performance of superhydrophilic OHPs and hydrophilic OHPs increased by 5–15% and 15–25%, respectively, in comparison with that of copper OHPs, the improvement was attributed to the fact that there was a thin liquid film between the wall and the vapor plug in the evaporation section, which led to high heat transfer efficiency.

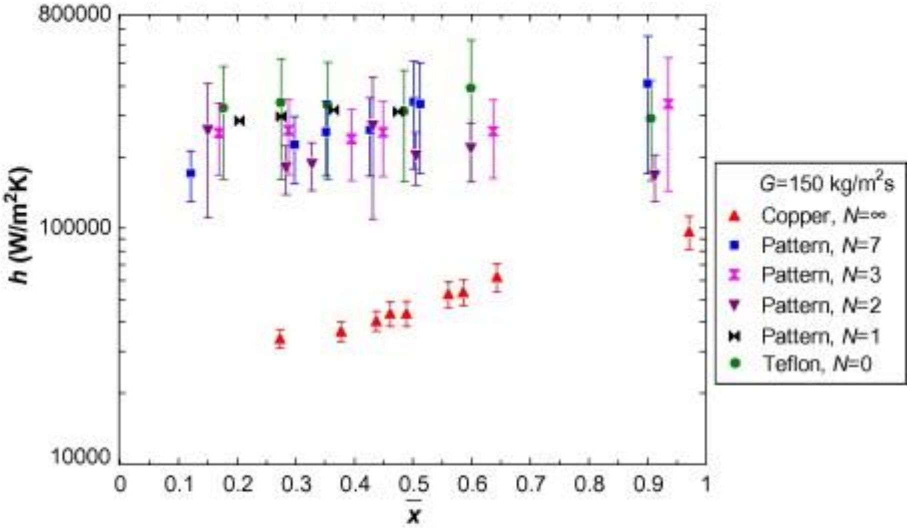

Figure A.18: Condensation heat transfer coefficients on hydrophobic/hydrophilic surfaces as compared to copper hydrophilic surface at mass flux G = 150 kg/m^{2}s. x is the average of the quality [167].

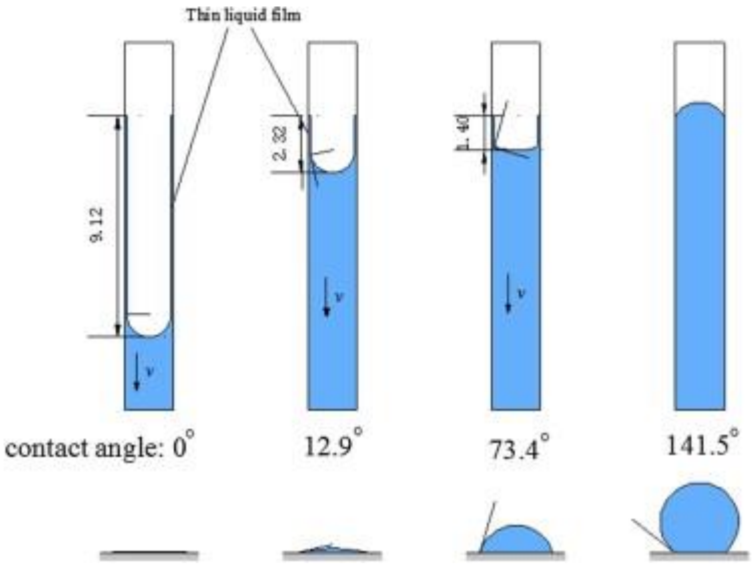

Figure A.19: Schematic of the liquid–vapor interface in the superhydrophilic, hydrophilic, copper, and hydrophobic OHPs [168].

The hydrophilic surface improved the heat transport capability of OHPs, and the maximum displacement and velocity of the liquid slug increased. The startup temperature of the four-turn and six-turn superhydrophilic OHPs varied from 40 to 55°C and from 35 to 50°C, respectively. The startup temperature of the four-turn and six-turn hydrophilic OHPs varied from 40 to 50°C and from 30 to 40°C, respectively. The hydrophilic OHP also showed a better startup performance than the copper OHP. On the other hand, the hydrophobic surface hindered the back flow of liquid causing a dryout phenomenon to occur in the OHP. At heat input of 150W, the thermal resistance for the four-turn hydrophobic OHPs was about two times greater than that of copper OHPs. The global heat transfer performance of the superhydrophilic OHP for the four-turn OHP was lower than that of the four-turn OHPs with hydrophilic and pure copper OHPs.

Appendix B

B. Thermally induced oscillating meniscus (Thomen) - Experimental apparatus design and assembly

A.6 Introduction

The present chapter provides a detailed description of the experimental test-rig (Figure B.1) designed, built and tested at the Thermal Physics Laboratories of the University of Bergamo. The modular approach allow to perform parametric investigations as well as simultaneous flow measurements aiming at the thermal characterization of a liquid/vapor meniscus oscillating in a capillary tube with different wettability levels.

As shown inFigure B.1, the rig is composed by a test cell and its peripheral facilities such as, a degassing/vacuum/filling system, an electrical power supply, a thermal bath, a data acquisition system, a computer.

The coupled effect of flow oscillation and surface wettability on the local two phase heat transfer coefficient is investigated by measuring the instantaneous wall-to-fluid temperature difference, the heat flux level as well as the meniscus oscillation global amplitudes and frequencies.

The fluid motion can be activated in two ways:

- thermally, typical of Pulsating Heat Pipes, where oscillation parameters (frequencies and amplitudes) are not known a priori (Figure B.2a);

- mechanically, by means of a moving membrane, where additional oscillation parameters can be imposed (Figure B.2b).

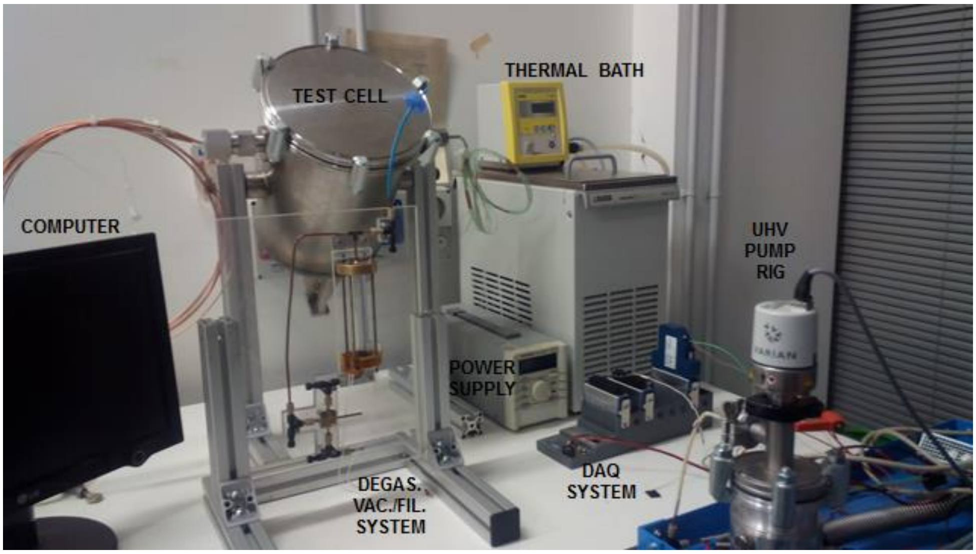

Figure B.1: Photo of the ThOMen experimental test-rig.

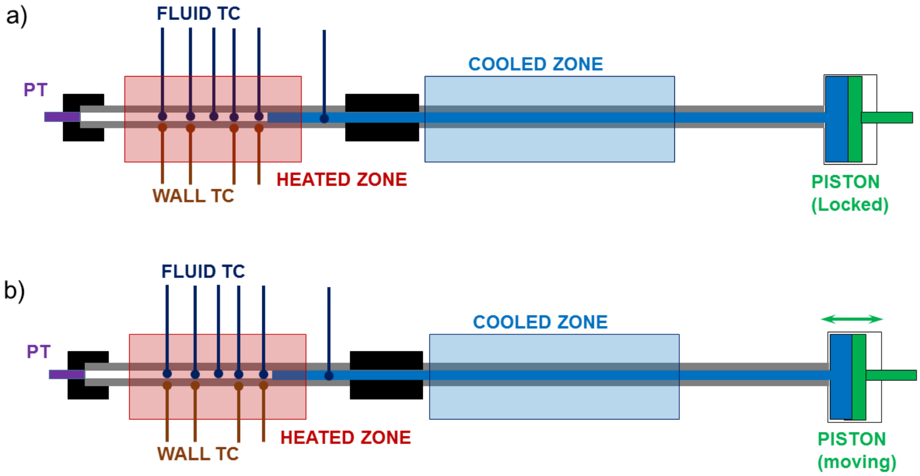

Figure B.2: ThOMen test cell sketch: a) thermally induced principle; b) thermally induced with additional flow control imposed.

A.7 Test cell

The test cell is divided in three main sections:

- the evaporator zone, where the device receives a controlled heat input by means of electric heaters (red spots in Figure B.2);
- the condenser zone where the heat is releases the by means of a liquid cooled heat sink (blue spots in Figure B.2);
- the fluid motion control system (green spots in Figure B.2).

The first two section are embedded into a vacuum chamber in order to minimize the conductive and convective heat losses to the environment. Finally the whole system is mounted on a tilting structure so as to investigate the effect of the device orientation with respect to gravity. A detailed description of each section is provided in the following paragraphs. An image of the 3D CAD of the device is shown in Figure B.3.

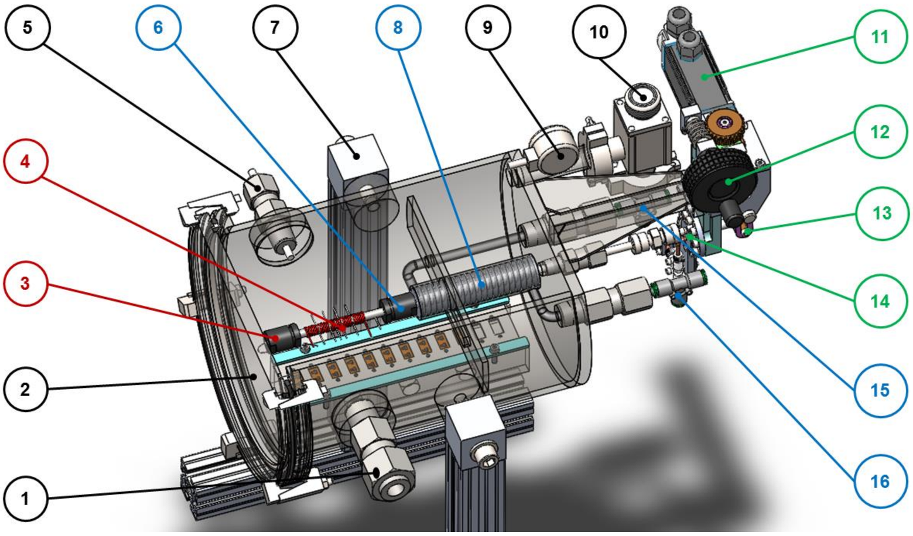

ITEM N°	DESCRIPTION	ITEM N°	DESCRIPTION
1	Pass-through (TC)	9	Vacuum chamber manometer
2	Vacuum chamber	10	Vacuum chamber valve
3	Leak proof joint (PT)	11	Control system motor
4	Evaporator section	12	Control system manual
5	Pass through (PT)	13	Control system piston

6	Evap./cond. Joint leak proof	14	Control system tank
7	Tilting structure	15	Cooler inlet
8	Condenser section	16	Cooler outlet

Figure B.3: ThOMen test cell.

A.7.1 Evaporator section

The test cell tube (7.0mm O.D. and 3.0mm I.D) is made of stainless steel (AISI 316) in order to minimize axial thermal conduction and avoid any oxidation process. An electrically insulated wiring heater (Thermocoax® Single core 1Nc Ac, 0.5mm O.D., 50Ω/m, 720mm long) has been wrapped covering a tube portion of 50mm.

This heating technique has already been successfully tested during previous ground tests, parabolic flights; the Large Diameter Centrifuge facilities in ESA assuring a very fast response due to the very low thermal inertia. The heater is connected to the power supply (GWInstek® 6006A, 60V, 6A DC) and can provide heating power according to the calculations shown in Table B.1.

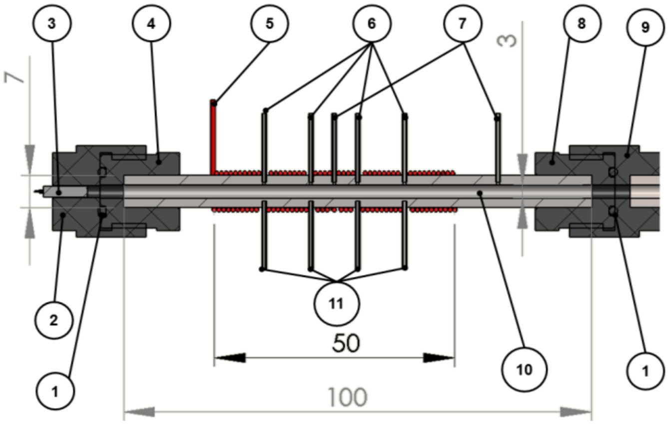

N°	ITEM
1	O-ring
2	Joint Cap PT
3	Pressure Transducer (PT)
4	Joint PT
5	Heater
6	TC fluid
7	Fluid check TC
8	Joint Eva./Cond. A
9	Joint Eva./Cond. B
10	Tube
11	TC wall

Figure B.4: Detail of the evaporator section.

Where the wall to fluid heat flux is evaluated, with a reasonable accuracy, as the ratio between the heating power and the inner tube surface following equation VI.

$$\dot{q}_{w-f} = \dot{Q}/A_{w-f} = \dot{Q}/(L_{ev}\pi R_{in}^2) \quad \text{(VI)}$$

ThOMen is equipped with a pressure transducer (Kulite® XCQ-093-1-1.7bar abs, accuracy ±0.5mbar) with the twofold aim of veryfing the channel leaking proof after the filling procedure and monitoring the fluid dynamic pressure variation during the experiments.

Voltage [V]	Current [A]	Power [W]	Heat Flux [W/cm^2]
12.0	0.35	4.2	0.8
23.9	0.7	16.7	3.5
35.9	1.05	37.7	7.9
47.8	1.4	67.0	14.2
59.8	1.75	104.6	22.2

Table B.1: Heat input capability.

Ten slots on the tube have been obtained by means of electroerosion. Each hole hosts the thermocouple needle where the TC itself is positioned (Figure B.4 and Figure B.5). Both needles and TCs are glued with a special epoxy for high vacuum levels applications (Varian Torr Seal®). Ten thermocouples (Omega®, model: KMTSS-IM025E-150, k-type, stainless steel sheath insulation 0.25mm, exposed hot junction 25μm) have been located in the evaporator section:

- six measuring the fluid temperature (as shown in Figure B.2, two of them are located for the purpose of checking the fluid level during the filling procedure);
- four measuring the wall temperature at the same location.

The TC bead dimension has been chosen with the well known lumped capacitance method assuming that the hot junction is spherical, axial conduction through the wires is negligible, radiative heat transfer to and from the tube inner walls is negligible. Since the fluid oscillation maximum frequency is 10Hz, according to the Nyquist criterion, measurements must be done, at least, at 20Hz in order to catch temperature variations. Consequently, the thermocouple is designed so as to be able to reach the 95% of the temperature difference in 0.05 seconds assuming a heat transfer coefficient between the fluid and the TC of 1000W/m^{2}K. A diameter below 30μm satisfies the above requirements. Preliminary tests on a simple air-water test rig confirm that the thermocouple response is suitable for the actual investigation.

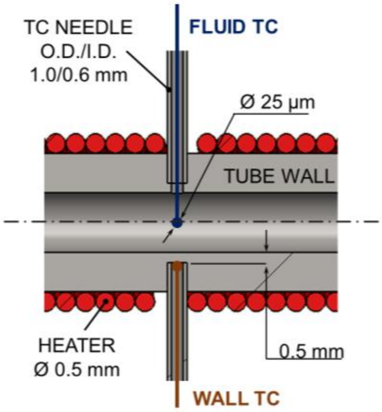

Figure B.5. Evaporator section detail: thermocouples location.

A.7.2 Condenser section

The condenser tube is inserted inside a stainless steel finned tube (helical fins) which is itself embedded in a cylindrical envelope (cooler shell) with an inlet and outlet. Cooling water, recirculated by the thermal bath (Lauda® Thermal system: Ecoline RE-107, Pump E-100), enters the inlet and swirls around the tube guided by the helical fins (Figure B.6).

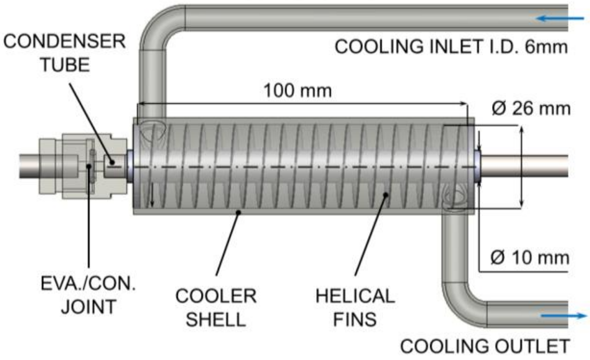

Figure B.6. Condenser section: detail of the cooler.

The preliminary design of the cooler elements is based on the balance between the maximum total wall-to-fluid heat transfer rate (equation 9) and the maximum total power dissipated by the cooling medium in steady conditions which has been set to 100W.

$$\dot{Q}_{conv} = \eta_{tot} A_{tot} h \left(T_w - \frac{T_{in} + T_{out}}{2} \right) \tag{VII}$$

Where T_w is the average assumed cooler wall temperature, T_{in} and T_{out} are respectively the cooler inlet and outlet temperatures, η_{tot} is the overall fins efficiency:

$$\eta_{tot} = 1 - \left(\frac{A_{fin}}{A_{fin} + A_{gap}} \left(1 - \eta_{fin} \right) \right) \tag{VIII}$$

Where A_{fin} and A_{gap} are respectively the fin area and the tube area between two adjacent fins. A_{tot} is the total heat exchange area depending on the number of fins:

$$A_{tot} = n_{fin} A_{fin} \left(n_{fin} - 1 \right) A_{gap} \tag{IX}$$

h is the heat transfer coefficient calculated for a laminar flow in helical ducts (Manlapaz-Churchill correlation):

$$h = \frac{k_l}{d} \left[\left(3.657 + \frac{4.343}{x_1} \right)^3 + 1.158 \left(\frac{De}{x_2} \right)^{3/2} \right]^{1/3} \tag{X}$$

$$x_1 = \left(1.0 + \frac{957}{De^2 \, \mathrm{Pr}} \right)^2, x_2 = 1.0 + \frac{0.477}{\mathrm{Pr}}$$

The maximum total power dissipated by the cooling medium in steady steady conditions is:

$$\dot{Q}_{cool} = \dot{m} c_p \left(T_{out} - T_{in} \right) \tag{X!}$$

where ṁ is the cooling water flow rate.

Table B.2 shows the main geometrical parameters and calculations for the design of the cooler.

ThOMen COOLER DESIGN			
Finned tube geometry			
T_ext_ tube	15	[°C]	External tube temperature (assumed)
L_tube	0.1	[m]	Finned tube length

thick_fin	0.0003	[m]	Fin thickness
gap_fin	0.005	[m]	Gap between two adjacent fins
n_fin	18.86	[-]	Total number of fins
n_fin_m	188.67	[m^{-1}]	Fins per meter
d_in_fin	0.01	[m]	Fin Internal diameter = tube external diameter
d_ext_fin	0.026	[m]	Fin External diameter
A_fin	0.000904	[m^2]	Fin Area
A_gap	0.000157	[m^2]	Tube area between two adjacent fins
A_cool	0.020035	[m^2]	Total finned tube area
A_flow_int	0.00004	[m^2]	Cooling medium flow area
d_hyd	0.0038	[m]	Hydraulic diameter
v_cool	0.176	[m/s]	Cooling flow mean velocity
Water loop characteristics			
T_in_loop	10	[°C]	Cooling medium inlet temperature (imposed by thermal bath)
T_out_loop	13.6	[°C]	Cooling medium outlet temperature (assumed)
DT_loop	3.6	[°C]	Cooling medium outlet-inlet temperature difference
v_loop	0.25	[m/s]	Cooling medium velocity at the inlet (constraint)
d_tube_in_loop	0.006	[m]	Cooling port diameter
A_flow_loop	0.000028	[m^2]	Cooling port flow area
m_dot_loop	0.007068	[kg/s]	Cooling loop actual mass flow rate
m_dot_TB	0.233333	[kg/s]	Thermal bath/pump maximum mass flow rate
Thermo-fluid properties and HTC for water			
cp	4180	[J/kgK]	Specific heat
μ	0.001005	[Pa.s]	Dynamic viscosity
ρ	1000	[Kg/m^3]	Density
k	0.6	[W/mK]	Thermal conductivity
Convective Heating Power			
Re	669.84	[-]	Reynolds Number
Pr	7.0015	[-]	Prandtl Number
De	435.80	[-]	Dean Number
x1	1.001439	[-]	Correlation coefficient 1
x2	1.068128	[-]	Correlation coefficient 2
Nu_cool_DB	21.58	[-]	Nusselt Number, Laminar flow in helical ducts (Manlapaz-Churchill correlation)
h_cool	3399.37	[W/m^{2}K]	Heat transfer coefficient
η_fin	0.4	[-]	Fin HTC effectiveness from table (Incropera)
η_tot	0.488757	[-]	Overall HTC effectiveness from table (Incropera)
Q_conv	106.52	[W]	Cooling Power based on heat transfer
Cooling medium Heating Power			
Q_cool	106.36	[W]	Cooling Power based on energy balance

Table B.2. ThOMen cooler design: geometrical details and calculations.

A.7.3 Flow motion control system

The elements composing the flow motion control system and its working principle are shown in Figure B.7. The fluid tank volume can be varied by means of a piston connected to a vacuum proof rubber membrane (Diacom® DC-62-10) in such a way that the meniscus is moved back and forward inside the test section. The piston oscillation frequency ranges from 0 to 10Hz depending on the motor (Minimotor® BSE35-30RP-1 single stage brushless) rotational speed (red arrows in Figure B.7). The motor, cam and Y-shaped crank are mounted on a sliding structure (green frame in Figure B.7) that can be finely regulated in order to set the meniscus oscillation amplitude from 1 to 50 mm (green arrows in Figure B.7).

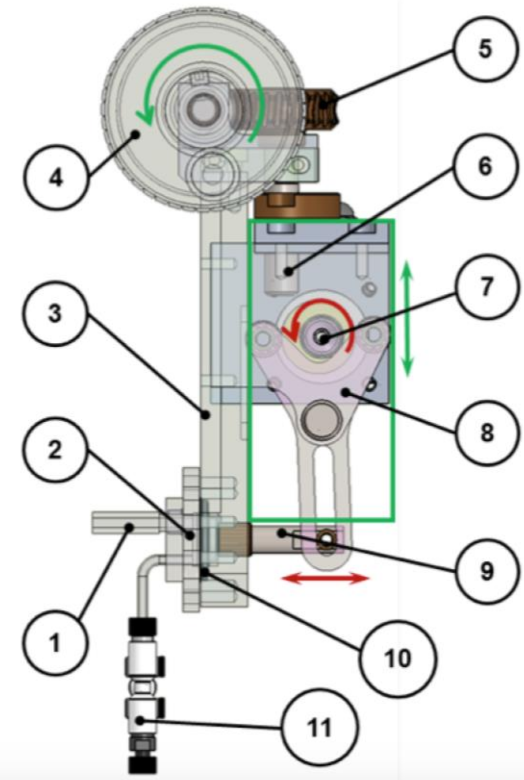

N°	ITEM
1	To condenser tube
2	Fluid tank
3	Slide
4	Regulator handle
5	Regulator gear
6	Regulator screw
7	Motor shaft
8	Y-shaped crank
9	Piston
10	Rubber membrane
11	Vacuum/filling Valve

Figure B.7. Layout of the flow motion system.

A.8 Peripheral facilities

A.8.1 Vacuum and filling system

The vacuum and filling system (Figure B.8) consists of one graduated cylinder (tank), four valves (Upchurch scientific® UP-P-447, leak rate < 1e-7mbar.l/s) and three ports: one connected to the fluid refill tank, one to the Ultra High Vacuum Pumping system (Varian® DS42 and TV81-T, minimum system vacuum 1e-6mbar) and finally one to the test cell.
The degassing/vacuum and filling procedure is described here below.

- The test cell is completely evacuated and the test cell valve (not shown in the figure) is closed.
- The tank is evacuated and completely filled by opening the refilling valve.
- The refilling port remains closed from now till the end of the entire procedure.
- The tank is heated from below till the fluid reaches the boiling point.
- Uncondensable gases accumulate at the top of the tank and are removed from above by opening the degassing circuit valve.
- The boiling/vacuming cycle is repeated untill a drop in the liquid level is recorded.
- The heater is shut down and the user waits for the boiling process to stop.
- The filling valve is opened and the liquid level is recorded.
- The test cell valve is opened and the device is filled up.

A.8.2 Data Acquisition System

The Data acquisition system is totally made of components by National Instruments® (Chassis: NI-cRIO-9074®, Modules: NI-9214®, NI-9205®, NI-9215®), it records the output of the thermocouples, of the pressure transducer and the total heat power input. A dedicated Labview® software have been developed in order to acquire temperatures and pressure at different frequencies up to 400Hz.

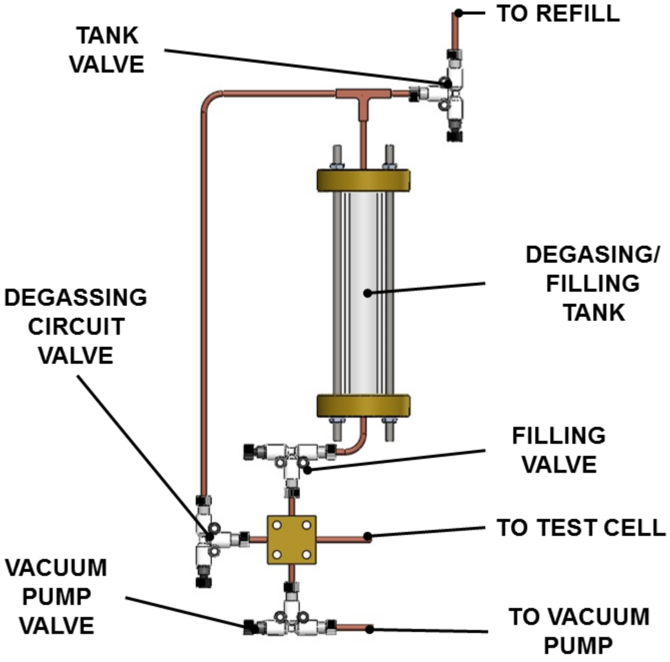

Figure B.8. Degassing/vacuum/filling system.

Bibliography Appendices

[1] S. Levy. Two-phase flow in complex systems, Wiley, 1999.

[2] S.M. Ghiaasiaan. Two-phase flow, boiling, and condensation in conventional and miniature systems. Cambridge University Press (2008).

[3] G.W. Govier, K. Aziz. The flow of complex mixtures in pipes. Van Nostrand Reinhold, New York (1972).

[4] J.M. Delhaye. Two-phase flow modeling and Thermo hydraulics of Two-phase Systems for Industrial Design and Nuclear Engineering, Chapter 3 and 10, Hemisphere Publishing Corporation, 1981.

[5] G.F. Hewitt, D.N. Roberts. Studies of two-phase flow patterns by simuitaneous X-Ray and flash photography. AERE-M 21 59, HMSO (1994).

[6] J.T. Rogers. Two-phase vertical up-flow regime boundaries and interphase drag models for advanced thermohydraulic codes. CEGB report (1985).

[7] J.G. Collier, J.R. Thome. Convective boiling and condensation, 3rd Edition, Oxford Science Publications, Clarendon Press, Oxford 1994.

[8] G.F. Hewitt. Measurement of two-phase flow parameters. Academic Press, New York 1978.

[9] G.E. Alves. Co-current liquid gas flow in a pipeline contractor. Chemical Engineering Progress 50 (1954) 449-456.

[10] O. Baker. Simultaneous flow of oil and gas. Oil and Gas Journal 53 (1954) 185-195.

[11] G.W. Govier, M.M. Omer. Horizontal pipeline flow of air-water mixtures. The Canadian Journal of Chemical Engineering 40 (1962) 93-104.

[12] J.M. Mandhane, G.A. Gregory, K. Aziz. A flow pattern map for gas-liquid flow in horizontal pipes. International Journal of Multiphase Flow 1 (1974) 537-553.

[13] E. Kordyban. Some details of developing slugs in horizontal two-phase flow. AIChE Journal 31(5) (1985) 802-806.

[14] M.G. Hubbard,A.E. Dukler. The characterization of flow regimes for horizontal two-phase flow: statistical analysis of wall pressure fluctuations. Proceedings of the Heat Transfer and Fluid Mechanics (1976) 101-121.

[15] G.B. Wallis, J.E. Dorbson. The onset of slugging in horizontal stratified air-water flow. International Journal of Multiphase Flow 1 (1973) 173-193.

[16] Y. Taitel,A.E. Dukler. A model for slug frequency during gas-liquid flow in horizontal and near-horizontal gas-liquid flow. International Journal of Multiphase Flow 19(5) (1977) 829-838.

[17] J. Kubie. The presence of slug flow in horizontal two-phase flow. International Journal of Multiphase Flow 5 (1979) 327-339.

[18] P.Y. Lin, T.J. Hanratty. Detection of slug flow from pressure measurements. International Journal of Multiphase Flow 13(1) (1987a) 13-21.

[19] D. Barnea, Y. Taitel. Model for slug length distribution in gas-liquid slug flow. International Journal of Multiphase Flow 19(5) (1993) 829-838.

[20] W.P. Jepson, R.E. Taylor. Slug flow and its transitions in large-diameter horizontal pipes. International Journal of Multiphase Flow 19(3) (1993) 411-420.

[21] https://www.thermalfluidscentral.org/encyclopedia/index.php/Two-Phase_Flow_Patterns_in_Vertical_Tubes.

[22] J.R. Thome. Engineering Data Book III, Wolverine Tube, Inc., Huntsville, AL (2004).

[23] C.T. Crowe. Multiphase flow handbook. Taylor and Francis Group (2006).

[24] S.G. Kandlikar. Heat transfer mechanisms during flow boiling in microchannels. Journal of Heat Transfer 126 (2004) 8-16.

[25] M.M. Shah. Chart correlations for saturated boiling heat transfer: equations and further study. ASHRAE Transactions 88(Part I) (1982) 185-196.

[26] C. Baldassari, M. Marengo. Flow boiling in microchannels and microgravity. Progress in Energy and Combustion Science 39 (2013) 1-36.

[27] S. Kandlikar, S. Garimella, D. Li, S. Colin, M. King. Heat transfer and fluid flow in minichannels and microchannels, Chapter 1 (2005).

[28] P.A. Kew, K. Cornwell. Correlations for the prediction of boiling heat transfer in small diameter channels. Applied Thermal Engineering 17 (1997) 705-715.

[29] J.M. Li, B.X. Wang. Size effect on two-phase regime for condensation in micro/mini tubes. Heat Transfer Asian Research 32 (2003) 65-71.

[30] M. Kawaji, P.M.Y. Chung. Adiabatic gas-liquid flow in microchannels. Microscale Thermophysical Engineering 8 (2004) 239-257.

[31] J.R. Thome. Boiling in microchannels: a review of experiment and theory. International Journal of Heat and Fluid Flow 25 (2004) 128-139.

[32] J.R. Thome, V. Dupont, A.M. Jacobi. Heat transfer model for evaporation in microchannels, part I: presentation of the model. International Journal of Heat and Mass Transfer 47 (2004) 3375-3385.

[33] P. Cheng, H.Y. Wu. Mesoscale and microscale phase change heat transfer. Advances in Heat Transfer 39 (2006) 461-563.

[34] A. Ullmann, N. Brauner. The prediction of flow pattern maps in minichannels. Multiphase Science and Technology 19(1) (2007) 49-73.

[35] T. Harichian, S.A. Garimella. A comprehensive flow regime map for microchannel flow boiling with quantitative transition criteria. International Journal of Heat and Mass Transfer 53 (2010) 2694-2702.

[36] D. Shiferaw, T.G. Karayannis, D.B.R. Kenning. A comparison with the three-zone model for flow boiling heat transfer in small diameter tubes. In: 13th international heat transfer conference, Sydney, Australia (2006).

[37] R. Revellin, V. Dupont, T. Ursenbacher, J.R. Thome, I. Zun. Characterization of diabatic two-phase flows in microchannels: flow parameter results for R-134a in a 0.5 mm channel. International Journal of Multiphase Flow 32 (2006) 755-774.

[38] R. Revellin, J.R. Thome. Experimental investigation of R-134a and R-245fa twophase flow in microchannels for different flow conditions. International Journal of Heat and Fluid Flow 28(1) (2007) 63-71.

[39] R. Revellin, J.R. Thome. A new type of diabatic flow pattern map for boiling heat transfer in microchannels. Journal of Micromechanics and Microengineering 17 (2007) 788-796.

[40] L. Consolini, J.R. Thome. A heat transfer model for evaporation of coalescing bubbles in micro-channel flow. International Journal of Heat and Fluid Flow 31 (2010) 115-125.

[41] C.L. Ong, J.R. Thome. Flow boiling heat transfer of R134a, R236fa and R245fa in a horizontal 1.030 mm circular channel. Experimental Thermal and Fluid Science 33 (2009) 651-663.

[42] G.P. Celata, M. Cumo, A. Mariani. Experimental evaluation of the onset of subcooled flow boiling at high liquid velocity and subcooling. International Journal of Heat Mass Transfer 40(12) (1997) 2879-2885.

[43] S.G. Kandlikar, V. Mizo, M. Cartwright, E. Ikenze. Bubble nucleation and growth characteristics in subcooled flow boiling of water. In: ASME national heat transfer conference 4 (1997) 11-18.

[44] C.A. Chen, W.R. Chang, K.W. Li, Y.M. Lie, T.F. Lin. Subcooled flow boiling heat transfer of R-407C and associated bubble characteristics in a narrow annular duct. International Journal of Heat and Mass Transfer 52 (2009) 3147-3158.

[45] R. Zhuan, W. Wang. Simulation of subcooled flow boiling in a micro-channel. International Journal of Refrigeration 34 (2011) 781-795.

[46] O.A. Kabov D.V. Zaitsev, V.V. Cheverda, A. Bar-Cohen. Evaporation and flow dynamics of thin, shear-driven liquid films in microgap channels. Experimental Thermal and Fluid Science 35 (2011) 825-831.

[47] L. Chen, Y.S. Tian, T.G.Karayiannis. The effect of tube diameter on vertical twophase flow regimes in small tubes. International Journal of Heat Mass Transfer 49 (2006) 4220-4230.

[48] T. Harirchian, S.V. Garimella. Effects of channel dimension, heat flux, and mass flux on flow boiling regimes in microchannels. International Journal of Multiphase Flow 35 (2009) 349-362.

[49] K. Cornwell, P.A. Kew. Boiling in small channels. In: Proceedings of conference on energy efficiency in process technology, Athens: Elsevier (1992) 624-638.

[50] S. Lin, P.A. Kew, K. Cornwell. Flow boiling of refrigerant R141B in small tubes. Transactions of the Institution of Chemical Engineers 79(A) (2001) 417-424.

[51] S. Lin, P.A. Kew, K. Cornwell. Two-phase flow regimes and heat transfer in small tubes and channels. In: Proceedings of 11th international heat transfer conference, Kyongju, Korea, 2 (1998) 45-50.

[52] G. Ribatski, L. Wojtan, J.R. Thome. An analysis of experimental data and prediction methods for two-phase frictional pressure drop and flow boiling heat transfer in micro-scale channels. Experimental Thermal and Fluid Science 31 (2006) 1-19.

[53] D. Shiferaw, T.G. Karayannis, D.B.R. Kenning. Flow boiling in a 1.1 mm tube with R134a: experimental results and comparison with model. International Journal of Thermal Sciences 48 (2009) 331-341.

[54] L. Zhang, J.M. Koo, L. Jiang, M. Asheghi, K.E. Goodson, J.G. Santiago, T.W. Kenny. Measurements and modeling of two-phase flow in microchannels with nearly Measurements and modeling of two-phase flow in microchannels with nearly constant heat flux, boundary conditions. Journal of Microelectromechanical Systems 11(1) (2002) 12-19.

[55] G. Nema, S. Garimella, B.M. Fronk. Flow regime transitions during condensation in microchannels. International Journal of refrigeration 40 (2014) 227-240.

[56] J.W. Coleman, S. Garimella. Two-phase flow regimes in round, square and rectangular tubes during condensation of refrigerant R134a. International Journal of Refrigeration 26 (2003) 117-128.

[57] A. Cavallini, G. Censi, D. Del Col, L. Doretti, G.A. Longo, L.Rossetto. Condensation of halogenated refrigerants inside smooth tubes. HVAC&R Research 8 (2002) 429-451.

[58] G. Breber, J.W. Palen, J. Taborek. Prediction of horizontal tubeside condensation of pure components using flow regime criteria. Journal of Heat Transfer 102 (1980) 471-476.

[59] T.N. Tandon, H.K. Varma, C.P. Gupta. New flow regimes map for condensation inside horizontal tubes. Journal of Heat Transfer 104 (1982b) 763-768.

[60] E. Jassim, T. Newell. Prediction of two-phase pressure drop and void fraction in microchannels using probabilistic flow regime mapping. International Journal of Heat and Mass Transfer 49 (2006) 2446-2457.

[61] J. El Hajal, J.R. Thome, A. Cavallini. Condensation in horizontal tubes Part 1: two-phase flow pattern map. International Journal of Heat and Mass Transfer 46 (2003) 3349-3363.

[62] E.W. Jassim, T.A. Newell, J.C. Chato. Probabilistic determination of two-phase flow regimes in horizontal tubes utilizing an automated image recognition technique. Experiments in Fluids 42 (2007) 563-573.

[63] N. Kattan, J.R. Thome, D. Favrat. Flow boiling in horizontal tubes Part I: development of a diabatic two-phase flow pattern map. Journal of Heat Transfer 120 (1998) 140-147.

[64] S.M. Kim, I. Mudawar. Universal approach to predicting heat transfer coefficient for condensing mini/micro-channel flow. International Journal of Heat and Mass Transfer 56 (2013) 238-250.

[65] H.M. Soliman. Analytical and experimental studies of flow patterns during condensation inside horizontal tubes. Ph.D. Dissertation, Kansas State University, Manhattan, KS (1974).

[66] C.C. Wang, C.S. Chiang, S.P. Lin, D.C. Lu. Two-phase flow pattern for R-134a inside a 6.5 mm (0.25 in) smooth tube. In: ASHRAE Winter Meeting, Philadelphia, PA (1997).

[67] C.C. Wang, C.S. Chiang, D.C. Lu. Visual observation of two-phase flow pattern of R-22, R134a and R-407c in a 6.5 mm smooth tube. Experimental Thermal and Fluid Science 15 (1997) 395-405.

[68] M.K. Dobson, J.C. Chato. Condensation in smooth horizontal tubes. Journal of Heat Transfer 120 (1998) 193-213.

[69] A. Tabatabai, A. Faghri. A new two-phase flow map and transition boundary accounting for surface tension effects in horizontal miniature and micro tubes. Journal of Heat Transfer 123 (2001) 958-968.

[70] J.W. Coleman, S. Garimella. Two-phase flow regime transition in microchannel tubes: the effect of hydraulic diameter. ASME Heat Transfer Division 366(4) (2000) 71-83.

[71] T.J. Rabas, P.G. Minard. Two types of flow instabilities occurring inside horizontal tubes with complete condensation. Heat Transfer Engineering 8 (1987) 40-49.

[72] L. Doretti, C. Zilio, S. Mancin, A. Cavallini. Condensation flow patterns inside plain and microfin tubes: a review. International Journal of Refrigeration 36 (2013) 567-587.

[73] M. Derby, H.J. Lee, Y. Peles, M.K. Jensen. Condensation heat transfer in square, triangular, and semi-circular mini-channels.International Journal of Heat and Mass Transfer 55 (2012) 187-197.

[74] W.W. Akers, H.A. Deans, O.K. Crosser. Condensing heat transfer within horizontal tubes. Chemical engineering progress symposium series 55(29) (1959) 171-176.

[75] W.W. Wang, T.D. Radcliff, R.N. Christensen. A condensation heat transfer coerrelation for millimeter-scale tubing with flow regime transition. Experimental Thermal and Fluid Science. 26 (5) (2002) 473-485.

[76] A. Agarwal, S. Garimella. Representative results for condensation measurements at hydraulic diameters ~100 microns. Journal of Heat Transfer 132 (2010) 041010.

[77] J.S. Shin, M.H. Kim. An experimental study of flow condensation heat transfer inside circular and rectangular mini-channels. Heat Transfer Engineering 26(3) (2005) 36-44.

[78] H.S. Wang, J.W. Rose. Film condensation in horizontal microchannels: effect of channel shape. International Journal of Thermal Sciences 45(12) (2006) 1205-1212.

[79] J.R. Baird, D.F. Fletcher, B.S. Haynes. Local condensation heat transfer rates in fine passages. International Journal of Heat and Mass Transfer 46(23) (2003) 4453-4466.

[80] H.S. Wang, J.W. Rose. A theory of film condensation in horizontal noncircular section microchannels. Journal of Heat Transfer 127 (2005) 1096-1105.

[81] S.D. Farahani, F. Kowsary, J. Jamali. Direct estimation of local convective boiling heat transfer coefficient in mini-channel by using conjugated gradient method with adjoint equation. International Communications in Heat and Mass Transfer 55 (2014) 1-70.

[82] C.B. Sobhan, S.V. Garimella. A comparative analysis of studies on heat transfer and fluid flow in microchannels. Microscale Thermophysical Engineering 5 (2001) 293-311.

[83] S.G. Kandlikar. Fundamental issues related to flow boiling in minichannels and microchannels. Experimental Thermal and Fluid Science 26 (2002) 389-407.

[84] A.E. Bergles, V.J.H. Lienhard, G.E. Kendall, P. Griffith. Boiling and evaporation in small diameter channels. Heat Transfer Engineering 24 (2003) 18-40.

[85] S.M. Ghiaasiaan, R.C. Chedester. Boiling incipience in microchannels. International Journal of Heat and Mass Transfer 45 (2002) 4599-4606.

[86] Y.Y. Hsu. On the size range of active nucleation cavities on a heating surface. ASME Journal of Heat Transfer 84 (1962) 207-216.

[87] E.J. Davis, G.H. Anderson. The incipience of nucleate boiling in forced convection flow. AIChE Journal 12 (1966) 774-780.

[88] D. Liu, P.S. Lee, S.V Garimella. Prediction of the onset of nucleate boiling in microchannel flow. International Journal of Heat and Mass Transfer 48 (2005) 5134-5149.

[89] F.P. Incropera, D.P. DeWitt, Fundamentals of Heat and Mass Transfer, third ed., Wiley (1995).

[90] Y.Y.Hsu. On the size range of active nucleation sites on a heating surface. Journal of Heat Transfer 84 (1962) 207-216.

[91] J. Lee, I. Mudawar. Two-phase flow in high-heat-flux micro-channel heat sink for refrigeration cooling applications: part II-heat transfer characteristics. International Journal of Heat and Mass Transfer 48 (2005) 941-955.

[92] L. Zhao, L. Guo, B. Bai, Y. Hou, X. Zhang. Convective boiling heat transfer and two-phase flow characteristics inside a small horizontal helically coiled tubing once-through steam generator. International Journal of Heat and Mass Transfer 46 (2003) 4779-4788,

[93] C. Huh, M.H. Kim. Pressure drop, boiling heat transfer and flow patterns during flow boiling in a single microchannel. Heat Transfer Engineering 28(8-9) (2007) 730-737.

[94] D. Shiferaw, X. Huo, T.G. Karayannis, D.B.R. Kenning. Examination of heat transfer correlations and a model for flow boiling of R134a in small diameter tubes. International Journal of Heat and Mass Transfer 50 (2007) 5177-5193.

[95] S. Lin, P.A. Kew, K. Cornwell. Two-phase heat transfer to a refrigerant in a 1 mm diameter tube. In: 6th UK heat transfer conference in Edinburgh (1999).

[96] T.H. Yen, M. Shoji, F. Takemura, Y. Suzuki, N. Kasagi. Visualization of convective boiling heat transfer in single microchannels with different shaped cross-sections. International Journal of Heat and Mass Transfer 49 (2006) 3884-3894.

[97] A.M. Jacobi, J.R. Thome. Heat transfer model for evaporation of elongated bubble flows in microchannels. Journal of Heat Transfer 124 (2002) 1131-1136.

[98] P. Cheng, G. Wang, X. Quan. Recent work on boiling and condensation in microchannels. Journal of Heat Transfer 131(4) (2009) 043211.

[99] T. Harirchian, S.V. Garimella. The critical role of channel cross-sectional area in microchannel flow boiling heat transfer. International Journal of Multiphase Flow 35 (2009) 904-913.

[100] V. Dupont, J.R. Thome, A.M. Jacobi. Heat transfer model for evaporation in microchannels, part II: comparison with the database. International Journal of Heat and Mass Transfer 47 (2004) 3387-3401.

[101] S.G. Kandlikar. A theoretical model to predict pool boiling CHF incorporating effects of contact angle and orientation. Journal of Heat Transfer 123 (2001) 1071-1079.

[102] H.Wang, S.V. Garimella, J.Y. Murthy. Characteristic of an evaporating thin film in a microchannel. International Journal of Heat and Mass Transfer 50 (2007) 3933-3942.

[103] H.K. Dhavaleswarapu, P. Chamarthy, S.V. Garimella. Experimental investigation of steady buoyant-thermocapillary convection near an evaporating meniscus. Physics of Fluids 19 (2007) 1-11.

[104] Y. Liaofei, J. Li, G. Peng, L. Fuhao. Evaporating momentum force and shear force on meniscuses of elongated bubble in microchannel flow boiling. Journal of Thermal Science 23(2) (2014) 160-168.

[105] A. Cioncolini, J.R. Thome. Algebraic turbulence modeling in adiabatic and evaporating annular two-phase flow. International Journal of Heat and Fluid Flow 32 (2011) 805-817.

[106] A. Cioncolini, J.R. Thome. Prediction of the entrained liquid fraction in vertical annular gaseliquid two-phase flow. International Journal of Multiphase Flow 36(4) (2010) 293-302.

[107] A. Cioncolini, J.R. Thome, C. Lombardi. Unified macro-to-microscale method to predict two-phase frictional pressure drops of annular flows. International Journal of Multiphase Flow 35(12) (2009) 1138-1148.

[108] S. Lin, P.A. Kew, K. Cornwell. Two-phase heat transfer to a refrigerant in a 1 mm diameter tube, International Journal of Refrigeration 24 (2001) 51-56.

[109] S.S. Bertsch, E.A. Groll, S.V. Garimella. Effects of heat flux, mass flux, vapor quality, and saturation temperature on flow boiling heat transfer in micro-channels. International Journal of Multiphase Flow 35 (2009) 142-154.

[110] K.O. Jatuporn, W. Somchai. Experimental investigation of evaporation heat transfer coefficient and pressure drop of R-410A in a multiport mini-channel. International Journal of refrigeration 32 (2009) 124-37.

[111] L. Consolini, J.R. Thome. Micro-channel flow boiling heat transfer of R-134a, R-236fa and R-245fa. Microfluid Nanofluid 6 (2009) 731-746.

[112] V. Dupont, J.R. Thome. Evaporation in microchannels: influence of the channel diameter on heat transfer. Microfluid Nanofluid 1 (2005) 19-27.

[113] T. Harirchian, S.V. Garimella. Boiling heat transfer and flow regimes in microchannels-a comprehensive understanding. Journal of Electronic Packaging 133 (2011) 011001.

[114] X. Huo, L. Chen, Y.S. Tian, T.G. Karayiannis. Flow boiling and flow regimes in small diameter tubes. Applied Thermal Engineering 24 (2004) 1225-1239.

[115] T. Harirchian, S. Garimella. Flow regime-based modeling of heat transfer and pressure drop in microchannel flow boiling. International Journal of Heat and Mass Transfer 55 (2012) 1246-1260.

[116] M.G. Cooper. Saturated nucleate pool boiling-a simple correlation. In: 1st UK national heat transfer conference, IChemE symposium series 86(2) (1984) 785-793.

[117] S. Riffat, X. Ma. Recent developments in heat pipe technology and applications: a review. International Journal of Low Carbon Technologies 2 (2007) 162-177.

[118] A. Faghri. Heat pipes: review, opportunities and challenges. Frontiers in Heat Pipes 5 (2014) 1-48.

[119] M. Mochizuki, T. Nguyen, K. Mashiko, Y. Saito, T. Nguyen, V. Wuttijumnong. A review of heat pipe application including new opportunities. Frontiers in Heat Pipes 2 (2011) 1-15.

[120] H.N. Chaudhrya, B.R. Hughes, S.A. Ghani. A review of heat pipe systems for heat recovery and renewable energy applications. Renewable and Sustainable Energy Reviews 16 (2012) 2249-2259.

[121] X. Tang, L. Sha, H. Zhang, Y. Ju. A review of recent experimental investigations and theoretical analyses for pulsating heat pipes. Frontiers in Energy 7(2) (2013) 161-173.

[122] Y. Zhang, A. Faghri. Heat transfer in a pulsating heat pipe with open end. International Journal of Heat and Mass Transfer 45 (2002) 755-764.

[123] L.L. Vasiliev. Heat pipes in modern heat exchangers. Applied Thermal Engineering 25 (2005) 1-19.

[124] S. Khandekar, V. Silwal, A. Bhatnagar, P. Sharma. Global effectiveness of pulsating heat pipe heat exchangers: modeling and experiments. Heat Pipe Science and Technology 1(3) (2010) 279-302.

[125] S. Lips, A. Bensalem, Y. Bertin, V. Ayel, C. Romestant, J. Bonjour. Experimental evidences of distinct heat transfer regimes in pulsating heat pipes. Applied Thermal Engineering 30 (2010) 900-907.

[126] M.B. Shafii, A. Faghri, Y. Zhang. Thermal modeling of unlooped and looped pulsating heat pipes. Journal of Heat Transfer 123(6) (2001) 1159-1172.

[127] Y. Zhang, A. Faghri. Advances and unsolved issues in pulsating heat pipes. Heat Transfer Engineering 29(1) (2008) 20-44.

[128] R.T. Dobson. Theoretical and experimental modelling of an open oscillatory heat pipe including gravity. International Journal of Thermal Sciences 43 (2) (2004) 113-119.

[129] R.T. Dobson. An open oscillatory heat pipe water pump. Applied Thermal Engineering 25(4) (2005) 603-621.

[130] S.P. Das, V.S. Nikolayev, F. Lefevre, B. Pottier, S. Khandekar, J. Bonjour. Thermally induced two-phase oscillating flow inside a capillary tube. International Journal of Heat and Mass Transfer 53 (2010) 3905-3913.

[131] R.T. Dobson. Theoretical and experimental modeling of an open oscillatory heat pipe including gravity. International Journal of Thermal Sciences 43 (2004) 113-119.

[132] Y. Zhang, A. Faghri. Heat transfer in a pulsating heat pipe with open end. International Journal of Heat and Mass Transfer 45 (2002) 755-764.

[133] S. Kato, K. Okuyama, T. Ichikawa, S. Mori. A single, straight-tube pulsating heat pipe (examination of a mechanism for the enhancement

of heat transport). International Journal of Heat and Mass Transfer 64 (2013) 254-262.

[134] M. Rao, F. Lefèvre, S. Khandekar, J. Bonjour. Understanding transport mechanism of a self-sustained thermally driven oscillating two-phase system in a capillary tube. International Journal of Heat and Mass Transfer 65 (2013) 451-459.

[135] S. Khandekar, A.P. Gautam, P.K. Sharma. Multiple quasi-steady states in a closed loop pulsating heat pipe. International Journal of Thermal Sciences 48(3) (2009) 535-546.

[136] S.G. Kandlikar. Scale effects on flow boiling heat transfer in microchannels: a fundamental perspective. International Journal of Thermal Science 49 (2010) 1073-1085.

[137] C.Y. Lee, S.Y. Lee. Influence of surface wettablity on transition of two-phase flow pattern in round mini-channel. International Journal of Multiphase Flow 34 (2008) 706-711.

[138] T. Takamasa, T. Hazuku, T. Hibiki. Experimental study of gas-liquid two-phase flow affected by wall surface wettability. International Journal of Heat and Mass Fluid Flow 29 (2008) 1593-1602.

[139] P. Rapolu, S.Y. Son. Capillarity effect on two-phase flow resistance in microchannels. In: Proceedings of 18th International Symposium on Transport Phenomena (2007) 1431-1436.

[140] C.Y. Lee, S.Y. Lee. Pressure drop of two-phase plug flow in round mini-channels: influence of surface wettability. Experimental Thermal and Fluid Science 32 (2008) 1716-1722.

[141] S.Y. Son, J.S. Allen. Visualization and predictive modeling of two-phase flow regime transition with application towards water management in the gas-flow channels of PEM fuel cells. In: Proc. of IMECE2005 IMECE2005- 82422 (2005).

[142] D. Yu, C. Choi, M.H. Kim. The pressure drop and dynamic contact angle of motion of triple-lines in hydrophobic microchannels. In: Proc.

of 8th Int. Conf. on Nanochannels, Microchannels and Minichannels, Montreal, Canada (2010).

[143] C. Choi, J.S. Shin, D. I.Y. Kim, M.H. Kim. Flow boiling behaviors in hydrophilic and hydrophobic microchannels. Experimental Thermal and Fluid Science 35(5) (2011) 816-824.

[144] H. T. Phan, N. Caney, P. Marty, S. Colasson, J. Gavillet. Flow boiling of water in a minichannel: the effects of surface wettability on two-phase pressure drop. Apllied Thermal Engineering 31 (2011) 1894-1905.

[145] A.M. Barajas, R.L. Panton. The effects of contact angle on two-phase flow in capillary tubes. International Journal of Multiphase Flow 19 (2) (1993) 337-346.

[146] M. Iguchi, Y. Terauchi. Boundaries among bubbly and slug flow regimes in air–water two-phase flows in vertical pipe of poor wettability. International Journal of Multiphase Flow 27(4) (2001) 729-735.

[147] M. Iguchi, Y. Terauchi. Microgravity effects on the rising velocity of bubbles and slugs in vertical pipes of good and poor wettability. International Journal of Multiphase Flow 27(12) (2001) 2189-2198.

[148] T. Cubaud, C.M. Ho. Transport of bubble in square microchannels. Physics of Fluids 16 (2004) 4575-4585.

[149] T. Cubaud, U. Ulmanella, C.M. Ho. Two-phase flow in microchannels with surface modifications. Fluid Dynamics Research 38 (2006) 772-786.

[150] J.C. Allen, S.Y. Son. High speed microscopic visualization of adiabatic gas–liquid flow in microchannels. In: Proc. 18th International Symposium on Transport Phenomena, Daejon, Korea (2007).

[151] H. Ide, R. Kimura, K. Inoue, M. Kawaji. Effect of wetting on adiabatic gas–liquid two-phase flow in a microchannel. In: Proceedings of the 6th International Conference on Nanochannels, Microchannels and Minichannels, Darmstadt, Germany (2008).

[152] D. Myers. Surfaces, interfaces, and colloids: principles and applications, second ed. Wiley–VCH, New York (1999).

[153] C.Y. Lee, S.Y. Lee. Pressure drop of two-phase dry-plug flow in round mini-channels: effect of moving contact line. Experimental Thermal and Fluid Science 34 (2010) 1-9.

[154] G.W. Govier, G.A. Sullivan, R.K. Wood. The upward vertical flow of oil–water mixtures. The Canadian Journal of Chemical Engineering 39 (1961) 67-75.

[155] M.E. Charles, G.W. Govier, G.W. Hodgson. The horizontal pipe line flow of equal density oil–water mixtures. The Canadian Journal of Chemical Engineering 39 (1961) 27-36.

[156] T.Y. Liu, P.L. Li, C.W. Liu, C. Gau. Boiling flow characteristics in microchannels with very hydrophobic surface to super-hydrophilic surface. International Journal of Heat and Mass Transfer 54 (2011) 126-134.

[157] C. Choi, D.I. Yu, M. Kim. Surface wettability effect on flow pattern and pressure drop in adiabatic two-phase flows in rectangular microchannels with T-junction mixer. Experimental Thermal and Fluid Science 35 (2011) 1086-1096.

[158] R.W. Lockhart, R.C. Martinelli. Proposed correlation data for isothermal two phase two-component flow in pipes. Chemical Engineering Progress 45 (1949) 39-45.

[159] D. Yu, C. Choi, M.H. Kim. Pressure drop and dynamic contact angle of triple-line motion in a hydrophobic microchannel. Experimental Thermal and Fluid Science 39 (2012) 60-70.

[160] W. Rose, R.W. Heins. Moving interface and contact angle rate-dependency. Journal of Colloid Science 17 (1962) 39-48.

[161] G.E.P. Elliott, A.C. Riddiford. Dynamic contact angles: I. The effect of impressed motion. Journal of Colloid Science 23 (1967) 389-398.

[162] A.M. Schwartz, S.B. Tejada. Studies of dynamic contact angles on solids. Journal of Colloid and Interface Science 38 (1972) 359-375.

[163] R.L. Hoffman. A study of the interface. I. The interface shape in liquid-gas systems. Journal of Colloid and Interface Science 50 (1975) 228-241.

[164] T.S. Jiang, S.G. Oh, J.C. Slattery. Correlation for dynamic contact angle. Journal of Colloid and Interface Science 94 (1983) 470-486.

[165] M. Bracke, F. De Voeght, P. Joos. The kinetics of wetting: the dynamic contact angle. Progress in Colloid and Polymer Science 79 (1989) 142-149.

[166] J.E. Seebergh, J.C. Berg. Dynamic wetting in the low capillary number regime. Chemical Engineering Science 47 (1992) 4455-4464.

[167] M.M. Derby, A. Chatterjee, Y. Peles, M. K. Jensen. Flow condensation heat transfer enhancement in a mini-channel with hydrophobic and hydrophilic patterns. International Journal of Heat and Mass Transfer 68 (2014) 151-160.

[168] T. Hao, X. Ma, Z. Lan, N. Li, Y. Zhao, H. Ma. Effects of hydrophilic surface on heat transfer performance and oscillating motion for an oscillating heat pipe. International Journal of Heat and Mass Transfer 72 (2014) 50-65.